## *The imaging properties of large reflecting astronomical telescopes*

Dunlop, Colin Nigel

# THE IMAGING PROPERTIES

# OF

# LARGE REFLECTING ASTRONOMICAL

# TELESCOPES

by

COLIN NIGEL DUNLOP



A thesis submitted to the University of Durham
in candidature for the degree of
Doctor of Philosophy

April 1986

To My Parents

## ABSTRACT

This thesis is concerned with some of the limitations concerned with the imaging properties of astronomical telescopes of large apertures. These arise from the atmosphere, the diffracting aperture, the residual errors in the optically worked surfaces and the characteristics of the detection devices. Methods of Fourier optics are used to determine modulation transfer functions and associated point spread function. They are applied to three problems.

The first of these is a comparison of the diffraction patterns that are expected from the multi-mirror telescopes. These are made either of separated individual mirrors or of segmented mirrors shaped to an overall parabolic shape. The effect of the dilution of the aperture in the former and the effect of misalignment in the latter is investigated.

In the second study, the factors contributing to the imaging of the UK Schmidt telescope are considered and design studies of this and other two variants are examined. In particular the limiting effect of the atmosphere and of the detecting photographic emulsion are noted.

Thirdly the overall limitation of the atmospheric seeing is considered experimentally. The Durham Polaris seeing monitor has been designed and built with a shear interferometer. It has been tested at local ground level where local measurements of seeing have been made. In the near future it will be taken and used at La Palma.

CONTENTS

# LIST OF FIGURES

## LIST OF TABLES



## LIST OF PLATES

# CHAPTER 1 INTRODUCTION

Large optical telescopes with their enhanced light collecting power have been developed and used for some time now to detect faint objects deep in the Universe. In recent times, improvements in methods of detection have increased the effective use of the light collection capability of telescope mirrors. For example, the 5m Hale telescope with charged coupled devices for detection is equivalent to a 50m telescope where light is detected and recorded by the photographic plates of 1950 vintage. The sensitivity of detection is unlikely to increase much further and so in order to penetrate deeper into the Universe (that is to detect the very distant, very faint objects) increases in mirror size are again being contemplated.

Apart from the technical difficulties of producing very large mirrors the main problem is that of cost. Doubling the size of a mirror is found to lead to an approximate eight-fold increase in price so that a 25m mirror telescope (including dome and other facilities) would cost in the region of 100M pounds. Instead of a large monolithic mirror the same light collecting power could be obtained with an array of mirrors each of small size and hence with correspondingly low cost. This would halve the price of the mirror approximately. Clearly an evaluation of the optical performances of monolithic and arrays of mirrors must be carried out. Furthermore, with costs so high the optimum performance of a system must be achieved. An optimum

becomes apparent when it is appreciated that the performance of a telescope (that is, the quality of the image produced) is determined by turbulence in the atmosphere and in the air inside the dome, by the mirror aperture, its surface irregularities, the stiffness of the support and the quality of the detector. Cost effectiveness is approached by considering the effects of each of these on the quality of the image and designing a telescope with these effects in mind.

The effects of atmospheric turbulence, aperture diffraction and surface errors will be determined either separately or together. Because of the complex nature of the interaction of these three effects it has not been possible to describe the imaging properties of the telescopes in a satisfactory way. However the effect of these degradations to the image can be handled by Fourier transform techniques which lead to the use of the modulation transfer function, MTF. The advantage of using the MTF is that if these functions can be calculated individually for atmospheric turbulence, aperture diffraction and surface error, then the MTF for the whole atmosphere-mirror system is the product of the individual values. The inverse Fourier transform then yields the distribution of light within the image (point spread function, PSF). To deal with this same problem using the point spread function directly, the individual PSFs must be convoluted together to obtain the system PSF. This is much more laborious and very consuming of computing time. The methods of Fourier transforms and the calculations of the PSF and MTF are outlined in chapter 2.

The image quality of a large ground based astronomical telescope is largely governed by turbulence in the atmosphere, with aperture diffraction and surface errors playing less important roles (except in the far infrared region, where atmospheric turbulence becomes less important). Changes of pressure and temperature in the atmosphere cause changes in its density and refractive index which will result in the distortion of the light wavefront passing through the atmosphere. This will cause the image to exhibit effects of motion, blurring and twinkling. In astronomical observations this effect is called "seeing" and represents the major limitation on resolution.

Three degradations of atmospheric turbulence, aperture diffraction and surface errors and their MTFs are described individually in chapter 3. The firm of Grubb-Parsons, Newcastle have made available to us some of their measurements of surface quality of several mirrors which enable us to find realistic MTFs for surface errors.

The development of MTF based methods of calculating optical system performance and the knowledge of the properties of the turbulent atmosphere have provided means by which the performance of ground based telescopes can be assessed in a realistic way, in which the whole process from the top of the atmosphere to the image in the photographic emulsion is taken into account. An example considered is the Schmidt telescope and this is described in chapter 4.

In a large multi-mirror telescope, there are many ways of combining the mirrors, of which there are broadly two choices.

The first is a large segmented aperture formed from a number of hexagonal mirrors which are joined at their edges and which are individually figured to give, in combination, a single parabolic mirror with one primary focus (see fig 1.1). The other choice is for an aperture made from a number of separate paraboloids each figured identically and mounted on a regular array with parallel optic axes to give a number of primary foci. These are then combined to give one single focus. The diffraction patterns of a variety of mirror combinations are shown in chapter 5.

The multi-mirror combination leads to a diluted aperture whose diameter can be controlled from a minimum value (when all mirrors are touching) to higher values which are controlled by the cost of mounting well separated mirrors. The effects of dilution are described in chapter 6.

Chapter 7 describes the measurement and monitoring of atmospheric seeing. A seeing monitor has been designed which uses a 30cm diameter mirror to image Polaris, whose light after passing through the atmosphere is examined by a shear interferometer. The interferometer shears the wavefront of light on itself so that variations in phase in the wavefront become apparent as changes in visibility of interference wedge fringes. By scanning across the fringes with a raster scan, the MTF can be measured as a function of shear. The seeing monitor has been built and tested at local seeing. The seeing monitor will be taken and tried at La Palma in the near future.

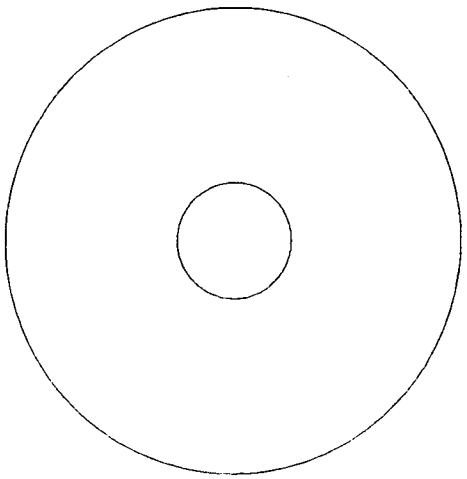

a) monolithic mirror

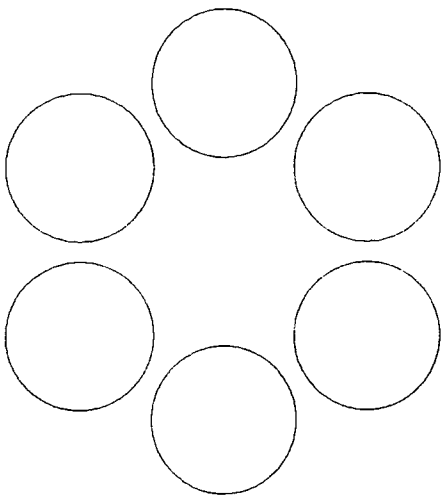

b) 6 circular mirrors

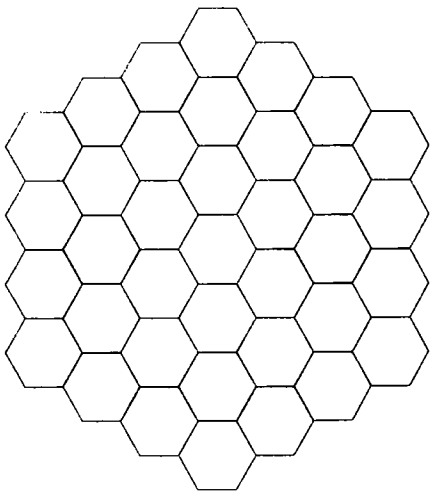

c) 36 hexagon segmented mirrors

FIG 1.1 Telescope mirrors

# CHAPTER 2 POINT SPREAD FUNCTION AND MODULATION TRANSFER FUNCTION

## 2.1 POINT SPREAD FUNCTION

In any imaging system light is gathered from a point or extended source and channelled into an image. The structure of the image is largely determined by the object but this is modulated by characteristics of the imaging system. For example in an astronomical telescope system there will be contributions to the image structure from the atmosphere, diffraction by the aperture, aberrations and noise from the recording system. Hence the light from a 'point' star is spread into a small area around the expected point image.

If $I_o(X,Y)$ is the intensity distribution in the object plane, the point X,Y will emit a radiant flux which is then processed by the imaging system represented by a lens (fig 2.1). The radiation will be imaged at the point x,y in the image plane (and the small area surrounding this point) where x,y is obtained by geometric imaging. The spreading of this radiant flux by the imaging system is described by the intensity distribution function $S(x-X,y-Y)$ for a point source, which is known as the point spread function, or PSF. Hence the intensity distribution at the image plane for an extended object is

$$I_i(x,y) = \iint I_o(X,Y)\, S(x-X,y-Y)\, dXdY \quad . \qquad (2.1)$$

This equation is a convolution integral which can be written as

$$I_i(x,y) = I_o(X,Y) \circledast S(x-X,y-Y) \quad . \qquad (2.2)$$

If the source is a point object (eg a star on the central axis,

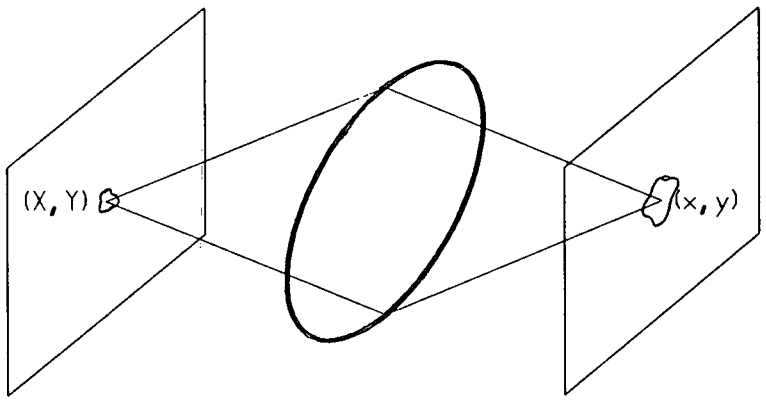


FIG 2.1 A lens system forming an image

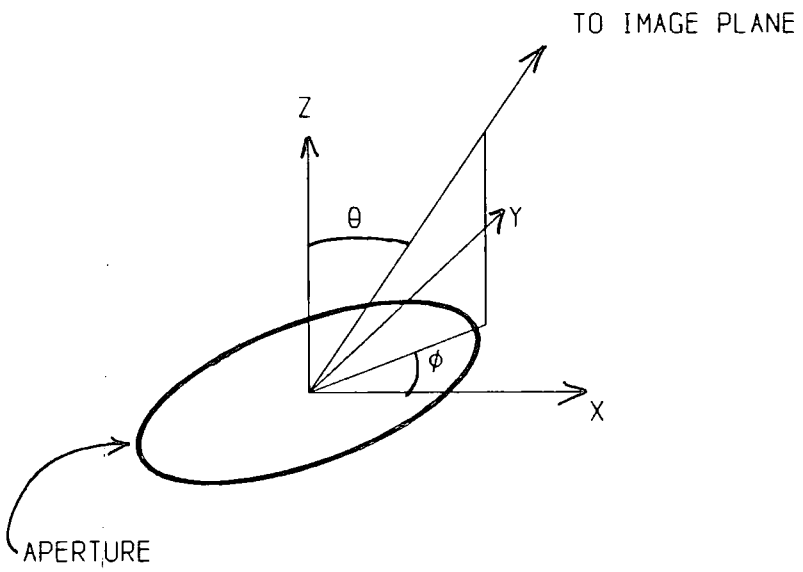


FIG 2.2 Aperture in polar coordinates

X=0, Y=0) then the intensity distribution of image, $I_i(x,y)$, becomes the PSF, $S(x,y)$.

For a diffraction-limited imaging system having no aberrations, $S(x,y)$ would correspond in shape to the diffraction pattern at x,y of a point source which is easily calculated for most geometries. Since the PSF is a squared modulus of the amplitude distribution, $a(x,y)$, then

$$S(x,y) = |a(x,y)|^2 . \qquad (2.3)$$

The amplitude distribution is a Fourier transformation of the aperture function $f(u,v)$, where u,v are spatial frequencies. The aperture function usually has a constant value of unity over the whole area of the aperture and is zero outside. (It would vary from unity with apodization). So the amplitude distribution is

$$a(x,y) = \iint f(u,v) \exp\{-2\pi i(xu+yv)\}\, dudv . \qquad (2.4)$$

In astronomy, measurements of the stellar image are usually made in terms of angular distance (such as arcsec or arcmin). In polar coordinates the PSF is, (fig 2.2),

$$S(\Theta,\phi) = |a(\Theta,\phi)|^2 , \qquad (2.5)$$

and

$$a(\Theta,\phi) = \iint f(u,v) \exp\{iksin\Theta\,(ucos\phi + vsin\phi)\}\, dudv , \qquad (2.6)$$

where $\Theta$ is the polar angle, $\phi$ is the azimuth angle and $k = 2\pi/\lambda$.

The Fourier transform, $\mathcal{F}$, of equation 2.2 gives

$$\mathcal{F}[\, I_i(x,y)] = \mathcal{F}[\, I_o(X,Y) \circledast S(x-X,y-Y)\, ] , \qquad (2.7)$$

and by application of the convolution theorem,

$$\mathcal{F}[\, I_i(x,y)] = \mathcal{F}[\, I_o(X,Y)]\, \mathcal{F}[\, S(x-X,y-Y)] , \qquad (2.8)$$

that is

$$i_i(u,v) = i_o(u,v)\ T(u,v)\ . \qquad (2.9)$$

Here $i_i(u,v)$ is the spatial frequency content of the image intensity distribution and it is given by the product of the spatial frequency content of the object intensity distribution and a complex quantity, $T(u,v)$, which is commonly known as the optical transfer function, OTF, ie

$$T(u,v) = \iint S(x,y)\ \exp\{-2\pi i(xu+yv)\}\ dxdy\ . \qquad (2.10)$$

Clearly this is the Fourier transform of the PSF. It can be expressed as

$$T(u,v) = MTF(u,v)\ \exp\{iPTF(u,v)\}\ , \qquad (2.11)$$

where the modulation transfer function, MTF, is a measure of the reduction in contrast from object to image over the frequency spectrum. The argument of the OTF is the spatial phase tranfer function, PTF, which represents the relative shift of the image pattern from its normal position. Phase shifts in centered imaging systems occur only off-axis and often the PTF is of less interest than the MTF. Consequently the MTF, rather than the OTF, is considered in the next section.

## 2.2 MODULATION TRANSFER FUNCTION

As seen above, in the absence of phase modulation the MTF becomes the Fourier transform of the point spread function. It is a measure of the modulation or contrast of features which exist in the exit aperture at various spatial frequencies and it can be expressed in either linear or angular dimensions as

$$MTF(cycles/arcsec) = MTF(cycles/mm) * f/(2.063x10^{4})\ , \qquad (2.12)$$

where f is the focal length of the imaging system in cms. The

MTF has become a widely used means of specifying the performance of a variety of systems such as lenses, telescopes, the atmosphere, the eye, photographic films and magnetic tapes.

To illustrate the meaning of MTF consider that the input to an imaging system has a sinusoidual intensity distribution in the object plane with a spatial frequency of w cycles/mm. Then the object modulation is defined as, (fig 2.3),

$$M_o(w) = \frac{I_a - I_b}{I_a + I_b} .$$

After passing through the imaging system, the image modulation becomes

$$M_i(w) = \frac{I'_a - I'_b}{I'_a + I'_b} .$$

The ratio between image modulation and object modulation is then the MTF at the spatial frequency, w,

$$MTF(w) = \frac{M_i(w)}{M_o(w)} . \qquad (2.13)$$

The structure of a general object is expressed as a spectrum of spatial frequencies for each of which an MTF(w) exists. These comprise the complete MTF for the system. It can be determined experimentally by measuring the modulation in the image obtained from a grating-like target having decreasing line separations (increasing spatial frequencies). Target patterns such as these are used routinely for assessing the reproduction quality of copying machines and television systems. The MTF of optical systems are usually measured by interferometric methods.

There are several methods for calculating the MTF of an optical system. One of the methods, which although it involves the computation of the aperture function including the effects

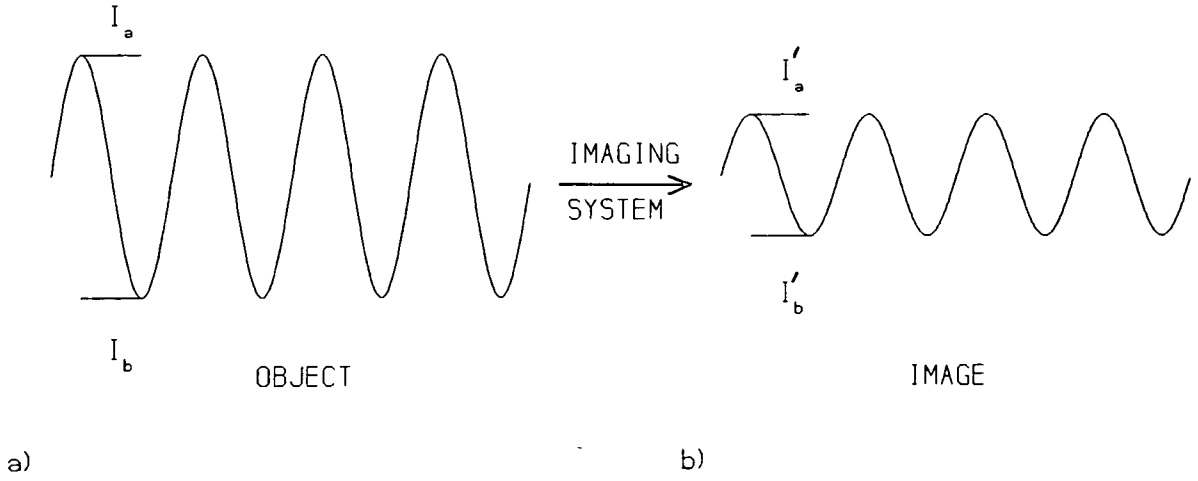


FIG 2.3 Harmonic object and resulting image

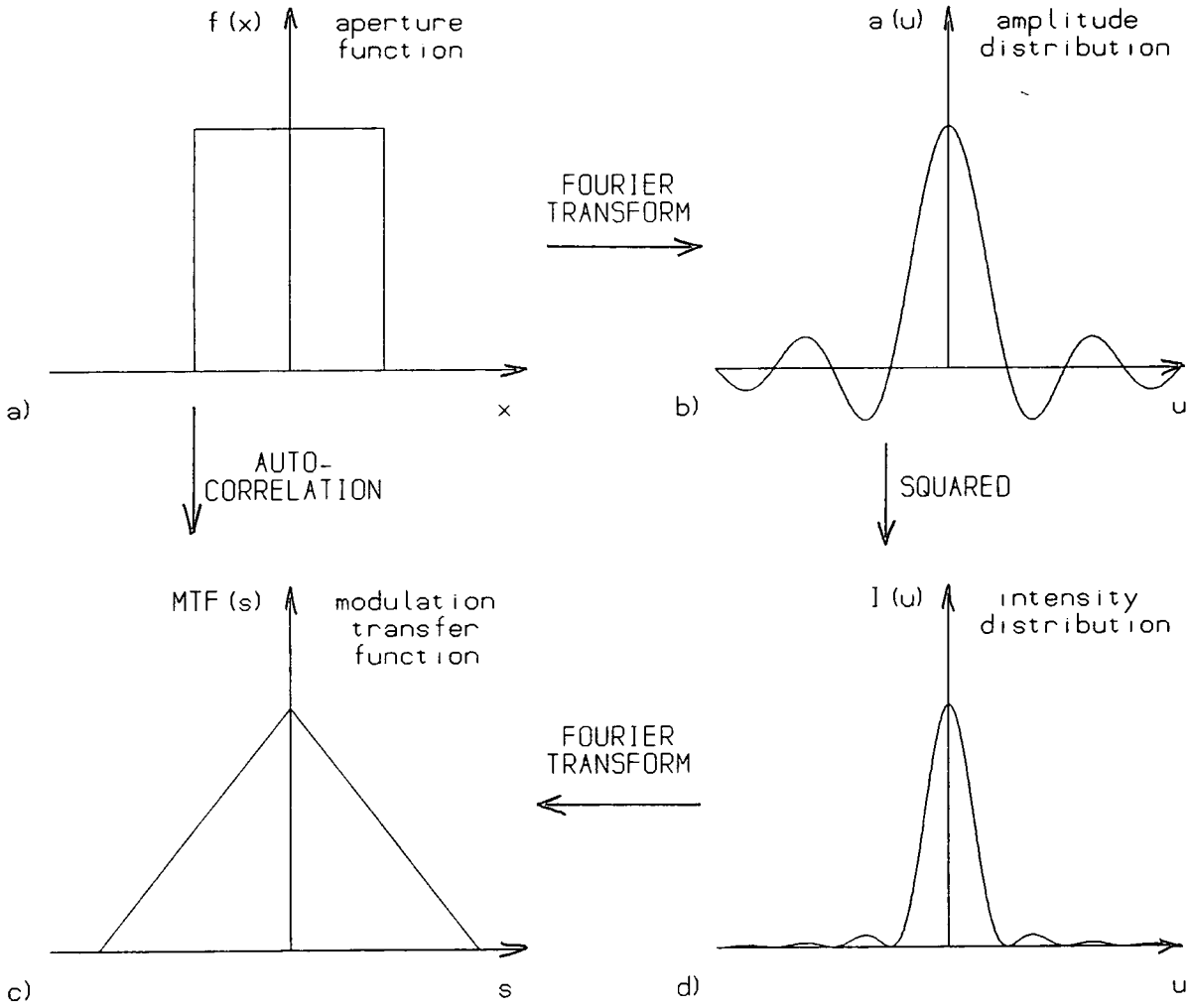


FIG 2.4 Example of Fourier transformation and autocorrelation

of aberrations does, however, lead to a quite straightforward calculation. The amplitude diffraction pattern of the image of a point source is a Fourier transform of the aperture function, f(x,y) of the diffracting system. The squared modulus of this is the PSF, and the Fourier transform of that is the MTF. This is shown symbolically in one dimension in fig 2.4. The calculation route just described is (a)→(b)→(d)→(c), ie

$$MTF(u,v) = \mathcal{F}\{|\mathcal{F}(f(x,y))|^2\} . \qquad (2.14)$$

We can use a short cut in the calculation (ie from (a) to (c)) by using the autocorrelation theorem. By calculation of the autocorrelation of the aperture function, the MTF is given by

$$MTF(u,v) = \frac{\iint f(x,y)\, f(x-\lambda u, y-\lambda v)\, dxdy}{\iint f(x,y)^2 dxdy} . \qquad (2.15)$$

Consider an imaging system with an aberration-free aperture, then the aperture function, $f(x-\lambda u, y-\lambda v)$ is identical in form with f(x,y) but shifted by a length, $\lambda(u^2+v^2)^{1/2}$. The expression 2.15 for the MTF has a geometrical interpretation. The numerator represents the overlap of two displaced aperture functions, one centered at (0,0) and the second centered at the shifted $(\lambda u, \lambda v)$ as shown in fig 2.5. The denominator simply normalises this area of overlap by the total area of the aperture. Thus

$$MTF = \frac{\text{area of overlap}}{\text{total area}} . \qquad (2.16)$$

When the aperture function has been displaced upon itself by the size of the aperture, D, the overlap area is zero and hence the MTF is zero. This occurs at a maximum, cut-off, $\frac{1}{\lambda}$ angular spatial frequency in the direction of displacement of

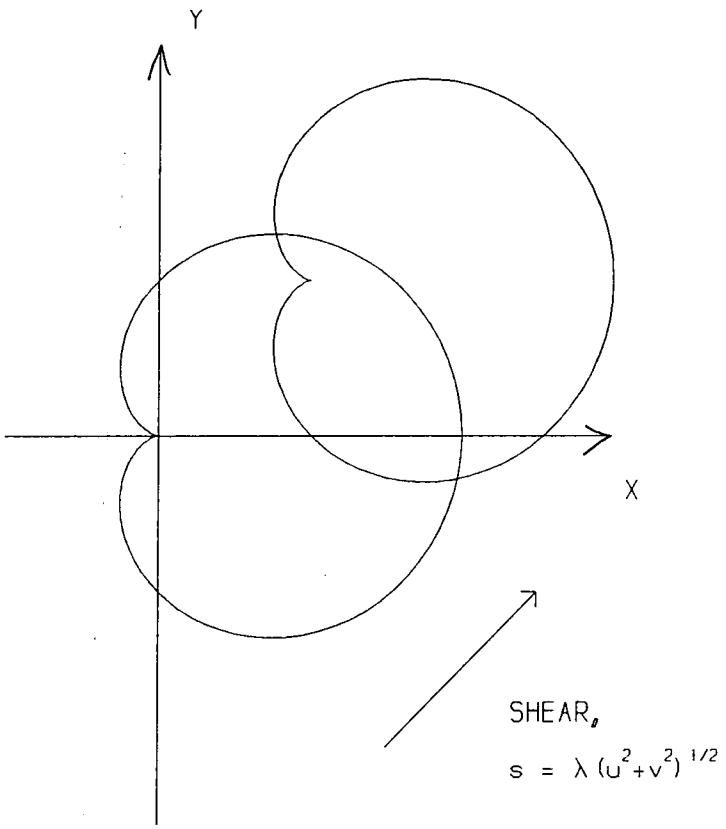


FIG 2.5 Two sheared aperture functions

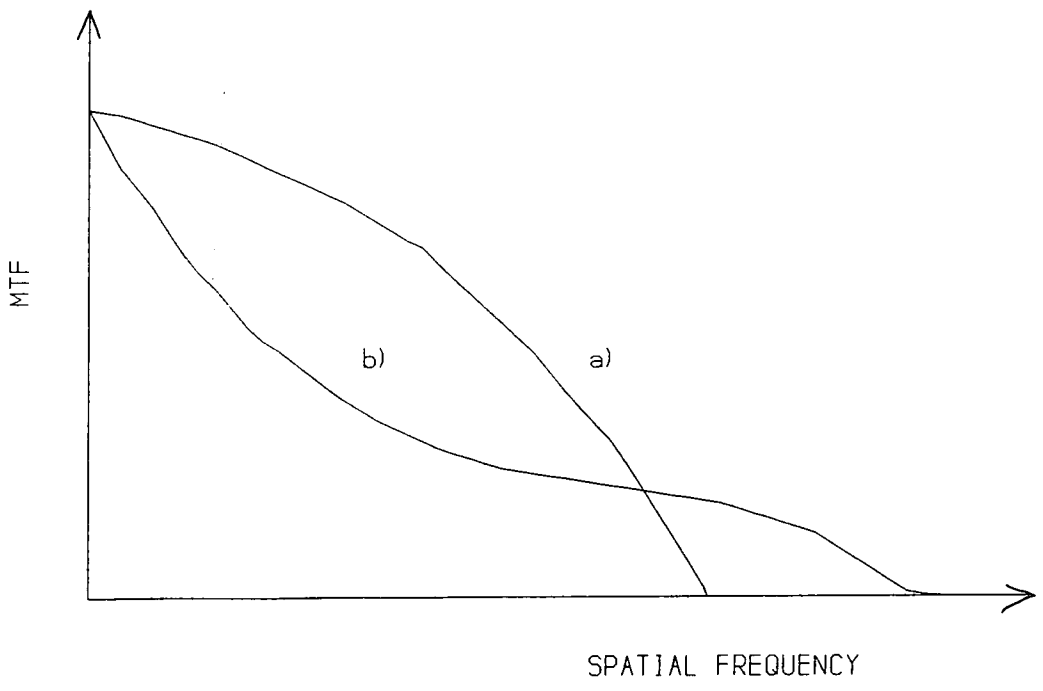


FIG 2.6 The MTF of two different apertures

$$w_c = \frac{D}{2.063 \times 10^5 \lambda} \text{ cycles/arcsec.} \qquad (2.17)$$

Thus, features which exist in the object at separations equivalent to spatial frequencies $w > w_c$ will not appear in the image since the system is incapable of transmitting information for frequencies beyond the cut-off value. Different imaging systems will have different values of cut-off frequency.

After measuring the MTF of different apertures the situation described in fig 2.6 might result. Curve (a) with the greater value of MTF at lower frequencies will lead to contrasting images but curve (b) will lead to better resolution since it has a higher cut-off frequency. When observing stellar images, the resolution is usually important ie the MTF values must be large at high values of spatial frequency. This will be seen in the case of an annular mirror as described in chapter 3.

The most important properties of the MTF are listed below:

a) $MTF(0,0) = 1$ ,

b) $MTF(-u,-v) = MTF(u,v)$ ,

c) $MTF(u,v) \leq MTF(0,0)$ .

When the wavefront errors at the aperture (such as focussing error, spherical aberrations or surface polishing errors) exist, the phase error in the wavefront at the point x,y in the exit aperture is represented by $kW(x,y)$ where W is an effective path length error. Then the aperture function becomes

$$f(x,y) = \alpha(x,y) \exp\{ikW(x,y)\} , \qquad (2.18)$$

where $\alpha(x,y) = 1$ inside the aperture and $= 0$ outside. For an aberration-free system, $W(x,y) = 0$ and so $f(x,y) = 1$ or 0. In general the aperture function is complex so it is the OTF rather

than the MTF that should be considered. Then

$$T(u,v) = \frac{\iint f(x,y)\, f^{*}(x-\lambda u, y-\lambda v)\, dxdy}{\iint |f(x,y)|^{2}\, dxdy} \qquad (2.19)$$

and this can be rewritten as

$$T(u,v) = \frac{1}{A}\iint \exp\{ik\delta\}\, dxdy\ , \qquad (2.20)$$

where the integral is evaluated over the area of overlap. Here $\delta$ is the wavefront difference between the wavefront, $W(x,y)$ and the sheared wavefront, $W(x-\lambda u, y-\lambda v)$ and A is the total area of the aperture. This expression can be written as

$$T(u,v) = \frac{1}{A}\iint [\cos(k\delta) + i\sin(k\delta)]\, dxdy\ . \qquad (2.21)$$

When there are random wavefront errors on the surface, the average of the sine function reduces to zero and the average of the cosine function becomes less than unity. Hence the OTF becomes real and the MTF is given by

$$MTF(u,v) = \frac{1}{A}\iint \cos(k\delta)\, dxdy\ , \qquad (2.22)$$

which is now smaller than it was when there were no wavefront errors. This expression allows us to relate the wavefront errors and the MTF. The expression 2.22 reduces to that of 2.16 when the wavefront errors are negligible.

In general, aberrations will lower the MTF of each spatial frequency component of image intensity and hence the PSF will be broadened.

## 2.3 NUMERICAL CALCULATION

There are two calculations considered - one involving a single individual system eg diffraction only or other degradation. The other involves an overall system ( with atmospheric seeing, diffraction, etc)

### 2.3.1 Individual System

When dealing with the intensity distribution of a point source due to diffraction by an aperture of simple geometry, the calculation is best performed using the analytic Fourier transform of the aperture function (eq 2.4). This will give a relatively simple analytic expression. For difficult geometries, or for simple apertures made complicated by surface errors and aberrations, the Fourier transform of the two-dimensional MTF is necessary. This is one of considerable numerical integration and it has become possible only by computer methods.

When calculating Fourier transforms numerically, the integral expression in equation (2.10) is replaced by a summation. The continuous function, MTF(u,v) is replaced by a step-wise function, MTF(jdu,kdv), where the indices j and k run from -N/2 to +N/2 covering N points in total where du and dv are the increments. Then a value of S(x,y) in the PSF is found by summation of values of MTF(u,v)exp{2πi(xu+yv)} for all values of u and v in the increments du and dv:

$$S(x,y) = S(ldx,mdy) ,$$

$$= \sum_j \sum_k MTF(jdu,kdv)\exp\{2\pi i(ldxjdu+mdykdv)\}\, dudv . \qquad (2.23)$$

This transform is specified by values dx,dy up to an angular distance of $x_m$, $y_m$ (see fig 2.7 for a one-dimensional example). The main calculational problem is that of selecting incremental sizes for the calculation which are small enough to give accuracy but big enough to give sensible computing times. The optimum values of the increments can be found by the sampling theorem:

$$dx = 1/u_c \ , \quad x_m = 1/du \ , \tag{2.24}$$

where $u_c$ is a cut off frequency.

The procedure is repeated for different values of x,y in the intervals dx and dy to give a complete two-dimensional PSF. This is usually normalised to unity at the centre of the image.

Some reduction in computing time can be made when there is circular symmetry ie MTF(w) where $w = (u^2+v^2)^{1/2}$. Then its Fourier transform simplifies to a one-variable Hankel transform:

$$S(r) = \int MTF(w)\ J_o(2\pi wr)\ w\ dw \ . \tag{2.25}$$

Here $J_o$ denotes the zero-order Bessel function and r is the angular distance measured from the centre of the image, $r = (x^2+y^2)^{1/2}$. Values of the Bessel function are available from the software library of the computer. This method is suitable for a circular or annular mirror and also for averaged effects of atmospheric turbulence which is circular symmetric.

### 2.3.2 Overall System

However, when dealing with the overall imaging system performance of a telescope, the combined effects of the sources of the various degradations (eg atomspheric seeing, aperture

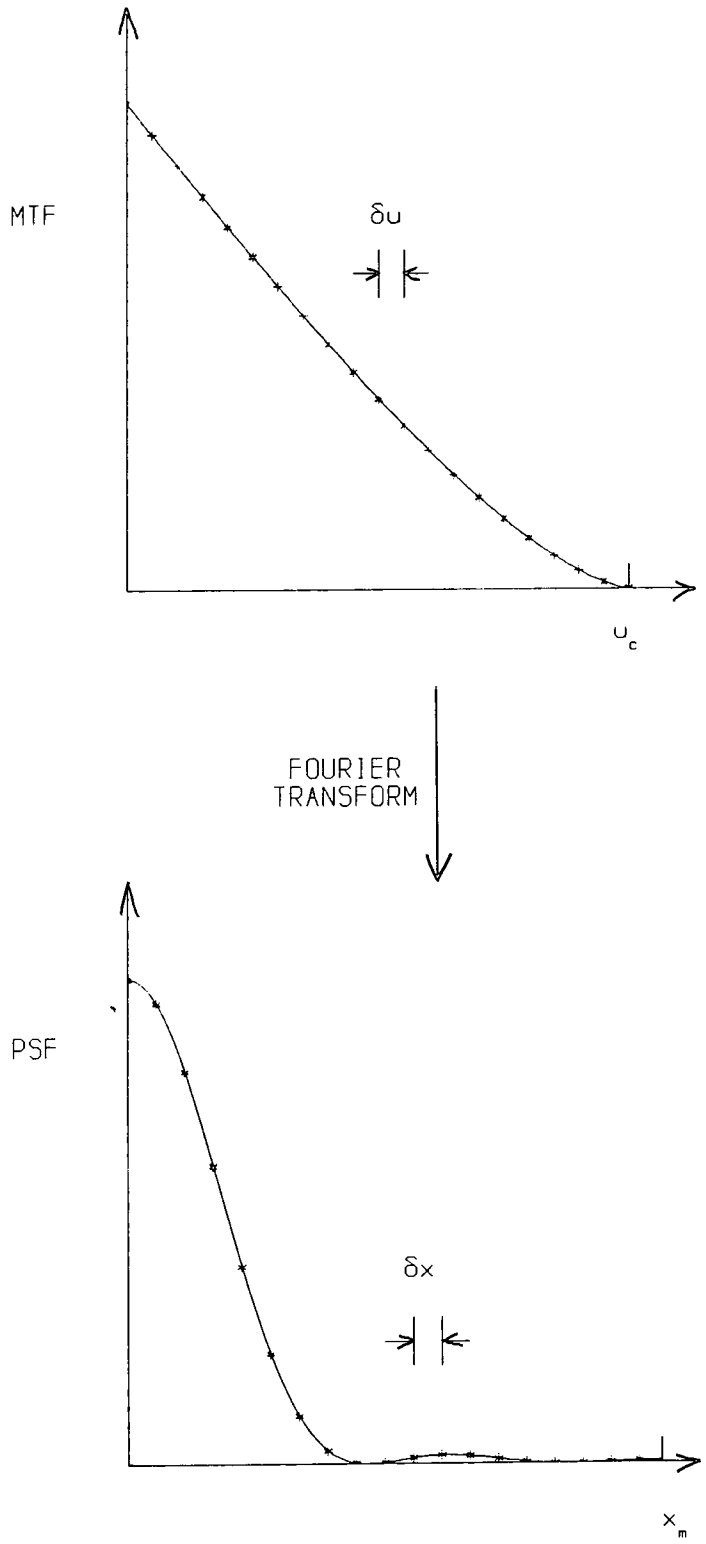


FIG 2.7 Illustration of the sampling theorem

diffraction, surface errors, etc) have to be calculated. If the individual PSFs for each degradation are known, the overall PSF is given by the joint convolutions:

$$S(x,y) = S_1(x,y) \circledast S_2(x,y) \circledast S_3(x,y)\ldots \quad , \qquad (2.26)$$

ie the individual PSFs are convoluted to obtain the system PSF. This series of convolutions is a laborious procedure. However from the Fourier transform of eq 2.26 (using the convolution theorem),

$$MTF(u,v) = MTF_1(u,v) \times MTF_2(u,v) \times MTF_3(u,v)\ldots \quad , \qquad (2.27)$$

provided the phase transfer functions are negligible. So the system MTF at any spatial frequency is the product of the individual MTFs of the system components. Multiplication is much simpler than convolution. After this, the intensity distribution in the image of a point source is readily calculated by the Fourier transform of the system MTF as described above.

The total MTF is often simply the product of individual MTFs. But, this is inapplicable to combined lenses since the aberrations in one lens may be designed to compensate for those of another lens to produce an image quality for the combination which is superior to that of either component. Then the wavefront errors due to the optical surfaces and optical misaligments must be added for the combined lenses to give an overall MTF which is then used with other MTFs in multiplication.

In the next chapter the modulation transfer function associated with the atmosphere, the diffracting aperture of the

mirror and the surface irregularities of the mirror are considered in detail. For these the overall MTF will be given by

$$MTF = MTF_{atmos} MTF_{aper} MTF_{surf} .$$

When the detection and recording of the image is considered then MTFs associated with these must also be taken into account. An example with photographic recording is considered in detail in chapter 4 in which the scattering of light in the emulsion and the graininess of the image are evaluated. Then

$$MTF = MTF_{atmos} MTF_{aper} MTF_{surf} MTF_{photo} .$$

The overall point spread function is the

$$PSF = \mathcal{F}(MTF) .$$

# CHAPTER 3 MODULATION TRANSFER FUNCTIONS ASSOCIATED WITH APERTURE DIFFRACTION, ATMOSPHERIC SEEING AND SURFACE ERRORS

## 3.1 APERTURE DIFFRACTION

As was seen in chapter 2, the modulation transfer function of the aperture diffraction due to an unobstructed circular mirror can be calculated as the ratio between the overlap area of the two sheared figures and the total area. Since the MTF of a circular mirror is symmetric, it can be calculated along a radial direction. As illustrated in fig 3.1, the MTF is given in terms of spatial frequency, w, by:

$$MTF(w) = \frac{2}{\pi}\left[\cos^{-1}\frac{\lambda w}{2r} - \frac{\lambda w}{2r}\sqrt{1-\left[\frac{\lambda w}{2r}\right]^2}\right], \qquad (3.1)$$

in the range between 0 and 2r. Outside the diameter, the MTF is zero and this gives the cut-off frequency:-

$$w_c = \frac{2r}{2.063\times10^5\lambda} \text{ cycles/arcsec.} \qquad (3.2)$$

The MTF for a single circular mirror is shown in fig 3.2.

However, many telescopes (such as Cassegrain, Maksutov, Schmidt- Cassgrain telescopes) have secondary mirrors that block light from reaching the centre of the primary mirror and hence make it effectively annular. Thus its diffraction characteristics are altered. The presence of the central obstruction of an annular mirror complicates the calculation of the MTF. However it can be solved analytically (O'Neill ref 3.1) as summarised in Appendix C. The MTFs of the annular aperture at various central obstructions are shown in fig 3.3.

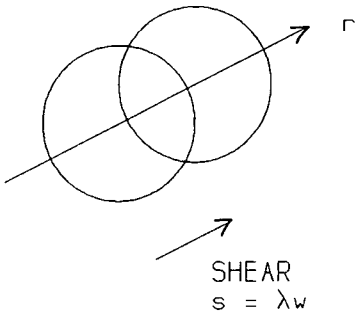


FIG 3.1 Two sheared circles

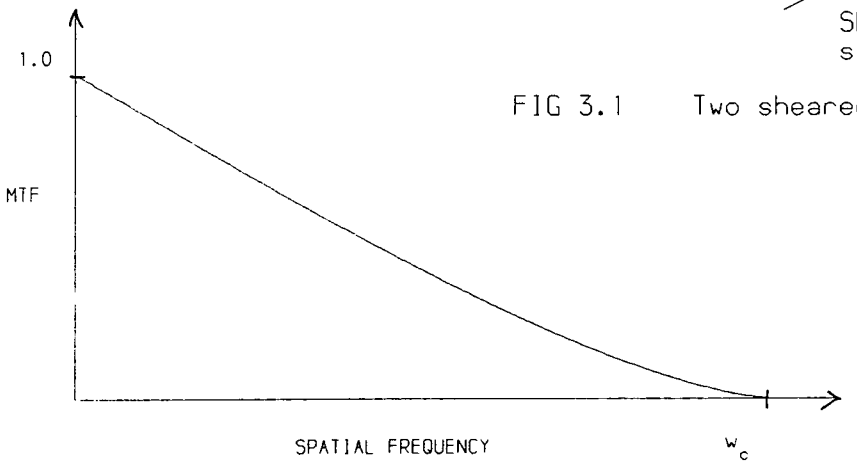


FIG 3.2 MTF of circular aperture

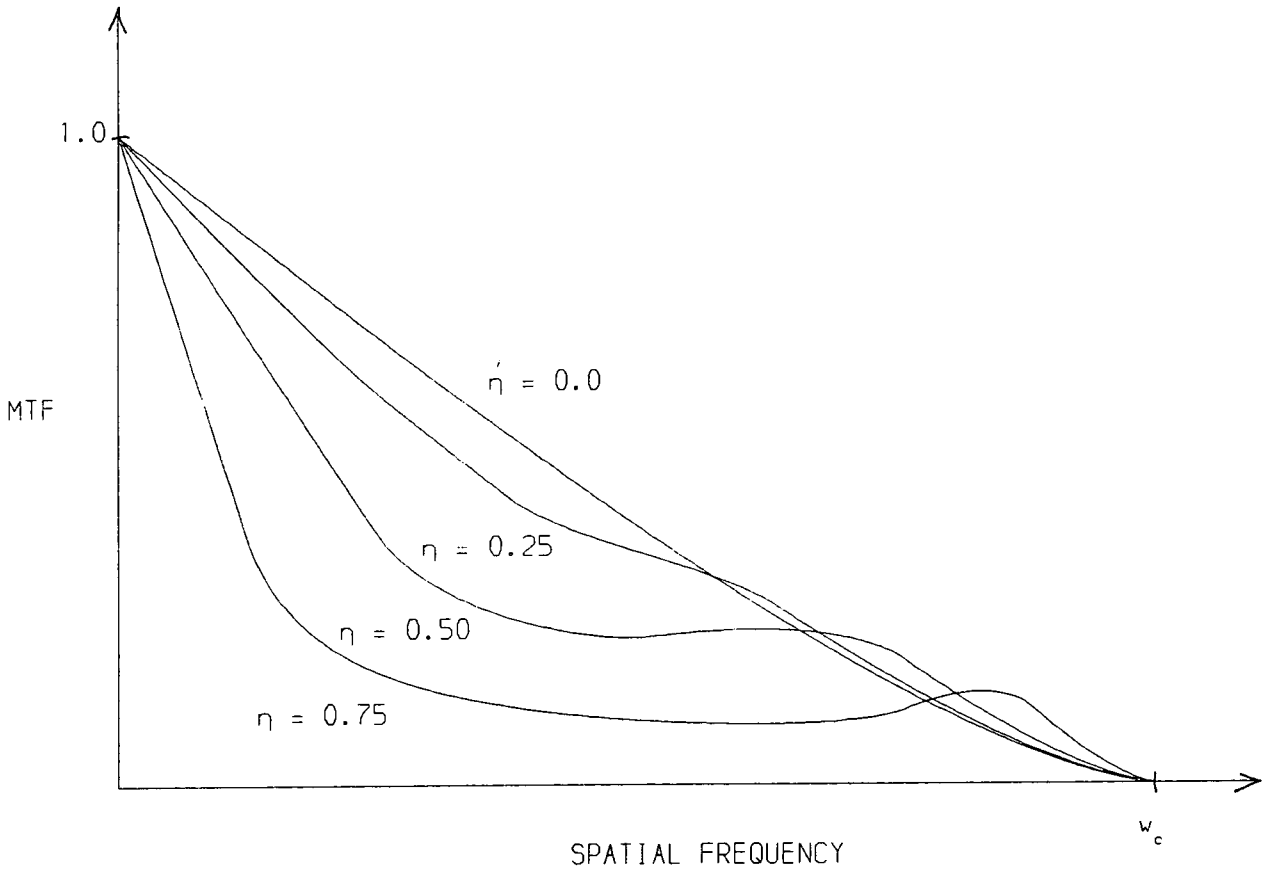


FIG 3.3 MTF of various annular apertures

($\eta$ is the ratio of the inner and outer radii of the annulus). These curves show that the high spatial frequency response of the system is improved at the expense of low frequency detail ie increased resolution but reduced contrast. After Fourier transformation, this implies a decrease in the width and height of the central maximum with more light passing into the outer rings of the point image diffraction pattern. These effects can be seen in the two - dimensional figures of MTF and PSF, (figs 3.4a-d) for increasing sized central obstructions. In figures 3.4a-d the intensity has been normalised to a fixed central maximum intensity of unity. This has been done so that the contraction of the Airy disc can be seen in the graphs. The task of handling these three - dimensional solids viewed in perspective, is conveniently done by computer graphics (GHOST).

There is a problem of computing time when making a Fourier transformation of a two-dimensional MTF to produce a two-dimensional PSF. However for a symmetric system, the 2-D PSF can be easily and much more quickly calculated from the square of the amplitude of the wavefront. For an unobstructed circular mirror, (following from equation 2.6 and because of circular symmetry) the amplitude depends only upon the polar angle, $\Theta$, and is written:

$$a(\Theta) = \frac{c\pi r^2 J_1 (krsin\Theta)}{krsin\Theta} , \qquad (3.3)$$

where c is a constant, $k = 2\pi/\lambda$ and $J_1$ is the first order Bessel function.

For the annular aperture with outer and inner radii of $r_1$ and $r_2$, the amplitude is then

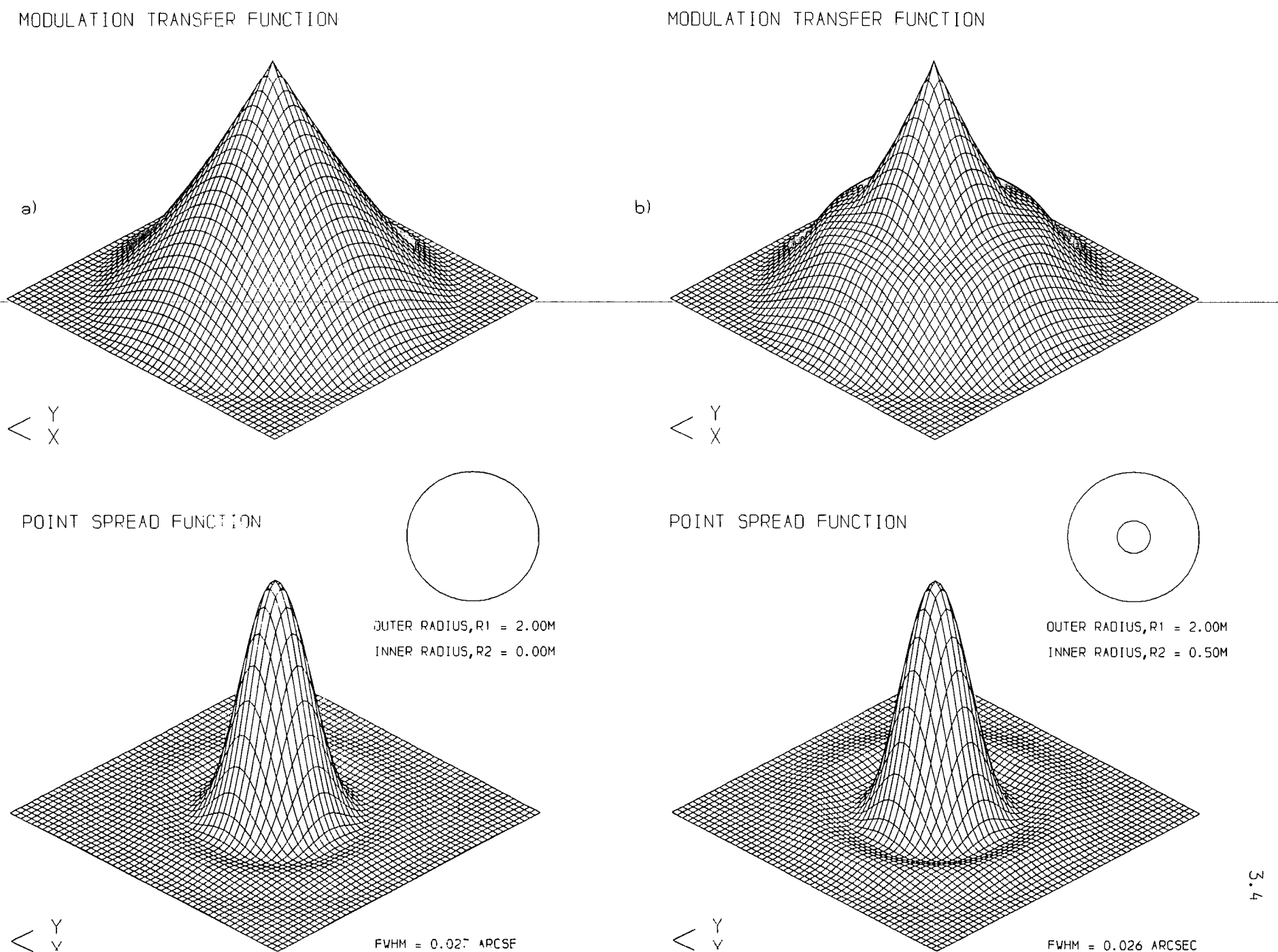


FIG 3.4 MTF and PSF of annular apertures, a) η = 0.0, b) η = 0.25

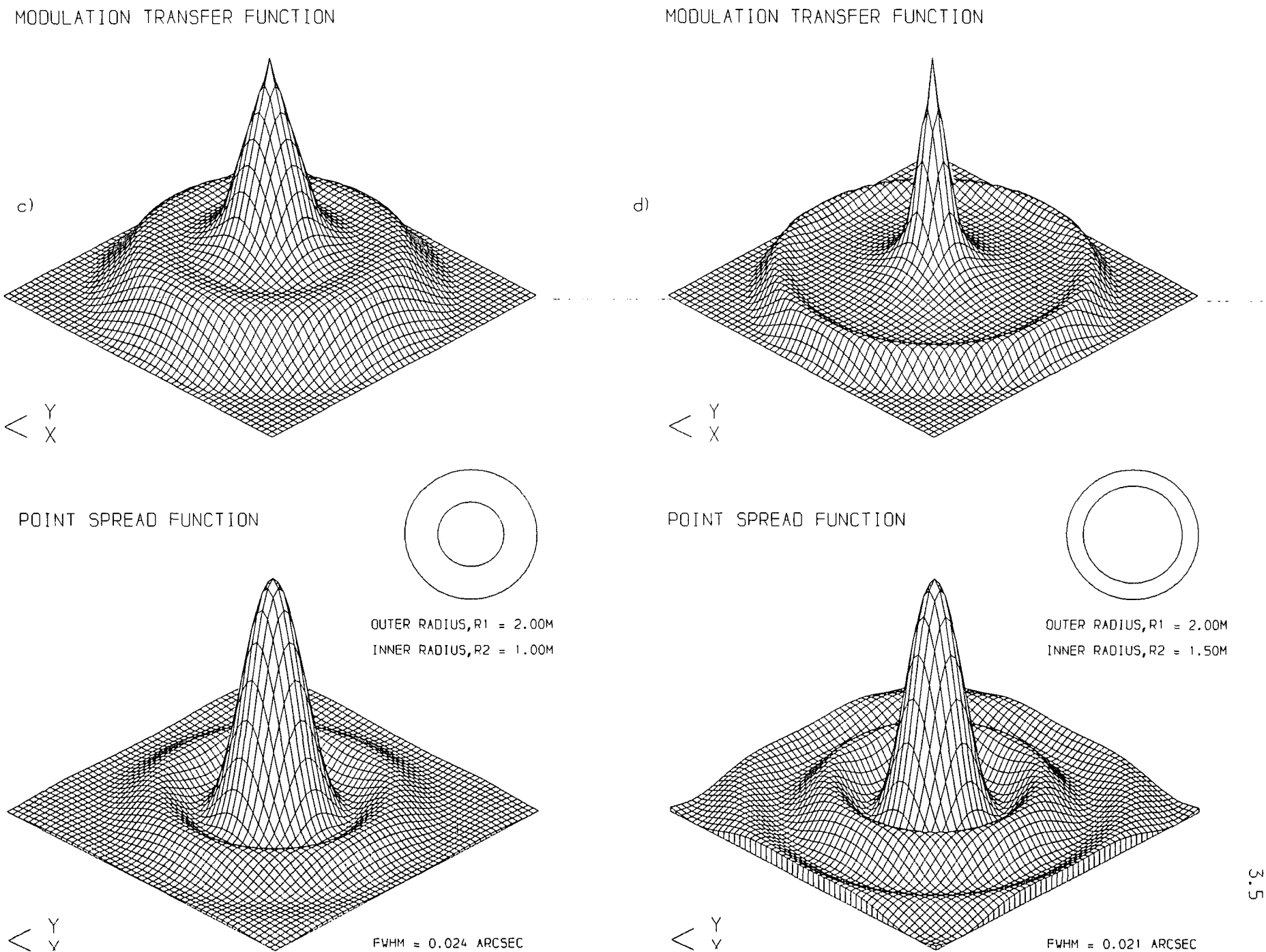


FIG 3.4 MTF and PSF of annular apertures, c) $\eta = 0.5$, d) $\eta = 0.75$

$$a(\Theta) = c\left[\frac{\pi r_1^2 J_1(kr_1 \sin\Theta)}{kr_1 \sin\Theta} - \frac{\pi r_2^2 J_1(kr_2 \sin\Theta)}{kr_2 \sin\Theta}\right] . \qquad (3.4)$$

The intensity distribution, or PSF, is therefore given by

$$I(\Theta) = |a(\Theta)|^2 . \qquad (3.5)$$

This will have a maximum at $\Theta = 0$ of $I_o = (c\pi(r_1^2 - r_1^2))^2$ ie $I_o$ depends upon the collecting area.

In fig 3.5 the contributions to the diffracted amplitude of equation 3.4 are shown as 'outer' and 'inner' curves. Their difference is the diffracted amplitude of the annulus. The first zero of this curve gives the first minimum in intensity (the Airy disc). Obviously this occurs at an angle less than that corresponding to the outer radius. Since this 'outer' curve corresponds to a solid aperture then the resolution of the annulus is higher than for the solid aperture. Furthermore, as the Airy disc contracts, light energy is transferred from the core of the central spot to the surroundings giving a less contrasted image. This can be seen in the figure 3.6 as the PSF with various obstruction ratios, $\eta = r_2/r_1$, where $r_1$ is fixed at 2.0m. Further details about the effects of the annular aperture with fixed area but variable overall radius are given in chapter 6.

Aperture MTF due to a diffraction from a number of similar apertures can be calculated, when the MTF of an individual aperture is known:

$$MTF(u,v) = \sum_i \sum_j MTF(\Delta_{ij}) , \qquad (3.6)$$

where $\Delta_{ij} = [(a_i - a_j - u\lambda) + (b_i - b_j - v\lambda)]$ ,

where $a_i$, $b_i$ are the centres of the apertures. For example, the MTF for six circular apertures on a hexagonal matrix as shown in

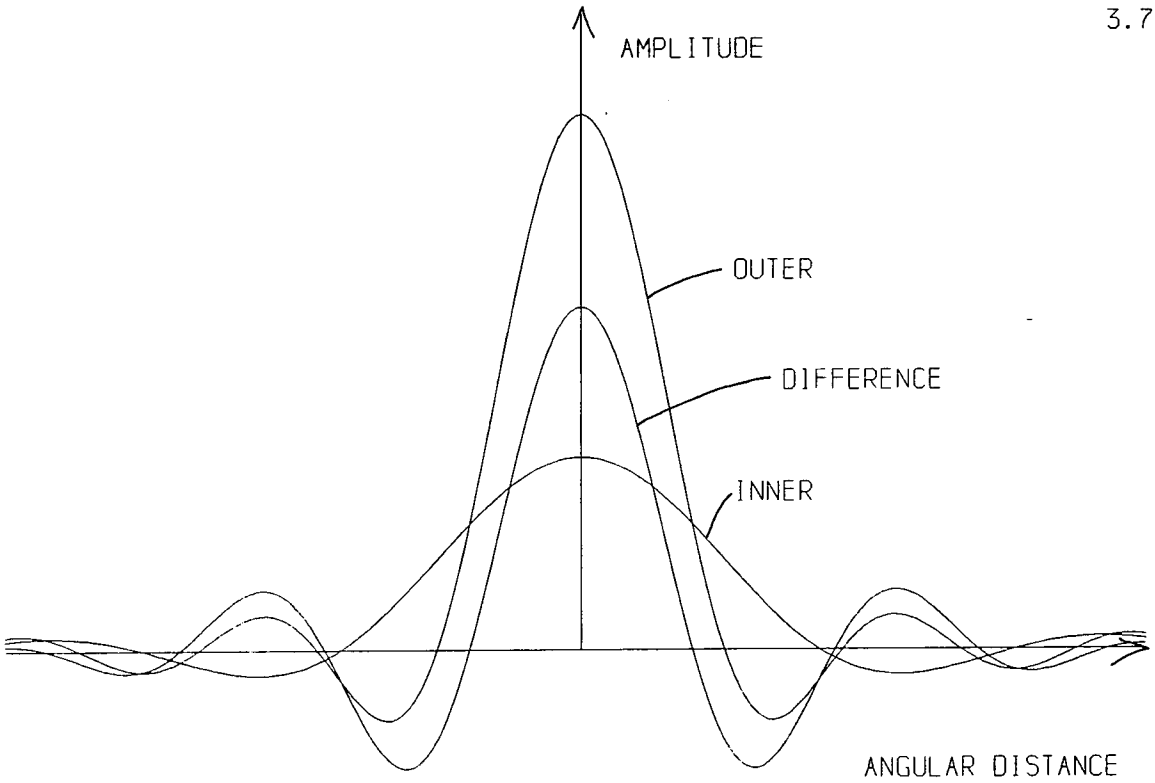


FIG 3.5 Amplitude pattern of annular aperture

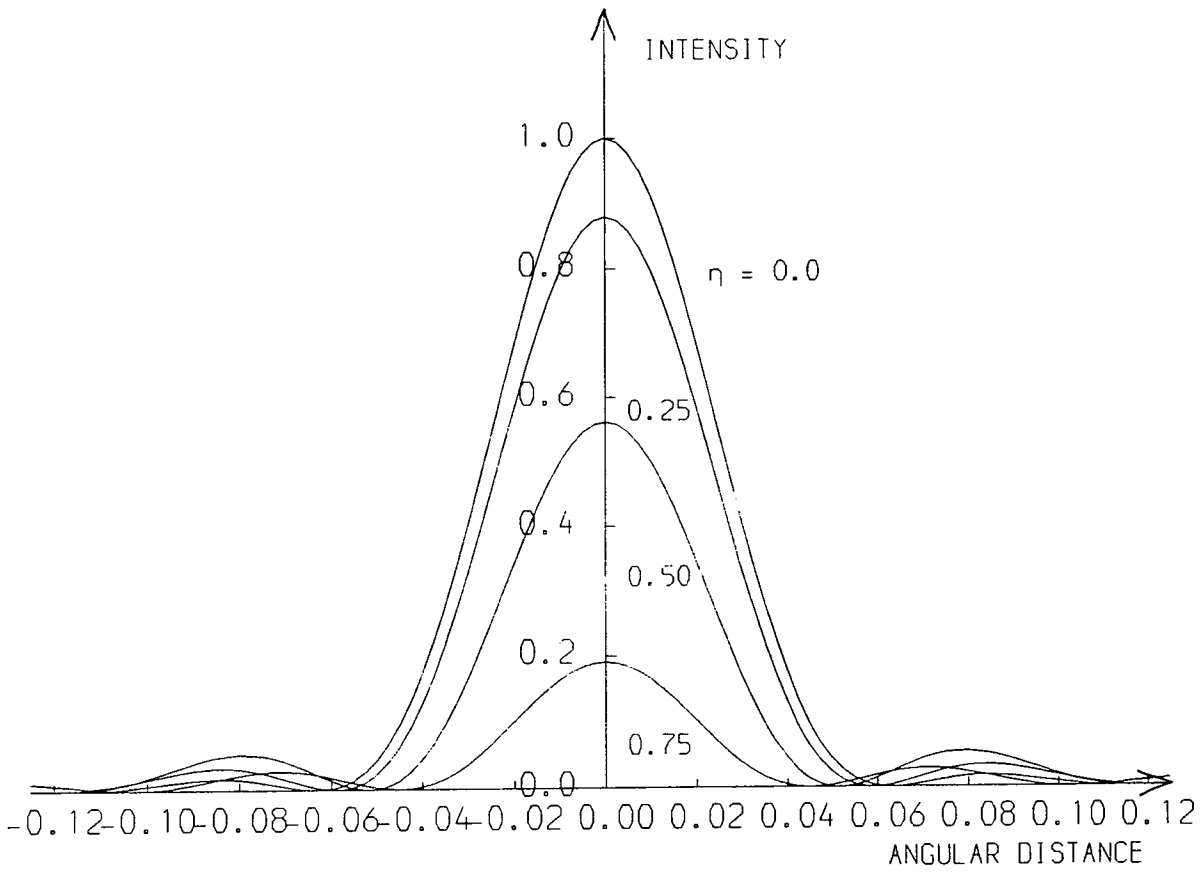


FIG 3.6 Intensity patterns of various annular apertures with fixed outer radius

figure 3.7, is

$$MTF(u,v) = \sum_i \sum_j \frac{2}{\pi} \left[ \cos^{-1}\left(\frac{\Delta_{ij}}{2r}\right) - \left(\frac{\Delta_{ij}}{2r}\right) \sqrt{1 - \left[\frac{\Delta_{ij}}{2r}\right]^2} \right] , \qquad (3.7)$$

where r is the radius of a single mirror. The aperture MTF for the six apertures is shown in figure 3.8. This figure shows that along the x-direction, from a central peak, there are two secondary peaks. The first secondary peak is caused by when two sheared circles nos. 3 and 5 overlap with two unsheared circles, nos. 2 and 6 respectively, to give a larger overall overlap area. The other smaller peak is caused by when a sheared circle, no. 4, overlaps with an unsheared circle, no. 1. At the $30^{\circ}$ direction to the x-direction, there is only one secondary peak which is caused by when two sheared circles nos. 4 and 5 overlap with two unsheared circles nos. 2 and 1 respectively. So this gives a sixfold symmetry MTF pattern, which will give a sixfold symmetry diffraction pattern. This will be discussed in chapter 5.

## 3.2 ATMOSPHERIC SEEING

### 3.2.1 Introduction

As seen in chapter 1, atmospheric turbulence is a major problem in optical astronomy as it drastically reduces the angular resolution of the telescopes. Because of the variations in atmospheric refractive index, which are noticed as "twinkling", the wavefront from a stellar object reaching the telescope is no longer plane parallel but is distorted so that the phase is constant only over a few cms distance. Thus, no

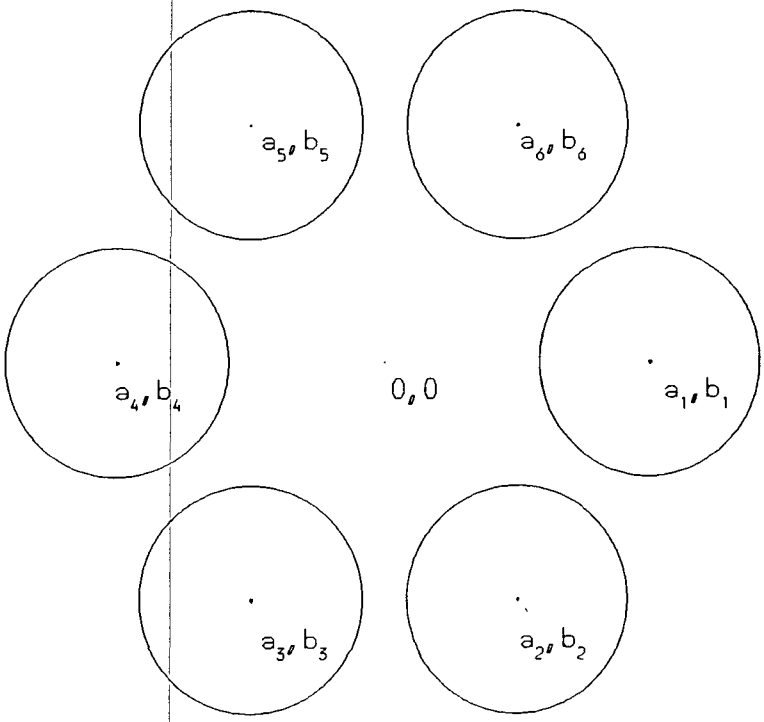


FIG 3.7 Six circular apertures

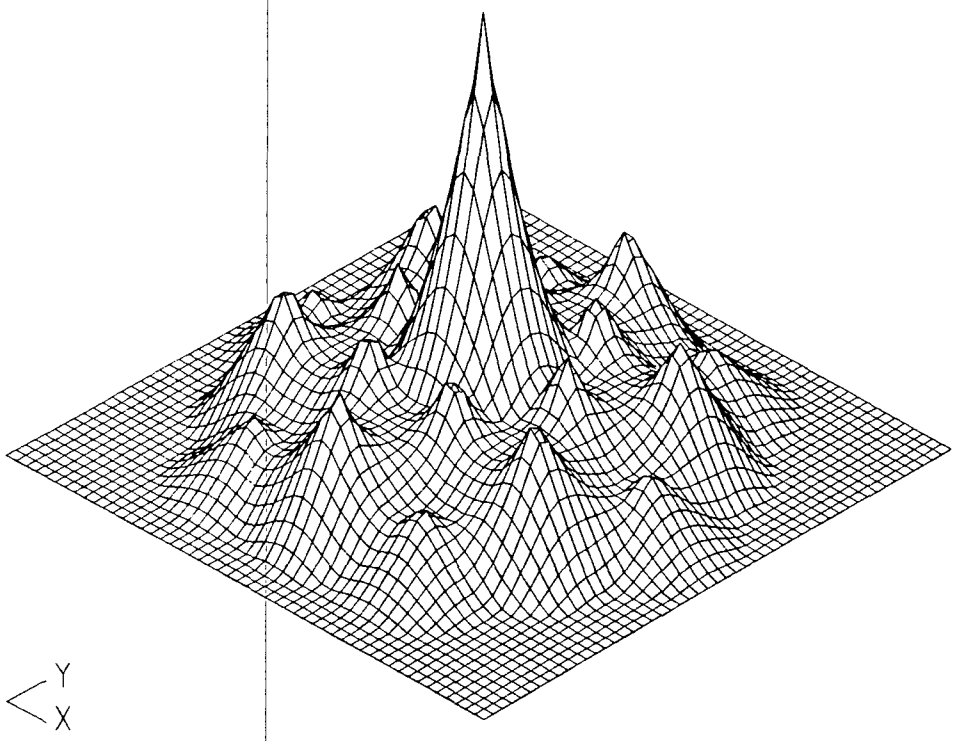


FIG 3.8 MTF of six circular apertures

matter how large the telescope, the resolution obtained is no better than that of a few cms telescope aperture. Hence the diameter of the stellar image varies from 0.5 to 10 arcseconds, or more according to weather conditions. Large telescope mirrors are merely collectors of light energy for poorly resolved stellar images. This limitation on performance is called "seeing".

Seeing is characterised by a coherence distance, $r_o$ . In average seeing, $r_o$ is equal to 10 cm and this gives 1 arcsec FWHM diameter (which is also the diffraction limit of a 10 cm aperture). Good seeing means $r_o \approx$ 20cm. During the course of a year the number of nights with good seeing is very low. Apart from the seeing of the atmosphere, the seeing of the dome in which the telescope sits is very important and this is thought to be responsible for about a half of the seeing. This can be reduced through proper attention to dome design, forced ventilation and temperture excess of mirror surfaces.

$r_o \geq 15$cm for 10% of time.

There are two cases considered- the short exposure case and the long exposure case. The atmospheric degradation leads to changes of image position with a characteristic time of a few milliseconds. The eye is therefore unable to follow them. In a high speed photograph, it is possible to freeze the movement of the distorted, speckled image. This is a short exposure case. In a conventional astronomical photograph, the exposure time is considerably longer than the characteristic time of seeing, in which case the recorded image is the whole ensemble of instantaneous image positions. This is a long exposure case.

3.2.2 Atmospheric Turbulence Model

In the early sixties, the physics of image degradation by atmospheric turbulence was little understood but since that time, the state of the model and the theory of atmospheric turbulence have been developed considerably.

The atmospheric turbulence model is based on the work of Kolmogorov (ref 3.2) who showed that the turbulent flow can be described statistically for turbulent eddies of scale size $l << L_o$. $L_o$ is called the outer scale of the turbulent flow and is usually large compared to the size of the telescope aperture, (few kms) The turbulence is damped out for eddies of size smaller than $l_o$, the inner scale of the turbulence. The range of $l_o$ varies from a few millimetres near the ground to about 1cm near the tropopause. For turbulent eddies within the range, $l_o << l << L_o$, the turbulence is isotropic and its intensity depends only on the single parameter, e, which is the turbulent-energy dissipation rate per unit mass. Energy is injected on a scale of $L_o$ and is degraded into smaller eddies at a scale of $l_o$.

In order to describe the strength of the turbulence on a scale comparable to the telescope aperture, more direct information is obtained by measuring the mean-square difference in refractive index at two points, distance r apart. The variation with r of this mean square difference is called a structure function, D(r). Tatarski (ref 3.3) showed that, following from Kolmogorov, the difference of the local atmospheric temperature at two points has a mean square value that is proportional to the two-thirds power of the distance

between the two points from dimensional analysis. Thus the temperature structure function is

$$D_T(r) = \left\langle [\, T(r')-T(r'-r)\, ]^2 \right\rangle, \qquad (3.8)$$

and can be written as

$$D_T(r) = C_T^2 r^{2/3}, \qquad (3.9)$$

where $C_T$ is a temperture structure constant. Similarly one can define the refractive index structure function as

$$D_n(r) = \left\langle [\, n(r')-n(r'-r)\, ]^2 \right\rangle. \qquad (3.10)$$

Since fluctuations in n depend linearly on fluctuations in T, it follows that

$$D_n(r) = C_n^2 r^{2/3}, \qquad (3.11)$$

where $C_n$ is the refractive index structure constant. $C_n$ is related to the temperature structure constant, $C_T$, by

$$C_n = 80 \times 10^{-6} C_T \frac{P}{T^2}, \qquad (3.12)$$

where the air pressure, P, is expressed in millibars and the air temperature, T, in degrees kelvin. Thus under normal conditions $C_n \sim 10^{-6} C_T$. The parameter $C_n^2$ expresses the contribution of turbulence to optical propagation. While $C_n^2$ is difficult to measure, $C_T^2$ can be measured in a relatively simple way as it is found to depend on the altitude.

Gur'yanov (ref 3.4) has made a survey of the published results of measurements of vertical profiles of the refractive index structure constant, $C_n^2$, in the atmosphere. These have measured $C_T^2$ (hence $C_n^2$) as a function of altitude using captive balloon-borne, high speed, temperature sensors. A wide spread in values at different times of the day was found. The typical values of $C_n^2$ at 12m above the ground are found to be in

the order of $10^{-13}$ $m^{-2/3}$ during the daytime and $10^{-14}$ $m^{-2/3}$ during the nighttime. There is found to be a steady decrease in these values with increasing altitude. An $h^{-4/3}$ dependence has been predicted under unstable daytime conditions on flat land by several authors (ref 3.5), and also an $h^{-2/3}$ dependence under nighttime and neutral conditions. Fig 3.9 shows the averaged measured $C_n^2$ dependence on the altitude. A bump on the curve in fig 3.9 occurs at about 10km and this is due to turbulence near the tropopause where strong wind shears frequently occur. Below about 4 km, the physical shape of the earth's surface certainly plays an important role, but above 4km, it is found that the behaviour of turbulence is almost independent of the location.

The Kolmogorov-Obukhov model of atmospheric turbulence (described above) appears to be substantially correct, and is supported by a large amount of experimental evidence. Both $D_n(r)$ and $D_T(r)$ have been found to exhibit a $r^{2/3}$ dependence under general meteorological conditions.

### 3.2.3 Long Exposure Atmospheric MTF and Imaging Properties

The modulation transfer function for imaging through a turbulent atmosphere in a long exposure can be calculated. Fried (ref 3.6) and Hufnagel and Stanley (ref 3.7) following Tatarski's work, have studied the detailed image structure which undergoes random changes related to the motion of the atmospheric inhomogeneities above the telescope aperture. They were able to show that it is possible to assign an MTF to atmospheric image transmission.

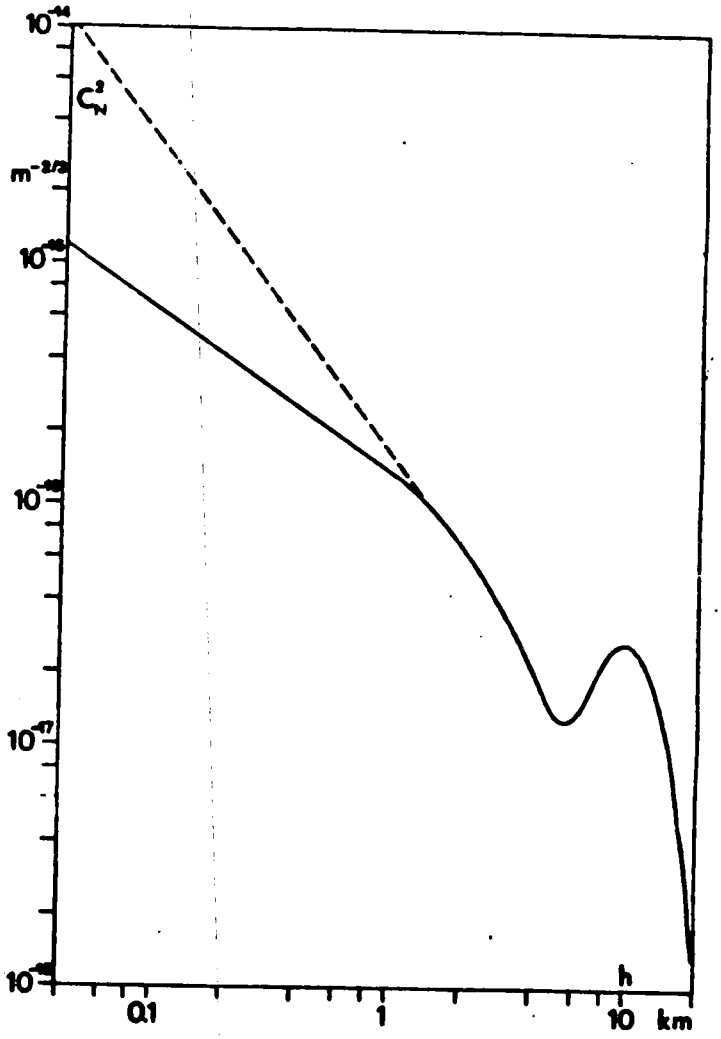


FIG 3.9 Average $C_N^2$ profile (HUFNAGEL [1974]) extended towards low altitudes according a $h^{-\frac{4}{3}}$ law (neutral nighttime conditions). Dotted line: extension according a $h^{-1}$ law (unstable daytime conditions).

After traversing the turbulent atmosphere, there will be two effects on a wavefront from a stellar object - one by phase disturbances and the other by amplitude disturbances. So the wavefront, collected by the telescope aperture, will deviate randomly from the uniform amplitude of a plane wavefront. The aperture function for this wavefront is

$$f(x,y) = \alpha(x,y)\ \exp[l(x,y)+i\phi(x,y)] \ , \qquad (3.13)$$

where $\phi(x,y)$ is the random variable which describes the phase variation at the point x,y and $l(x,y)$ is the random perturbation of the logarithm of the amplitude. The effect on amplitude is usually taken to be small unless the origin of the seeing is very distant. In that case the propagation of a corrugated wavefront will ultimatly lead to interference between originally separated parts of the wavefronts and amplitude variations will result. However, when these are taken into account then it is estimated that these effects are about 20% of the effects of phase. In the following discussion only phase variations are considered.

The optical transfer function for an overall telescope and atmosphere system is

$$T(u,v) = \frac{1}{A}\iint \alpha(x,y)\alpha(x-\lambda u, y-\lambda v)\ * \exp[i\phi(x,y)-i\phi(x-\lambda u, y-\lambda v)]\ dxdy \ , \qquad (3.14)$$

with $l(x,y)$ now set to zero. Here $\phi(x,y)$ varies randomly with time (the average period is a few milliseconds), so the average OTF over a long exposure is

$$T(u,v) = \frac{1}{A}\iint \alpha(x,y)\alpha(x-\lambda u, y-\lambda v)\langle\exp[i\delta]\rangle\ dxdy \ , \qquad (3.15)$$

where the angle brackets $\langle\ldots\rangle$ are used to denote an ensemble

average and $\delta$ is the difference between the phase variations, $\phi(x,y)$ and $\phi(x-\lambda u, y-\lambda v)$. If this difference has a Gaussian distribution, then

$$\langle \exp[i\delta] \rangle = \exp[-\tfrac{1}{2}\langle \delta^2 \rangle] ,$$

where

$$\langle \delta^2 \rangle = \langle [\phi(x,y) - \phi(x-\lambda u, y-\lambda v)]^2 \rangle = D(u,v) .$$

$D(u,v)$ is the structure function for a random field of $\phi$. Hence

$$T(u,v) = \frac{1}{A} \iint \alpha(x,y)\alpha(x-\lambda u, y-\lambda v) \exp[-\tfrac{1}{2} D(u,v)] \, dxdy . \quad (3.16)$$

Since the right hand side of $T(u,v)$ is now expressed in terms of real quantities only, then $T(u,v)$ has become a real MTF, ie

$$MTF(u,v) = MTF_{tele}(u,v)\exp[-\tfrac{1}{2} D(u,v)] , \quad (3.17)$$

where $MTF_{tele}(u,v)$ is the MTF of the telescope aperture and the phase fluctuations now give rise to intensity variations in the image. This equation 3.17 can be considered as the product of the telescope MTF and a quantity $\exp[-1/2D(r)]$, which we can consider to be the atmospheric MTF since it is independent of the telescope's parameters. $D(u,v)$ can be related to the statistical properties of the refractive index field by a straighforward, but lengthy, calculation which will not be given here. This calculation (ref 3.8) gives the relation

$$D(r) = 2.91k^2 r^{5/3} \int C_n^2(z) \, dz , \quad (3.18)$$

where $k = 2\pi/\lambda$ and the integral is taken over the propagation path, z.

When observing at an angular distance, $\Theta$, from the zenith, the thickness, dh, of each layer become $dh\sec\Theta$ and so

$$D(r) = 2.91k^2 r^{5/3} \sec\Theta \int C_n^2(z) \, dz . \quad (3.19)$$

Fried introduced a very convenient measure of seeing which is a coherence diameter, $r_o$. From calculations involving the resolution of a telescope through the atmosphere, he gave the MTF for the atmosphere as

$$\text{MTF}(w) = \exp\left[-3.44\left(\frac{\lambda w}{r_o}\right)^{5/3}\right], \qquad (3.20)$$

and so the wave structure function is

$$D(r) = 6.88\left(\frac{\lambda w}{r_o}\right)^{5/3}. \qquad (3.21)$$

The convenience of the use of a coherence diameter, $r_o$, derives from the fact that it 'represents' the equivalent diameter of a telescope aperture giving the same size as the seeing-limited stellar image. So the resolving power is limited by the telescope when its diameter, D, is smaller than $r_o$ and it is limited by the atmosphere when D is greater than $r_o$. Large $r_o$ values mean good seeing while small values mean bad seeing.

The relation between the coherence diameter, $r_o$, and the profile, $C_n^2$, with respect to height is obtained by equating 3.19 and 3.21. We get

$$r_o = \left[0.423k^2 r^{5/3} \sec\Theta \int C_n^2(z)\, dz\right]^{-3/5}, \qquad (3.22)$$

which shows that $r_o$ depends upon the zenith angle and the wavelength, $\lambda = 2\pi/k$, ie

$$r_o(\Theta) = r_o(0^\circ)(\cos\Theta)^{3/5}. \qquad (3.23)$$

The wavelength dependence is given by

$$r_o \propto (\lambda^{-2})^{-3/5} = \lambda^{6/5}, \qquad (3.24)$$

and is comfirmed experimentally by Boyd (ref 3.9) and by Selby, Wade and Sanchez Magro (ref 3.10). The turbulence-limited optical resolution is of the order of $\lambda/r_o$, so from equation

3.24, it is thus proportional to $\lambda^{-1/5}$. The turbulence-limited resolution of conventional imaging in the visible region is almost, but not quite, independent of wavelength. Between the visible and ten microns region, there is a factor of 1.79 difference in the turbulence-limited angular resolution. Boyd's results are in good agreement with this theoretical prediction. He compared the infrared and visible seeing by taking pictures of the sun's limb simultaneously at 10 microns and at visible wavelengths, and he found the RMS width of the point spread function for seeing to be 1.9±0.2 times greater at 0.55 micron than at 10 microns.

Selby, Wade and Sanchez Magro measured the size of the seeing disc at infrared wavelengths by studying infrared speckle patterns with various filters, and they found that the resolution obeys a $\lambda^{-1/5}$ law.

The coherence diameter, $r_o$, is usually measured at one wavelength, $\lambda_o = 0.5$ micron, so for other wavelengths, $\lambda$, the MTF for the atmosphere is given by

$$MTF(w) = \exp\left[-3.44\left[\frac{\lambda w}{r}\right]^{5/3}\right] , \qquad (3.25)$$

where the parameter, r, is related to the known value $r_o$ at wavelength, $\lambda_o$, by

$$r = r_o \left[\frac{\lambda}{\lambda_o}\right]^{6/5} . \qquad (3.26)$$

So on subtitution,

$$MTF(w) = \exp\left[-3.44\left[\frac{\lambda w}{r_o}\right]^{5/3}\left[\frac{\lambda_o}{\lambda}\right]^{2}\right] . \qquad (3.27)$$

Experimental measurements of the atmospheric MTF and the coherence diameter, $r_o$, are described in chapter 7.

From equation 3.27, the MTF curves for the atmospheric turbulence at average seeing, ie $r_o$ = 10cm, can be obtained at infrared wavelengths. These are shown in fig 3.10a, and from these the beneficial effects of the $\lambda^{-1/5}$ law at longer wavelengths can be seen. The broader the MTF is then the narrower the PSF becomes. Also fig 3.10b shows the MTF curves at $r_o$ = 20cm and here the width of the MTF has been doubled, hence the image is narrower. A useful rule of thumb is that the cut-off frequency in cycles/arcsec for the atmosphere is of the order of $r_o/10$ for the visible region.

For an aberration free system, the MTF due to diffraction by the aperture of the exit pupil and the atmospheric turbulence can be calculated quite simply, that is

$$MTF = MTF_{tele} \times MTF_{atmos}.$$

Then the PSF can be calculated using a Hankel transformation, since the atmospheric MTF has rotational symmetry.

For average seeing fig 3.11 shows the resolution for the seeing-limited image at the visible wavelength $\lambda$ = 0.5 micron, for various aperture diameters, D. The resolution at good seeing is shown as a dotted line. As can be seen, the resolution achieved by a very large system in the presence of turbulence is just equal to the resolution that would be achieved if the aperture diameter were $r_o$, and there was no turbulence-induced wavefront distortion. This image has a size which is equal to a FWHM value of 1 arcsec corresponding to $\lambda$ = 0.5 micron and $r_o$ = 10cm. When the value of the aperture diameter is smaller than $r_o$, the angular resolution is inversely

a)

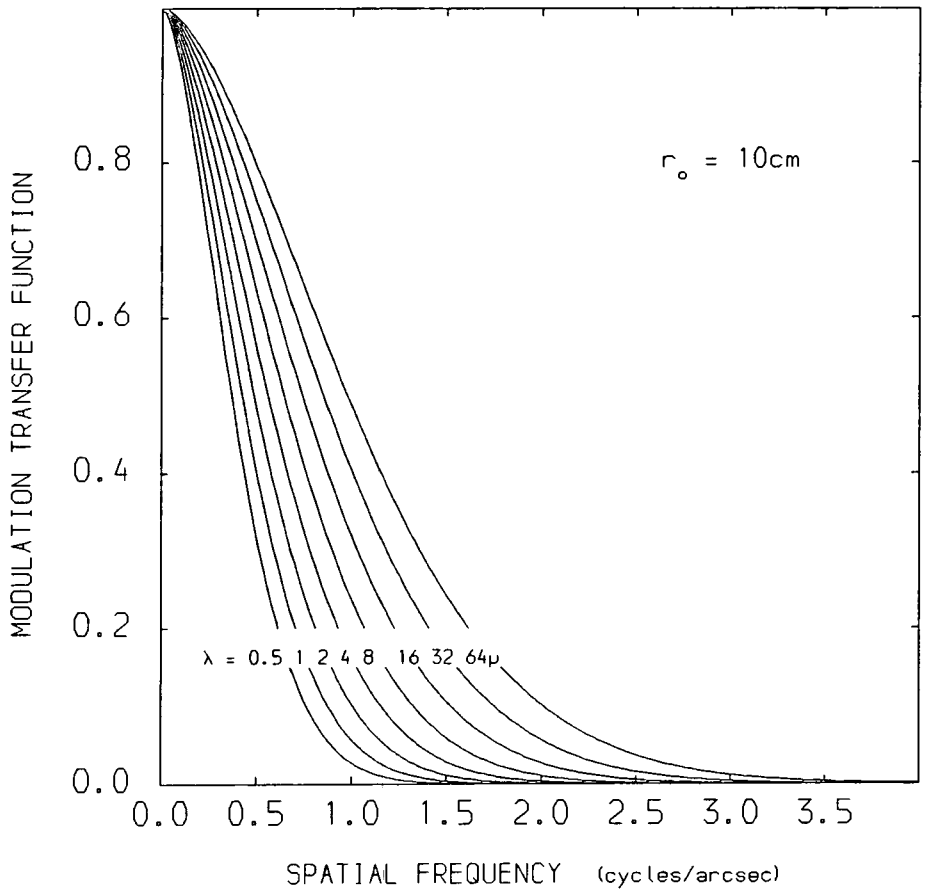


b)

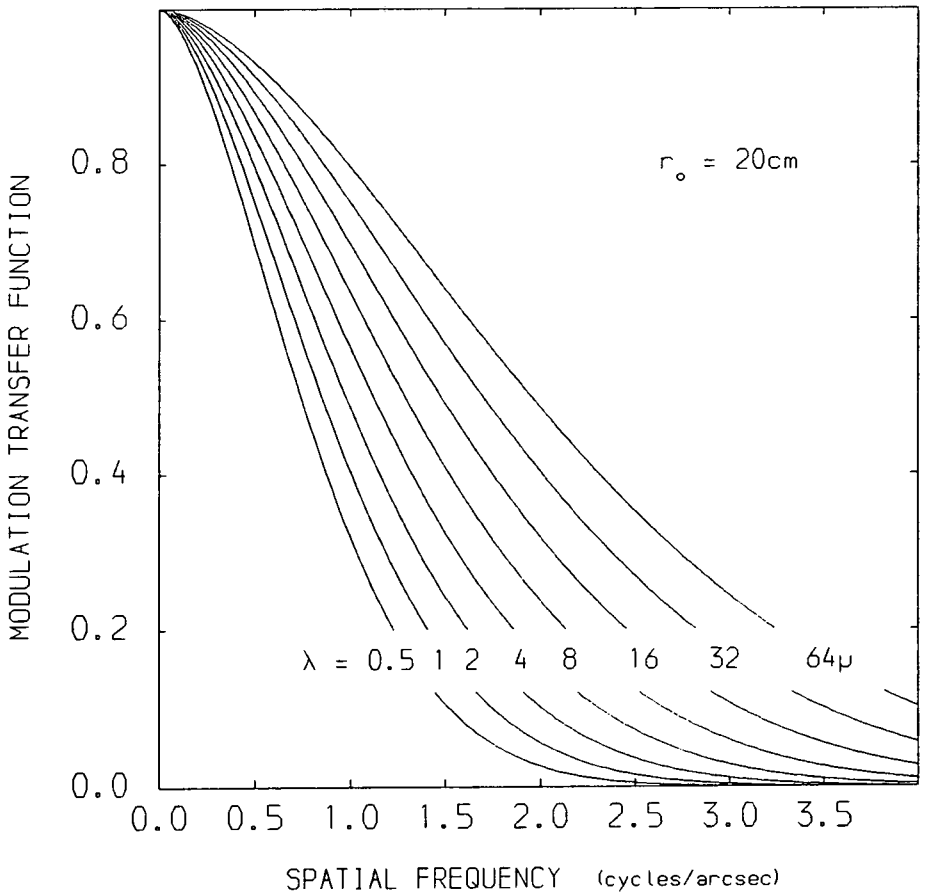


FIG 3.10 Atmospheric MTF for a) $r_o$ = 10cm, b) $r_o$ = 20cm

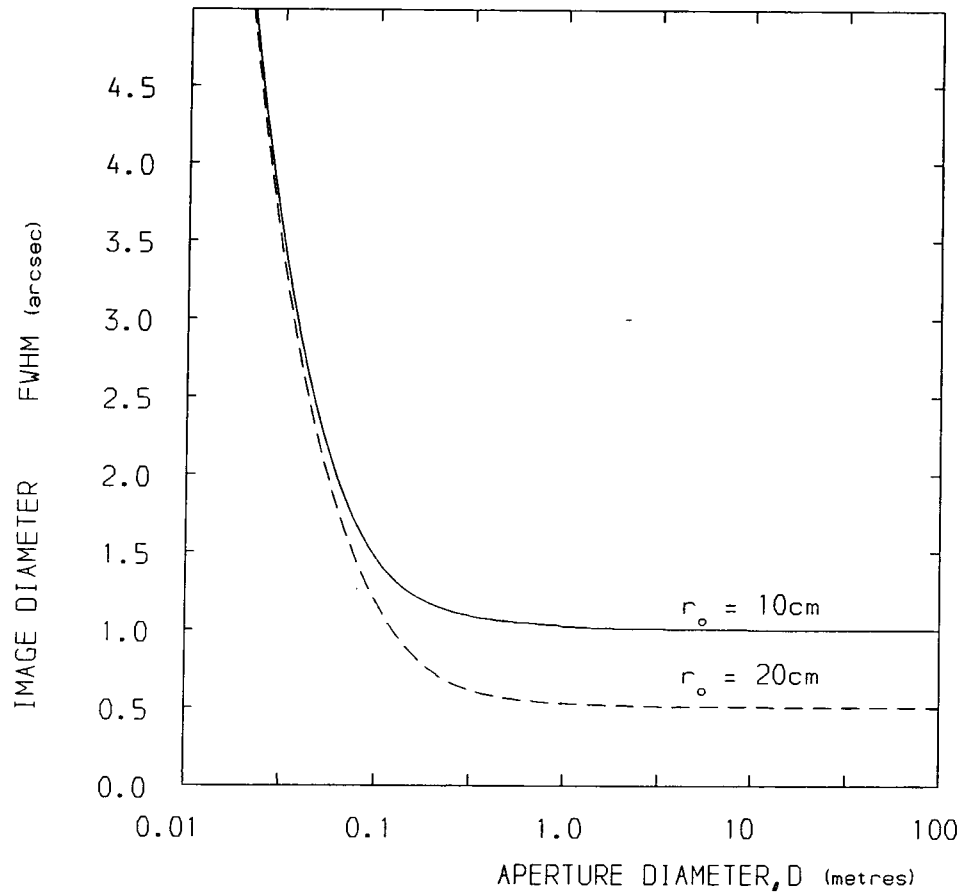


FIG 3.11 Image by a combined system of a telescope and the atmosphere

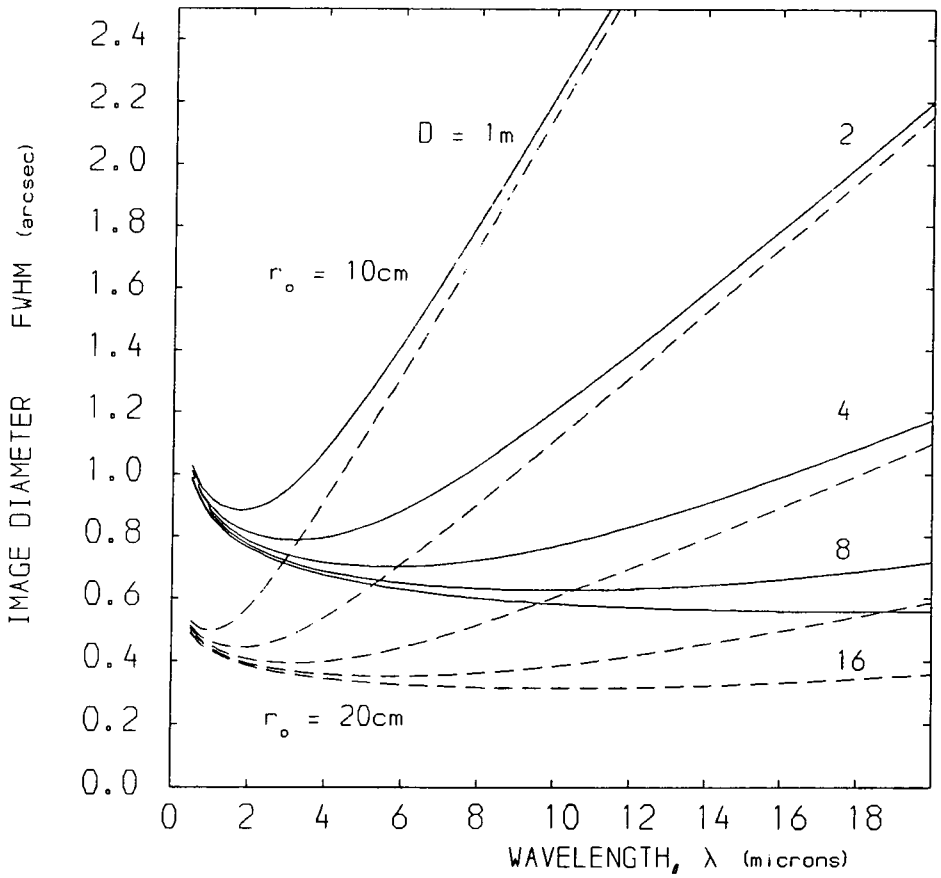


FIG 3.12 Wavelength dependent imaging performance for telescope of various apertures in conditions of $r_0$ = 10cm and 20cm seeing

proportional to the diameter which corresponds to the diffraction limited performance. The elbow of the curves, ie the point of intersection of the two curves, (PSF for aperture only and PSF for atmosphere only) occurs at $D = r_o$ . For $r_o$ = 20cm, the limited resolution is equal to a FWHM value of 0.5 arcsec.

The two sets of curves, shown in fig 3.12 for $r_o$ = 10cm and 20cm are obtained for various aperture diameters, D, and wavelengths, $\lambda$. It is desirable to examine the combined effects of atmospheric turbulence and aperture diffraction to determine if the improvement of the atmospheric image quality with wavelength produces an optimum wavelength for imaging efficiency for attainable apertures.

The minima exhibited by the curves arise from the opposing effects of increasing diffraction-limited image size and decreasing seeing-limited image size as the wavelength increases. Although in all cases the images at visible wavelengths are seeing-limited, the steeply rising portions on the long wavelength side of the minima become more and more diffraction-limited. Furthermore, due to the minima, there exist aperture-dependent wavelengths at which optimum angular resolution may be obtained. In the $r_o$ = 10cm case the minimum occurs at a wavelength in microns equal to the telescope aperture in metres as first noted by D.S.Brown (ref 3.11). With better seeing conditions, ($r_o$ = 20cm) the wavelength minimum moves to shorter wavelengths by a factor of up to 2.

Infrared telescopes are not usually regarded as high

resolution instruments, probably because aperture diffraction and the limitations of present day detectors restrict their performance. So large apertures are required (eg greater than 4m) to obtain a significant benefit from the $\lambda^{-1/5}$ improvement in atmospheric seeing at infrared wavelengths as seen in fig 3.18. The UK Infrared Telescope (3.8m diamter) at Mauna Kea is capable of producing better resolution than in a visible image. Hence at far infrared, millimetre and radio wavelengths, the angular resolution attainable is determined by aperture diffraction and not by atmospheric seeing.

### 3.2.4. Short Exposure Atomspheric MTF and Imaging Properties

In a small aperture ($D \approx$ several $r_o$), the image will consist of several speckles giving an asymmetrical instantaneous point spread function which will require a complex optical transfer function in its description. This image is blurred by the instantaneous MTF and displaced by the PTF. Over a long time each speckle will move about randomly and cover an area $\sim\lambda/r_o$ (ie typically 1 arcsec). As the aperture is increased and includes more $r_o$ patches, then there will be increase in the number of speckles which are distributed over about 1 arcsec. The typical speckle size is about $\lambda/D$ and since the size of the seeing disc is of the order of $\lambda/r_o$, the number of speckles in the image is $(D/r_o)^2$. If the intantaneous sizes and centroids of speckles were to be recorded then when $D \sim r_o$, the pattern would be one speckle displaced from the origin. Further with three or four speckles, the centroid would, in general, be displaced from the

origin and the circle centered on the centroid which just includes all the speckles would be less than 1 arcsec. As more speckles are included the full arcsec is covered and of course the centroid moves closer to the origin. So for a very large mirror the instantaneous speckle pattern will tend to become a continuous distribution centered on the origin and being approximately 1 arcsec in size. This is exactly the same result as for long exposure seeing.

So it is expected that at small apertures, where the Airy disc is more than 1 arcsec, the seeing effects will add some small blurring instantaneously and it will have the same effects as the long exposure seeing. At large apertures the short and the long exposure cases are the same. In between the small and large apertures when few speckles are seen, then the enclosing circle based on the centroid will be smaller than the long exposure case of seeing.

Fried (ref 3.6) calculated the short exposure atmospheric MTF where the random displacement of the image (centroid of speckles) is ignored and the average of a series of short exposures is taken. He found that

$$MTF(w) = MTF\ \exp\left\{-3.44\left[\frac{w\lambda}{r_o}\right]^{5/3}\left[1 - \left[\frac{w\lambda}{D}\right]^{1/3}\right]\right\} . \qquad (3.28)$$

The term in the square brackets represents the tilt suppression effect, and this involves a dependence on the telescope aperture diameter, D. The optimum value of D to give the minimum PSF is $D \approx 4r_o$ . For large apertures, the term in the square brackets becomes equal to unity and the MTF then equals that for long exposures.

For a short exposure, the combined system of the telescope and atmosphere can be calculated using eq. 3.28. Figure 3.13 shows the angular diameter, FWHM of the PSF, as a function of aperture diameter, D, for both long and short exposure images at $r_o$ = 10cm seeing. The minimum of the short exposure curve occurs at $D \approx 4r_o$. The angular diameter (FWHM) is improved to about 0.34 arcsec from 1 arcsec (seeing disc). In Fried (ref 3.12) a similar calculation is made using the "resolution" which is an integration taken over the short exposure optical transfer function. This can be used to advantage as a controlled plane mirror can be used to keep the centroid of the speckles at the origin, or a series of short exposures can be added together to a resultant image, with all their centroids at the origin.

## 3.3 MIRROR SURFACE ERRORS

### 3.3.1 Introduction

In the polishing of mirrors, there will be some surface errors which act as a phase grating, diffracting light out of the central maximum of the point spread function and thus reducing image quality. The effects of surface errors on image quality are examined here with the aid of computer simulations using the shear interferometric measurements made by Grubb Parsons on several mirrors. These are:-

a) European Southern Observatory 1.4m telescope

b) Isaac Newton Telescope (2.5m)

c) Danish - Copenhagen telescope (1.5m)

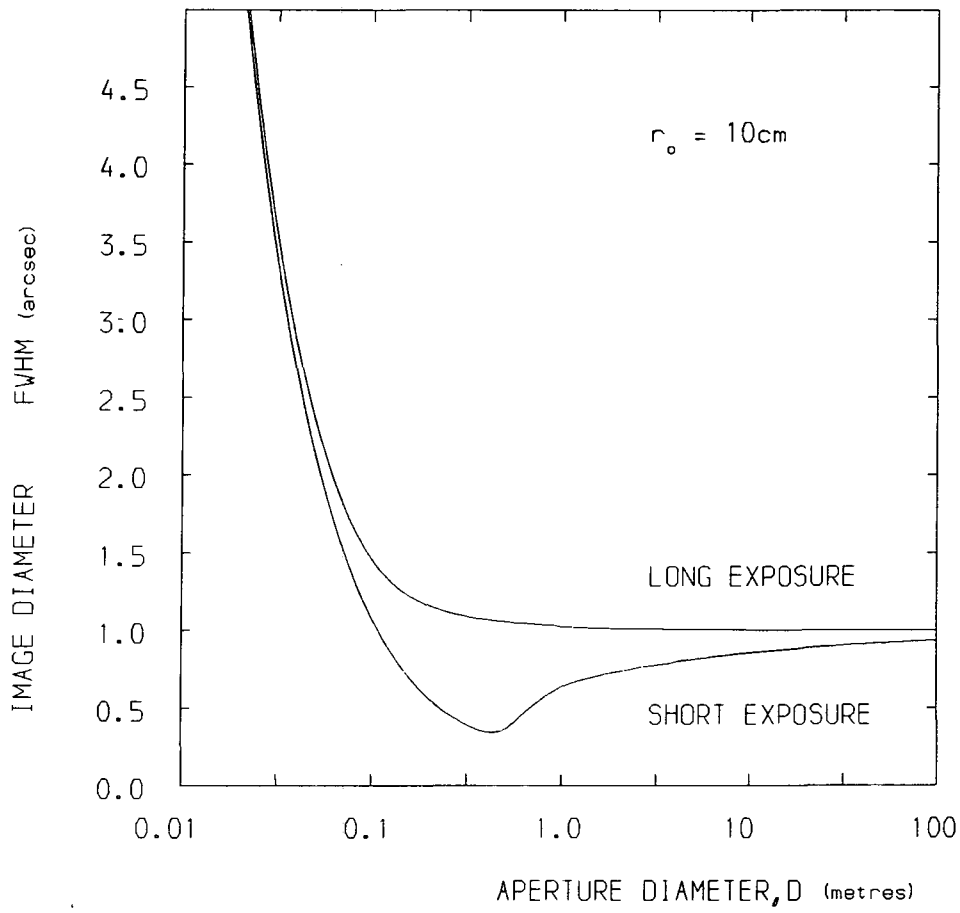


FIG 3.13 Image by a combined system of a telescope and the atmosphere

d) Anglo-Australian telescope (3.9m)

A set of measurements of interferograms have been supplied by Grubb Parsons after their formal acceptance testing for several mirrors. Image quality is usually evaluated in terms related to the performance requirements of large astronomical telescopes that must perform in visible light. In practice the polishing is stopped when the requirements are reached.

### 3.3.2 Basis of Calculation

Mirror surface deformations act as an irregular phase grating, advancing or retarding the reflected wavefront by twice the height or depth of the corresponding point on the mirror surface measured relative to the normal surface shape. The deformed wavefront is represented by a interferogram that plots departure from the normal shape in wavelengths of optical path difference as a function of position in the aperture of the telescope, $W(x,y)$. So the aperture function is then

$$f(x,y) = \exp[ikW(x,y)] \ , \qquad (3.29)$$

and the MTF can be computed from the measured wavefront error interferogram using equation 2.21,

$$MTF(u,v) = \frac{1}{A} \iint \cos(k\delta) \, dxdy \ . \qquad (3.30)$$

The integral is taken over the overlap area of the mirror aperture. $\delta$ is the wavefront difference between the zero sheared wavefront, $W(x,y)$ and the sheared wavefront, $W(x-\lambda u, y-\lambda v)$. The PSF can be obtained by a Fourier transform.

The measurements of the interferograms from Grubb Parsons represent the wavefront slope between the points on the surface.

This is then converted to the wavefront difference, $\delta$. The MTF is calculated using eq 3.30 and this is repeated for every step in shear units in the x-direction to give an MTF in a spectrum of spatial frequency, up to the cut-off frequency where there is no overlap area. This procedure is repeated for the y-direction. Then the MTF for overall surface errors is given by averaging both the x- and y-direction MTFs.

### 3.3.3 Results

The data were processed for the European Southern Obervatory 1.4m telescope. These data consist of an average of four parts for a constant mirror where the mirror and its support are both orientated at four different angle positions, $0^{\circ}$, $90^{\circ}$, $180^{\circ}$, $270^{\circ}$, to remove the aberrations of the shear interferometer and null lens. The MTF can be seen in fig 3.14 showing x- and y-direction and the averaged MTF. The averaged MTF for Isaac Newton Telescope, Danish telescope and AAT are shown in figs 3.15, 3.16 and 3.17 respectively.

The range of MTFs for different telescopes are shown drawn to the same scale in fig 3.18 and it is interesting to note that as the diameter is increased, the MTF becomes smaller, that is, it becomes more difficult to polish a large mirror.

To a good approximation, the image degradation due to telescope surface errors can be treated in a similar way to atmospheric seeing with a large value of $r_o$. For comparison the MTF for the atmosphere is drawn in fig 3.18 for a value of $r_o$ of 200cm; and it is noted that surface errors of recently

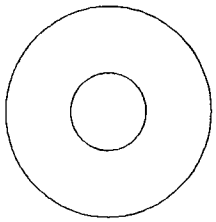

OUTER RADIUS, R1= 0.72M

INNER RADIUS, R2= 0.26M

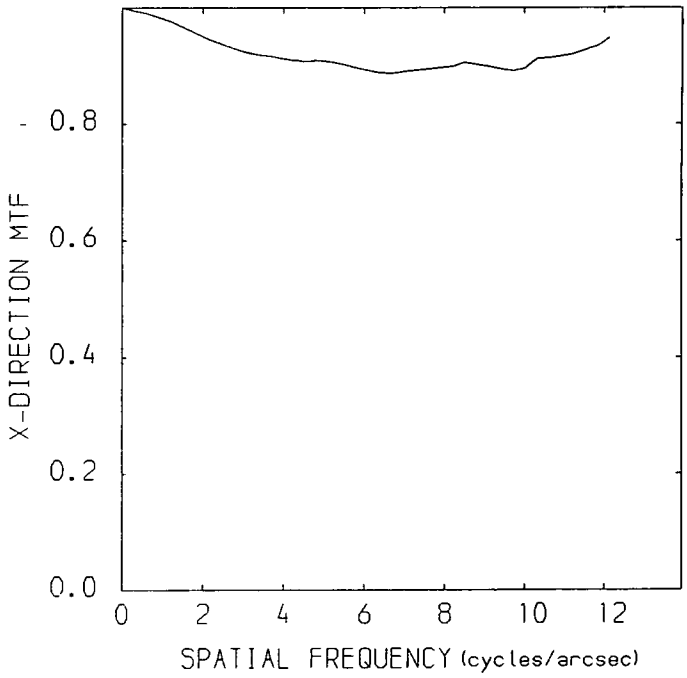


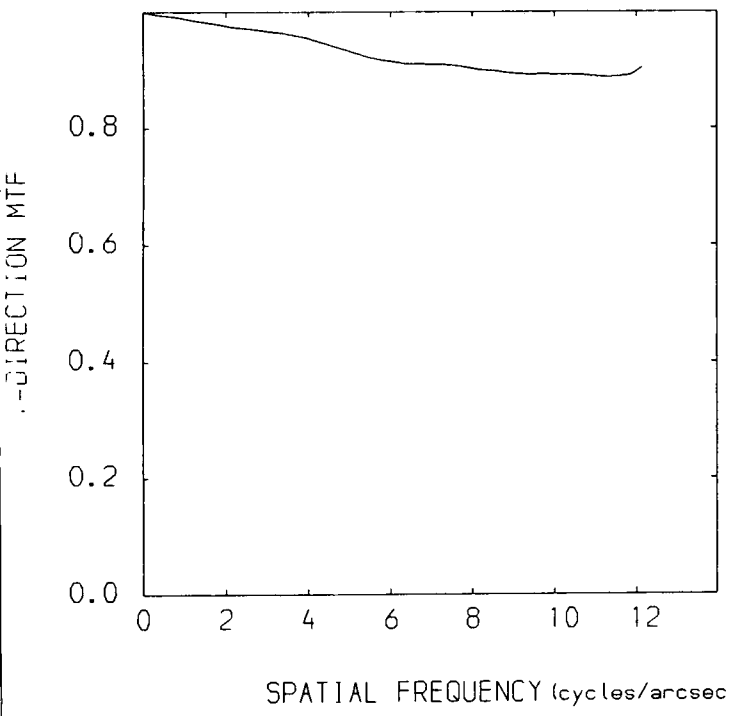


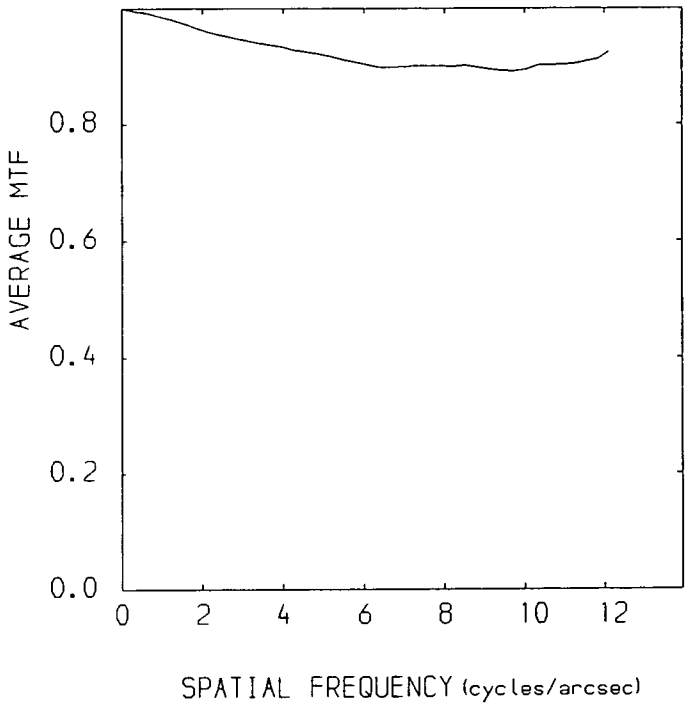


FIG 3.14 Surface error MTF for ESO telescope

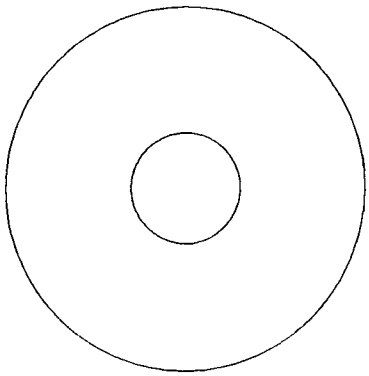

R1 = 1.25M
R2 = 0.38M

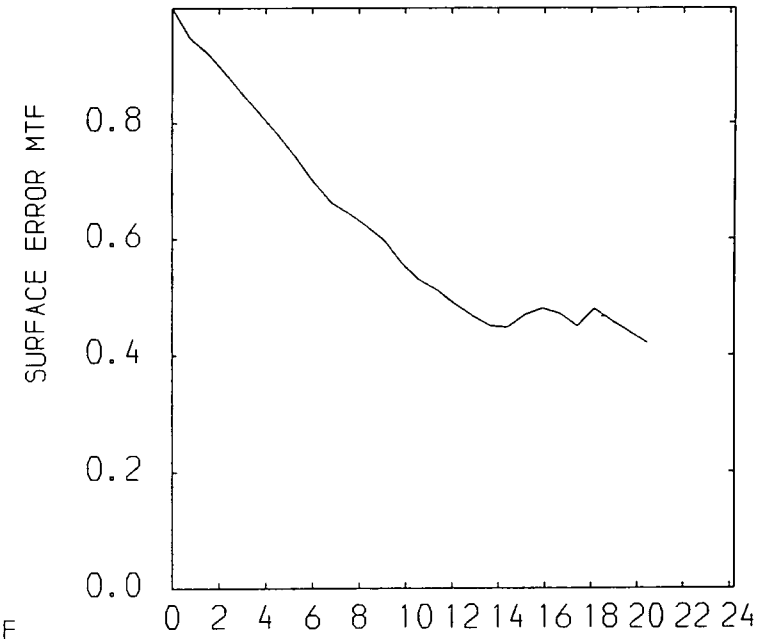


FIG 3.15 ISAAC NEWTON TELESCOPE

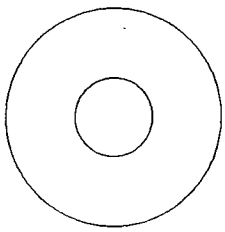

R1 = 0.75M
R2 = 0.27M

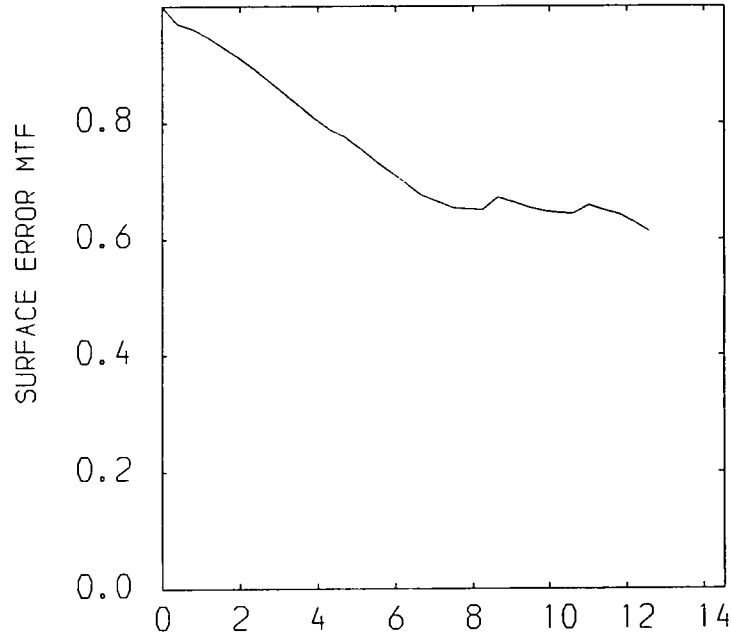


FIG 3.16 DANISH TELESCOPE

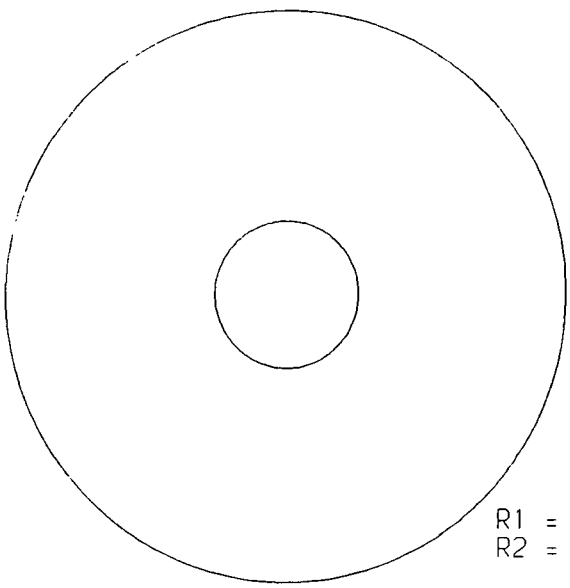

R1 = 1.95M
R2 = 0.50M

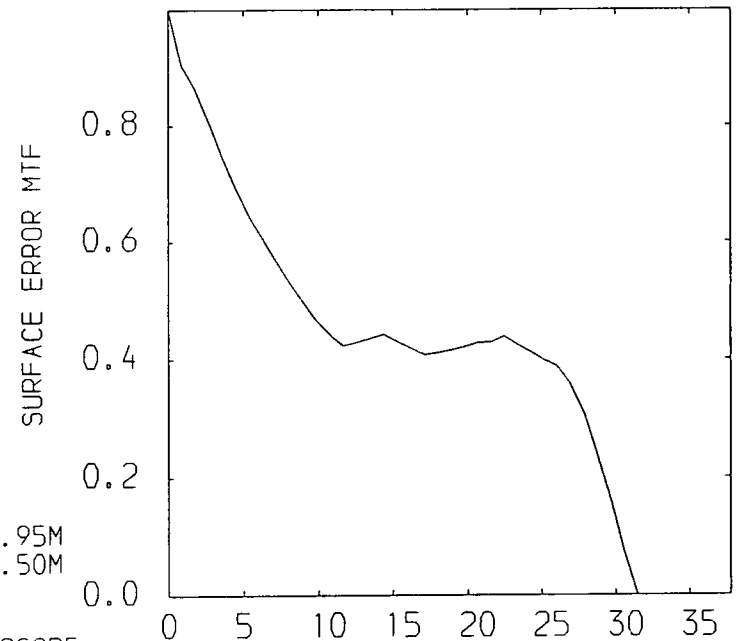


FIG 3.17 ANGLO-AUSTRALIAN TELESCOPE

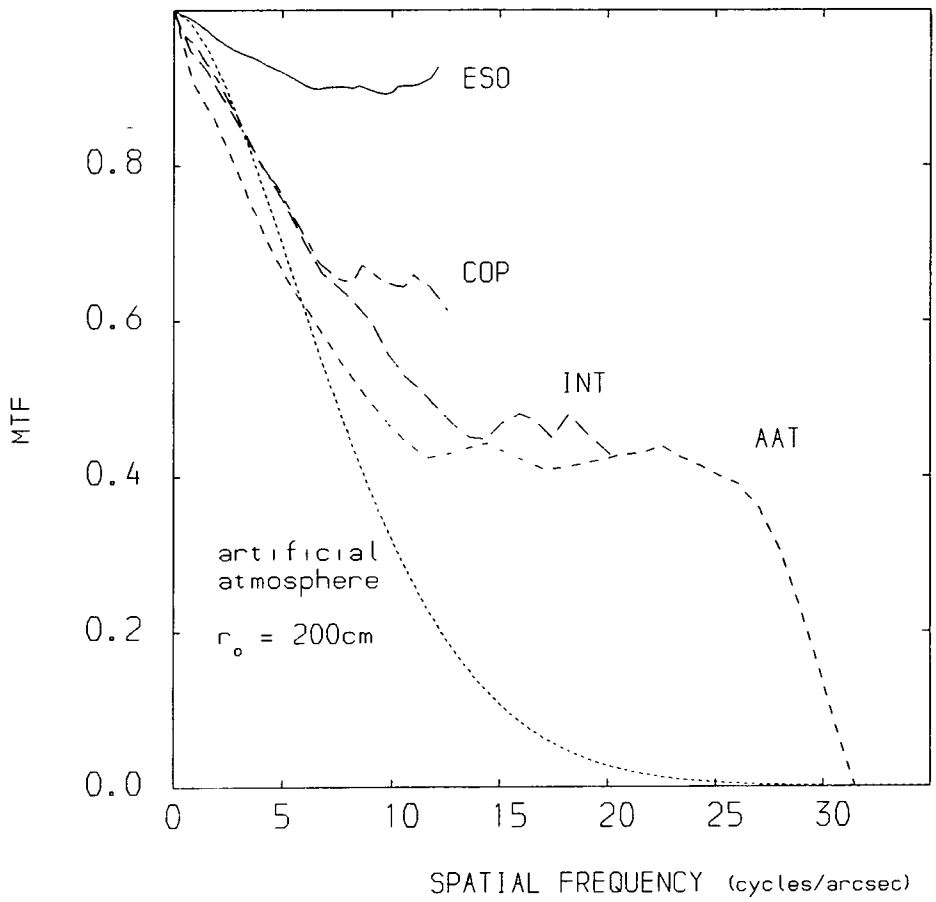


FIG 3.18 Surface error MTF for several telescopes

constructed large mirrors are equivalent to extraordinarily good seeing.

# CHAPTER 4 SCHMIDT TELESCOPES

## 4.1 INTRODUCTION

Aperture diffraction, surface errors and seeing as limitations to imaging have been considered in chapter 3. In this chapter all these effects are examined in a real system where the whole process from the top of the atmosphere to the image in the photographic emulsion is taken into account. By doing this it will be possible to see how a telescope system may be optimised. The example considered is a Schmidt telescope.

At present, the two largest Schmidt telescopes are the 1.2m (48") Palomar Scdmidt telescope at the Hale Observatory on Mount Palomar, USA and the 1.2m (48") United Kingdom Schmidt telescope at the Anglo-Australian Observatory at Siding Spring, Australia. There are also several smaller ones.

In the future, there will be a need to build bigger Schmidt telescopes to capture more starlight so fainter stars can be recorded. A detailed examination of the contributions to imaging by the different parts of the telescope and recording system will indicate in which way future designs might go.

## 4.2 BASIC FEATURES OF SCHMIDT TELESCOPES

When a plane wavefront is reflected from a parabolic mirror it becomes a converging spherical wavefront giving rise to good imaging. However, when a plane wavefront is reflected from a spherical mirror, the wavefront becomes parabolic and converges to an extended image (spherical aberration). The parabolic

mirror gives perfect imaging for the axial rays but off-axis rays suffer from coma. Therefore the mirror has limited ability to cover more than a small angular field of view. However, the spherical mirror, with an aperture stop at its centre of curvature, would give images over a wide field free from off-axis aberrations, but suffering from spherical aberration. It should be noted that if the stop is not at the centre of curvature, then coma and astigmatism would be present.

To correct this residual spherical aberration, Schmidt introduced a thin glass aspheric corrector plate into the aperture stop. The purpose of this plate was to pre-correct the plane wavefronts entering the system by introducing wavefront changes that would compensate exactly the spherical aberration introduced by the spherical mirror. This is the basic principle of Schmidt telescopes and it permits critical definition over a large field with a focal ratio that is an order of magnitude smaller than is possible with a lens system ie faster system.

The same aspheric correction is required for each wavelength but with a single glass corrector this can only be properly done at a single chosen value of wavelength. However, by introducing extra optical power into the corrector plate (by changing from a second order to a third order surface) it is possible to minimise the chromatic aberration. Nowadays achromatic corrector plates can be made by using two glasses of different refractive index and then there is precise correction at two wavelengths and good correction at all other wavelengths in between.

Before entering the Schmidt telescope, the wavefront of the starlight suffers from "seeing" giving an alteration in intensity and phase from variations in the refractive index of the atmosphere.

On entering the telescope, the wavefront further suffers from three degradations before reaching the recording photographic emulsion; firstly by diffraction at the aperture of the mirror, secondly from changes in phase by the manufacturing errors in the mirror surface and surfaces of the aspheric corrector plate. Thirdly, although the achromatic corrector plate gives perfect correction at two wavelengths, there will be some small residual wavefront errors for wavelengths in between.

As the starlight is directed and focussed into the photographic emulsion, its wavefront is further degraded by scattering in the emulsion. Further, the composition of the emulsion (graininess) leads to fluctuations in the structure of the image which is a further degradation. The photographic emulsion is exposed to starlight and the night sky (sky background) long enough to ensure that the photographic density of the sky background is unity after processing. At this exposure the ratio of the signal (due to the image of the stellar objects) to noise (due to graininess and fluctuations of the background) is at a maximum, so that the system is optimised to detect faint stellar objects against the background.

The effect of all these degradations is examined by simulating them in three different models of Schmidt telescopes in order to determine their relative importances. The basic

model telescope, S1, is similar to the United Kingdom Schmidt telescope (UKST). This has a 1.24m (48") f/2.5 mirror. The other two models are:

a) S2, 2.5m (96") f/2.5. This is a telescope whose size is doubled both in aperture and focal length relative to S1.

b) S3, 2.5m (96") f/3.0. In this telescope, extra focal length is included.

It is expected that larger Schmidt telescopes will lead to an improvement in detection sensitivity through enhanced signal to noise ratios. However, the degree of improvement will depend upon the relative importance of the degradations which contribute to the size and structure of the stellar images. From these the limiting sensitivities of Schmidt telescopes can be evaluated.

Of course in the future the photographic systems will probably be replaced by direct reading by charge-coupled device. CCD detectors register up to 80 per cent of incident photons compared to one or two per cent for a photographic plate

## 4.3 THE THEORY OF THE CORRECTOR PLATE

The corrector plate of the Schmidt telescope is used to correct the residual spherical aberration which is produced by a spherical mirror. The aspheric glass corrector plate is less difficult to fabricate than the aspheric surface of a paraboloid mirror. This is because the refractive index difference across the glass corrector is about 0.5 compared to the effective index difference of 2.0 at the reflecting surface of the paraboloid,

making it only a quarter as sensitive to fabrication errors.

The theory of the aberrations of a Schmidt telescope and the shape of corrector plate has been treated by several authors (ref.4.1). The following is a simplified theory which will be sufficient for the simulations of the computer model.

### 4.3.1 Spherical aberration

The wavefront aberration produced by reflection of a plane wavefront at a spherical mirror can be calculated from the difference in surface height between the sphere and a paraboloid which gives an axial image without aberration.

In fig 4.1, we have a parabola, OA of focal length, F. y is the distance from the axis while z is the axial direction. The shape and slope of the parabola are:

$$z = y^2/4F \text{ and } dz/dy = y/2F \ .$$

Further, if AN is the normal to the parabola at A then:

$$BN = 2F \ ; \ PQ = y^3/8F^2 \text{ and } \phi = y^3/16F^3 \ .$$

Now $\phi$ represents the difference in slope between the parabola and circle centered at P of the same focal length. Using h to represent the height difference between them, then

$$\phi = dh/dy = y^3/16F^3, \text{ hence } h = y^4/64F^3 \ .$$

For the case of the paraboloid and sphere, the equation becomes:

$$h = (x^2 + y^2)^2/64F^3, \qquad (4.1)$$

where x and y are the two coordinates normal to the paraboloid axis.

When a wavefront passes through a surface, its shape is changed and the amount of change depends on the difference in

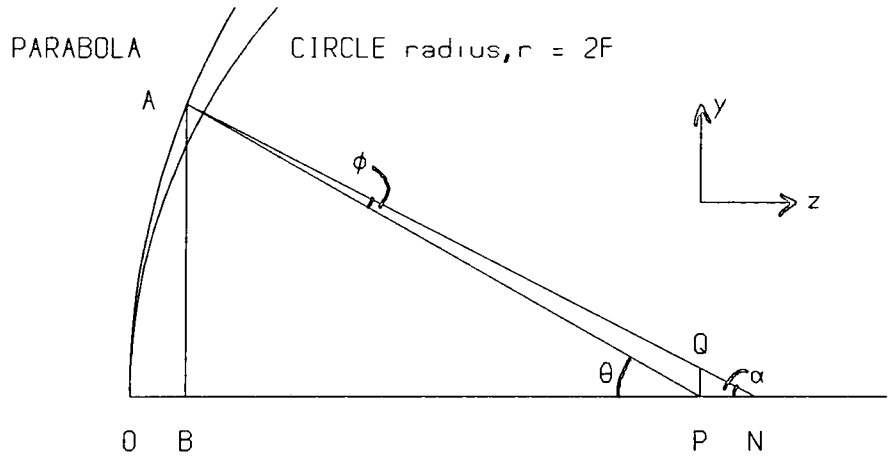


$OB = PN = y^2/4F$

$OP = BN = 2F$

FIG 4.1 Difference between parabola and circle

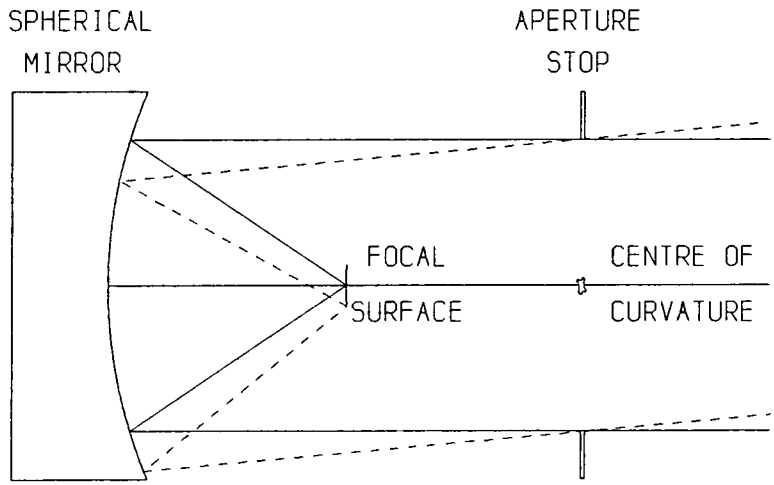


FIG 4.2 Spherical mirror with aperture stop

refractive index. The change in wavefront form, W, is given by $W = (n_2 - n_1)h$ where $n_1$ and $n_2$ are the refractive indices and h is the surface height. The reflection of a wavefront is denoted by a reversal of sign of the refractive index, so that for a reflection in air, $W = -2h$. So for a reflecting spherical surface, the wavefront aberration, W is

$$W = -(x^2+y^2)^2/32F^3. \qquad (4.2)$$

4.3.2 Aberrations in Schmidt telescope and shape of corrector plate

A circular aperture is placed at a distance 2F in front of the spherical mirror as shown in fig 4.2. The coordinates x,y are in the plane of the aperture and its origin is at the centre of curvature of the sphere. For small angles of incidence the wavefront aberration is then $W = -(x^2+y^2)^2/32F^3$, regardless of the angle of incidence at the aperture stop. Therefore it has no off-axis aberrations. The focal surface will be spherical and concentric with the mirror so we have to use curved photographic plates (or flat plates by using a field flattening lens in front of them).

If a refracting element (corrector plate), which introduces an equal and opposite aberration, is placed in the plane of the aperture stop, it will correct the spherical aberration of the optical system. The variation of thickness of the corrector plate with refractive index, n, required for this is:

$$t = \frac{(x^2+y^2)^2}{32F^3(n-1)}. \qquad (4.3)$$

However, the corrector plate does introduce an axis and

therefore must produce off-axis aberrations but these are usually very small. Hence the useful angular field is made larger by this device.

Since the refractive index of the corrector plate varies with wavelength, the spherical aberration of the sphere can be corrected accurately for only one value of the refractive index and therefore for only one wavelength. If the corrector plate is calculated for use at a wavelength for which the glass has an index $n_c$(corrected index), but is then used for a wavelength for which the index is n, it is evident that the wavefront produced from the corrector plate is

$$W = \frac{(x^2+y^2)^2 (n-1)}{32F^3(n_c-1)} \quad . \qquad (4.4)$$

The difference between corrected wavefront and non-corrected wavefront gives the residual aberration caused by the lack of achromatism of the corrector plate, so

$$\Delta = \frac{(x^2+y^2)^2 (n-n_c)}{32F^3(n_c-1)} \quad , \qquad (4.5)$$

ie when $n = n_c$, then $\Delta = 0$. Clearly the chromatic aberration becomes worse at the thicker parts of the corrector plate. This can be reduced by introducing extra optical power into the corrector plate and alter its shape. This will, of course, change the focal length of the combined system. The shape of the corrector plate depends on how the chromatic aberration is to be minimized. There are two different ways of looking at this as described below.

The cartesian equation of its surface which is given in eq 4.3, becomes, with higher powers,

$$t(r) = a_1 r^2 + a_2 r^4 + a_3 r^6 + \ldots\ldots ,$$

where $r^2 = x^2 + y^2$ . To a good approximation, the terms in $r^6$ and higher powers can be neglected giving a quadratic term:

$$t(r) = Ar^4 - Br^2, \qquad (4.6)$$

where $A = \dfrac{1}{32F^3(n-1)}$ .

When the surface slope is zero at radius, $r_z$, we have

$$\frac{dt}{dr} = 4Ar_z^2 - 2Br_z = 0, \qquad (4.7)$$

or

$$B = 2Ar_z^2 . \qquad (4.8)$$

This occurs where a ray parallel to the axis and incident to the surface is not deflected overall on its passage through the corrector plate. This is known as the neutral zone and is usually fairly close to the edge of the plate. There are two values of $r_z$ :

i) when the difference in thickness at the outer radius, R, of the plate is equal to zero, so from eq 4.6,

$$t(R) = AR^4 - BR^2 = 0 .$$

Hence $B = AR^2$ and substituting in eq 4.8, this gives

$$r_z = R/\sqrt{2} . \qquad (4.9)$$

ii) when the surface slope at the outer radius, R, of the plate is equal and opposite to the maximum slope in the area $r < r_z$. Differentiating eq 4.7 to give the maximum slope

$$\frac{d^2t}{dr^2} = 12Ar^2 - 2B = 0 ,$$

or

$$B = 6Ar^2 .$$

Substituting in eq 4.8, gives $r = r_z/\sqrt{3}$. This point has a

maximum slope inside $r_z$, and hence the outer radius which has the opposite slope, is

$$R = 2r_z/\sqrt{3} \quad , \qquad (4.10)$$

ie the neutral zone radius, $r_z$ is equal to $\sqrt{3}/2$ of outer radius.

Fig 4.3a shows an aspheric corrector plate with the neutral zone radius which is equal to 0.707 of outer radius, while in fig 4.3b $r_z$ is equal to 0.866R.

In practice, the value of neutral zone radius, $r_z$, is usually specified, and the chromatic error would be minimised by changing the coefficient, B. If the chromatic error is small then $r_z = R/\sqrt{2}$ is used (equal height) and this is the most common case. If the chromatic error is large then $r_z = \sqrt{3}R/2$ is used (equal slope).

So in the Schmidt telescope with this form of corrector plate, the wavefront due to residual aberration is modified from that of eq 4.4 to:

$$\Delta = A' r^4 - B' r^2, \qquad (4.11)$$

where $A' = \frac{1}{32F^3} \frac{(n-n_c)}{(n_c-1)}$ and $B' = 2A' r_z^2$.

### 4.3.3 Achromatic Doublet Corrector Plate

Despite the minimising feature above, the singlet corrector plate is corrected for only one value of the refractive index, $n_c$, and therefore for only one wavelength. At other wavelengths, refractive index, n, the image will broaden due to a minimised chromatic aberration.

The chromatic aberration can be made smaller by introducing a further refractive index into the corrector plate. An

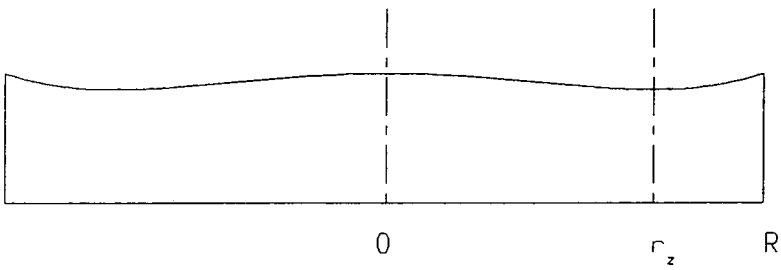


a) $r_z = 0.707R$

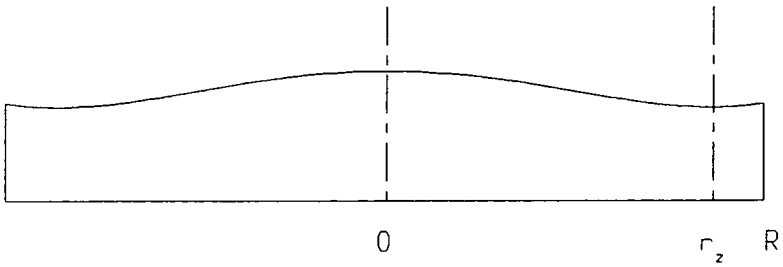


b) $r_z = 0.866R$

FIG 4.3 Profiles of Schmidt singlet corrector plates

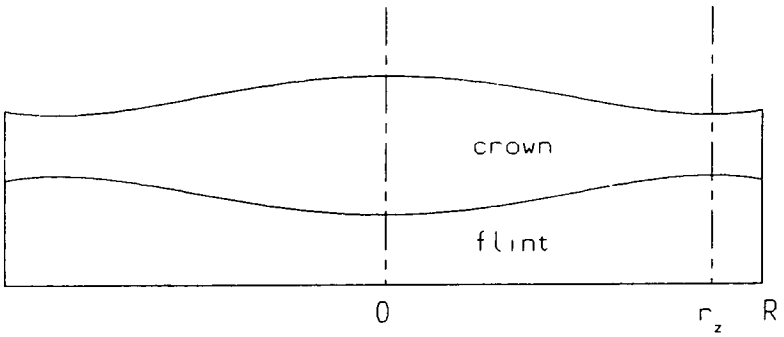


FIG 4.4 Profile of achromatic doublet corrector plate

achromatic doublet is made from two different refractive index glasses (usually crown and flint) cemented together and then there is precise correction at two wavelengths and good correction between these values. Fig 4.4 shows a typical shape of a doublet corrector plate.

The residual wavefront aberration produced from a doublet corrector plate is given by

$$\Delta = A'' r^4 - B'' r^2, \qquad (4.12)$$

where $A'' = \frac{1}{32F^3}(a_c(n_c - 1) + a_f(n_f - 1) - 1)$ and $B'' = 2A'' r_z^2$,

where $a_c$ , $a_f$ and $n_c$, $n_f$ are asphericities and refractive indices of crown and flint glass respectively. Eq 4.12 is similar to eq 4.11 except for an extra asphericity term. The term asphericity is used to describe the departure of an optical surface from the true spherical form and having the fourth power of r in the polynomial surface.

In the UK Schmidt Telescope, there are two corrector plates available, of which one is a singlet corrector plate made of Schott BK7 glass and is corrected at a wavelength of 0.42 micron. The other is an achromatic cemented doublet of Schott UBK7 and LLF6 glass which is corrected at wavelengths of 0.38 and 0.80 micron.

## 4.4 MODULATION TRANSFER FUNCTION

As described previously in this chapter (4.2), there are five degradations of the light wavefront as it passes from a star through the atmosphere and the Schmidt telescope to reach the recording photographic emulsion. To simulate these

degradations, the cumulative convolution of these on the image structure of a star is calculated and for this it is easier to use the response in Fourier space through the modulation transfer function, MTF. The advantage of using the MTF is that by the convolution theorem, the overall MTF of a system is the product of the transfer functions of successive degradations of the system (see chapter 2).

The MTF of each degradation is described as follows:

### 4.4.1 Seeing

From chapter 3, there is an accepted model of turbulence for the atmosphere which leads to an MTF at spatial frequency, w, of:

$$MTF_1(w) = \exp[-3.44(\lambda w/r)^{5/3}] , \qquad (4.13)$$

where the coherence length parameter, r, is related to the known value $r_o$ at wavelength $\lambda_o$ by

$$r = r_o(\lambda/\lambda_o)^{6/5} . \qquad (4.14)$$

On substitution we set

$$MTF_1(w) = \exp[-3.44\{(\lambda_o/\lambda)^2(w\lambda/r_o)^{5/3}\}] . \qquad (4.15)$$

The value of $r_o$ has to be determined experimentally, but $r_o = 10$cm is a typical value.

### 4.4.2 Diffraction

The MTF of the aperture has a geometrical interpretation which is used to calculate the MTF (see chapter 3). It corresponds to the ratio of the area of the overlap of the aperture shifted on itself (by $w\lambda$) to the area of the aperture. Then

$$MTF_2(w) = \frac{1}{A}\int_{overlap} dA \ , \qquad (4.16)$$

where A is the total area.

4.4.3 Surface errors

The wavefront errors in the surfaces of the mirror and the corrector plate should really be calculated from the manufacturer's data. To a good approximation, the surface errors can be expected to behave in a similar way to atmospheric seeing with $r_o$ at higher values (section 3.3). In the present calculation the surface errors have been regarded as equivalent to very good seeing and are represented by equation 4.12 with $r_o$ of 30cm, as there are three surfaces from which the light is reflected or through which the light passes.

4.4.4 Optical design

The optical design of the corrector plate can be conveniently introduced into the MTF for the aperture. When the residual wavefronts errors are taken into account the MTF of the aperture becomes

$$MTF_4(w) = \frac{1}{A}\int_{overlap} \cos(2\pi\delta/\lambda)\,dA \ , \qquad (4.17)$$

where $\delta$ is the difference in phase between the wavefront and the shifted wavefront at dA, ie

$$\delta = \Delta(r) + \Delta(r+\lambda w) \ .$$

From equations 4.11 and 4.12, for a singlet

$$\Delta(r) = \frac{1}{32F^3}\frac{(n-n_c)}{(n_c-1)}\,(r^4 - 2r^2 r_z^2),$$

and for an achromatic doublet

$$\Delta(r) = \frac{1}{32F^3}[a_c(n_c-1)+a_f(n_f-1)-1](r^4-2r^2r_z^2) \ .$$

As we will want to calculate the MTF for the optical design only and to compare this and other MTFs, we simply divide this equation 4.17 by the MTF for the aperture only (eq 4.16).

It is assumed that the corrector plates used in the S1 telescope are scaled in diameter for the S2 and S3 telescopes but are otherwise made of the same glasses.

4.4.5 Photographic emulsion

There are two contributions to the MTF in the photographic emulsion, one from the scattering of light in the emulsion and other due to latent image formation and chemical development.

a) Scattering of light

Light incident at one point of an emulsion is scattered into neighbouring areas primarily because of refractive non-uniformities within the emulsion. This and other mechanisms, such as finite grain size and halation, will cause blackening over a larger emulsion area than expected. This spreading corresponds to a value of MTF less than 1.0 at all spatial frequencies.

b) Development

During exposure, the grain size will change (latent image formation) as silver halide is reduced to silver. In the development, the exposed point in the emulsion may influence the image at neighbouring points. These effects are primarily due to the diffusion of by-products of development and spent developing solution across the emulsion area. This is an

adjacency effect and it usually makes the MTF values greater than 1.0 at low spatial frequencies.

The MTF values for an emulsion are to be found in the manufacturer's data books. The MTF for the emulsion considered in these calculations (IIIa-J, Kodak Ltd (ref.4.2)) is shown in fig 4.5. Manufacturers usually quote spatial frequency in cycles/mm. These can be converted to cycles/arcsec as follows:

$$\text{cycles/arcsec} = \text{cycles/mm} \times F/2.063\times10^{2}, \qquad (4.18)$$

where F is the focal length of the telescope mirror in metres.

Clearly the effect of the emulsion will depend upon the size of the broadened image falling on it. For a long focal length mirror, the image will be proportionately bigger and so the effect of the emulsion MTF will be smaller than for a short focal length.

### 4.4.6 The Cumulative MTF

The cumulative MTFs have been calculated for the three models of Schmidt telescopes, S1, S2 and S3, over a range of wavelengths. The telescopes have been assumed to have, in turn, both a singlet and an achromatic doublet corrector plate. Further, the calculations have been made under conditions of average seeing ($r_o$ = 10cm) and of good seeing ($r_o$= 20cm). To summarise these calculations, the value of MTF at a typical spatial frequency (w = 0.3 cycles/arcsec) is shown as a function of wavelength in figs 4.6a,b,c for a telescope S1.

The cumulative effects of seeing, diffraction, surface

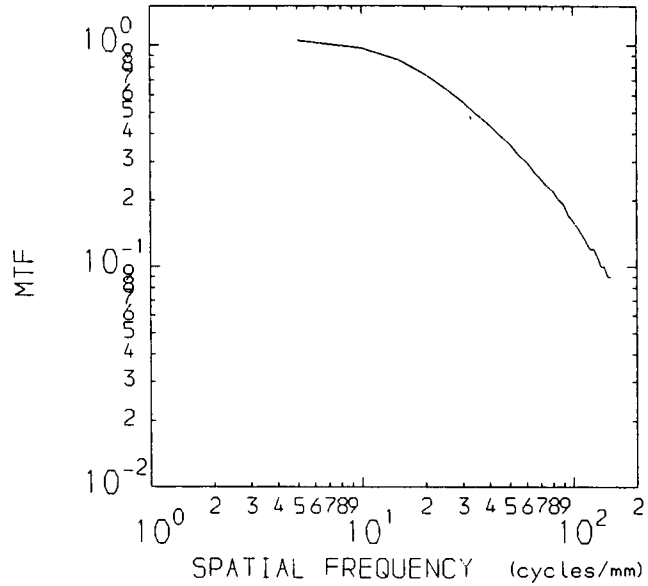


FIG 4.5 Photographic MTF for 111a-J plate

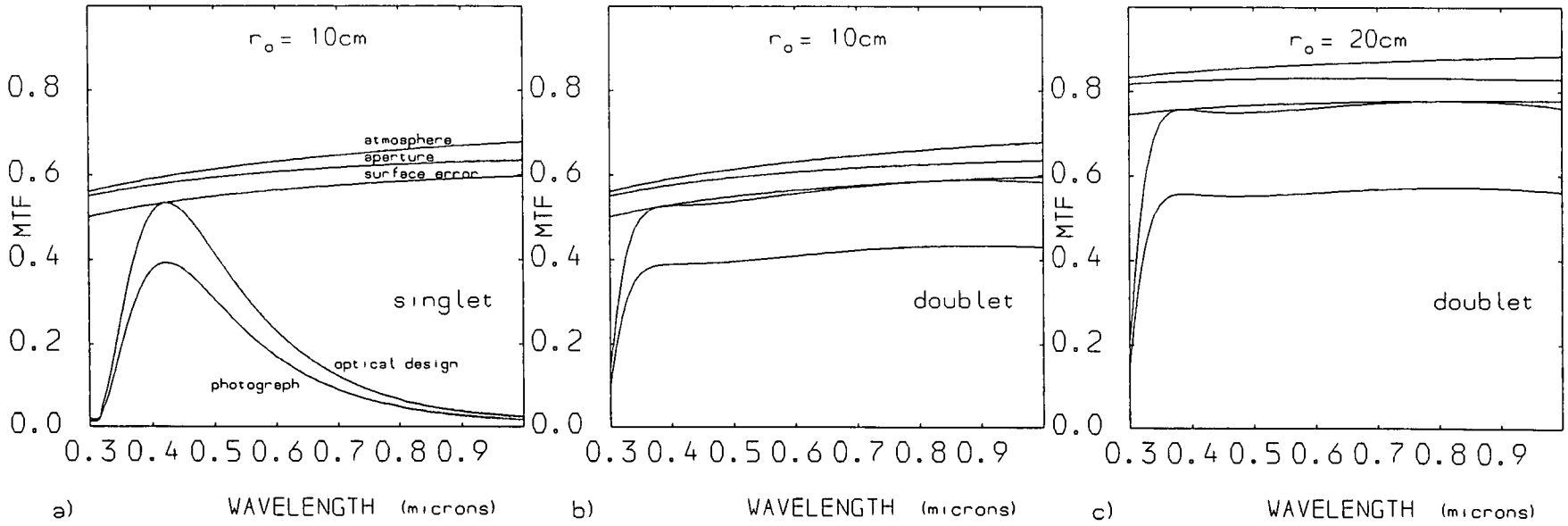


FIG 4.6 Modulation values at 0.3 cycle/arcsec for SI telescope

errors, optical design of the corrector plate and the effects of the emulsion are shown. In all the figures 4.6a,b,c, the seeing reduces the MTF considerably, although its effect is less at longer wavelengths as expected. While the aperture diffraction and surface errors have little effect, the optical design of the plate has a much greater effect. For example, for the singlet (fig 4.6a) the MTF is severely reduced for wavelengths away from its corrected wavelength ($\lambda$=0.42micron). However the achromatic doublet (fig 4.6b and 4.6c) is very well corrected and contributes negligibly to the reduction of MTF except in the UV region. Finally the effect of scattering in IIIa-J emulsion is seen to be quite important. Indeed, with good seeing, the emulsion becomes the limiting feature, (fig 4.6c).

The calculations have been repeated for two larger Schmidts S2 (in fig 4.7a,b,c) and S3 (in fig 4.8a,b,c). The effects on these telescopes are similar to, but smaller than, S1. As the focal length is increased the image on the photographic plate increases and so the effect of the emulsion is reduced. So for telescopes S2 and S3, the image continues to be limited by seeing, even when the seeing is good ($r_o$ = 20cm). Also, the effect of the residual aberrations (particularly for the singlet corrector plate) is reduced.

So although telescope S2 will collect four times as much light as S1 and distribute it over a focal area four times larger for sky background, the improvement in MTF with longer focal length will lead to relatively narrower and hence brighter star images. This is apparent in the next section.

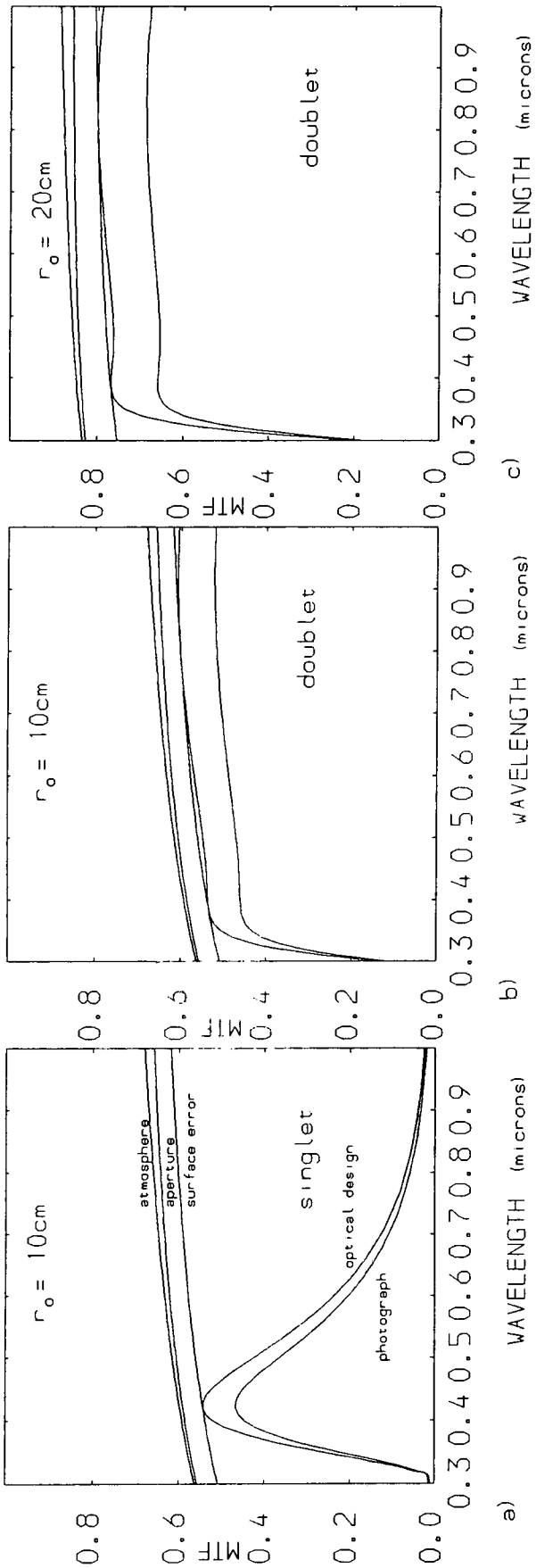


FIG 4.7 Modulation values at 0.3 cycle/arcsec for S2 telescope

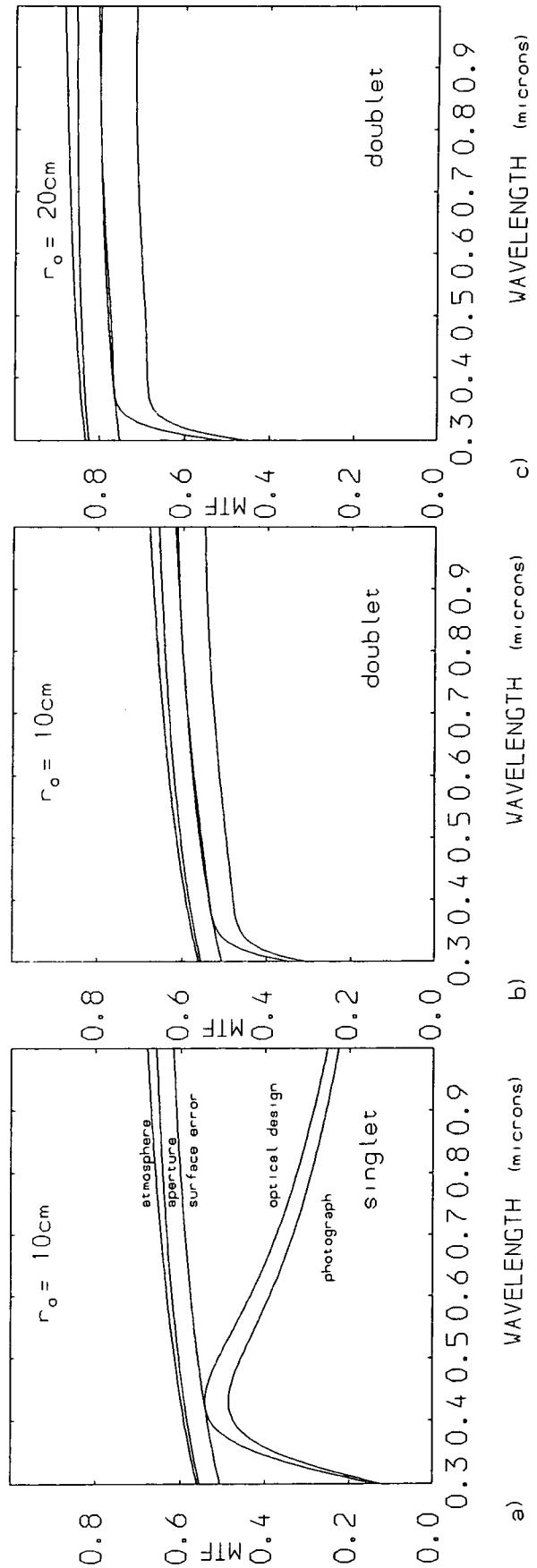


FIG 4.8 Modulation values at 0.3 cycle/arcsec for S2 telescope

## 4.5 POINT SPREAD FUNCTION

The image structure, or point spread function, is given by the inverse Fourier transform of the MTF and the broader the distribution of the MTF, the narrower is the PSF. This is illustrated in figs 4.9 and 4.10, which show the intensity patterns, as a function of angular size, expected for the three telescopes at a wavelength of 0.5 micron and at an average seeing of $r_o$ = 10cm. In fig 4.9, the telescopes have a singlet corrector plate whilst in fig 4.10, they have a doublet corrector plate.

In figs 4.9a and 4.10a, the normalised intensity patterns are shown to illustrate the small sharpening of the image due to an increase in aperture size. In figs 4.9b and 4.10b, the relative intensities are shown where increased apertures have a large effect on intensity. Furthermore, when figs 4.9a and 4.10a are compared the extra sharpening of the image can be seen because of the improved performance of the achromatic corrector plate at $\lambda$ = 0.5 micron.

## 4.6 THE PHOTOGRAPHIC IMAGE

The star image has to be detected from the photographic plates. The photometric use of photographic plates depends on the blackening of the developed emulsion after exposure to light and this response is non-linear and depends on various factors. The usual photometric function considered is the density. This is defined as the logarithm to base 10 of the ratio of the radiant flux, $I_o$, incident on the developed image to the radiant

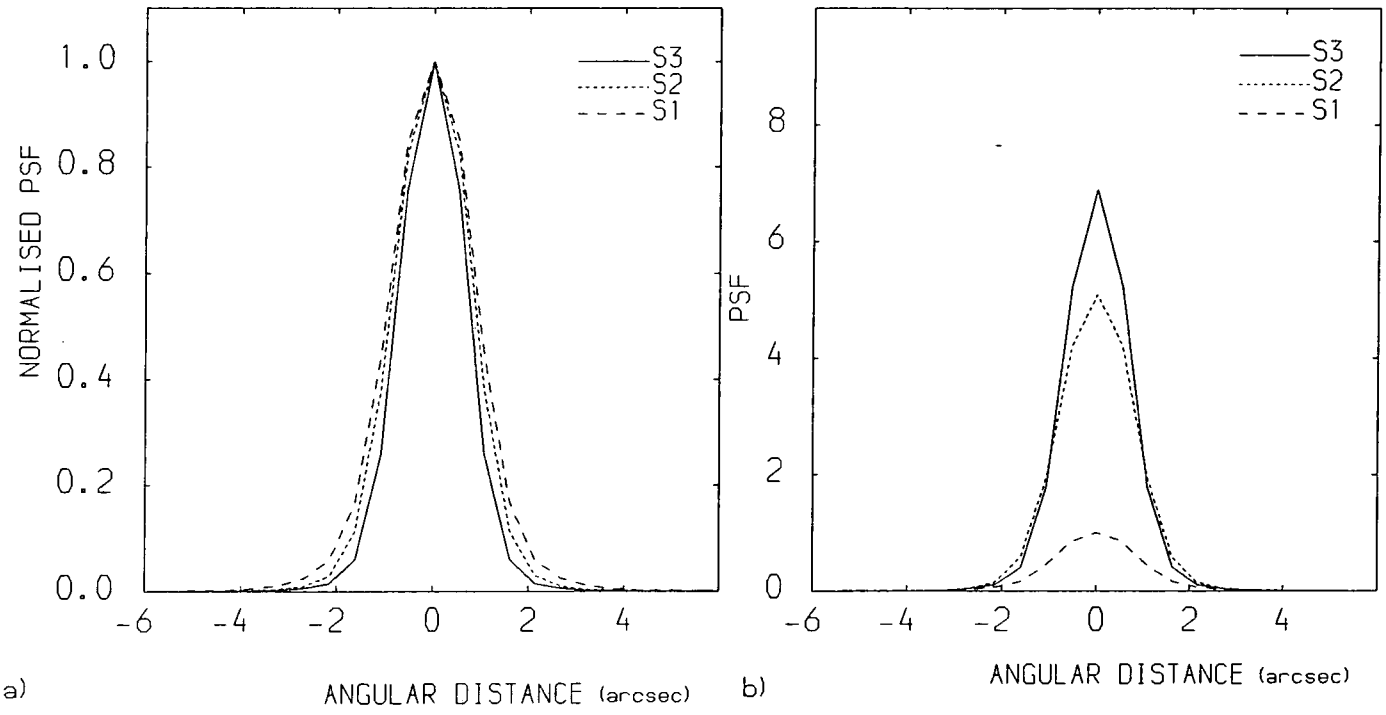


FIG 4.9 Point spread function - singlet corrector plate

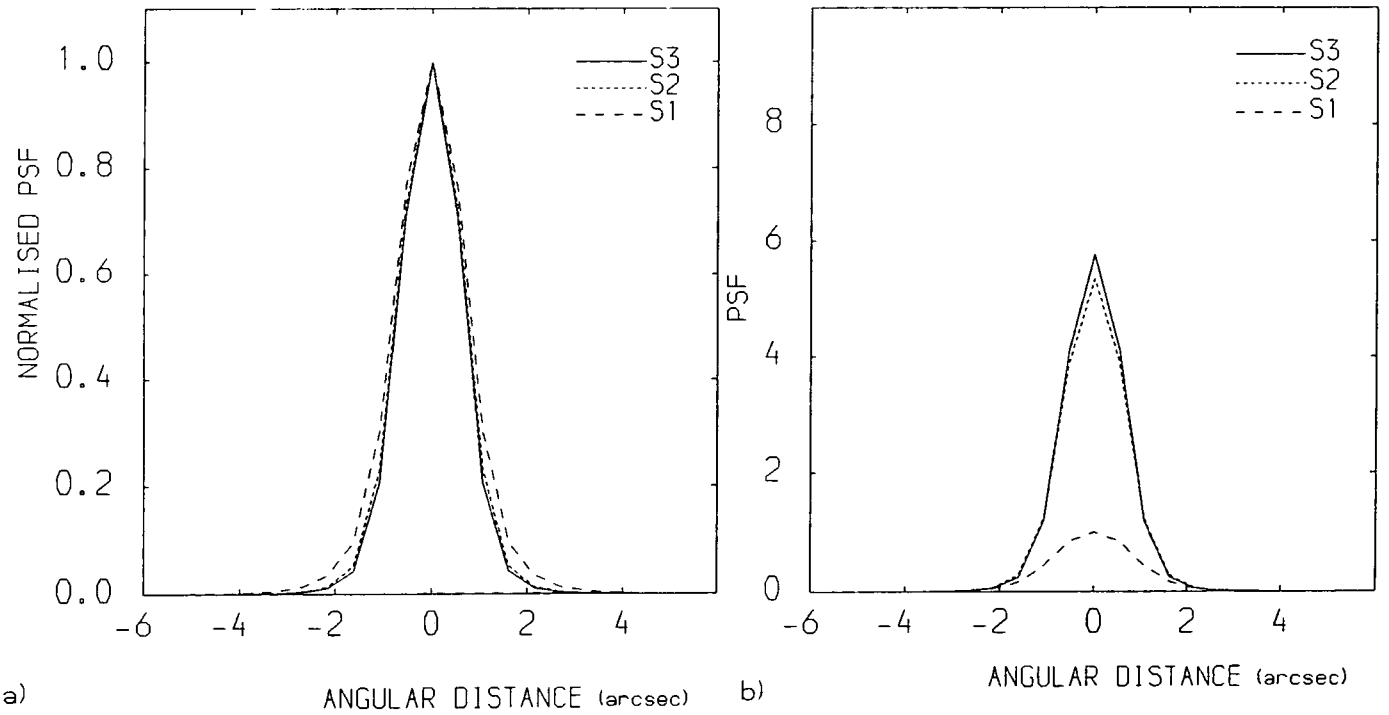


FIG 4.10 Point spread function - doublet corrector plate

flux, $I_t$, transmitted by the developed image. This ratio is also known as the transmittance of the developed image, T. Thus the photographic density is given by:

$$D = \log_{10}(I_o / I_t) = - \log_{10}(T) \quad . \qquad (4.19)$$

The curve relating density to the logarithm of exposure is called a characteristic curve (Hurter and Driffield, 1890) (fig 4.11). This curve is a function of emulsion type, development, wavelength, exposure time, etc. The gradient of the approximately straight portion is the contrast or 'gamma', $\gamma$. Fog usually occurs when photographic material is developed and some grains are reduced in areas that have received no exposure. The maximum density occurs when all the grains are fully developed.

The exposure is most commonly a simple product of intensity and time,

$$\text{Exposure} = It \quad . \qquad (4.20)$$

It is usually expressed in photometric units such as metre-candle-seconds or can be expressed in photons per unit area. When long exposure times are used, this reciprocity law fails so equation 4.16 becomes the 'effective' exposure

$$E = It^p \quad , \qquad (4.21)$$

where p is usually 0.8. To reach a given density, the required It product is a minimum for some optimum exposure time in the region of seconds and increases for exposures of minutes and hours. However Kodak make special 'astronomical' emulsions (such as IIIa-J) with reduced low-intensity reciprocity failure, so we are not concerned about this in our calculations.

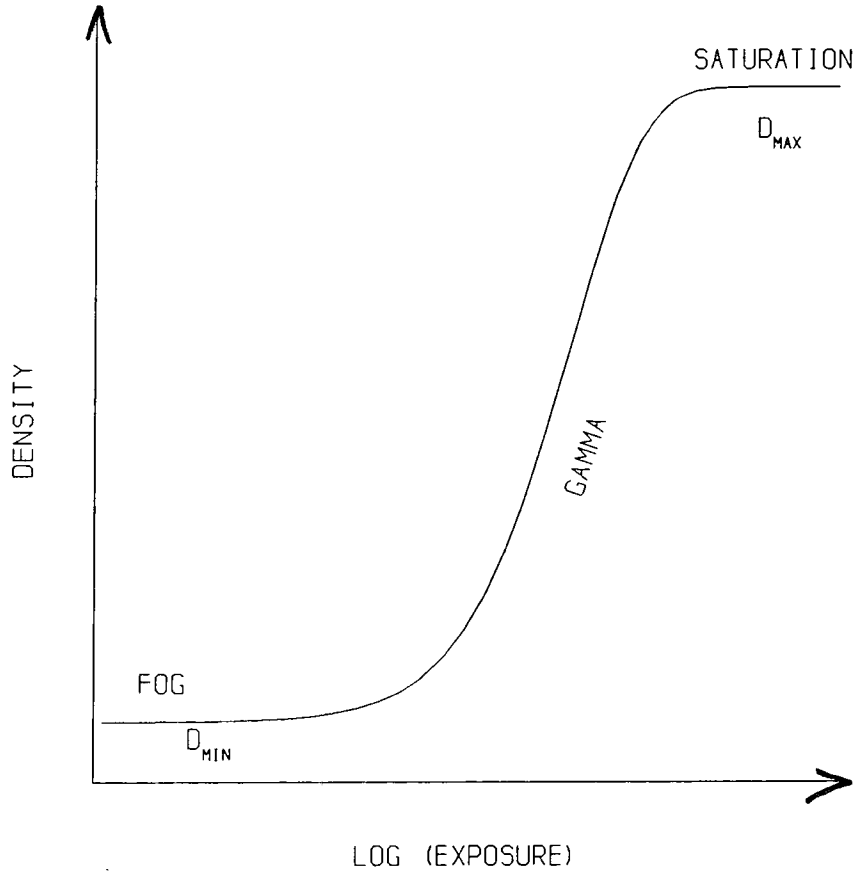


FIG 4.11 Characteristic curve

The emulsion is approximately 10% silver halide (chiefly bromide) and 90% gelatine by volume. The latent image consists of developable centres on the surface of the AgBr grains where, starting from these centres, development causes each exposed grain to be reduced to metallic silver. Before we can calculate the density of the stellar image, we need to find a basic model of photographic density. A good account of such a model is given in Dainty and Shaw (ref. 4.3) and is summarised in Appendix A.

4.6.1 Basic model of photographic density

In the unprocessed emulsion, there are $N_A$ grains in projected area, A. There is a distribution of grain sizes, a, and quantum sensitivities, Q (where Q is the minimum number of photons to be absorbed by a grain to make it developable.). The proportion of grains of size, a, is $\beta_a$ and the proportion of grains with quantum sensitivities, Q, is $\alpha_Q$. From Appendix A, the photographic density is then:

$$D = D_{max}\{1 - \sum_{Q} \sum_{a} \alpha_Q \beta_a a/\bar{a} \exp(-aq) \sum_{r=0}^{Q-1} (aq)^r/r!\} + D_{min} \qquad (4.22)$$

This is an analytical equation for a characteristic curve which can be used to find out the distribution of the grain size and the quantum sensitivities using a curve fitting method to a known experimental characteristic curve.

4.6.2 IIIa-J emulsion

From electron micrographs, (see fig 4.12), the IIIa-J emulsion has a cubical grain of constant size, a = 0.36 micron$^2$. If it is assumed that the developed grain size, d, is equal to undeveloped size, a, then $\beta_a = 1$, $a/\bar{a} = 1$, and eq 4.22 becomes

$$D = 0.434 N_A \frac{a}{A} \{1 - \sum_Q \alpha_Q \exp(-aq) \sum_{r=0}^{Q-1} \frac{(aq)^r}{r!}\} \quad . \qquad (4.23)$$

The gamma (slope of the characteristic curve) can be calculated from eq 4.23:

$$\gamma = \frac{dD}{d(\log_{10}(aq))} = 2.3 D_m \sum_Q \alpha_Q \exp(-aq) \frac{(aq)^Q}{(Q-1)!} \quad . \qquad (4.24)$$

This has a maximum when $d\gamma/d(aq) = 0$ and occurs when Q is equal to aq. So,

$$\gamma_m = 2.3 D_m \sum_Q \alpha_Q \exp(-Q) \frac{Q^Q}{(Q-1)!} \quad . \qquad (4.25)$$

The photograpic characteristic of IIIa-J has been fitted with a physical model based on a fixed grain size (0.36 micron$^2$) using a minimising computer programme 'MINUIT' (ref. 4.4). It is found that, to a good approximation, a fixed quantum sensitivity of two photons per grain is adequate. This is shown in fig 4.13 where the fitted curve predicts a maximum value of density, $D_m = 3.269$. Hence its photographic density is

$$D = 3.269\{1 - \exp(-aq)\ (1-aq)\} + 0.343 \ ,$$

and its maximum gamma,

$$\gamma_m = 3.269 \times 2.3 \times \exp(-2) \frac{2^2}{(2-1)!} = 4.07 \ .$$

This is in good agreement with the value given in the Kodak data book (ref. 4.2).

This fit to the characteristic curve can be used to

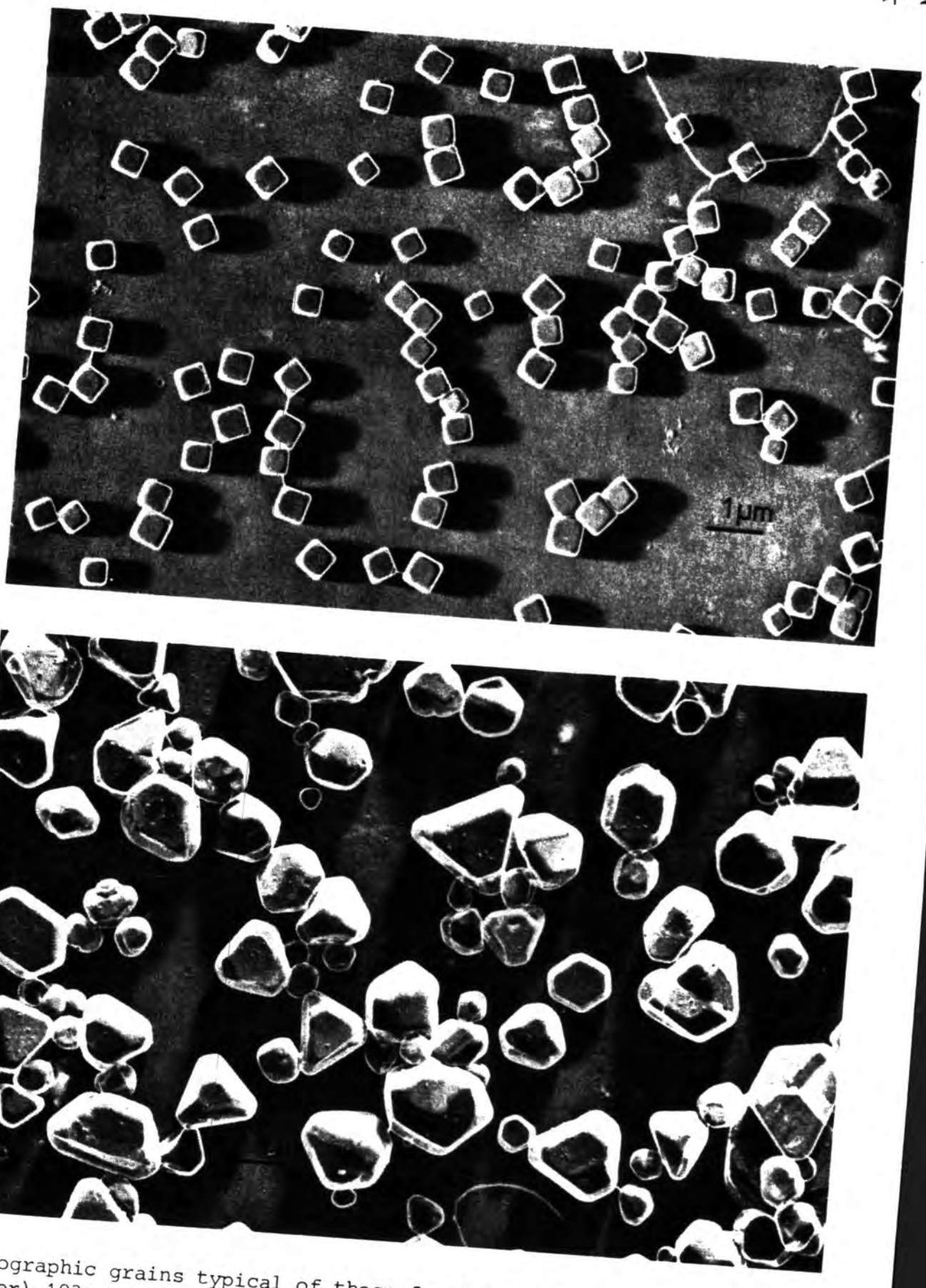


2 Photographic grains typical of those found in IIIa-J (upper) and (lower) 103a-O emulsions.

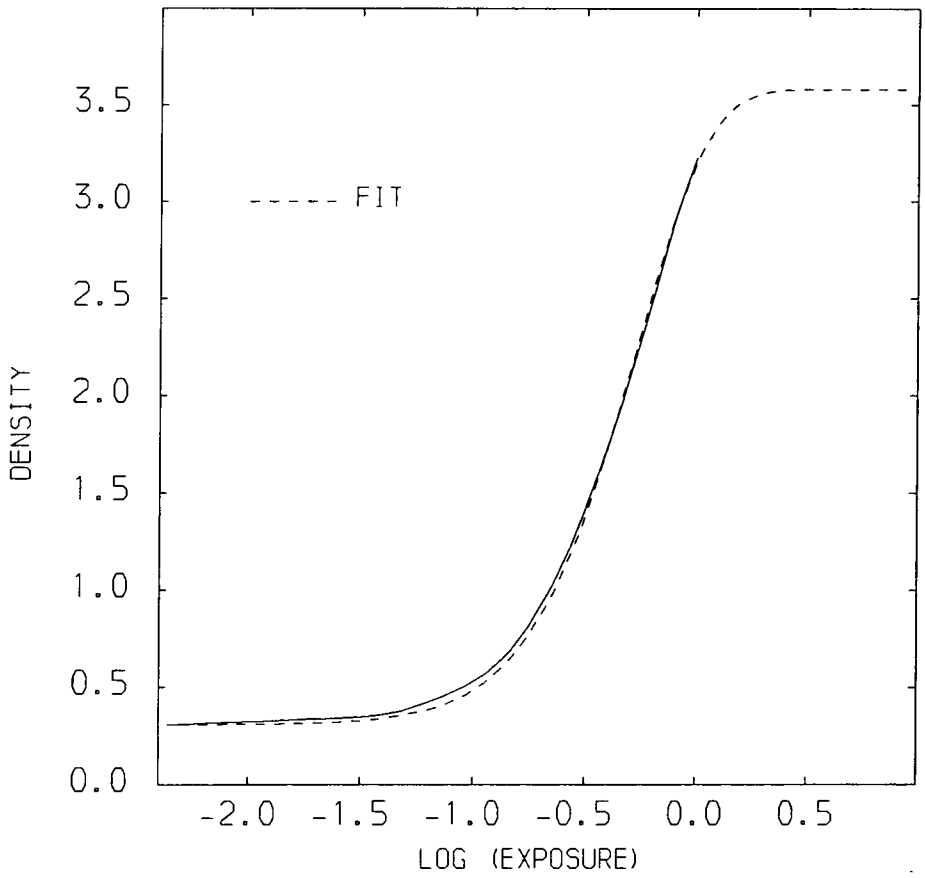


FIG 4.13 Photographic characteristic of 111a-J

determine the photographic densities in exposures. There is a difficulty in finding the exposure, (aq), since this is the number of absorbed photons in the exposure rather than the total number of photons per grain. However, in the case of the Schmidt photographic plates exposure is continued until the sky background gives a photographic density of unity. This can be used to define a sky background exposure $(aq)_o$ as described below.

After development, the transmission of the plate is

$$T = \exp(-n_d a/A) \quad , \qquad (4.26)$$

where $n_d$ is the number of grains with area, a, in the developed plate within a projected area, A. For IIIa-J emulsion, a is constant; for others (eg 103a-O) there is a spectrum of sizes and a is replaced by the average size.

For the sky background, the photographic density is

$$D = -\log_{10}T = \log_{10}\exp(n_d a/A) = 0.434 n_d a/A = 1.$$

Hence the number of the developed grains, $n_d$, can be found, ie

$$n_d = \frac{1}{0.434}\frac{A}{a} \quad \text{grains/cm}^2.$$

If A is a pxp microns$^2$ pixel size (a microdensitometer scanning beam), then the number of developed grains per pixel size is

$$n_d = \frac{1}{0.434}\frac{p^2}{a} \quad \text{grains/pixel.} \qquad (4.27)$$

At the maximum density,

$$D_m = 0.434 N_A \frac{a}{A} \quad ,$$

and this is a saturated level where all the grains are developed. Hence an original number of undeveloped grains

before exposure to light can be found, ie

$$N_A = \frac{1}{0.434}\frac{A}{a} D_m \text{ grains/cm}^2$$

For a pxp microns$^2$ pixel size, the number of undeveloped grains is

$$N_p = \frac{1}{0.434}\frac{p^2}{a} D_m \text{ grains/pixel.} \qquad (4.28)$$

The number of photons from a star of apparent magnitude, m, is given by

$$i = 1.26\lambda x10^{7} x10^{-0.4m} \text{ photons/cm}^2\text{/sec,} \qquad (4.29)$$

where $\lambda$ is measured in microns. The apparent magnitude for sky background, $m_b$ is usually expressed in arcsec$^{-2}$ of the sky. So the number of sky background photons collected by a telescope aperture, diameter D (cm), is

$$i_b = 1.26\lambda x10^{7} x\frac{\pi D^2}{4} x10^{-0.4m_b} \text{ photons/sec/arcsec}^2 \text{ of sky.} \qquad (4.30)$$

Now the angle subtended by a pixel of size p (microns) at the mirror is $p/f x10^{-4}$ radians where f is a focal length (cm). So the number of sky background photons entering a pixel is

$$i_b = 5.36\lambda x10^{9} x\frac{\pi D^2}{4}(p/f)^2 x10^{-0.4m_b} \text{ photons/sec.} \qquad (4.31)$$

Only a small percentage of these photons are absorbed and lead to the latent image (~1%). This scaling factor can be determined from the number of photons incident on a pixel during an exposure to give unit density ie to give $n_d$ developed grains/pixel (eq 4.27). This scaling factor is then to used to determine the exposures for stars of various apparent magnitudes and hence to determine their photographic densities which are added to the sky background.

4.6.3 IIIa-J results for (aq)$_o$

When the Schmidt telescope, S1, with IIIa-J photographic plate and a microdensitometer scanning beam of 8x8 microns$^2$ pixel size, is used, then the number of developed grains after exposure to sky background is (from eq 4.28), $n_d$ = 410 grains/pixel, and the number of undeveloped grains is $N_\rho$ = 1,338 grains/pixel. The total number of sky background ($m_b$ = 22.5 arcsec$^{-2}$) light photons collected by the 124cm diameter Schmidt telescope, S1, is 76 photons/sec/arcsec$^2$ of sky in the visible spectrum. The number of sky background light photons entering a 8x8 microns$^2$ pixel (= 0.289 arcsec) at a focal length of 307cm is 22 photons/sec/pixel.

Typically about one hour is required to give a sky background density of unity. In this time there are 79,200 photons/pixel which produce 410 developed grains. (Note that the quantum sensitivity for IIIa-J is 2 ie, it needs 2 photons to make 1 grain developable). Hence the fraction of absorbed photons is 0.0104, that is 1% of the incident photons contribute to the image. This is fairly typical of absorption probabilities of AgBr grains in the visible region.

4.6.4 Exposure Times

The plate is exposed to the sky background until the photographic density reaches unity. Exposure depends on time, t, telescope aperture diameter, D, and its focal length, f, as follows:

$$\text{exposure} \propto t\, D^2 / f^2.$$

So for the same exposure using two telescopes (S1 and S2)

$$t_1 D_1^2 / f_1^2 = t_2 D_2^2 / f_2^2 . \qquad (4.32)$$

In the S2 telescope, the diameter and focal length are doubled, $D_2 = 2D_1$, $f_2 = 2f_1$, so the time taken to give the same exposure as for S1 is

$$t_2 = t_1 (D_1 / D_2)^2 (f_2 / f_1)^2 = t_1 ,$$

ie the same exposure time as S1. The S3 telescope has the same diameter as S2 but its focal length is further increased, ie $D_3 = 2D_1$, $f_3 = 2.4f_1$, so the exposure time, $t_3$, is 1.44 S1's exposure time to give same sky background density of unity.

4.6.5 Simulation of Photographic Plate

The simulations in the photographic plate were made in two dimensions. For the S1 telescope, the densities were evaluated in a microdensitometer scanning beam with pixel size of 8x8 microns$^2$ where the point spread function, PSF, of a stellar image (seeing disc) covers a 21x21 matrix of such pixels (a total angular size 10x10 arcsec$^2$). The PSF has been calculated in arbitrary units normalised to unity at the centre, so by integrating over each pixel it represents the total number of photons collected from a star.

The total number of photons collected from a star of apparent magnitude, m, by a telescope aperture with diameter D cm is:

$$i = 1.26\lambda \times 10^7 \times \frac{\pi D^2}{4} \times 10^{-0.4m} \text{ photons/sec.} \qquad (4.33)$$

Then the numbers of photons per pixel are found by integrating the PSF over each pixel. These pixels are added to a constant

sky background given in photons/pixel and then are converted to developed grains by simple scaling. The scaling factor is $n_d / i_b$ where $i_b$ is the number of photons from the sky background, giving $n_d$ , the number of developed grains, for an exposure made until the density is unity. Then the number of grains per pixel is converted to the photograpic density by eq 4.22.

An example of a one dimensional simulated measurement of density through a star of $22^m$ is shown in fig 4.14, for the three designs of telescope with the singlet corrector plate and fig 4.15 with the doublet corrector plate.

4.6.6 Grain Noise

There will be random fluctuations of grains from one pixel to another giving the noise of the system. This is the granularity. From Poisson statistics it is expected that this is $\sqrt{n}$, where n is the number of grains in the pixel. From the relationship of density and number of grains, it is expected that the fluctuations of density are given by

$$\sigma_D = C \sqrt{D} , \qquad (4.34)$$

where C is a constant for the particular material. The standard deviation of the density fluctuations, $\sigma_D$ , has been measured by Furenlid (ref. 4.5). He standardised to a measuring area of 1,000 microns$^2$. He found that the characteristic value of $\sigma_D$ for astronomical emulsions varied between 0.01 and 0.08 over a density range of about $0 \leqslant D \leqslant 3$ and that such values appear to be a function of the emulsion type and density only, and to depend very little on the developer and hypersensitization.

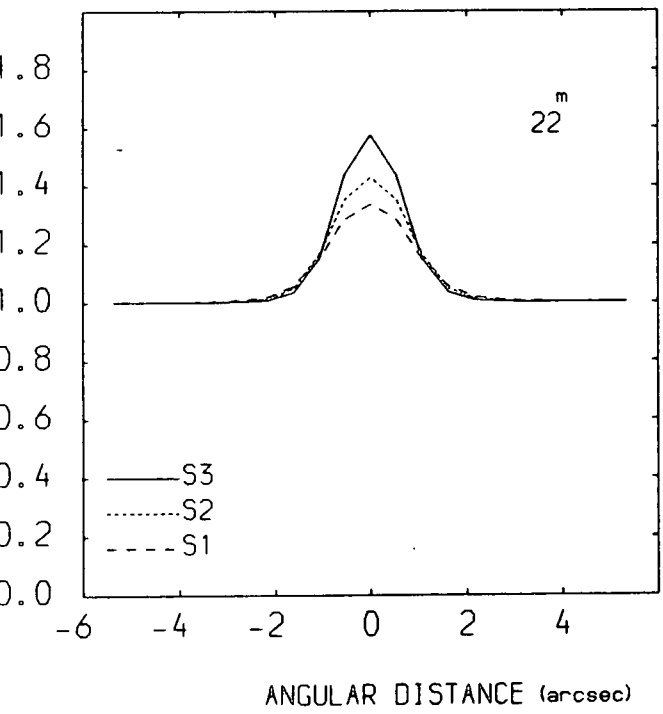


FIG 4.14 Stellar density - singlet

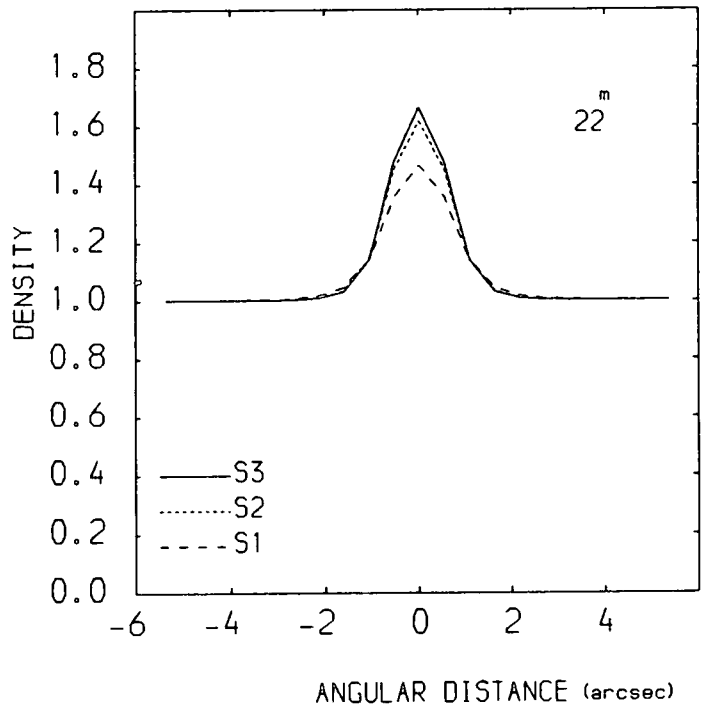


FIG 4.15 Stellar density - doublet

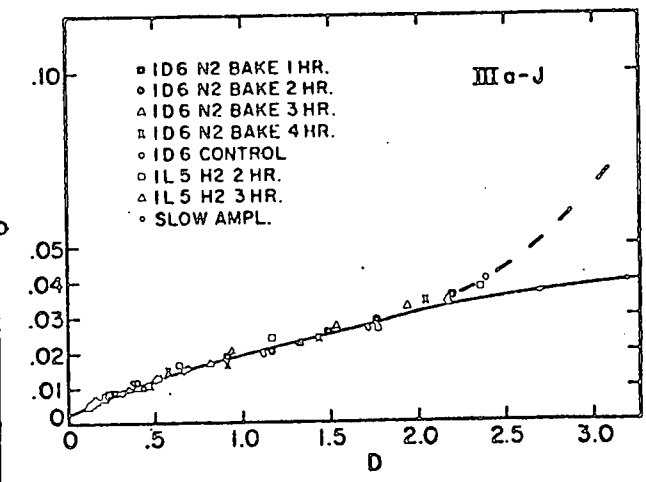


FIG 4.16 Furenlids result

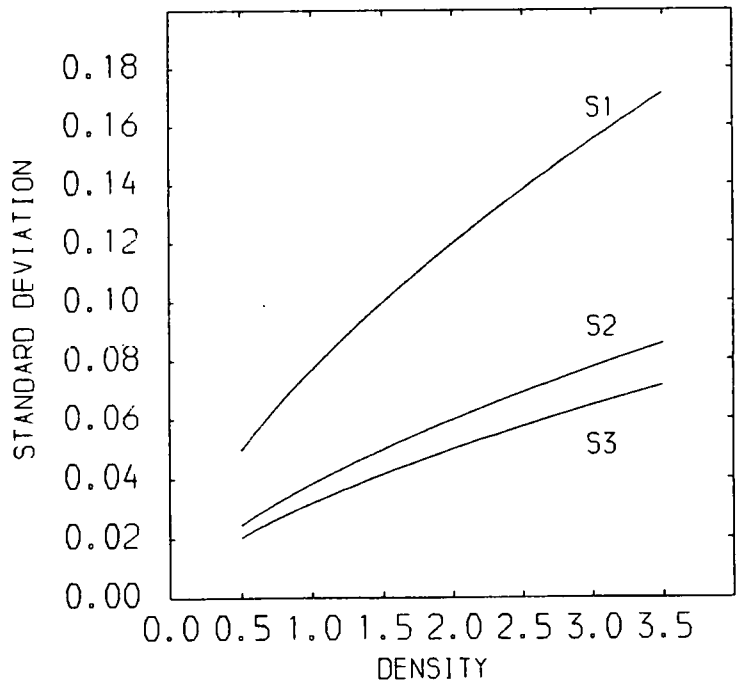


FIG 4.17 Converted Furenlids result

Furenlid's results for a $\sigma_D$(area, 1,000 microns$^2$) of IIIa-J are shown in fig 4.16. Using Furenlid's results and fitting a curve to them, it is found that

$$\sigma_D = 0.0195D^{0.638}, \qquad (4.35)$$

rather than the $\sqrt{D}$ form. As this is measured in an area of 1,000 microns$^2$, then for a pixel on a plate of area A microns$^2$, then

$$\sigma = \sigma_D(A/1000)^{1/2}. \qquad (4.36)$$

To simulate this, the results of Furenlid have been scaled to pixels of the sizes used here. For the longer focal length telescopes, it is the linear size of the image which is increased, and not the angular size. To give the same angular resolution, the pixel size is increased from 8 microns to 16 microns for S2 and to 19.2 microns for S3. As these larger pixels now cover more grains, the relative fluctuations will be reduced. This is seen in fig 4.17 where Furenlid's results have been converted for the three pixel sizes.

The 2-dimensional distributions of photographic density are then randomised by the standard deviation in density fluctuations corresponding to the density and pixel size. An example of a one-dimensional simulated measurement of density with fluctuations through a star of $22^m$ are shown in figs 4.18 and 4.19. It can be seen that a star at $22^m$ is just seen by the S1 telescope.

### 4.6.7 Sensitivity and Signal/Noise

Because of the complexity of the photographic process,

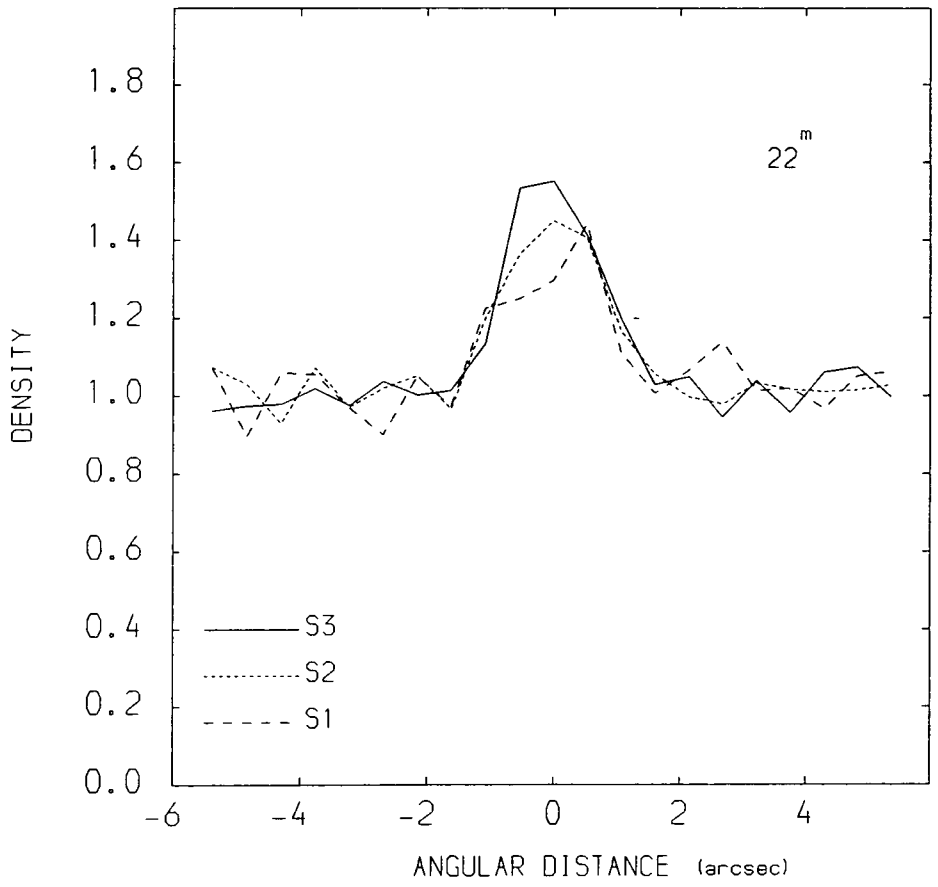


FIG 4.18 Stellar density after fluctuations - singlet

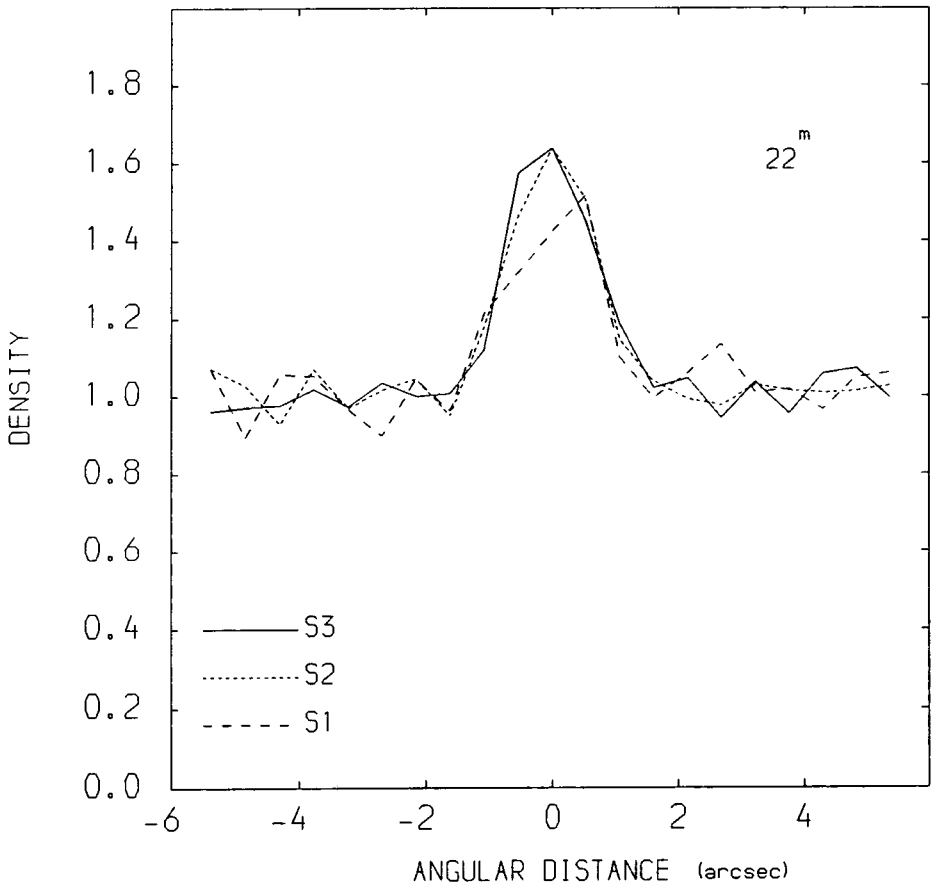


FIG 4.19 Stellar density after fluctuations - doublet

sensitivity and signal/noise cannot be assessed as simply as in the case of direct photoelectric detection. Nevertheless data is now available that enables the signal/noise performance of the photographic detector to be estimated and optimised. The details of the photographic process can be avoided by treating the photographic emulsion plate as a 'black box' with an input of photons and an output of a measurable signal/noise ratio, SNR. The detective quantum efficiency is defined as

$$DQE = (SNR)^2_{OUT} / (SNR)^2_{IN}, \qquad (4.37)$$

that is the ratio of the number of ideally detected photons that would produce the observed SNR to the number of photons actually required. Furenlid points out that there is a difficulty in interpreting the DQE and there is no way to determine, from the DQE alone, the amount of change in either $SNR_{OUT}$ or $SNR_{IN}$ without measuring at least one of them. He uses $SNR_{OUT}$ to refer any value to the photometric properties of the plate.

The output SNR in a photographic emulsion is defined as the ratio of the exposure to the rms fluctuation in exposure (noise). This quantity cannot be measured directly on a photographic plate because of the non-linear relationship between input and output signals, but it is related to density via the characteristic curve which can be measured. SNR is given by

$$SNR = 0.434\gamma/\sigma_D, \qquad (4.38)$$

where $\gamma$ is the gamma, or slope, of the characteristic curve. It can be measured graphically from the curve and it is a function of density. The standard deviation of the density fluctuations,

$\sigma_D$ , can be measured by a microphotometer or other kind of measuring equipment. Furenlid has tabulated $\sigma_D$ as a function of D for various astronomical photographic emulsions. One example of this for IIIa-J emulsion is shown in fig 4.16.

IIIa-J emulsion is found to have a lower $\sigma_D$ than any other astronomical photographic emulsion. In fact a 'fast' emulsion, such as 103a-O, has quite a high $\sigma_D$ and hence it has a poorer SNR than IIIa-J, resulting in the limiting sensitivity for 103a-O being reduced. The IIIa-J emulsion was produced by Kodak in response to astronomers demands for a reasonably fast plate capable of a high SNR.

For the detection of the faintest possible objects on a single exposure, it is the SNR that determines the detectability of a faint image above the sky background. The output SNR usually increases with increasing exposure, reaches a maximum, and then, with some photographic materials, decreases with further exposure.

In practice, the exposure is continued until the image is recorded at a density level corresponding to the lower portion of the straight line of the D-logE relation, and this occurs when the SNR is at a maximum. This means that a faint stellar object can be detected against the sky background. For IIIa-J, the maximum SNR occurs when the density is equal to unity and, this is shown in fig 4.20. The improvement in the SNR between the telescopes, S1, S2 and S3 can be shown as follows.

The number of grains in the emulsion depends on a pixel size with area $p^2$ which also depends on the focal length

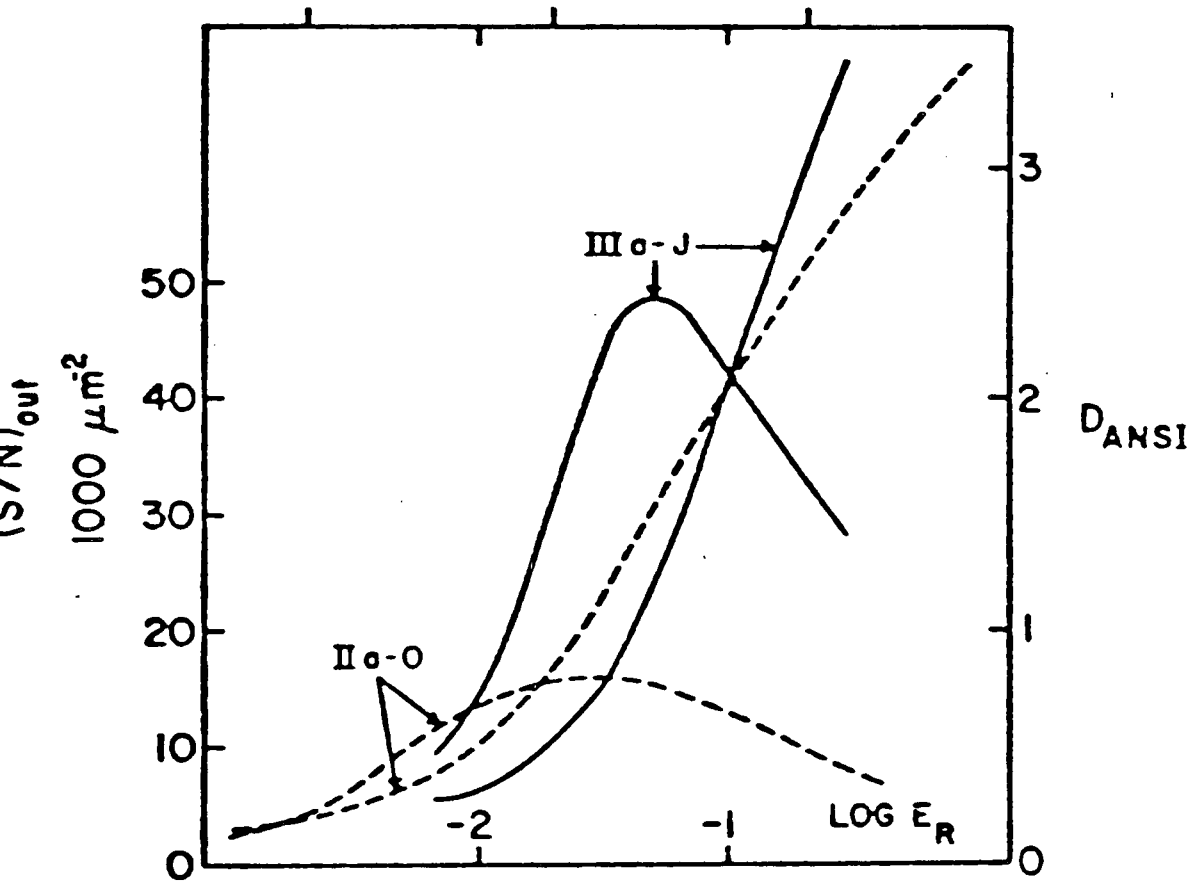


FIG 4.20 SNR curve for IIIa-J plate with a characteristic curve

($p = \Theta f$). For a constant angular size, $\Theta$,

$$n \propto f^2 \text{ grains.}$$

For the same blackening in the emulsion, the noise due to sky background, emulsion fluctuations, etc, is

$$N = \sqrt{n} \propto f, \tag{4.38}$$

ie the noise is proportional to the focal length.

The signal depends on the pixel size ie $S \propto f^2$, and also on the intensity distribution of the stellar image which is proportional to the square of the MTF. So the signal is

$$S \propto f^2 (MTF)^2, \qquad \text{see below for MTF values.} \tag{4.39}$$

and the SNR is

$$S/N \propto f\ (MTF)^2. \tag{4.40}$$

For the same density of the sky background in the IIIa-J emulsion and with $r_o$ = 10cm seeing at $\lambda$ = 0.5 microns and with a doublet corrector plate, the MTF values at 0.3 arcsec are 0.38 for the S1 telescope and 0.46 for the S2 telescope, so the $MTF^2$ ratio is 1.46. Then the SNR for the S2 telescope is

$$(S/N)_2 = (S/N)_1\ (f_2/f_1)(MTF_2/MTF_1)^2, \tag{4.41}$$

$$= 2.92\ (S/N)_1 .$$

The change in apparent magnitude of a star that can just be detected is given by

$$\Delta SNR = 10^{-0.4\Delta m}. \tag{4.42}$$

For the S2 telescope $\Delta m = -1.167$, ie it gains about one magnitude improvement from S1, and hence it increases the limiting sensitivity.

In the S3 telescope, the MTF value at 0.3 arcsec is 0.511, so the $MTF^2$ ratio between S1 and S3 is 1.8, and thus the SNR for

the S3 telescope is

$$(S/N)_3 = 4.34(S/N)_1 .$$

So it improves SNR by a factor of 4.34 and it gains a factor of 1.59 magnitude from S1. It must be recalled that with S3, the change in f number requires a longer exposure to reach unit density for the sky background.

The limiting magnitude of stars that are just seen has been determined by quantifying a 'significance' for the stellar density. For the field of a stellar images of 21x21 pixels, the density is made up from starlight (S) and sky background (BG), and is randomised according to the grain noise. A further 50 randomised sky background fields have been generated and a significance, Sig, calculated where

$$Sig = \frac{1}{50} \sum_{i=1}^{50} [(S+BG) - BG_i]^2 . \qquad (4.43)$$

The significance is shown in fig 4.21 (for a singlet corrector plate) and fig 4.22 (for a doublet) with increasing stellar magnitude. When this such that the star is 'lost' in the noise, the Sig approaches $\sqrt{2}$. With the doublet corrector plate, this occurs at about $22^m$ for S1, at about $23^m$ for S2 and at about $23.5^m$ for S3. Thus there is an improvement in S2 by a one magnitude from S1 and in by a 1.5 magnitude from S1, and these values are the same as the values given above.

To demonstrate this improvement in sensitivity, nine stars of $22^m$ have been generated in a stellar field of 121x121 pixel for the three telescopes S1,S2 and S3. The fields are shown in figs 4.23a,b and c for the doublet corrector plate.

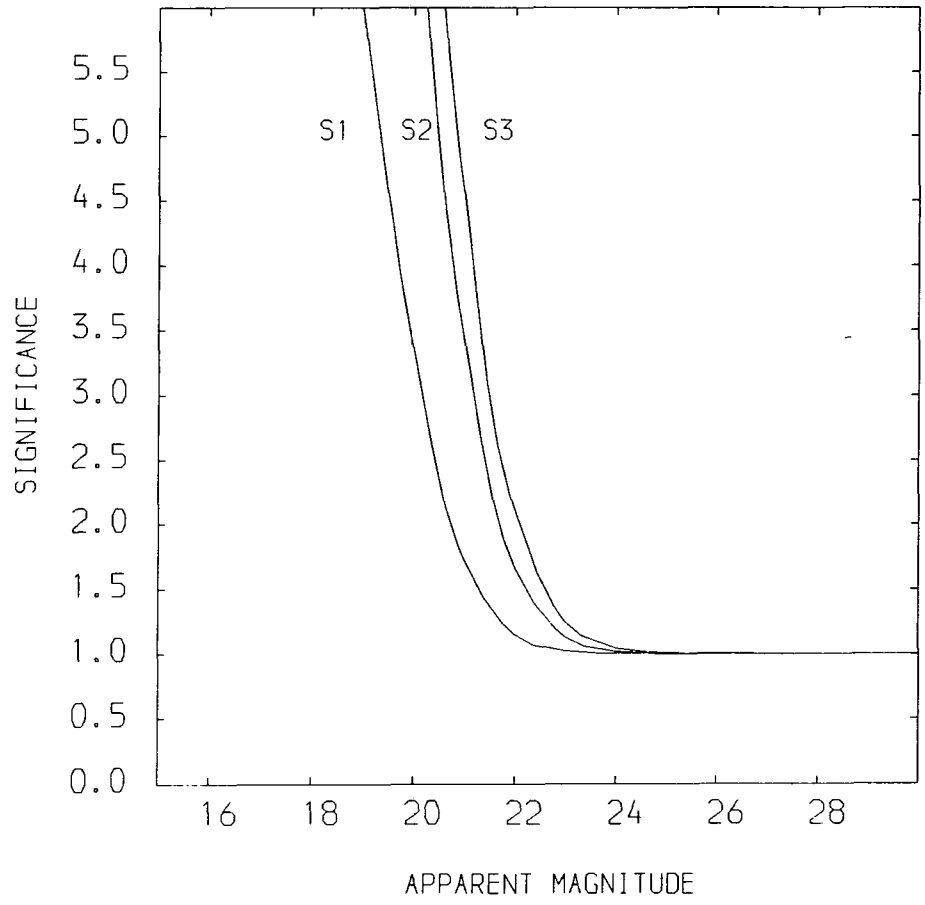


FIG 4.21 Significance of stellar density - singlet

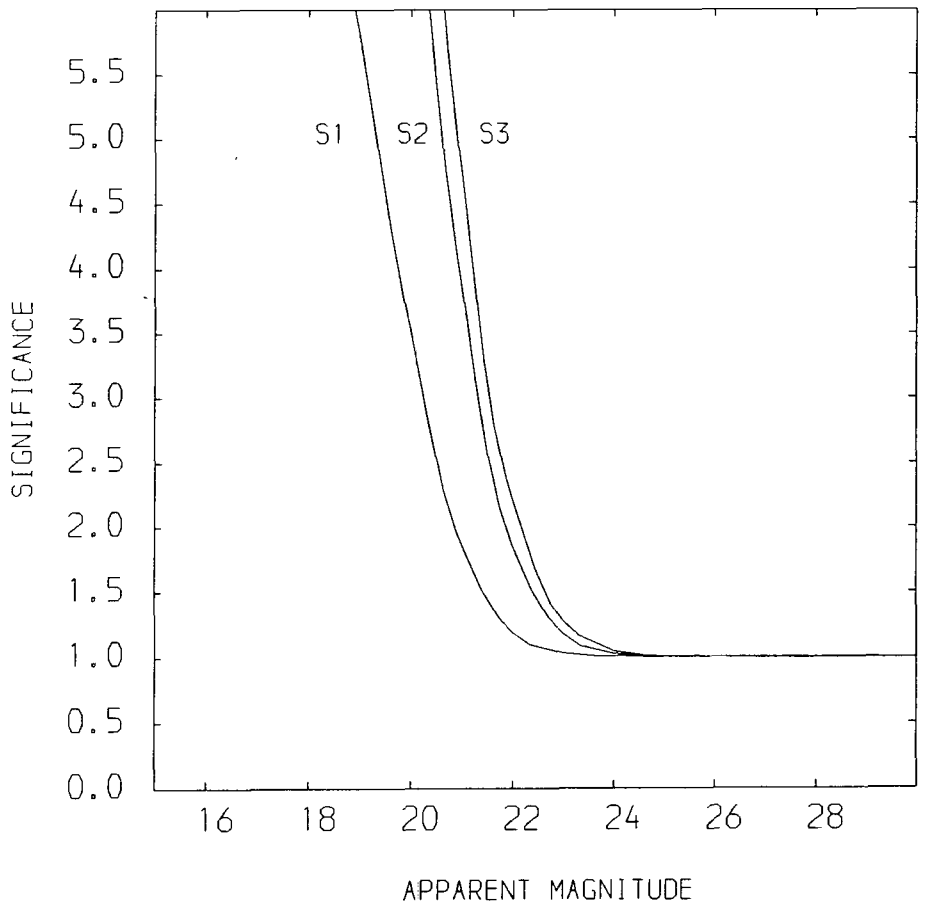


FIG 4.22 Significance of stellar density - doublet

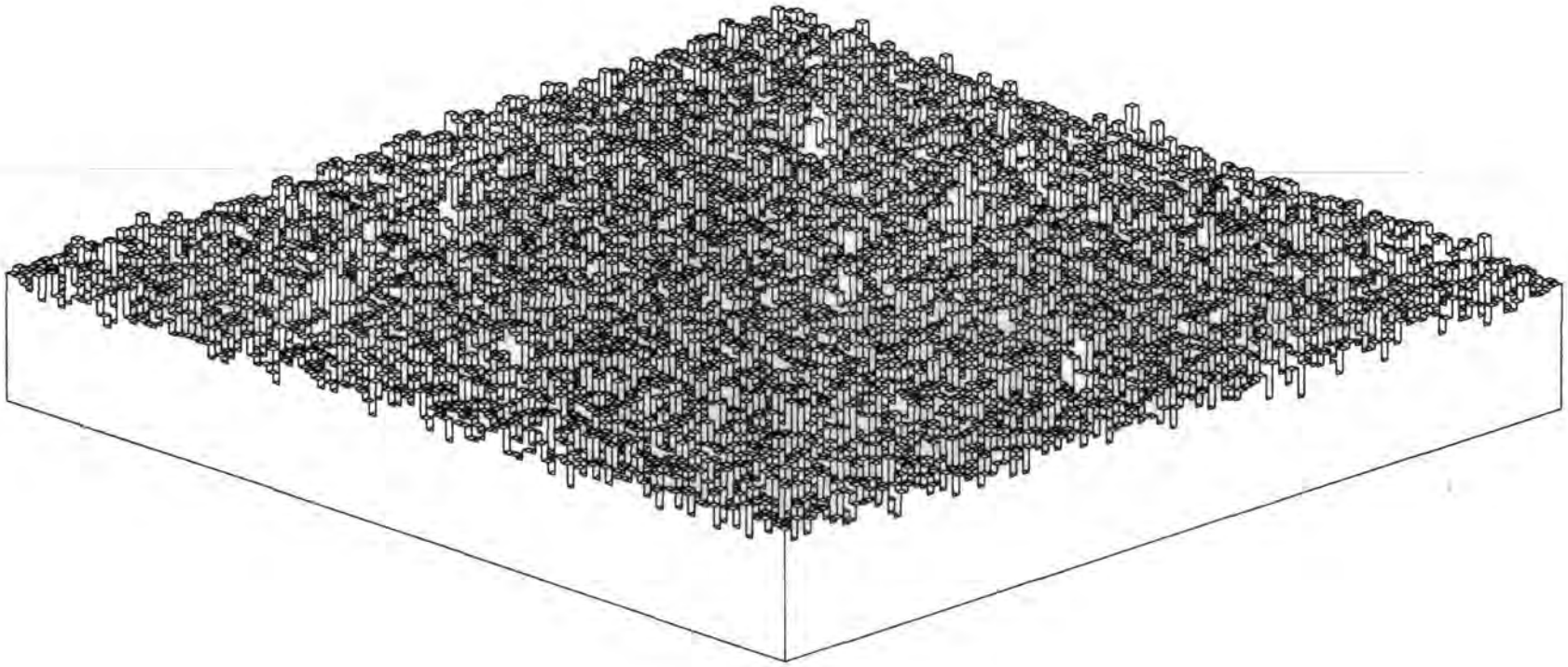

FIG 4.23 A) SIMULATED DENSITOMETER TRACE OF STAR-FIELD OF S1 TELESCOPE

AZIMUTH = 315. ALTITUDE = 20.
*WIDTH = 6.00 *HEIGHT = 3.00

* BEFORE FORESHORTENING OCT 14, 1985

$r_o = 10cm$

$22^m$

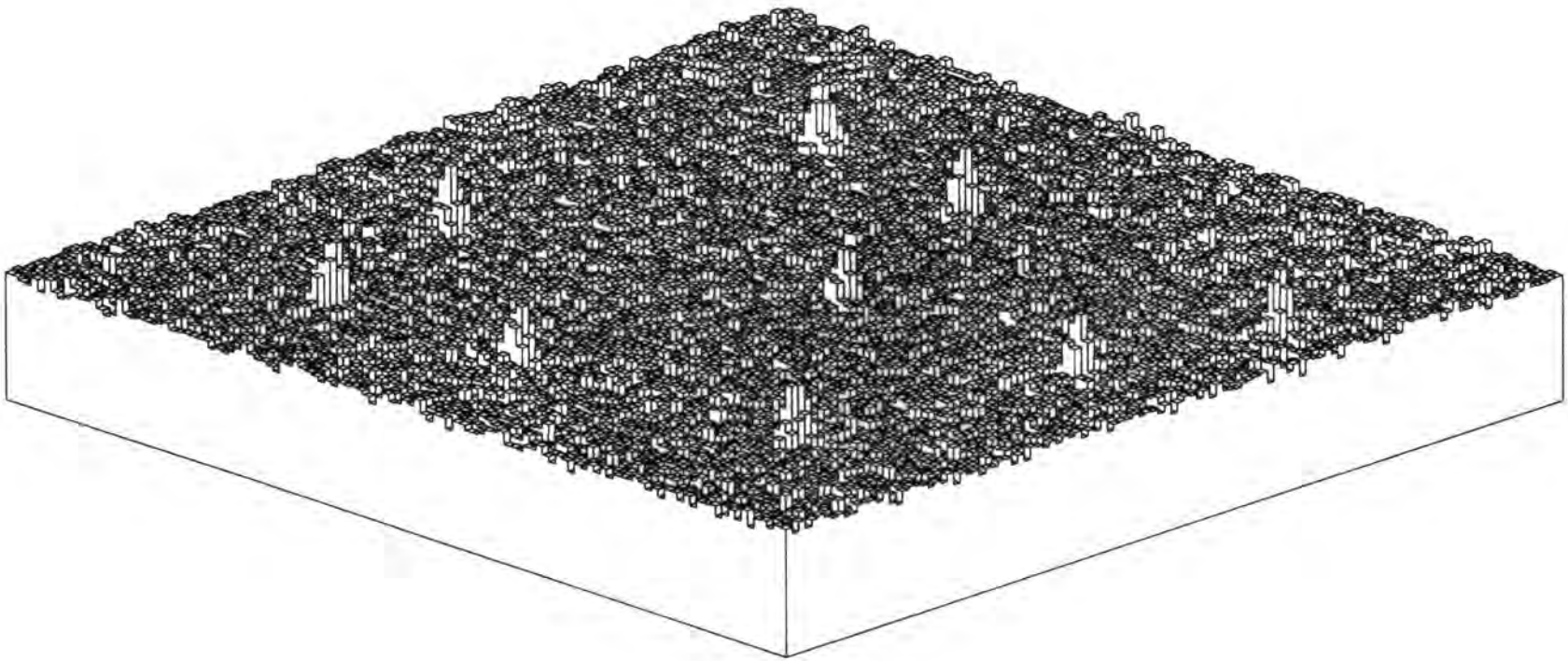

FIG 4.23 B) SIMULATED DENSITOMETER TRACE OF STAR-FIELD OF S2 TELESCOPE

AZIMUTH = 315. ALTITUDE = 20.
*WIDTH = 6.00 *HEIGHT = 3.00

* BEFORE FORESHORTENING OCT 14, 1985

$r_0 = 10\,cm$

$22^m$

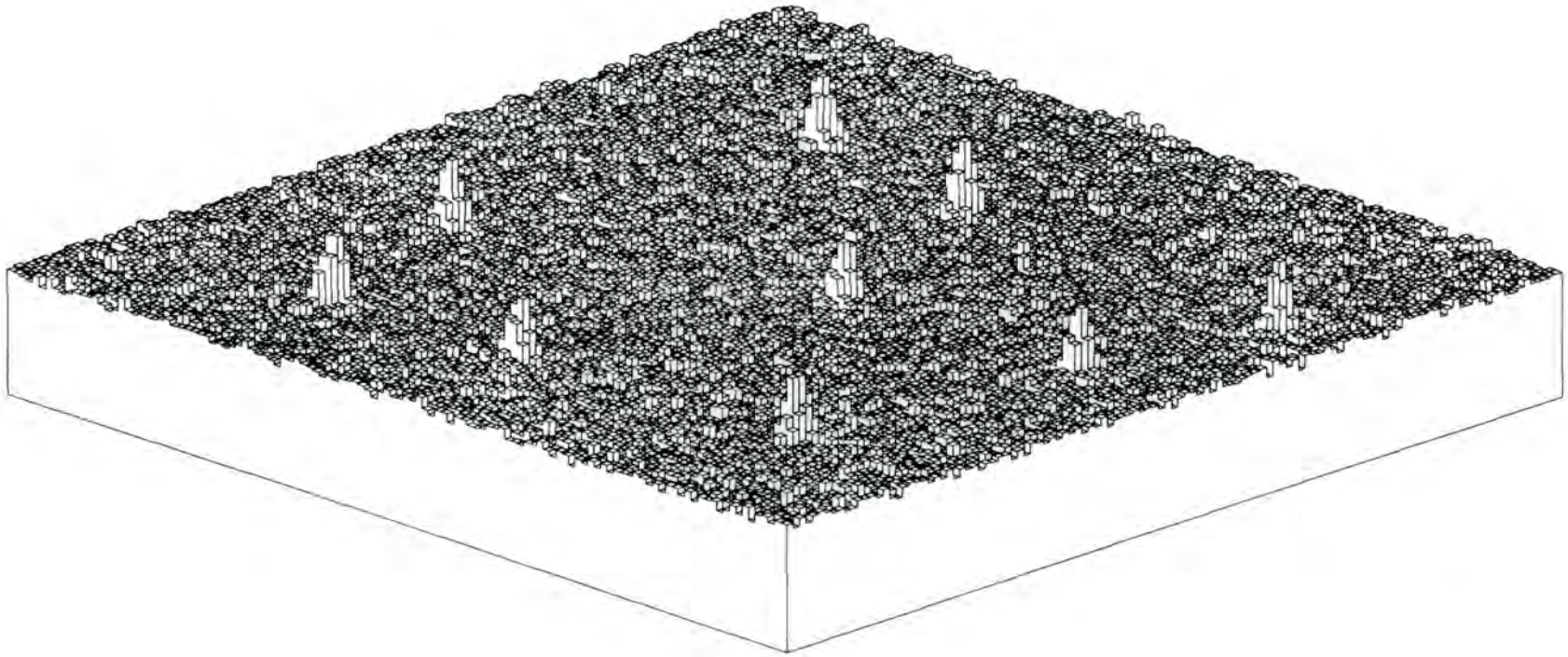

FIG 4.23 C) SIMULATED DENSITOMETER TRACE OF STAR-FIELD OF 53 TELESCOPE

AZIMUTH = 315. ALTITUDE = 20.
*WIDTH = 6.00 *HEIGHT = 3.00

* BEFORE FORESHORTENING OCT 14, 1985

$r_o = 10\,cm$

$22^m$

444

All these results have been summarised in Table 4.1 where the three telescopes, each with a doublet corrector plate were exposed to a photographic background sky density of unity in $r_o$ = 10cm seeing at $\lambda$ = 0.5 micron.

The above calculations were repeated but with good seeing, ie $r_o$ = 20cm. The significance is shown in fig 4.24 and there is an improvement of all three telescopes by about half a magnitude each. In the S1 telescope, it can be seen that there ia an improvement in sensitivity by comparing fig 4.25 and fig 4.23a of 9 stars of $22^m$ in a stellar field of 121x121 pixels.

Farnell (ref 4.6) has shown that the quantum sensitivity of photographic grains is independent of grain size and the speed of the photographic plate is increased with grain size only up to an area of 1.0 micron$^2$. When the grain size is doubled to 0.72 micron$^2$ or halved to 0.18 micron$^2$, it is found that the photographic characteristic of the IIIa-J emulsion has exactly the same fitting with a physical model based on a fixed quantum sensitivity of 2 as before except that the exposure scale factor is changed. So when the grain size is doubled then the exposure is halved to give the same photographic density as before.

When the photographic plate, with reduced grain size, $a_1$, is exposed to sky background to give unit density, it has no effect on the shape of the photographic image. But now there are more grains per pixel size, so the standard deviation of the grain fluctuation is decreased as

$$\sigma_D = 0.0195(a_1/a\ D)^{0.638}, \qquad (4.44)$$

where a is equal to 0.36 micron$^2$.

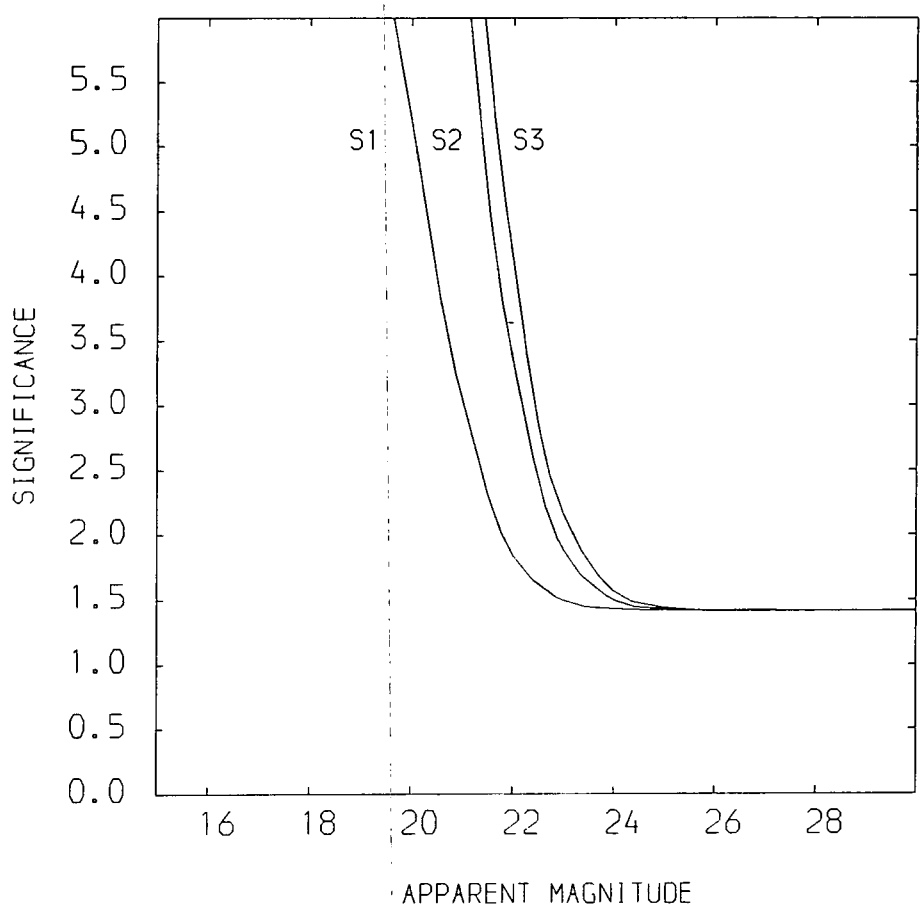


FIG 4.24 Significance of stellar density - $r_o$ = 20cm

| | S1 | S2 | S3 |
|---|---|---|---|
| exposure | t | t | 1.44t |
| signal/noise | $S/N$ | $2.93\,S/N$ | $4.34\,S/N$ |
| limiting sensitivity | $22^m$ | $23^m$ | $23.5^m$ |

TABLE 4.1 Limiting sensitivity of three telescopes

| | S1 | S2 | S3 |
|---|---|---|---|
| $a = 0.36\mu m^2$ $r_o = 10cm$ | $22^m$ | $23^m$ | $23.5^m$ |
| $a = 0.18\mu m^2$ $r_o = 10cm$ | $22.5^m$ | $23.5^m$ | $24^m$ |
| $a = 0.72\mu m^2$ $r_o = 10cm$ | $21.5^m$ | $22.5^m$ | $23^m$ |
| $a = 0.36\mu m^2$ $r_o = 20cm$ | $22.5^m$ | $23.5^m$ | $24^m$ |

TABLE 4.2 Limiting sensitivity of three telescopes with various grain sizes and seeing

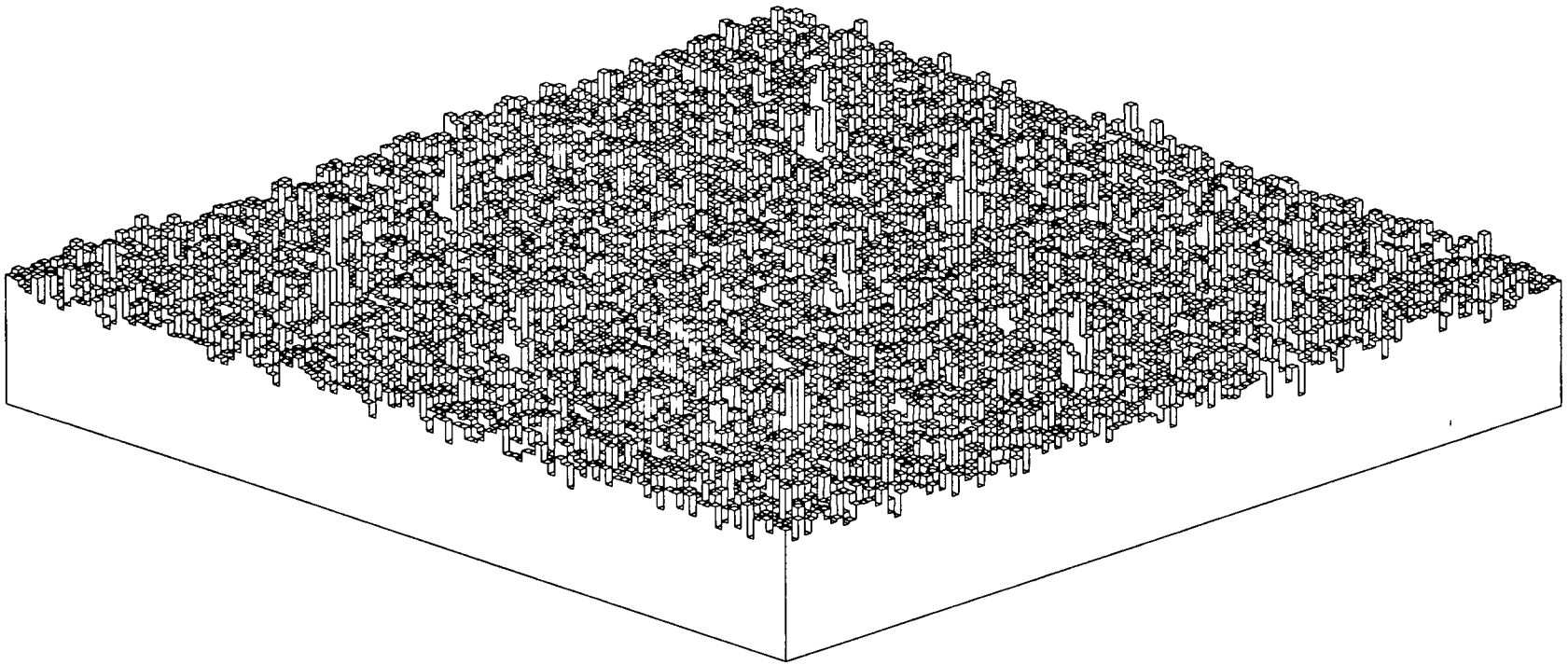

FIG 4.25 SIMULATED Ddensitometer TRACE OF STAR-FIELD OF S1 TELESCOPE

AZIMUTH = 315. ALTITUDE = 20.
*WIDTH = 6.00 *HEIGHT = 3.00

* BEFORE FORESHORTENING OCT 22, 1985

$r_o = 20\,cm$

$22^m$

The significance is shown in fig 4.26 for a grain size of 0.18 micron$^2$ and fig 4.27 for a grain size of 0.72 micron$^2$. The limiting sensitivities (ie when the star is 'lost' in the noise) for various grain sizes and seeing are summarised for the three telescopes in Table 4.2. From this Table, it can be seen that, in all three telescopes, the limiting sensitivity is improved by a half magnitude when the grain size is halved from 0.36 micron$^2$ to 0.18 micron$^2$ (which is similar to a good seeing, $r_o$ = 20cm), but is reduced by a half magnitude when the grain size is doubled to 0.72 micron$^2$.

In summary, if limiting magnitude is the criterion, then the equivalent of doubling the telescope dimensions (and increasing the cost by a factor about 8) can be achieved with better site selection and finer grained emulsions.

This work has been published in Brown, Dunlop and Major (1983) (ref. 4.7).

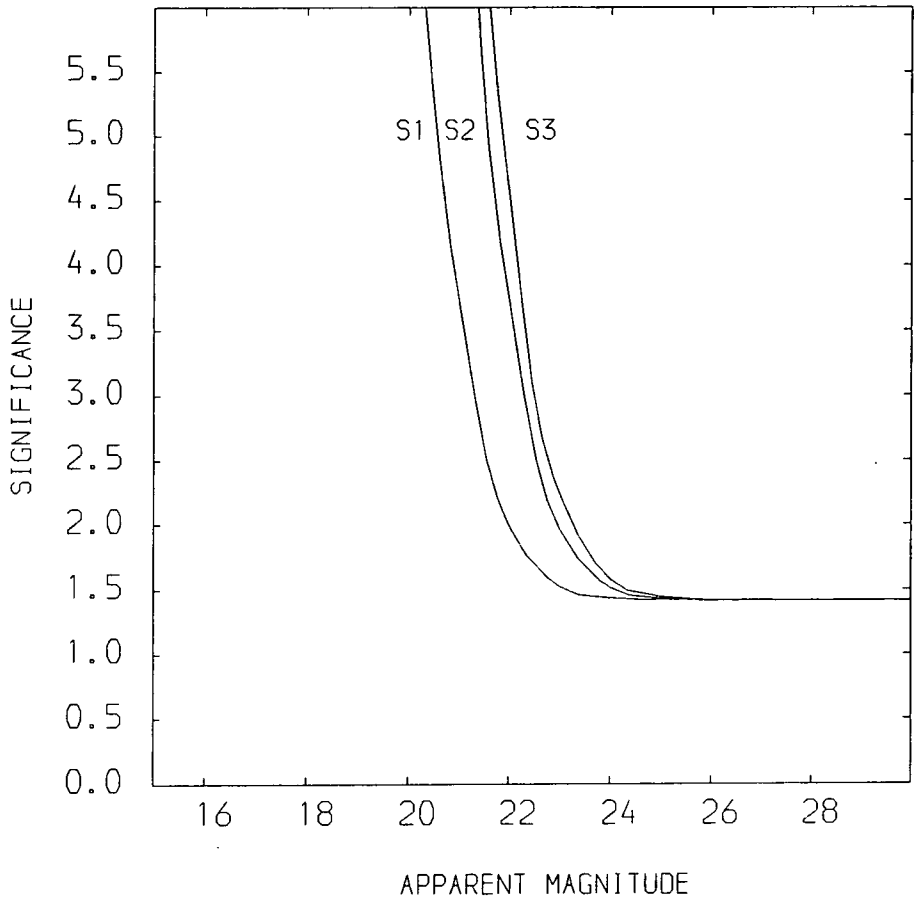


FIG 4.26 Significance of stellar density - a = 0.18$\mu m^2$

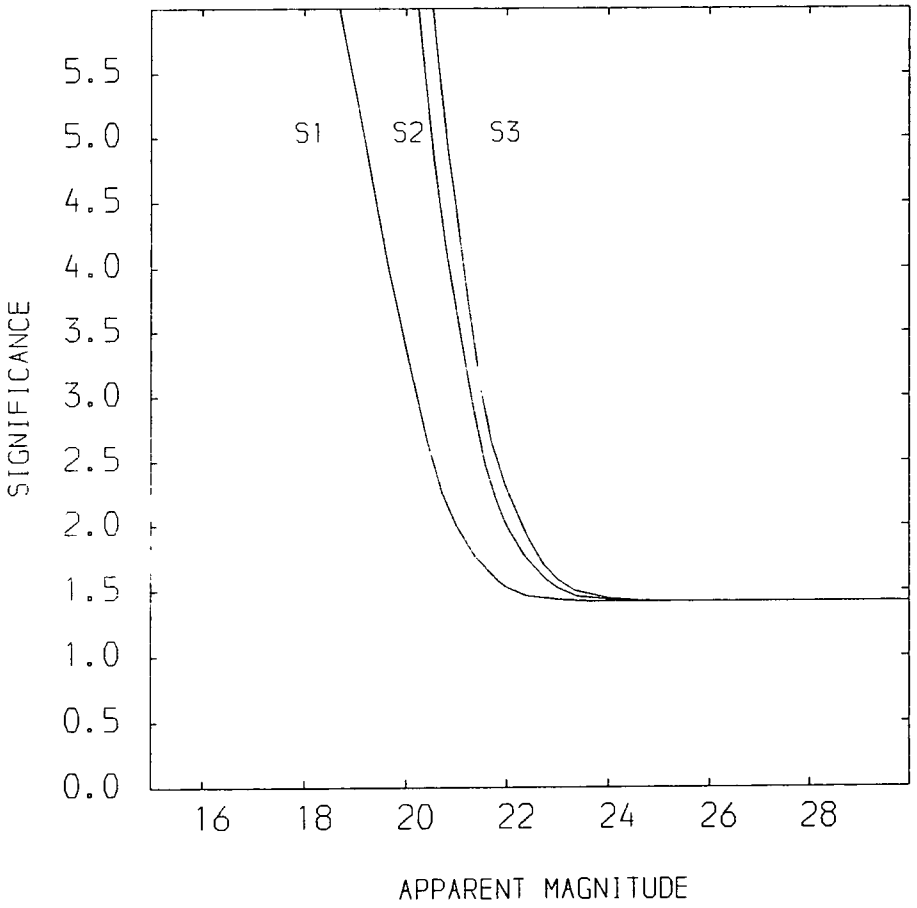


FIG 4.27 Significance of stellar density - a = 0.72$\mu m^2$

# CHAPTER 5 MULTI-MIRRORS

## 5.1 INTRODUCTION

The limitations of technology in fabricating, transporting and mounting large mirrors at somewhat inaccessible altitudes leads to a largest mirror diameter of about 7.5m. Further cost effectiveness (with the cost of telescopes going up by the 2.5 to 3 power of the aperture diameter) can be roughly doubled by forming the large collecting area from smaller mirrors. Although there are several ways of combining the mirrors there are broadly two choices.

The first is a large segmented aperture formed from a number (eg 36) of hexagons which are joined at the edges and which are individually figured to give a single parabolic mirror with one primary focus. The problems associated with this model are the wavefront errors that will arise from the figuring and particularly from the phase errors due to poor alignment of the large number of mirrors. The University of Califorina has planned to build a ten metre diameter Keck telescope with 36 hexagonal mirrors joined in this manner.

The second choice is for an aperture made from a number (eg 6) of separate, circular, paraboloid mirrors, each of which is figured identically, mounted on a regular matrix array (eg hexagonal) with parallel optic axes to give a number of primary foci. These are then combined to give one single focus. The problems of this method arise from the combination of these images to give an in-phase image. The existing multi-mirror

telescope has been built at Arizona as the first of the New Telescopes of the Future. It did succeed in reducing the cost of construction by two thirds. Other MMTs have been discussed or planned, for example by RGO (6MT) and Kitt Peak National Observatory (4MT).

In this chapter, the diffraction pattterns for several geometries will be considered. Although these can be generally examined by first determining the modulation transfer function for the aperture, and from its inverse Fourier transform finding the diffraction intensity distribution, the computing time is a severe limitation. For the simple geometries of circles and hexagons diffraction amplitude distributions are more quickly calculated directly and this will be the approach taken here. However, the MTF will be shown so that it can be compared with other systems in terms of spatial frequency.

The seeing will always dominate the structure of the stellar images, but the diffraction calculations are essential for determining the limitations of speckle pattern analysis in short exposure recording and for determining the limitations under very good seeing, or where seeing is not important in the regions of the far infrared. Further in the future, active optics may reduce the seeing disc to the diffraction limit.

A combination of multi-mirrors leads to a diluted aperture whose diameter can be controlled from a minimum value ie when all the mirrors are touching, to higher values which are controlled by the cost of mounting well separated mirrors. As the overall diameter largely controls the resolving power, the

Airy disc size is reduced as the individual mirrors are separated (or the aperture is diluted). Further details about dilution can be seen in chapter 6.

Several diffraction patterns of various numbers of circular mirrors on a regular array will be shown to demonstrate their different characteristic patterns.

## 5.2 TELESCOPES OF THE FUTURE

### 5.2.1 Arizona MMT

There is a multi-mirror telescope which has been successfuly built and operating at Mount Hopkins, Arizona, as the first of the Next Generation telescope concepts (ref 5.1). The overall cost has been reduced to a third of the likely cost of a conventional single mirror telescope with same overall area. The telescope consists of six parabolic primary mirrors each of 1.8m diameter, positioned in a hexagonal array of base length, 2.25m giving the equivalent of a 4.5m telescope in collecting area. The configuration of the Arizona MMT is shown in fig 5.1a.

The light beams from each of the six mirrors, are brought together near the centre by plane mirrors where a six-sided beam combiner produces a single image. There are two problems associated with this image:

i) the individual focal planes are inclined which results in defocusing with distance off-axis. This can be avoided by extra reflections to make the inclined angle very small.

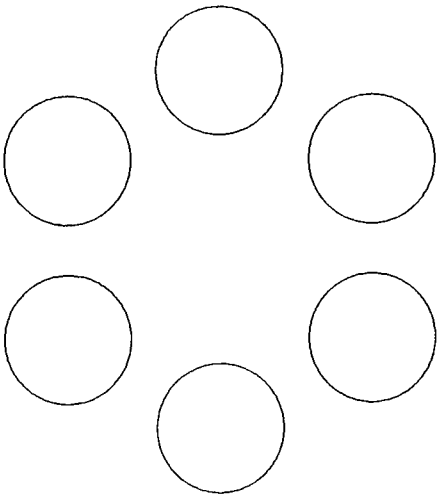

a) Arizona MMT

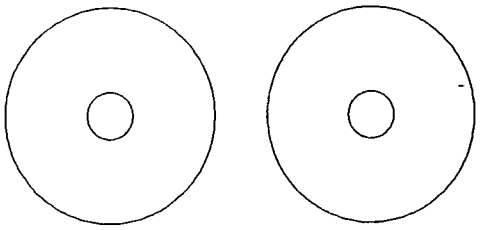

b) Two-mirror telescope

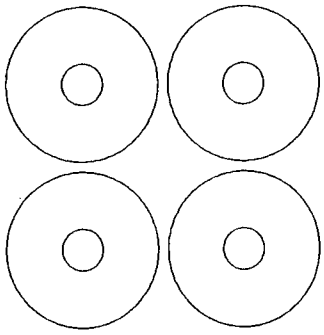

c) Kitt Peak NNTT

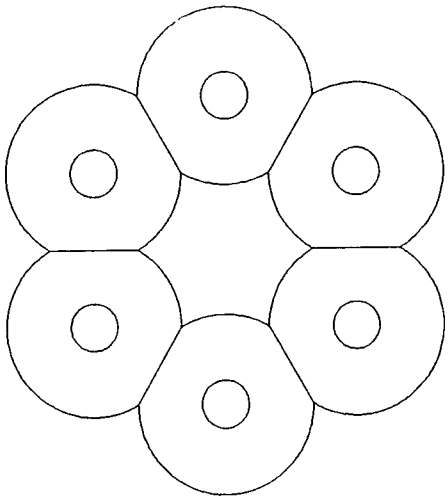

d) RGO Large MMT

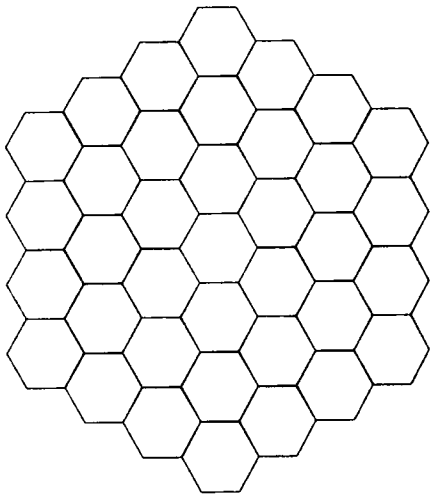

e) Univ. of California Keck telescope

FIG 5.1 TELESCOPES OF THE FUTURE

ii) the alignment of the six mirrors may give a unphased image. This can be controlled by active optical coalignment to give a phased image.

The MMT acts also as multi-interferometric system when opposing pairs of telescope mirrors are used; as it has a maximum 690cm baseline from edge to edge. It has been used for infrared Michelson interferometry (where seeing is less important in the far infrared) and for optical speckle interferometry.

5.2.2 Two Mirror Telescope (2MT)

We shall now consider one of the Next Generation telescope concepts such as the two mirror telescope as developed by Bingham at the RGO (ref 5.2). His design as shown in fig 5.1b has the individual primary mirrors of eight metre diameter with a ten metre separation between the two mirror centres (ie a two metre gap between the two mirrors).

The aim of this arrangement is to provide a $\underline{1}$8 metre maximum span (edge to edge) for angular resolution. At the same time it is possible to provide separate spectrographs or other detectors for the two primary mirrors, which is the efficient way of using them, when combined beams are not required. The beam combining and phasing are simpler than with some other concepts eg Arizona MMT.

The configuration of fig. 5.1b gives better angular resolution in one dimension than the single mirror without troublesome secondary peaks. However these secondary peaks can

be removed by a filtering process on the output of the detector in an actual observation.

The only way of taking advantage of the enhanced lateral resolution associated with the interference fringes will be by a very good seeing or by short exposure recording with speckle pattern analysis, or by adaptive optics.

### 5.2.3 Kitt Peak Four mirror telescope

Kitt Peak National Observatory has proposed to build a very large ground-based optical and infrared telescope with an overall aperture of at least 15 metres, known as National New Technology Telescope (NNTT) (ref 5.3). There will be four mirrors made of a honeycombed structure to reduce the mirror weight, and each of 7.5m diameter. The configuration of these four mirrors is shown in fig 5.1c. The beam combining is simpler than for six beams as there only four beams to be combined into one focus. Each of the four mirrors would be able to act as an independent telescope but tracking on the same object, which might be useful for spectrographic work at various wavelengths.

### 5.2.4 RGO Large Multi-Mirror Telescope

There has been a proposal that RGO should design and build a large telescope with a collecting area - 250m as one of the Next Generation Telescope concepts (ref 5.4). The telescope would consist of six parabolic primary mirrors each of 7.5m diameter with central holes of 2m diameter, as shown in fig

5.1d. This shows a different configuration from Arizona's MMT, as each circular mirror has a slice cut off two of its sides to form 'scallops'. These correspond to the hexagons with circumscribed circles which form a compact system. The calculation of the diffraction pattern for this telescope is considered in Appendix D.

5.2.5 University of California Ten Metre Keck Telescope

The University of California has designed a segmented, ten metre diameter optical and infrared telescope which it plans to build and erect on Mauna Kea in Hawaii (ref 5.5). The segmented mirror telescope consists of 36 hexagonal mirrors joined at the edges and which are individually figured to give the effect of a single parabolic mirror with one primary focus. There will be some problems of which the first concerns the wavefront errors that will arise from the overall figuring and particularly from the phase errors due to poor alignment of the large number of mirrors. However these can be refigured overall during operation, controlled by the sensors which measure the displacement of each element relative to its neighbours. Secondly, it is not an easy task to polish each of 36 mirror elements which have to be individaully figured as off-axis segments of a paraboloid. However there are several methods which are available. The group (ref 5.6) at California has successfully figured a 0.4m mirror using stressed-mirror polishing, ie the mirror is first warped mechanically, and then, after a sphere has been polished in its surface the loading is

removed. The mirror is allowed to relax, thus creating the desired off-axis figure.

A configuration of a 36 hexagonal segmented mirror is shown in fig 5.1e and this has an overall diameter of about 10m. Each hexagonal mirror elements has a base length of 0.9m, and there is a gap of 1cm between elements. Each element is only 7.5cm thick and hence is lighter and this allows a reduction in the weight of the telescope. It is expected that reducing the weight will be effective in reducing the cost of the telescope.

The diffraction patterns of 36 hexagonal segmented mirror and the effect of the phasing will be considered in section 5.5

## 5.3 CALCULATION OF DIFFRACTION PATTERNS

The determination of the diffraction amplitude distribution (and intensity) of a number of similar apertures is straightforward, provided there is symmetry. For example, fig 5.2 shows 6 circular mirrors on an hexagonal matrix, $(X_1, Y_1, X_2, Y_2, \ldots X_j, Y_j)$. From eq 2.6, the general expression for the amplitude distribution is given by

$$a(\Theta,\phi) = \iint_{\text{over area}} \exp\left[\frac{2\pi i \sin\Theta}{\lambda}(x\cos\phi + y\sin\phi)\right] dxdy \quad . \qquad (5.1)$$

For the configuration shown in fig 5.2

$$a(\Theta,\phi) = \iint \sum_j \exp\left[\frac{2\pi i \sin\Theta}{\lambda}\{(X_j+x)\cos\phi + (Y_j+y)\sin\phi\}\right] dxdy, \qquad (5.2)$$

and this can be rewriten as:

$$a(\Theta,\phi) = \sum_j \exp\left[\frac{2\pi i \sin\Theta}{\lambda}(X_j\cos\phi + Y_j\sin\phi)\right] * \iint \exp\left[\frac{2\pi i \sin\Theta}{\lambda}(x\cos\phi + y\sin\phi)\right] dxdy \quad . \qquad (5.3)$$

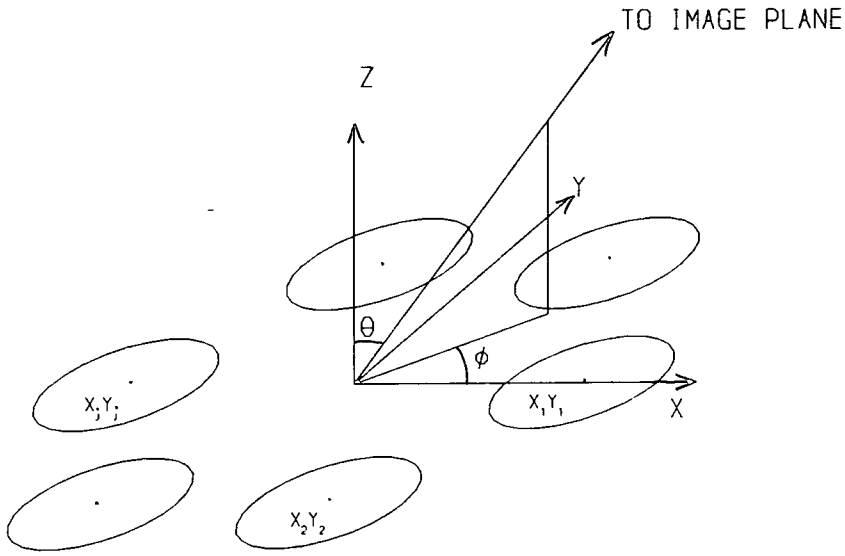


FIG 5.2 Six circular apertures in polar coordinates

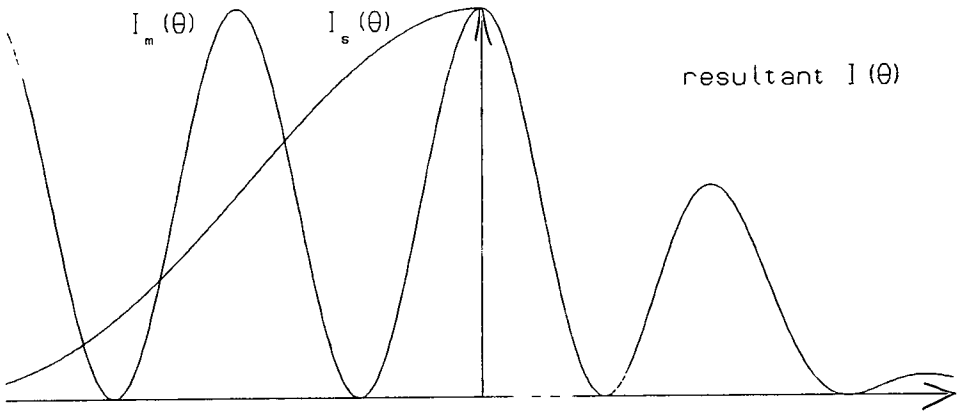


a) with touching edges

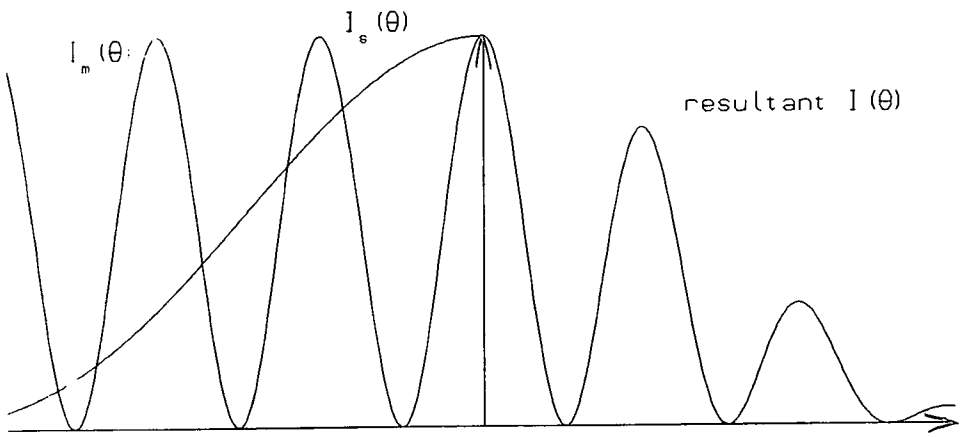


b) with a half of diameter gap

FIG 5.3 Resultant image from two parts - $I_m(\theta)$ and $I_s(\theta)$

In this expression the amplitude has divided into a product of two terms. The first of these is the amplitude for a matrix of pinholes at the centres of the mirrors and the second is that for a single mirror, ie

$$a(\Theta,\phi) = a_m(\Theta,\phi)\ a_s(\Theta,\phi)\ , \qquad (5.4)$$

where $a_m$ refers to the amplitude distribution for the matrix of centres and $a_s$ to single mirror. The condition for this amplitude separation is that the angle characterising the mirror should be an integral multiple of the angular separation of the mirrors. Hence separation of amplitudes can be obtained for octagonal mirrors arranged on a square or octagonal matrix, hexagons on a triangular or hexagonal matrix and circles on any regular matrix.

With similar nomenclature, the intensity distribution in the diffraction pattern (calculated from the square of the amplitude) is

$$I(\Theta,\phi) = I_m(\Theta,\phi)\ I_s(\Theta,\phi)\ . \qquad (5.5)$$

This approach gives considerable insight to the formation of diffraction patterns. For example in fig 5.3a, the intensities, $I_m(\Theta)$ and $I_s(\Theta)$ are given for a fixed value of $\phi$ and lead to the resultant $I(\Theta)$. In fig 5.3b the dilution has been increased by separating the mirrors on to a larger matrix of centres. This is shown by the maxima of $I_m(\Theta)$ being closer together. The pattern of the single mirror gives the overall envelope to the total pattern. For increased dilution the Airy disc becomes smaller and contains less energy whereas the secondary maxima become more enhanced.

## 5.4 DIFFRACTION PATTERNS

In this section, the diffraction patterns for a variety of circular aperture configurations are presented. For each, the number of circular aperture configurations, the three-dimensional MTF and the 3-D PSF with a contour (plan) of the PSF are calculated and shown diagramatically. All these configurations have 1m diameter circular aperture for each mirror and 1.2m separation between the centres ie there is 0.2m gap between the edges of the mirrors. We start with a simple form of a multiple aperture - two aperture configuration and increase the number by one extra aperture each time up to six apertures and then eight apertures. Of course, the resolution will be improved since the overall diameter of these configurations increases as the number of apertures increases. But the size of Airy disc for a single mirror remains unchanged and it is shown as a dotted line around the contoured diffraction pattern (plan of the PSF).

These configurations will produce several fine structures surrounding the central peak in the diffraction patterns. These structures usually have a number of secondary maxima which are distributed in the azimuth direction depending on the particular geometry of the configuration.

The radial intensity and enclosed energy distribution as a function of radial distance from the centre are calculated by an average of the azimuth directions, for several configurations except for the two-aperture case since it does not have a symmetric central peak.

5.4.1 Two apertures

Two circular apertures on a line provide an increased resolution in a direction along the length of the line. The simplest stellar interferometers are based on this principle. Two apertures produce fringes similar to Young's slit fringes, but the peak intensities of this pattern are reduced to an envelope by the diffraction pattern for a single aperture. The Airy disc for a single aperture is shown as a dotted line on the plan of the PSF (fig 5.4d). The maximum resolution of the Airy disc is 0.043 arcsec from the centre in one direction, while in the other direction, the resolution is 0.126 arcsec from the centre. The enclosed energy of the central maximum is 63% of the total energy while each of the two secondary maxima has 9% of total energy.

5.3.2 Three apertures

Three apertures on a triangular array give a diffraction pattern which consists of a central maximum intensity and six surrounding secondary maxima (fig 5.5c). It can be understood in terms of the two-aperture system where now there are three combinations of two apertures each pair producing its own diffraction pattern. These patterns overlap with each other at angles of 120°, so there is an approximately hexagonal pattern produced at the lower part of central peak and six secondary maxima rather than three. These maxima are slightly fused together with the central peak and so zero intensity around the central peak is not observed. Hence it is rather difficult to

FIG 5.4 Two apertures

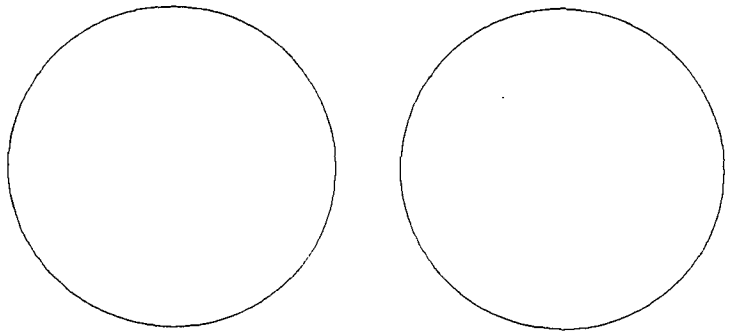

radius, r = 0.500m

separation between centres = 1.200m

a)

MODULATION TRANSFER FUNCTION

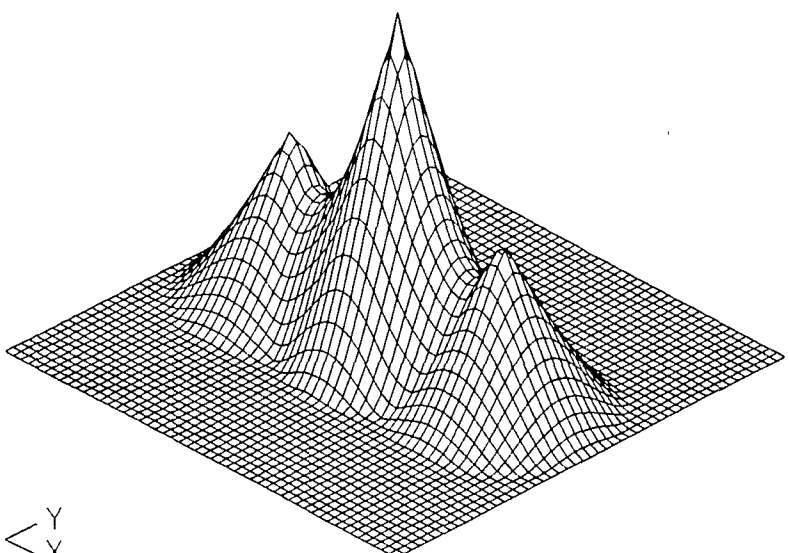


b)

POINT SPREAD FUNCTION

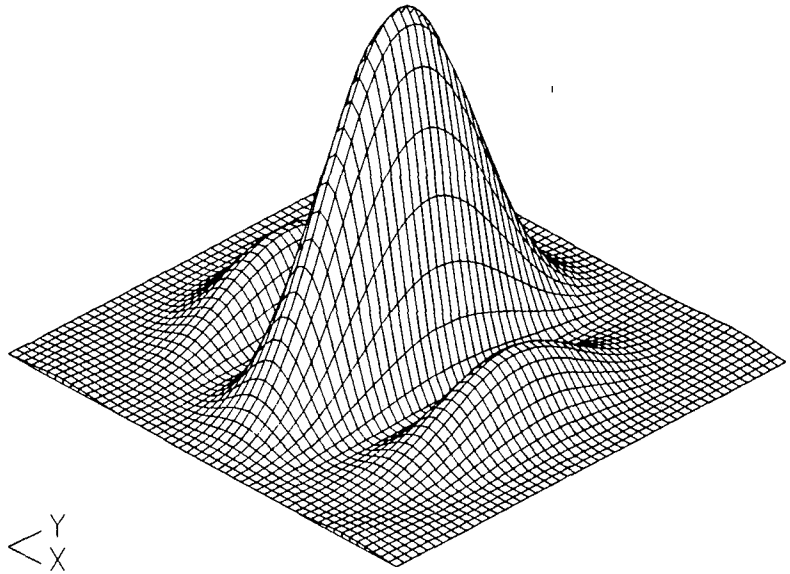


c)

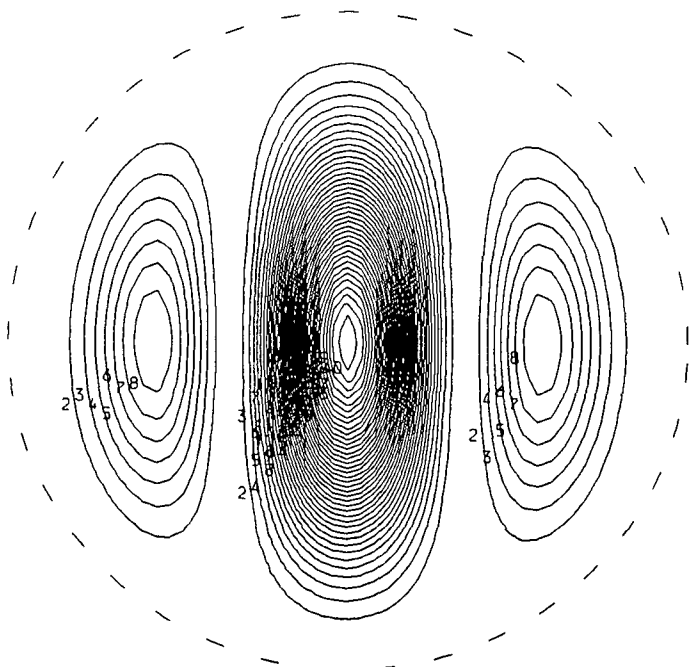

d)

FIG 5.5 Three apertures

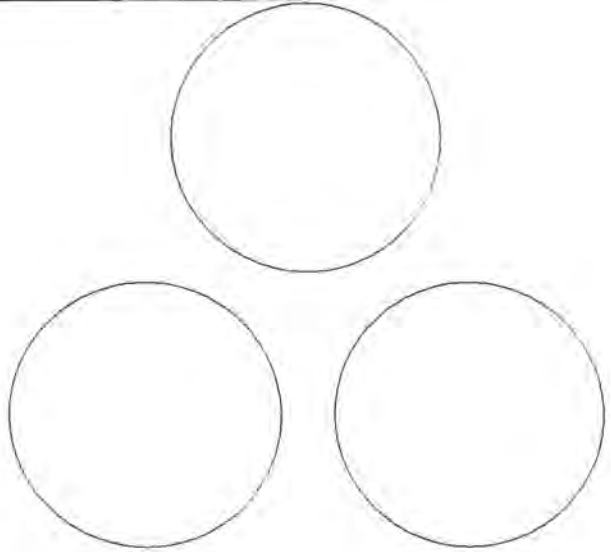

radius, r = 0.500m

separation between centres = 1.200m

a)

MODULATION TRANSFER FUNCTION

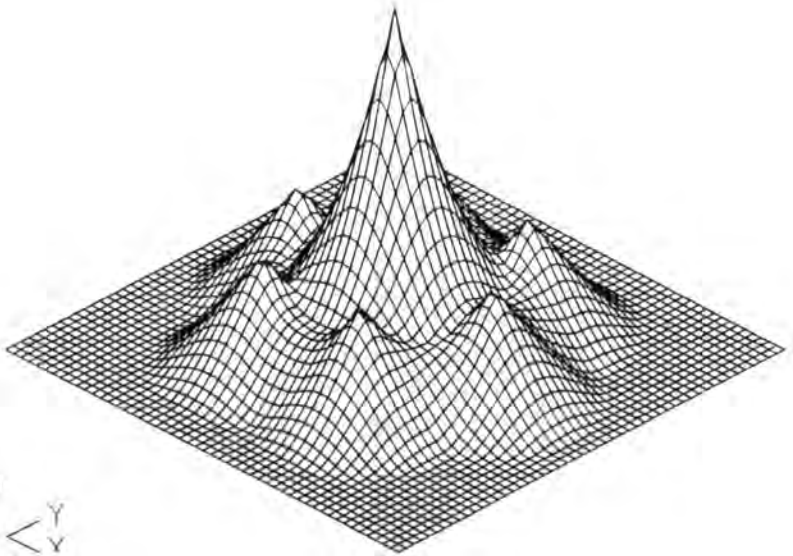


b)

POINT SPREAD FUNCTION

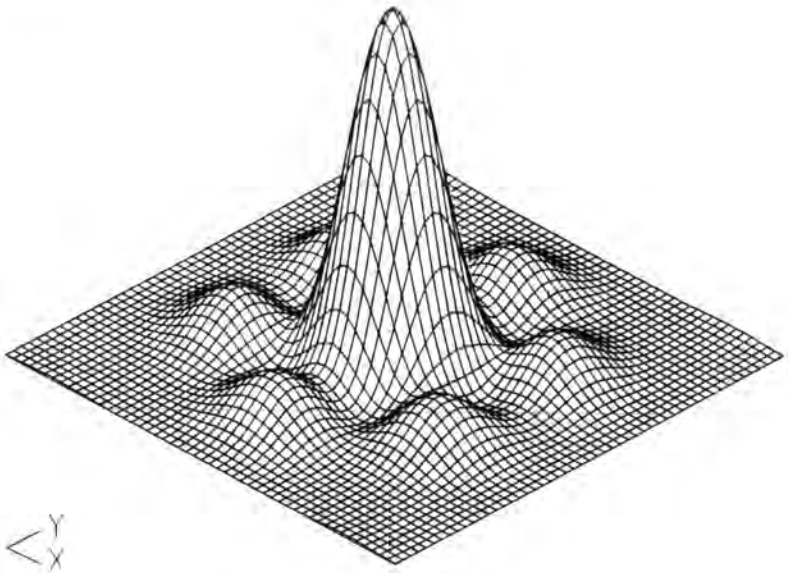


c)

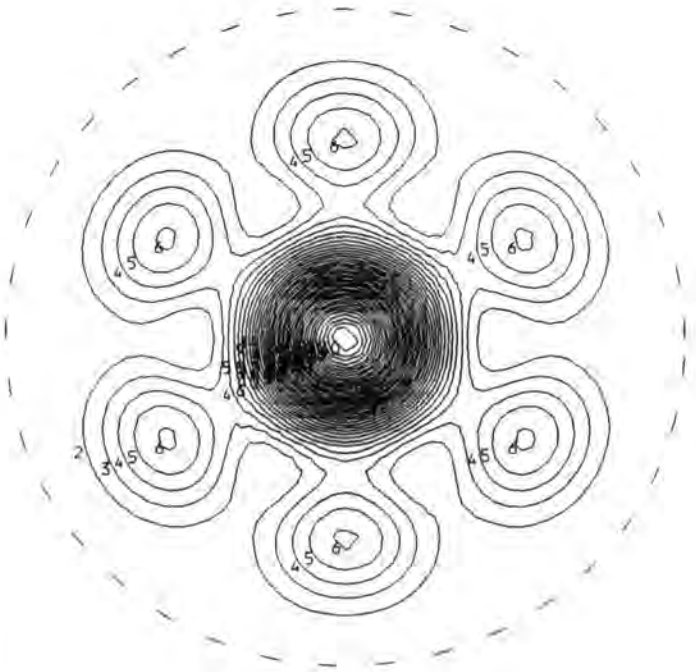


d)

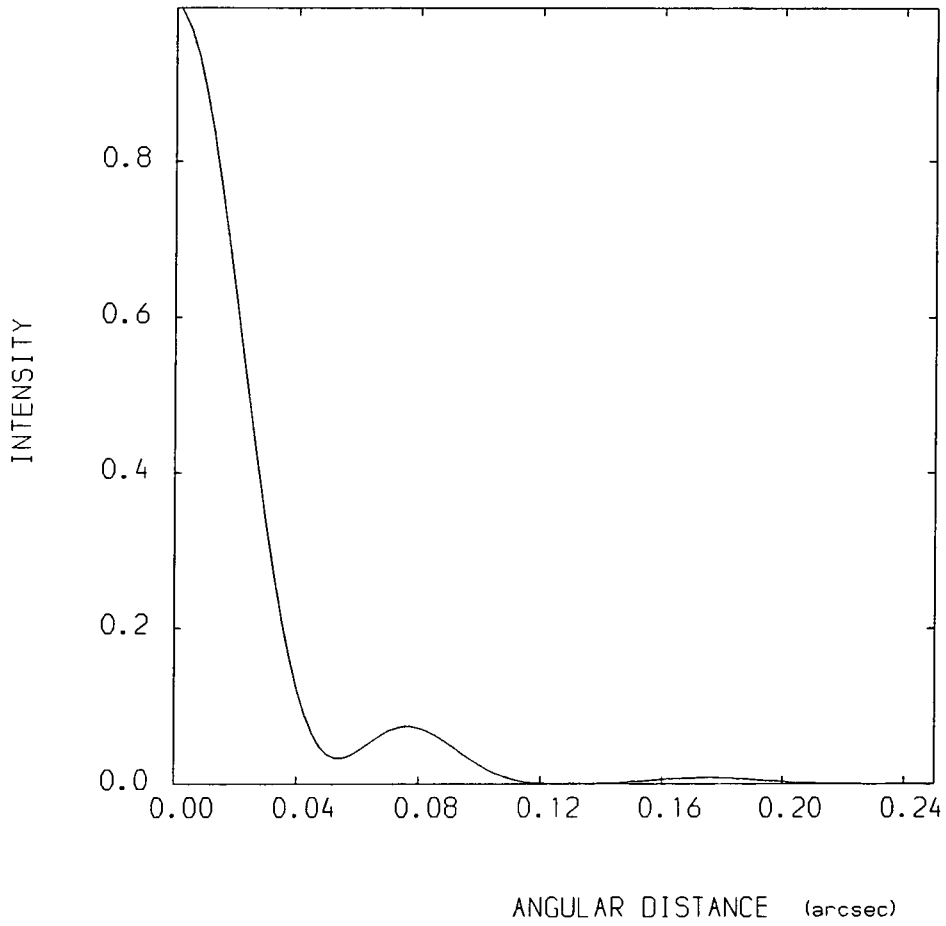


e)

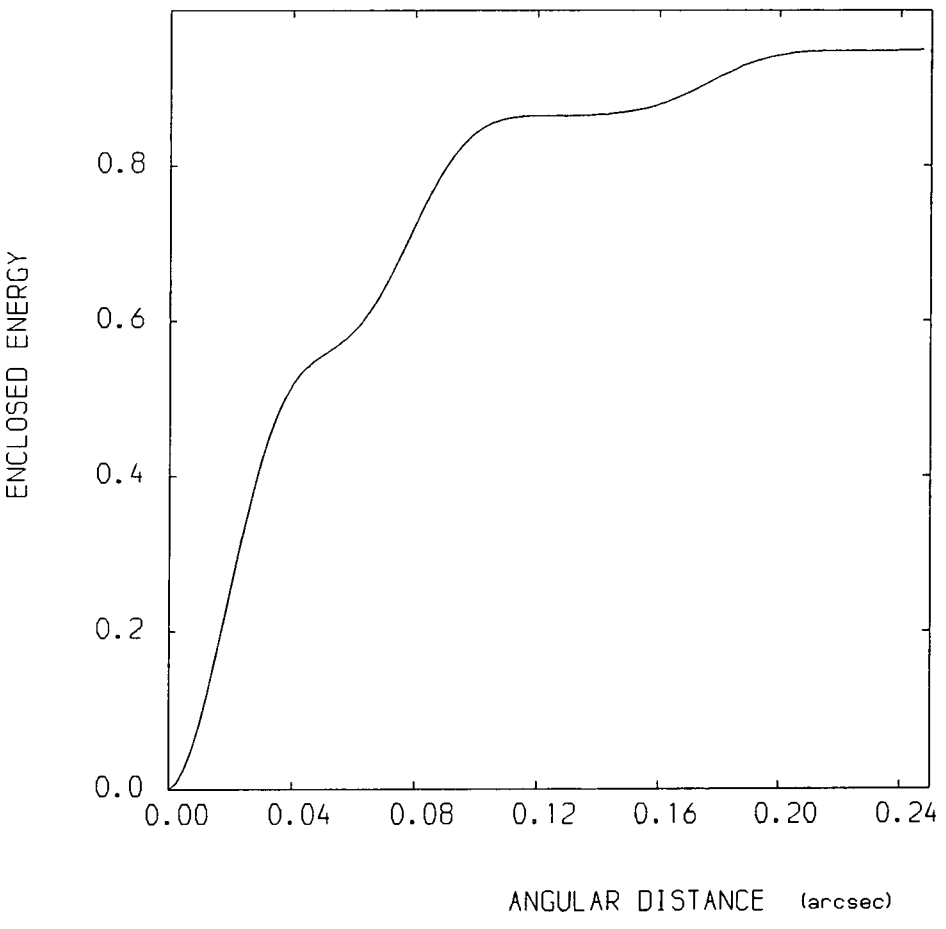


f)

FIG 5.5 Three apertures

be precise about the extent of the central maximum and to calculate its enclosed energy. However, from average radial energy distribution (fig 5.3f), the enclosed energy of the central peak is about 56% of the total energy. This is less than for the two-aperture system, as it transfers energy into the secondary maxima from the central peak. Its Airy disc is approximately 0.05 arcsec in radius, which is less than two apertures because of the fused secondary maxima to the central peak.

5.4.3 Four apertures

Four apertures on a square array lead to four combinations of two apertures with separation of 1.2m and another two combinations of two apertures with $1.2\sqrt{2}$m separation. These produce an orthogonal pattern in the diffraction image (fig 5.6c) with four secondary maxima in principal directions packed around a central maximum peak. It produces an almost dark zone at $\pm 45^{\circ}$ of the principal directions.

An interesting change in the diffraction pattern becomes apparent when an odd number of apertures is used. The four-aperture pattern shows only four secondary maxima while the three-aperture pattern shows six secondary maxima rather than three. This doubling of the diffraction details will be seen in other cases with an odd number of circular apertures (eg five apertures).

This is the minimum that would have useful application to a multi-mirror telescope since it does produce an Airy disc which

FIG 5.6 Four apertures

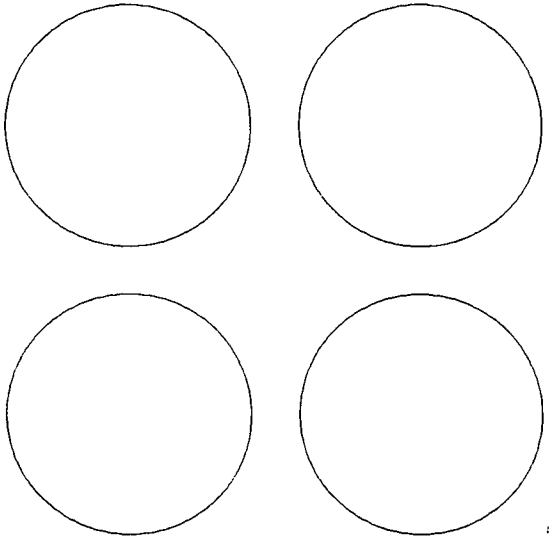

radius, r = 0.500m

separation between centres = 1.200m

a)

MODULATION TRANSFER FUNCTION

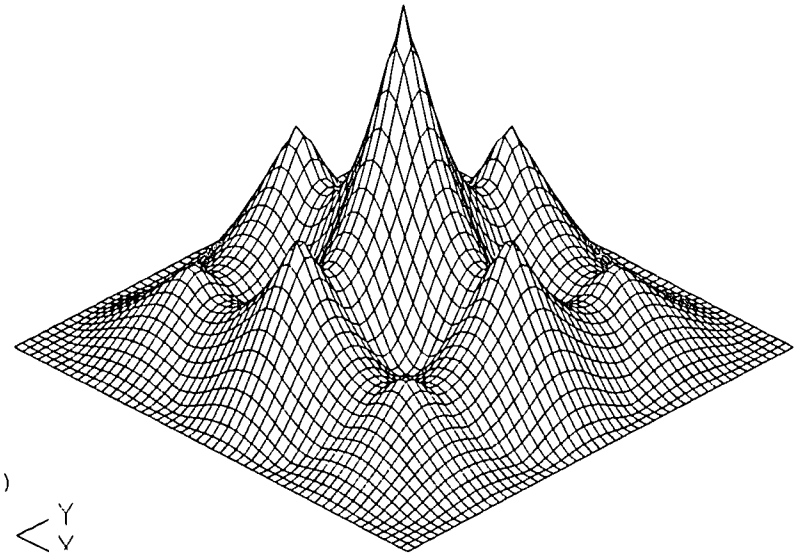


b)

POINT SPREAD FUNCTION

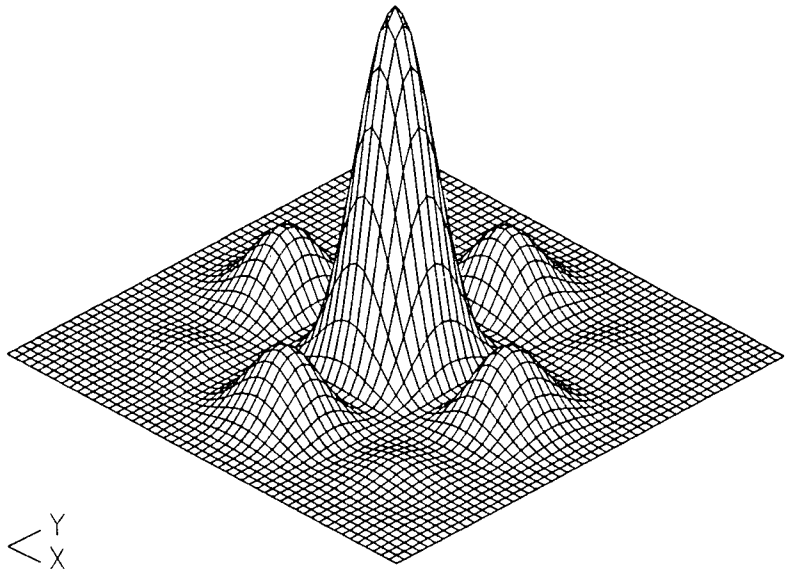


c)

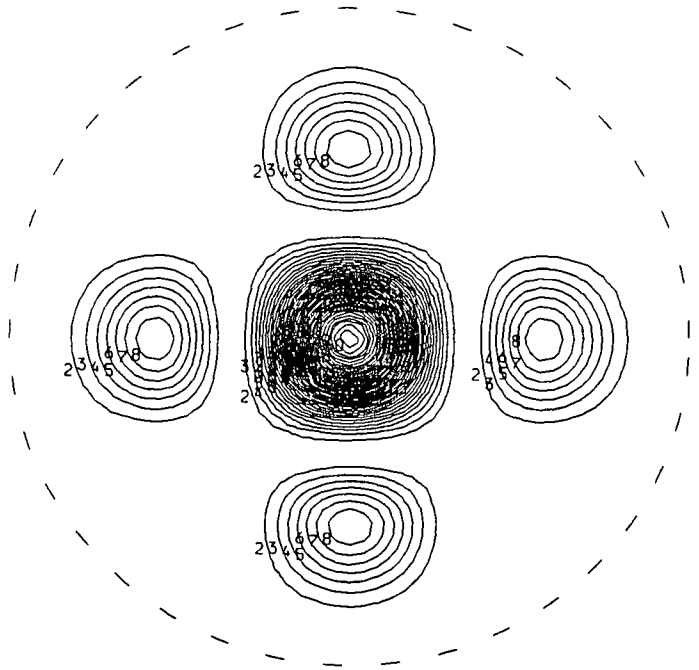

d)

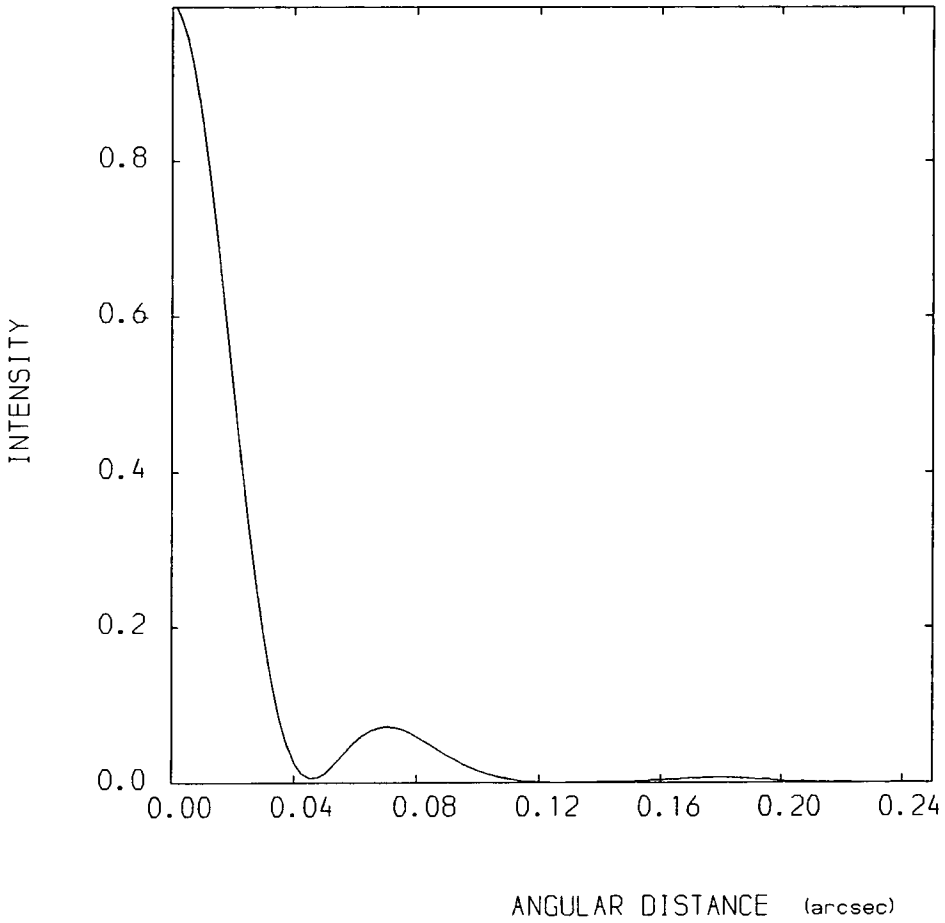


e)

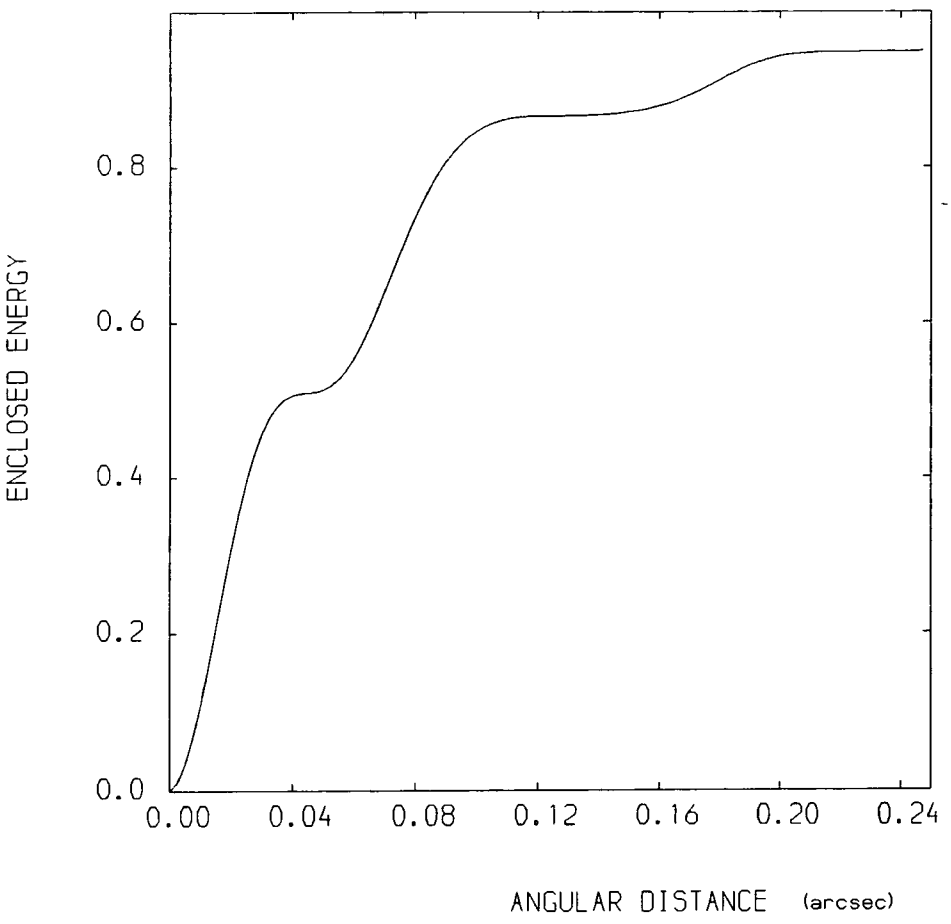


f)

FIG 5.6 Four apertures

is almost circular with zero intensity. Two apertures produce an elongated pattern, while three apertures do not produce zero intensity around the central maximum as six secondary maxima are fused together.

In fig 5.4f, the average radial energy distribution shows that the central peak has 51% of total energy and the first ring of secondary maxima has 36% of total energy. The Airy disc is 0.046 arcsec in radius.

### 5.4.4 Five apertures

The diffraction pattern for five circular apertures on a pentagonal array is shown in fig 5.6c. The central maximum is surrounded by a ring being broken up into ten elements. From the average radial energy distribution (fig 5.6f) the central peak has 45% of total energy while the secondary maxima has 41%. The Airy disc is 0.038 arcsec in radius.

### 5.4.5 Six apertures

Six apertures on a hexagonal array produce a diffraction pattern as shown in fig 5.7c. The central maximum peak is surrounded by continuous ring with six secondary maxima while a further six maximum peaks form a third ring at $\pm 30^{\circ}$ to the secondary maxima. Its average radial intensity and energy distribution are shown in figs 5.7e,f. From these the Airy disc is 0.033 arcsec in radius and the enclosed energy of the central peak has 40% of total energy. The second and third maxima have 29% and 17% of total energy respectively.

FIG 5.7 Five apertures

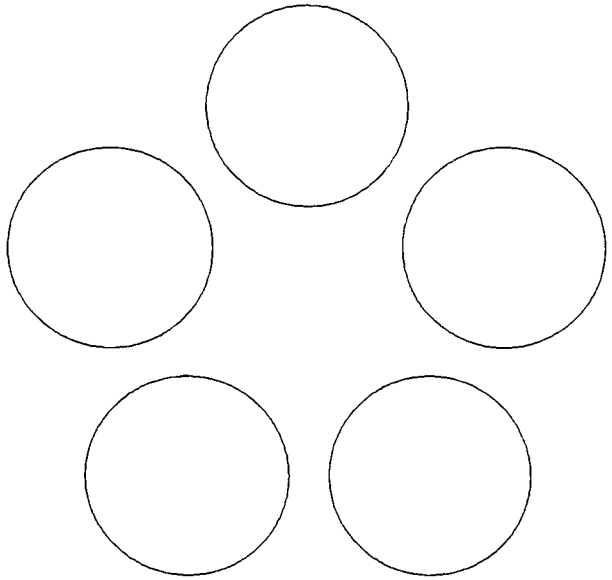

radius, r = 0.500m

separation between centres = 1.200m

a)

MODULATION TRANSFER FUNCTION

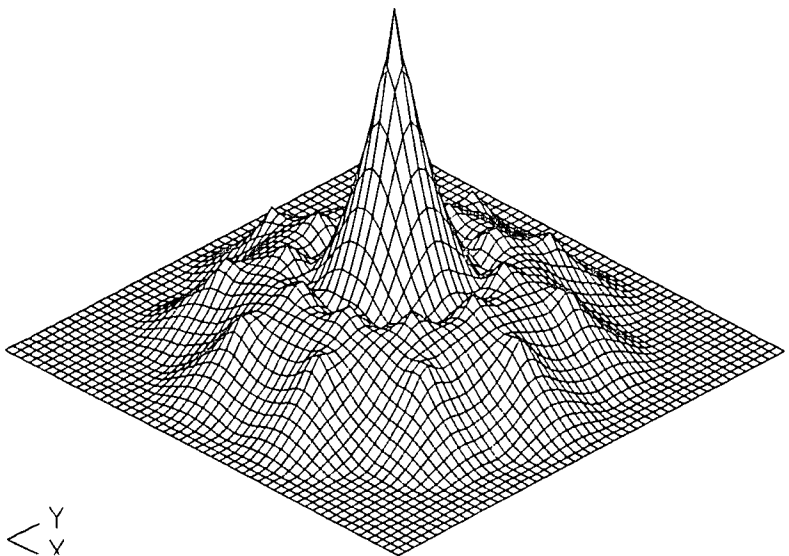


b)

POINT SPREAD FUNCTION

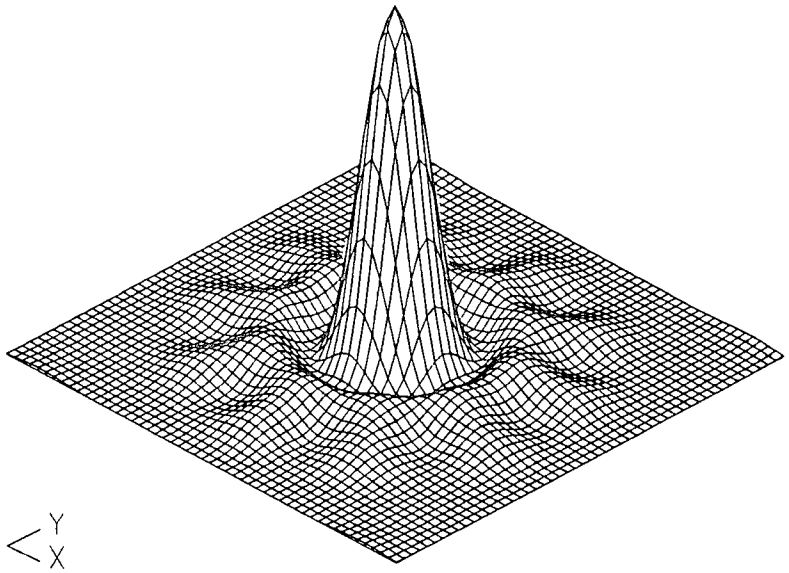


c)

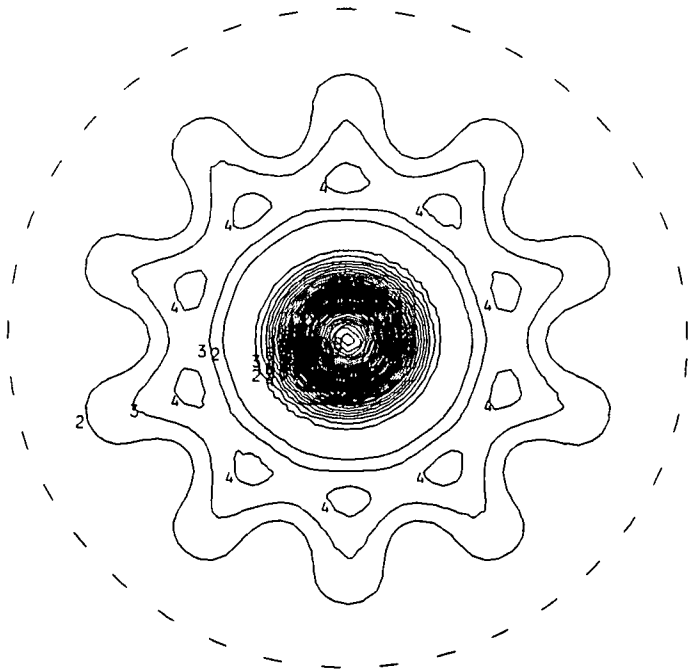


d)

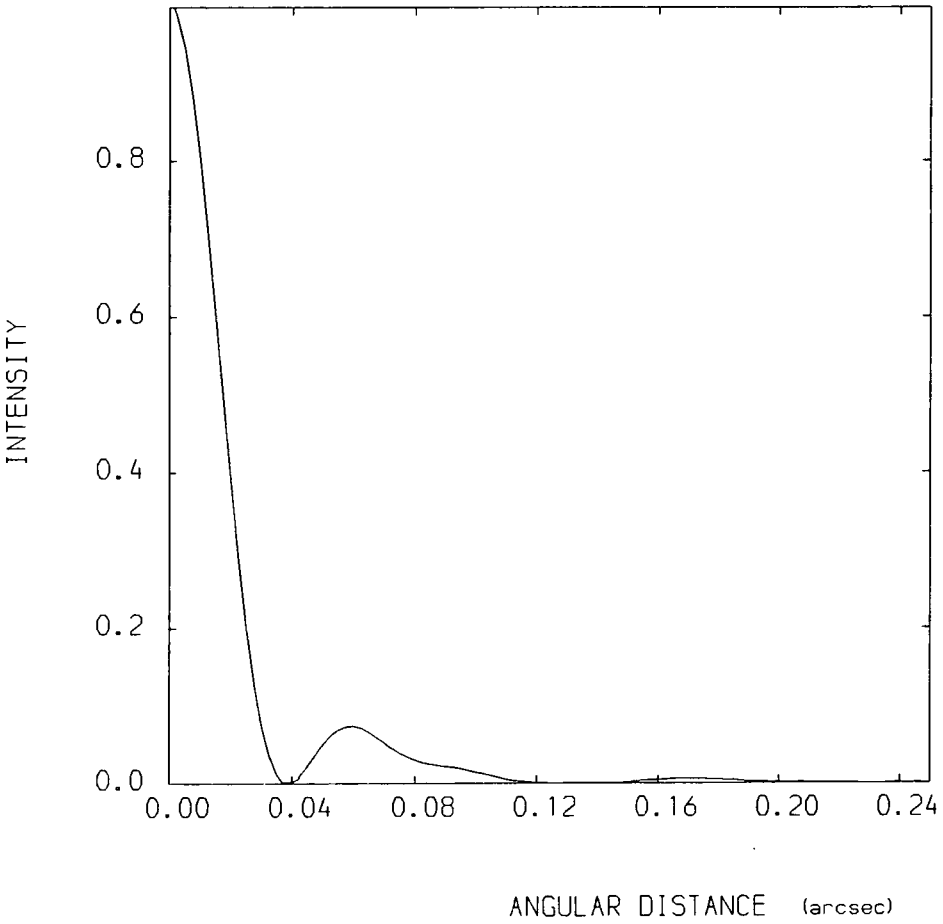


e)

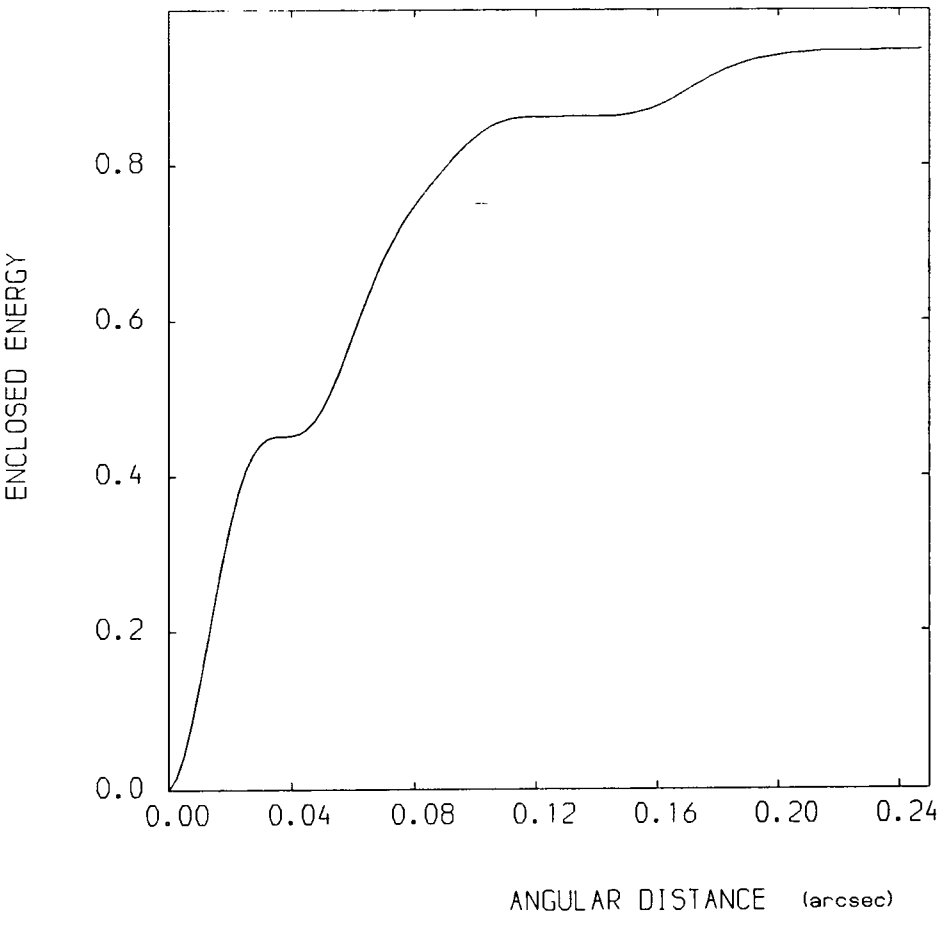


f)

FIG 5.7 Five apertures

FIG 5.8 Six apertures

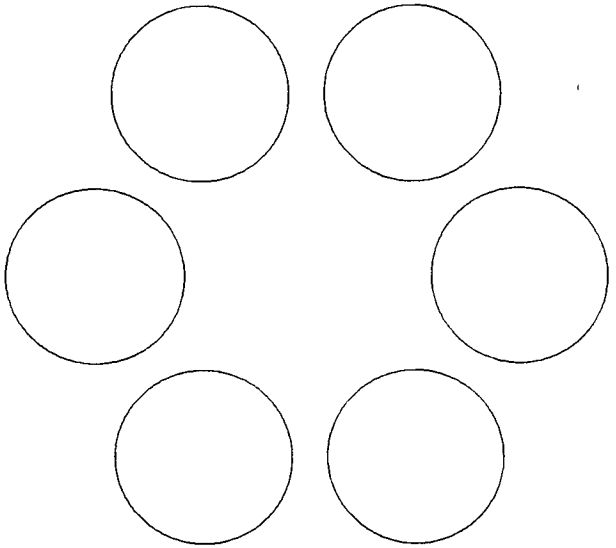

radius, r = 0.500m

separation between centres = 1.200m

a)

POINT SPREAD FUNCTION

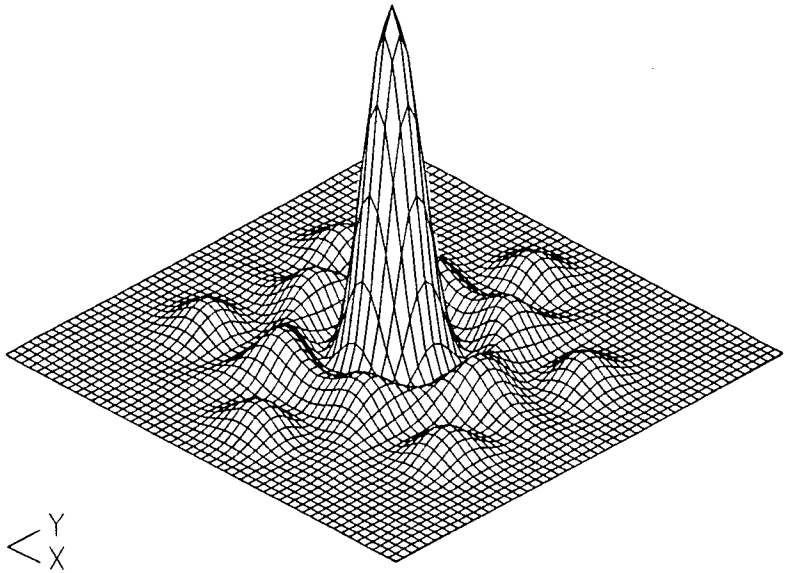


c)

MODULATION TRANSFER FUNCTION

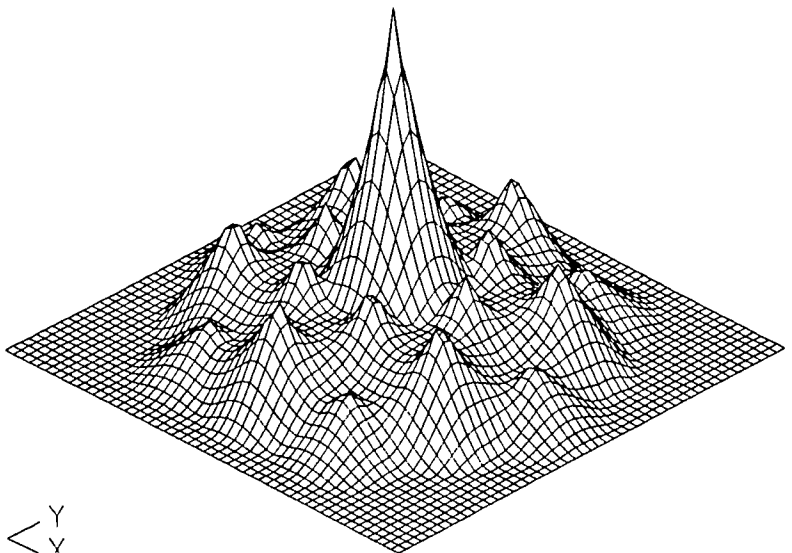


b)

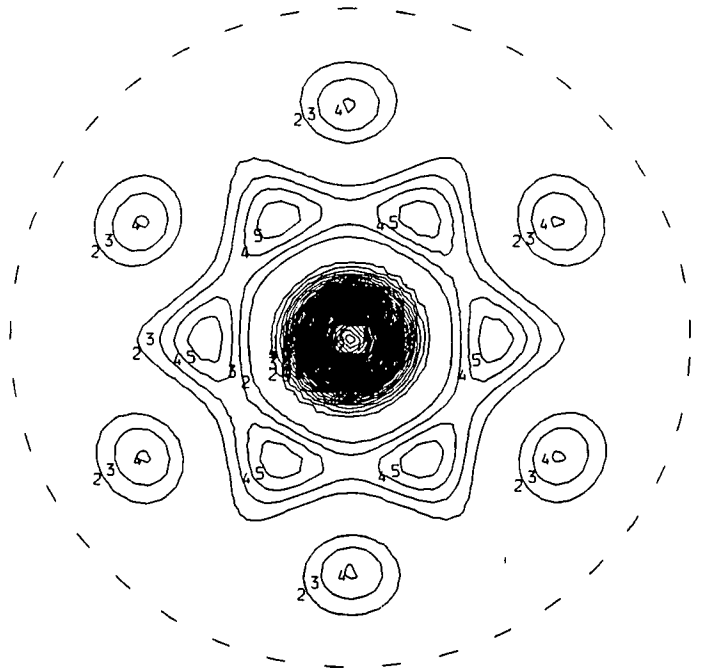

d)

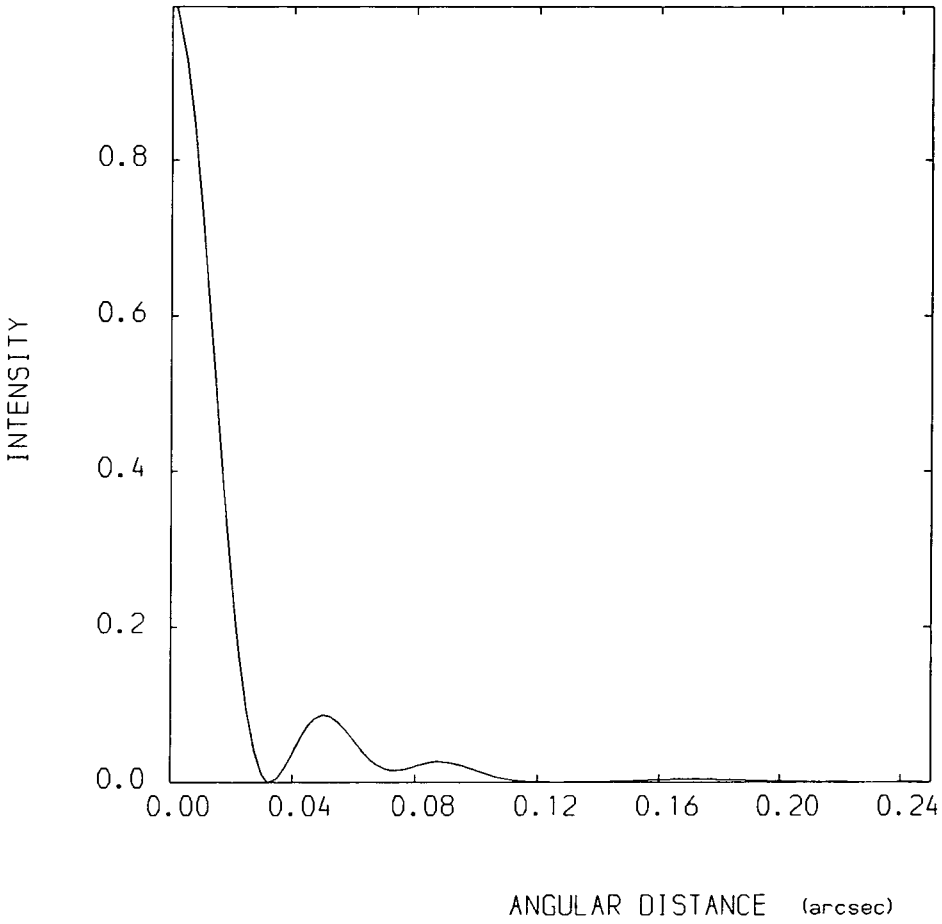


e)

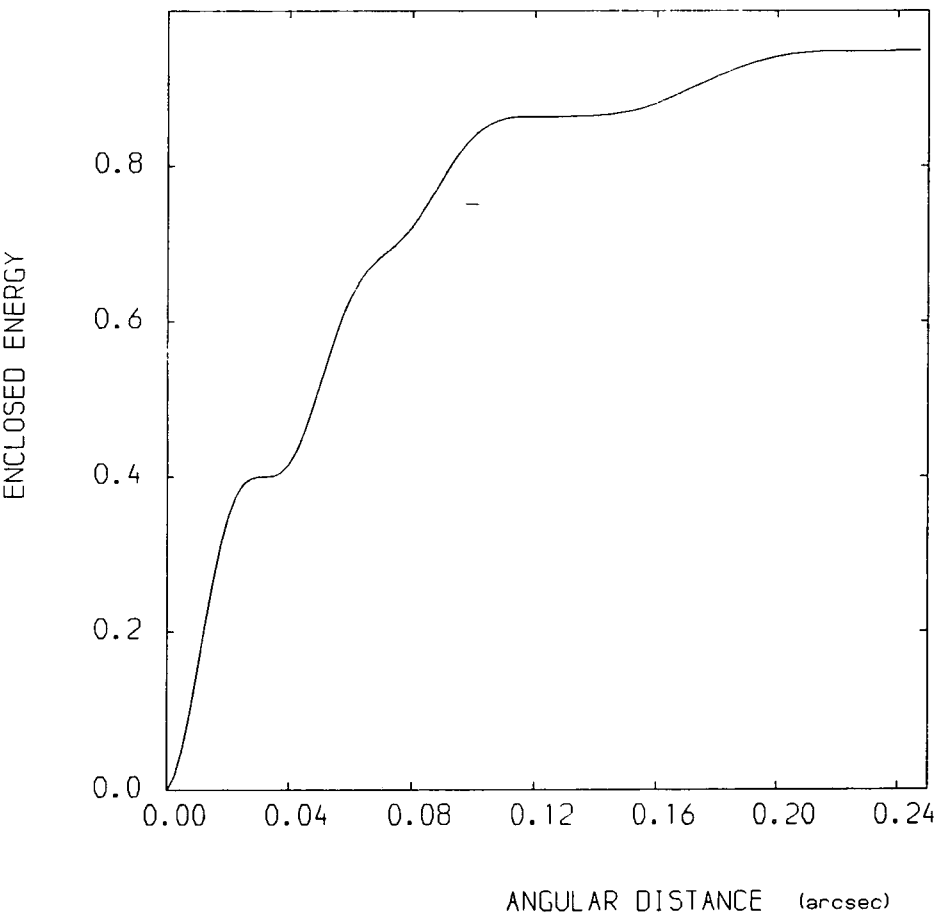


f)

FIG 5.8 Six apertures

It should be noted that in the average radial energy distribution, the enclosed energy inside a radius corresponding to the Airy disc of a single mirror is always the same despite the number of apertures.

5.4.6 Eight apertures

The diffraction pattern for eight apertures on an octogonal array is shown in fig 5.8c. This pattern resembles that for an annular aperture with a circular, continuous, diffraction ring and with the third ring being broken up into an inner and an outer part. The inner ring part consists eight brighter intervening wedge shaped details while the outer part consist of eight lower intensity maxima. In effect it forms 16 maxima in the third ring.

The Airy disc is 0.025 arcsec in radius and the enclosed energy of the central peak is 32% of total energy. The secondary and third maxima has 28% and 27% of total energy respectively.

5.4.7 Summary

The effects due to the various numbers of apertures considered are summarised in a Table 5.1 giving the size of the Airy disc, the radial enclosed energy of the Airy disc and the radial enclosed secondary energy. Because of the increased overall diameter, the size of the Airy disc is reduced as the number of apertures increases.

Table 5.2 shows the various numbers of apertures with a

FIG 5.9 Eight apertures

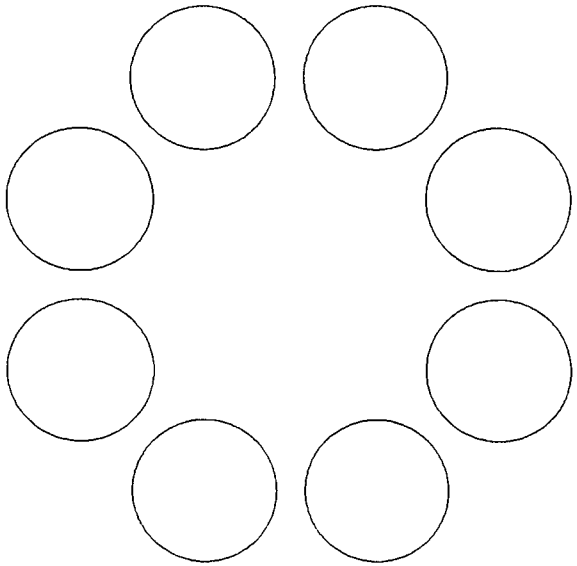

radius, r = 0.500m

separation between centres, 1.200m

a)

MODULATION TRANSFER FUNCTION

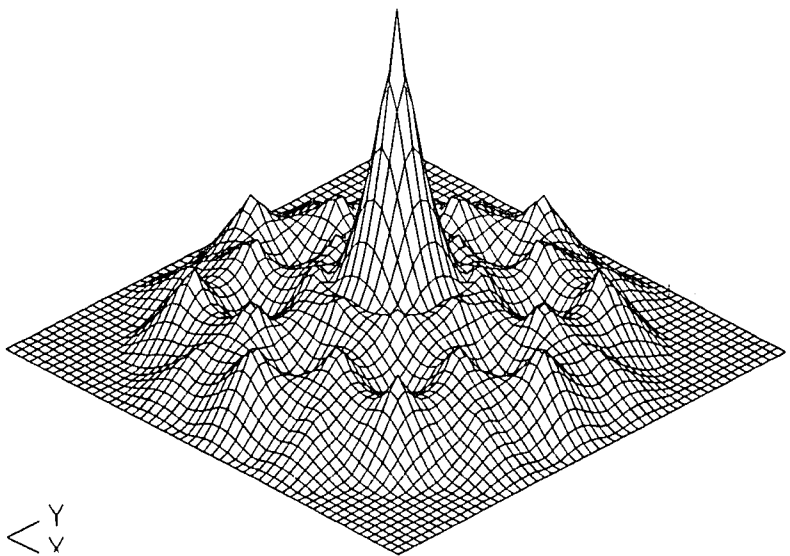


b)

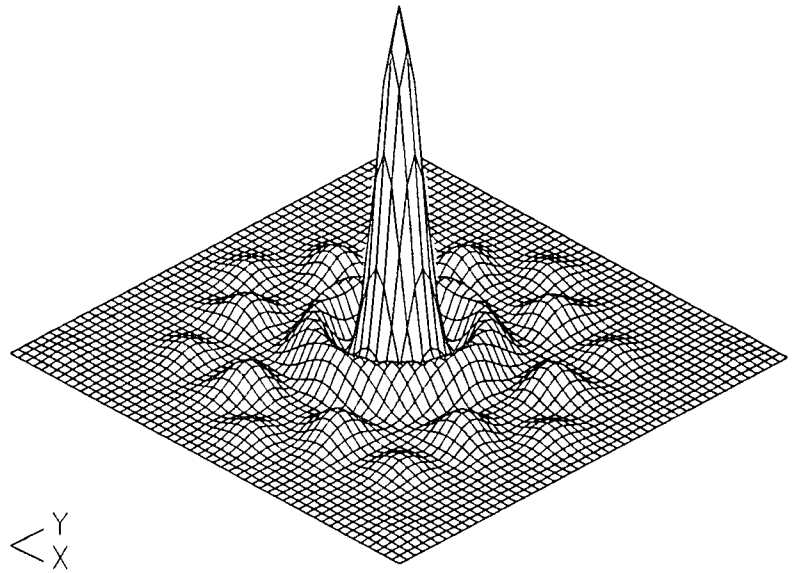


c)

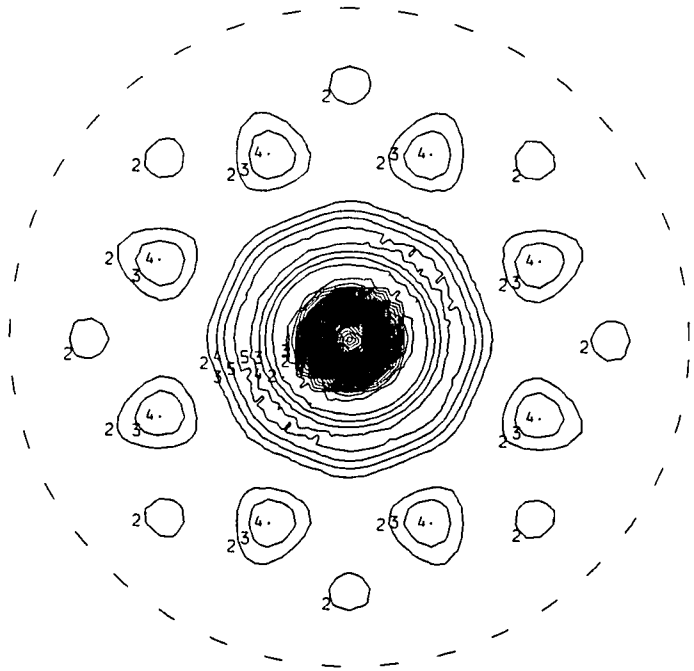

d)

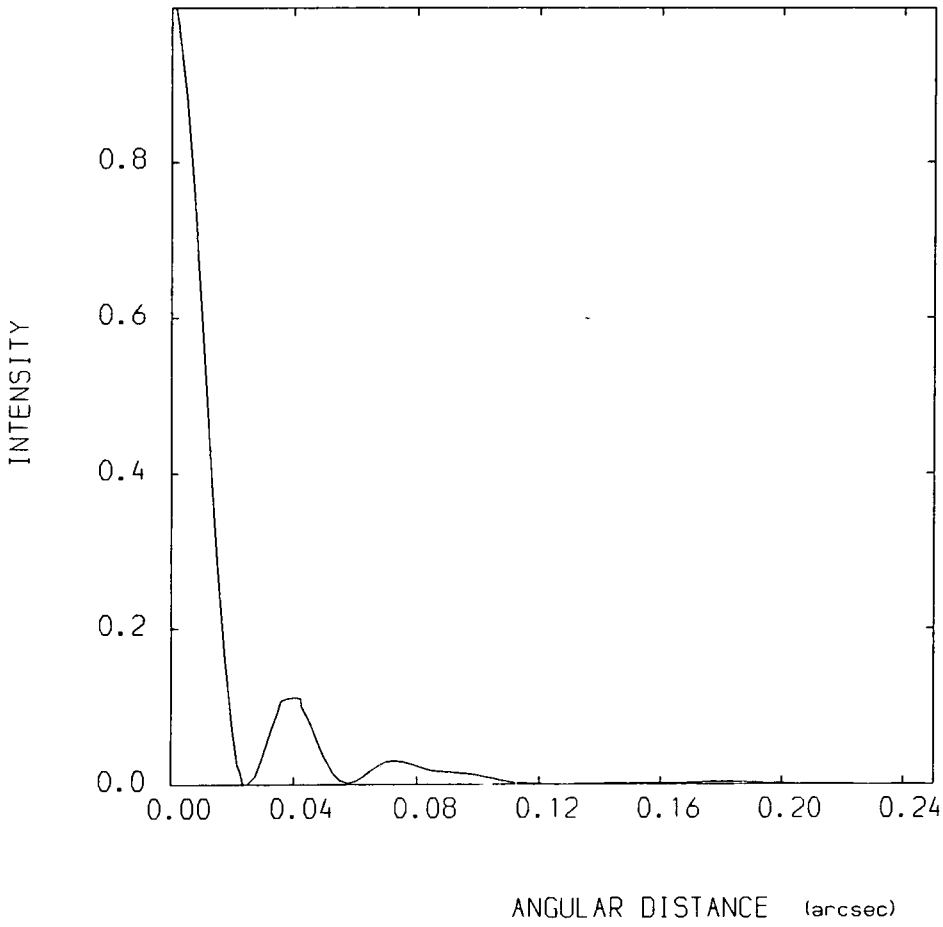


e)

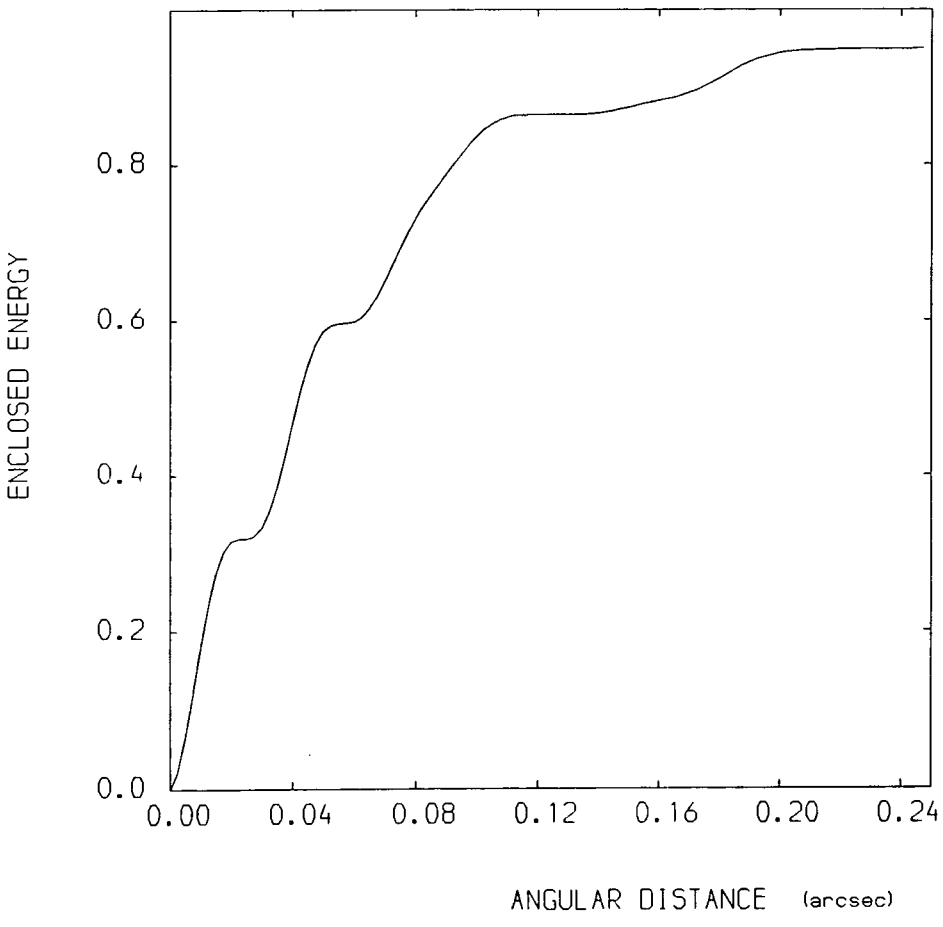


f)

FIG 5.9 Eight apertures

| No of apertures | overall diameter (maximum edge to edge) (metre) | average radial Airy disc (arcsec) | enclosed energy of Airy disc (radial) | enclosed energy of secondary peak (radial) (1st ring) |
|---|---|---|---|---|
| 2 | 2.20 | 0.043 (max. resol.) | 63% (not radial) | 18% (both peaks) |
| 3 | 2.20 | 0.052 | 56% | 20% |
| 4 | 2.70 | 0.046 | 51% | 36% |
| 5 | 2.94 | 0.038 | 45% | 41% (2nd ring) |
| 6 | 3.40 | 0.033 | 40% | 29% (+17%) |
| 8 | 4.14 | 0.025 | 32% | 28% (+27%) |

TABLE 5.1 Various number of apertures with 1.0m diameter aperture

| No of apertures | diameter of each aperture (metre) | overall diameter (maximum edge to edge) (metre) | average radial Airy disc (arcsec) | enclosed energy of Airy disc (radial) |
|---|---|---|---|---|
| 2 | 1.00 | 2.20 | 0.043 | |
| 3 | 0.82 | 1.80 | 0.063 | AS ABOVE |
| 4 | 0.71 | 1.56 | 0.065 | |
| 5 | 0.63 | 1.85 | 0.061 | |
| 6 | 0.58 | 1.97 | 0.057 | |
| 8 | 0.50 | 2.07 | 0.050 | |

TABLE 5.2 Various number of apertures with the same area as two apertures.

constant area, firstly as two apertures, ie as two 1.0m diameter mirrors with a 0.2m gap. For a higher number of apertures with the same total area, the gap between adjacent apertures is equal to one fifth of the diameter of each aperture.

## 5.5 SEGMENTED MIRRORS

The segmented mirror telescope such as as a University of California Keck telescope, consists of 36 hexagonal mirrors joined at the edges. The configuration of the Keck telescope is shown in fig 5.10. There is a very small dilution - 1/37 of the total area, resulting from the absence of the central hexagon to allow the formation of a single Cassegrain focus.

The modulation transfer function is calculated and is shown in fig 5.11. It can be seen that it is similar to the shape of the MTF for single hexagon (see fig B.5 in Appendix B). The diffraction patterns for a 36 hexagonal mirror system have been calculated from that of a single mirror, $I_s(\Theta,\phi)$ modulated by that for the matrix of centres of the hexagons, $I_m(\Theta,\phi)$ to give

$$I(\Theta,\phi) = I_s(\Theta,\phi)\ I_m(\Theta,\phi)\ . \qquad (5.6)$$

The point spread functions of the image for a single mirror, $I_s(\Theta,\phi)$ and of the array matrix, $I_m(\Theta,\phi)$ are shown in fig 5.12 and fig 5.13. The PSF for the whole system, $I(\Theta,\phi)$, ie a diffraction pattern of a 36 hexagonal mirror system, is shown in fig 5.14a and its enlarged pattern is given in fig 5.14b which it can be seen that it has a similar shape to single hexagon mirror (fig 5.12). The encircled energy in the Airy disc is shown in fig 5.15. The encircled energy has been calculated for

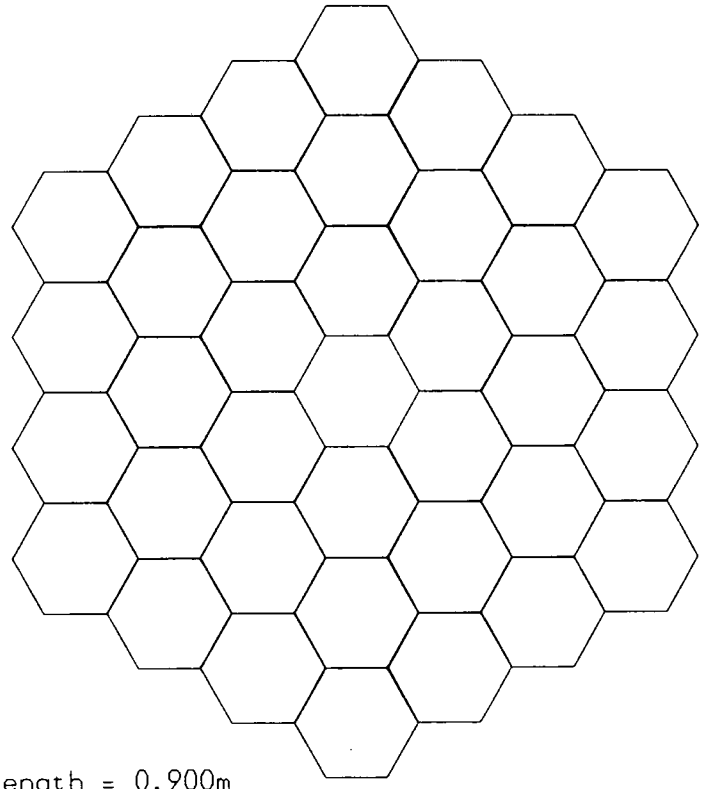


FIG 5.10 Configuration of 36 hexagonal mirrors

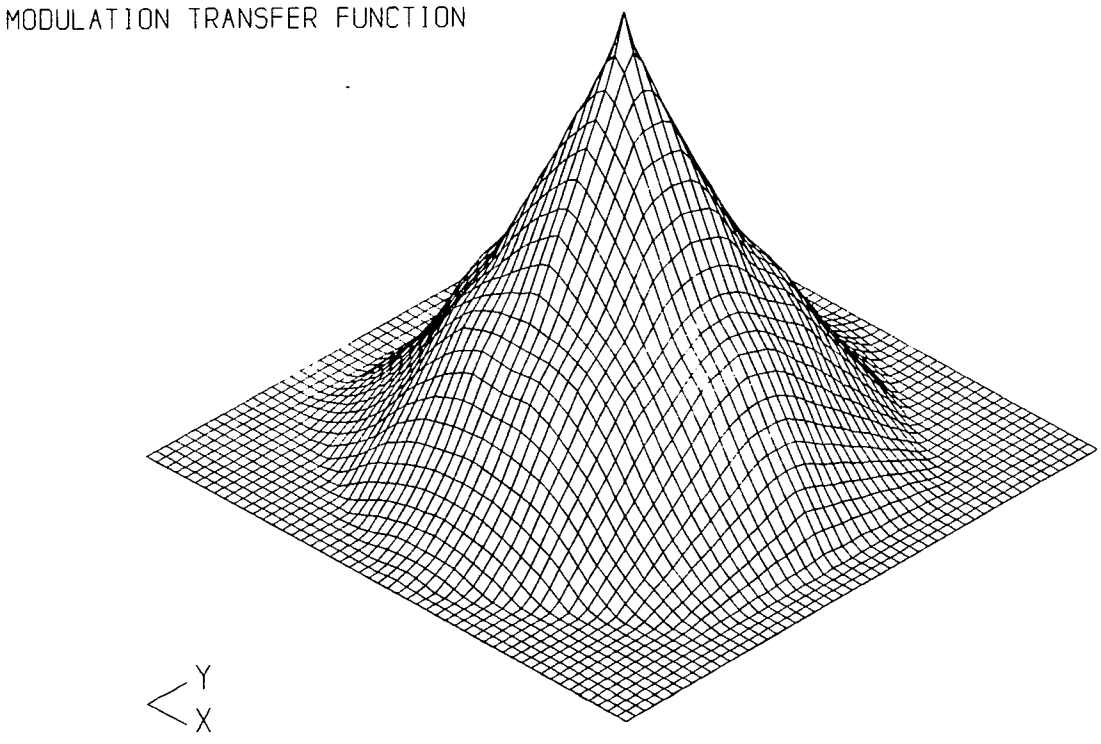


FIG 5.11 MTF of 36 hexagonal mirrors

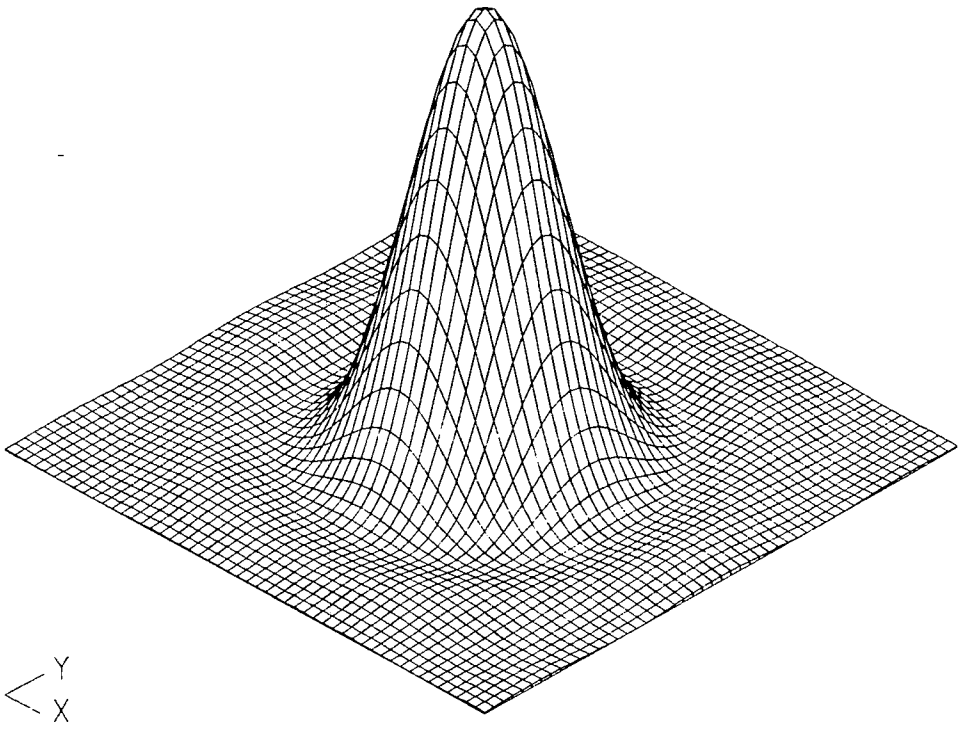


FIG 5.12 PSF of single hexagonal mirror

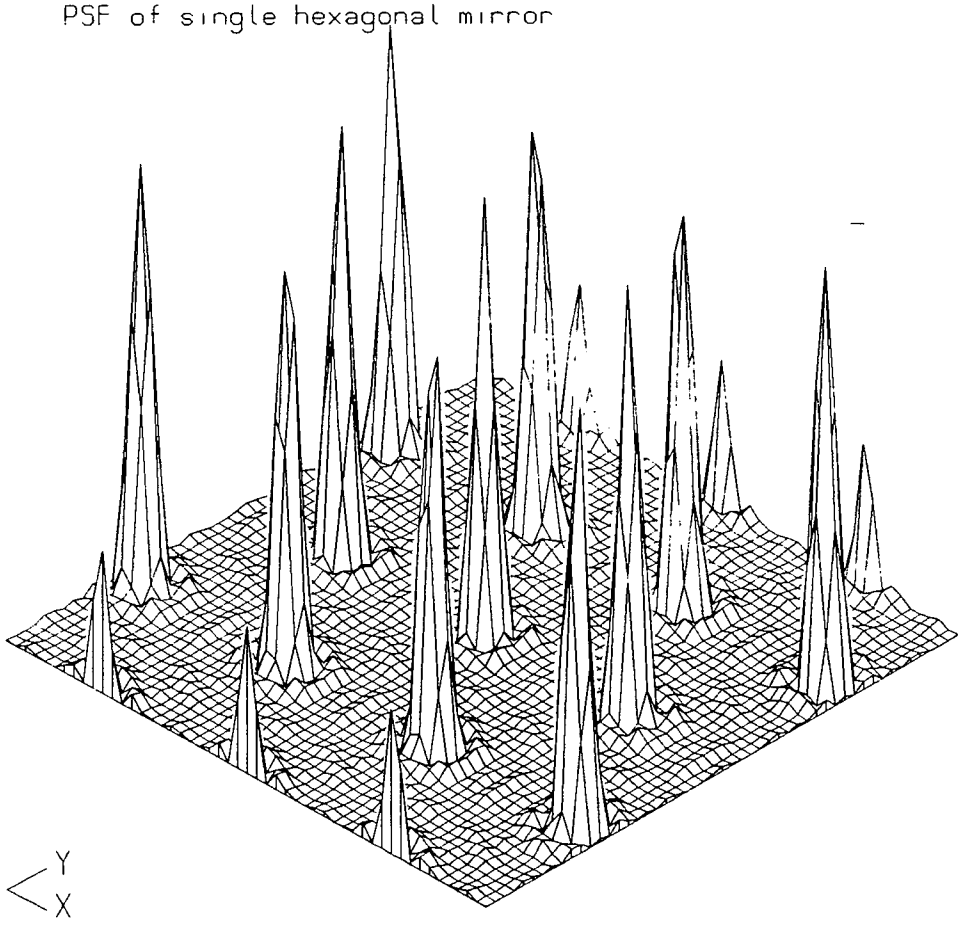


FIG 5.13 PSF of 36 mirror centres

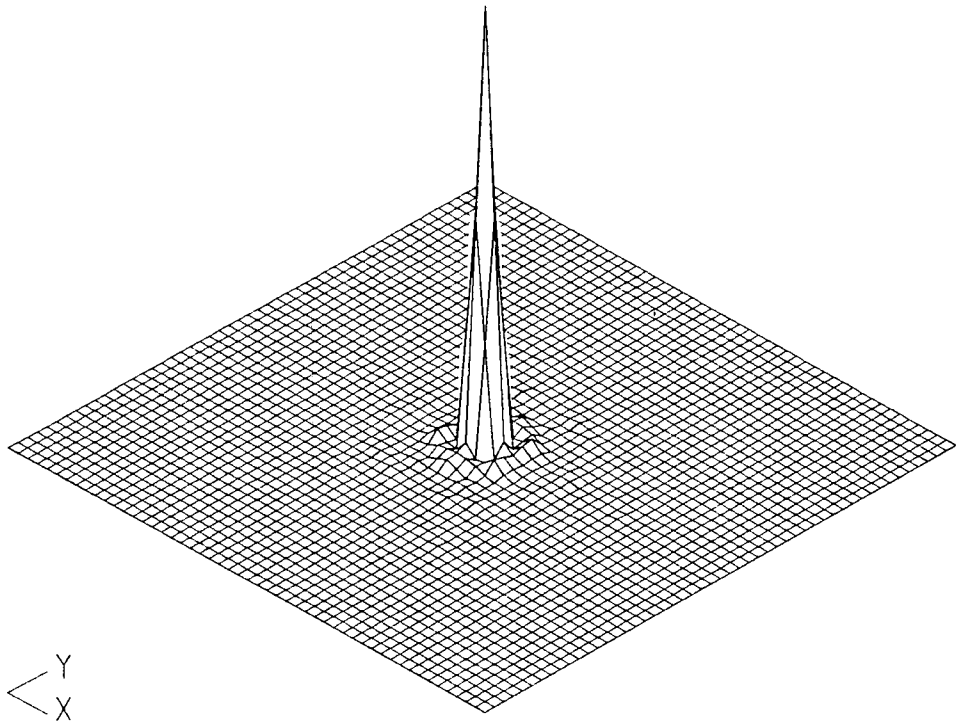


FIG 5.14a PSF of 36 hexagonal mirrors

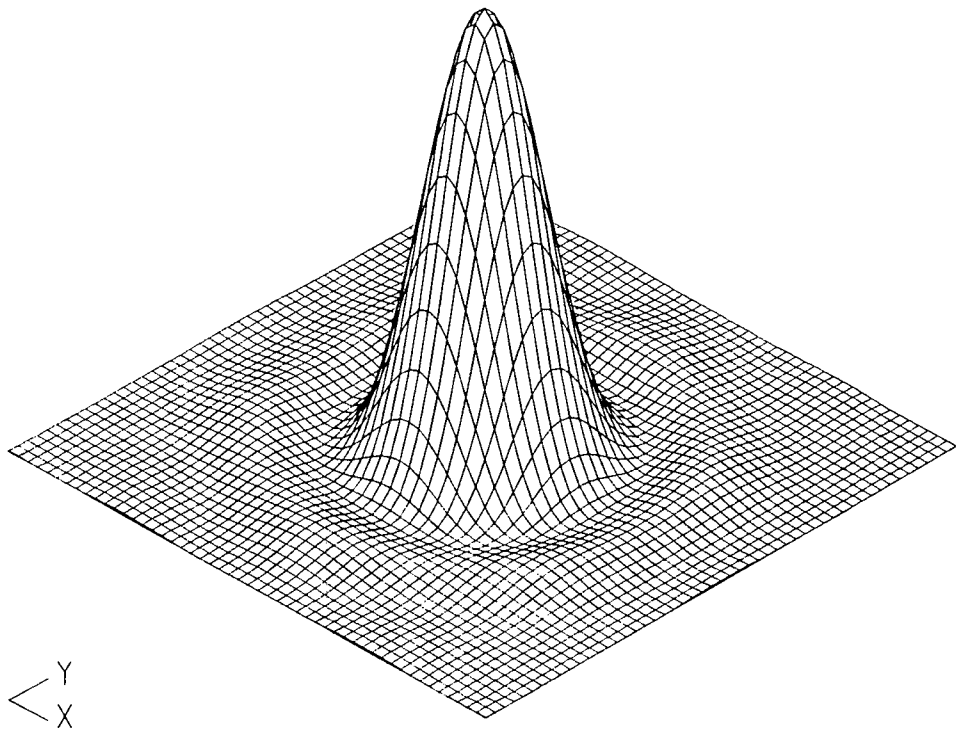


FIG 5.14b Expanded of FIG 5.14a

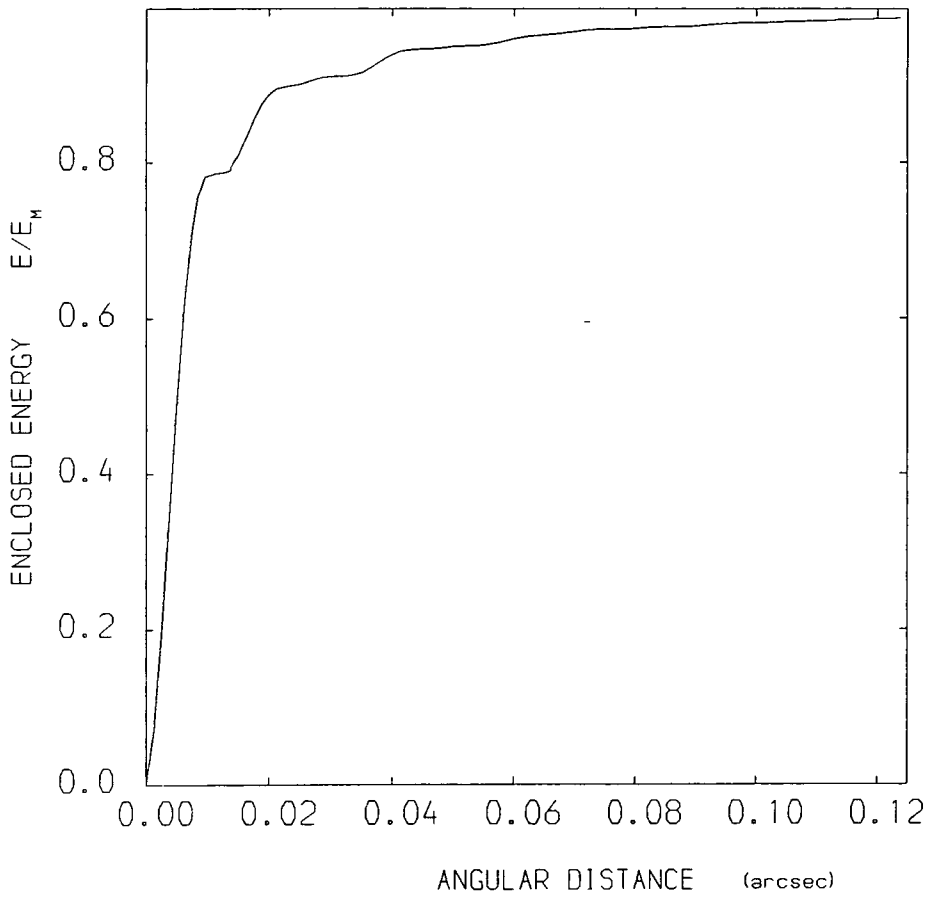


FIG 5.15 Enclosed energy of 36 hexagonal mirrors

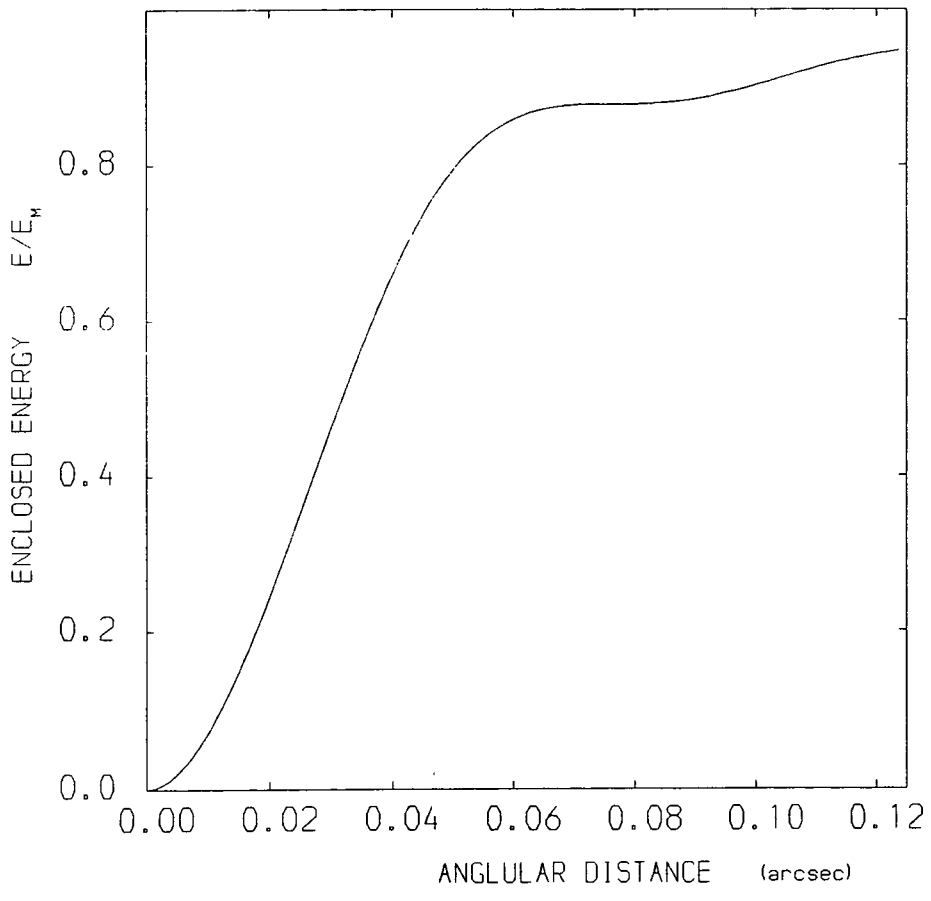


FIG 5.16 Enclosed energy of single hexagonal mirror

the single mirror and is shown in fig 5.16.

With this system, the relative phasing of the mirrors is of prime importance. The lack of phasing has been simulated by assigning phases to the 36 hexagonal mirrors chosen randomly between specified limits. This is done by changes to the PSF of the array matrix, $I_m(\Theta,\phi)$. The effects are shown in figs 5.17a, 5.18a and 5.19a of the resulting patterns for random axial displacements of the mirrors between $\pm$ $\lambda/8$, $\lambda/4$ and $\lambda/2$, respectively from the mean positions. The corresponding encircled energies are shown in figs 5.17b, 5.18b and 5.19b. When the mirror movement is limited to $\pm$ $\lambda/2$, ie varying by a wavelength, the 36 hexagonal mirrors become independent optically and produce an intensity pattern corresponding to that of a single mirror. The encircled energy (average) becomes identical with that for the single mirror. This result may be seen by comparing figs 5.19a, 5.19b with figs 5.12, 5.16. When the mirror movement is limited to $\pm$ $\lambda/8$ it is noticeable that this is almost idential with figs 5.14a and 5.15 as there is little effect on the pattern.

The Keck telescope will also work in the 10 microns region so the phasing is not very important when controlled in the visible region. As seen before (Brown's law in section 3.2.3) this telescope will work best in this region at the average seeing conditions ($r_o$ = 10cm).

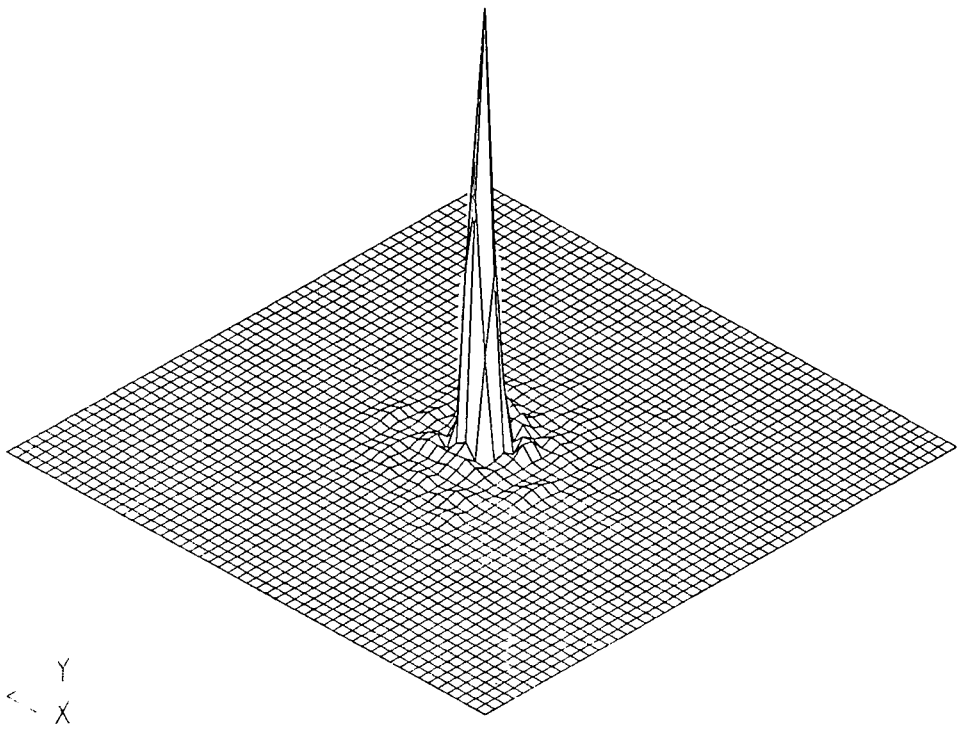


FIG 5.17a PSF of 36 hexagonal mirrors with random displacements ± λ/8

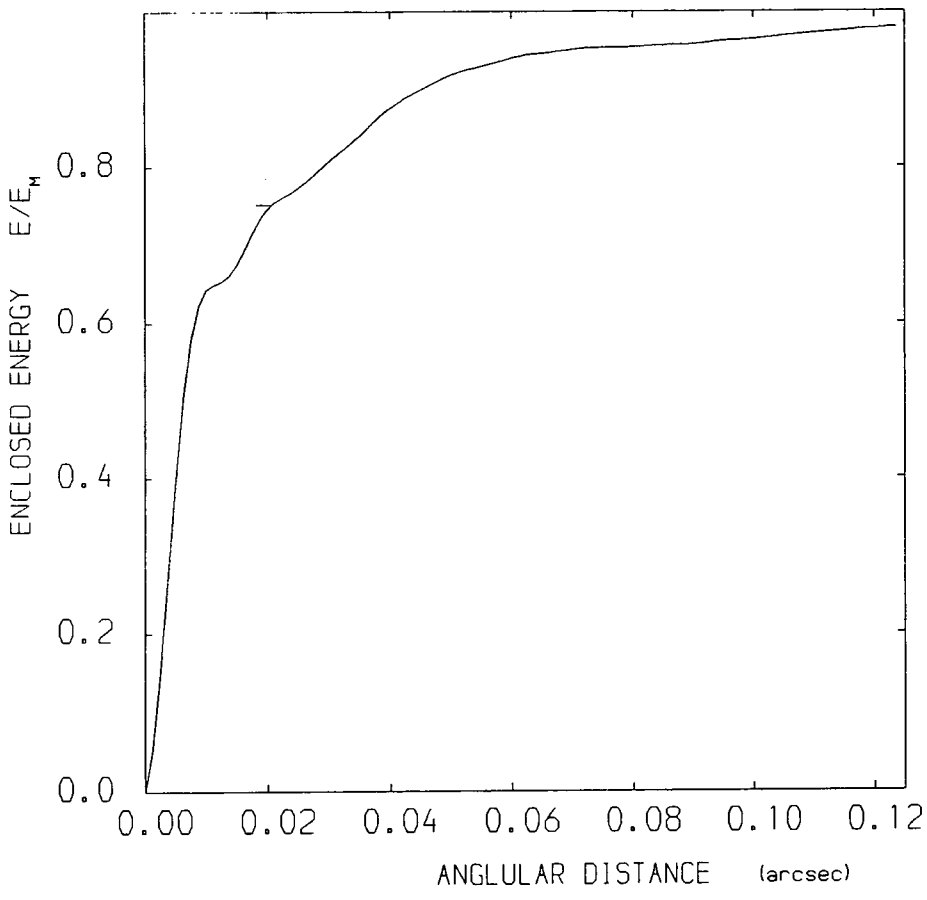


FIG 5.17b Enclosed energy of FIG 5.17a

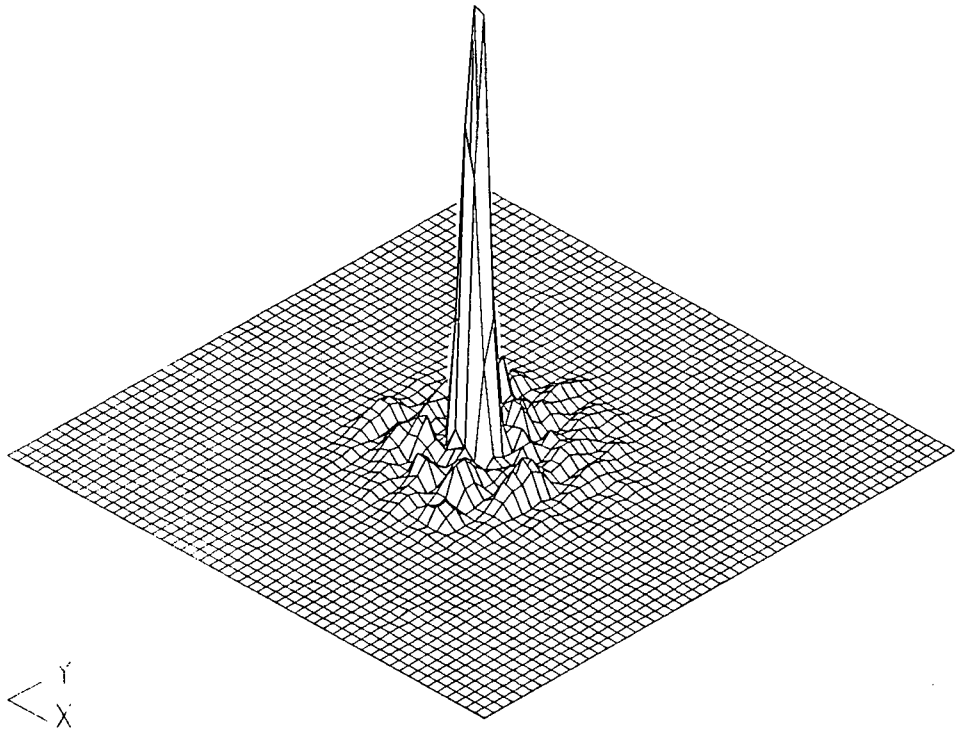


FIG 5.18a PSF of 36 hexagonal mirrors with random displacements ± λ/4

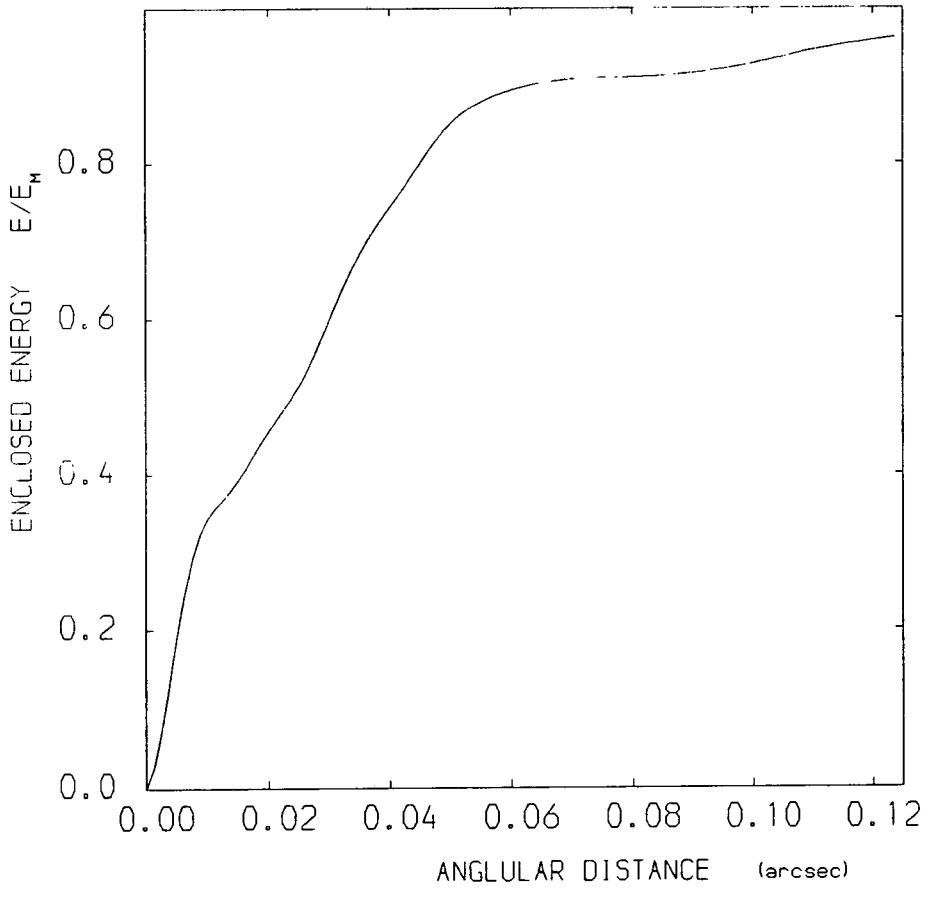


FIG 5.18b Enclosed energy of FIG 5.18a

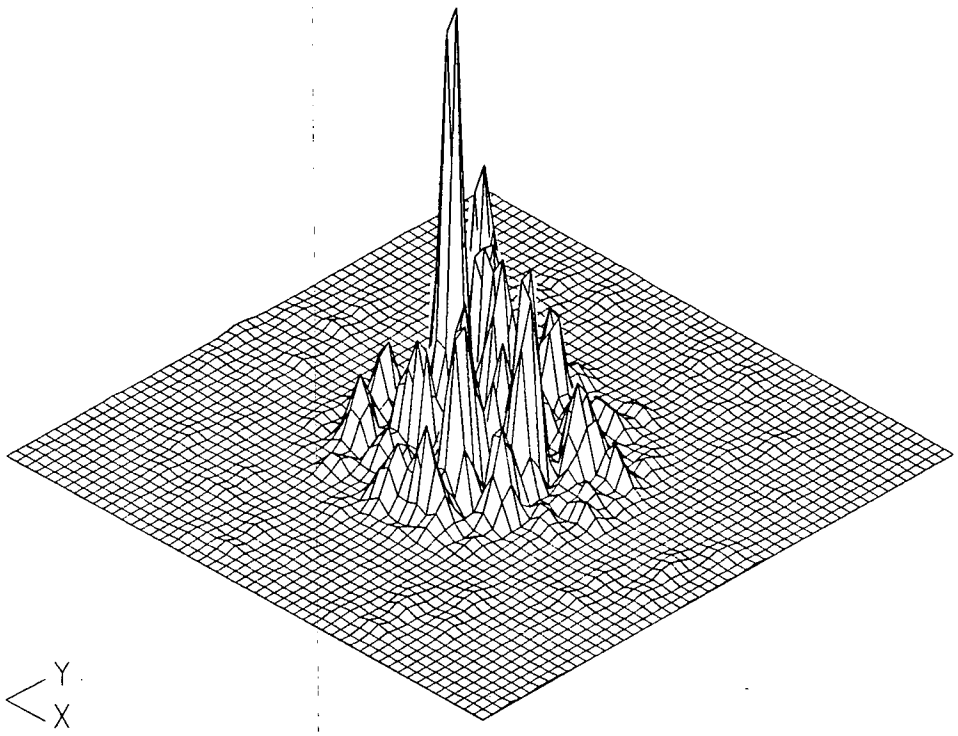


FIG 5.19a PSF of 36 hexagonal mirrors with random displacements ± λ/2

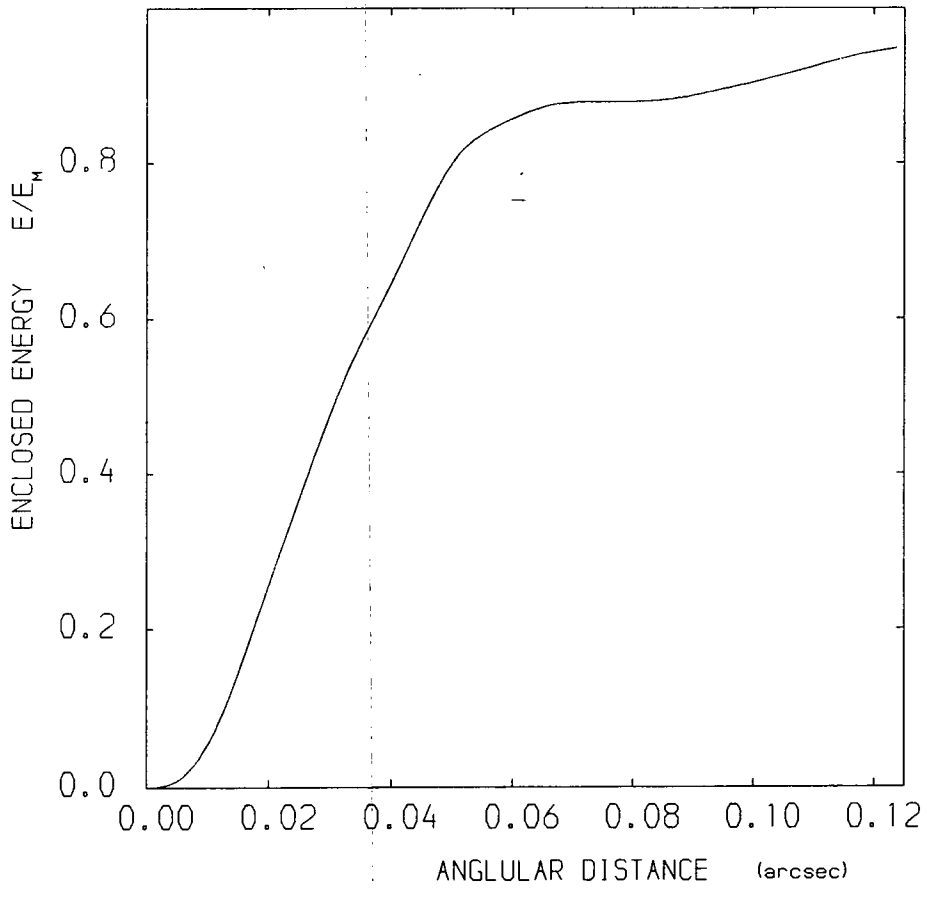


FIG 5.19b Enclosed energy of FIG 5.19a

# CHAPTER 6 DILUTION

## 6.1 ANNULAR APERTURE

The effects of the dilution are more readily understood for the case of an annulus of fixed area and hence of fixed light collecting power. The dilution of the aperture is controlled by adjusting the ratio $r_2/r_1$ of the internal to external radii whilst keeping the collecting area constant. This is done to emphasise that apertures of equal area all have the same central ($\Theta = 0$) intensity since the geometry of the aperture is only manifest in the angular dependence of the intensity. This is illustrated diagramatically in fig 6.1a. It can be seen that as dilution increases, the resolving power improves, since the outer radius increases. This means that the Airy disc decreases in size. However, as the central intensity is fixed the encircled energy in the Airy disc must decrease. The average brightness of the disc cannot be calculated analytically. However if the Airy disc region of fig 6.1b is approximated by a linear fit up to the first minimum, $\Theta_m$, then

$$I(\Theta) \doteq I_o(1-\Theta/\Theta_m) \quad , \tag{6.1}$$

and the encircled energy is

$$E(\Theta) = \int_0^{\Theta} I(\Theta)\Theta d\Theta = I_o\left[\frac{\Theta^2}{2} - \frac{\Theta^3}{3\Theta_m}\right] \quad . \tag{6.2}$$

The energy in the Airy disc is then

$$E(\Theta_m) = \frac{I_o\Theta_m^2}{6}, \tag{6.3}$$

and the average brightness of the disc is

$$B = \frac{E(\Theta_m)}{\Theta_m^2} = \frac{I_o}{6} \quad . \tag{6.4}$$

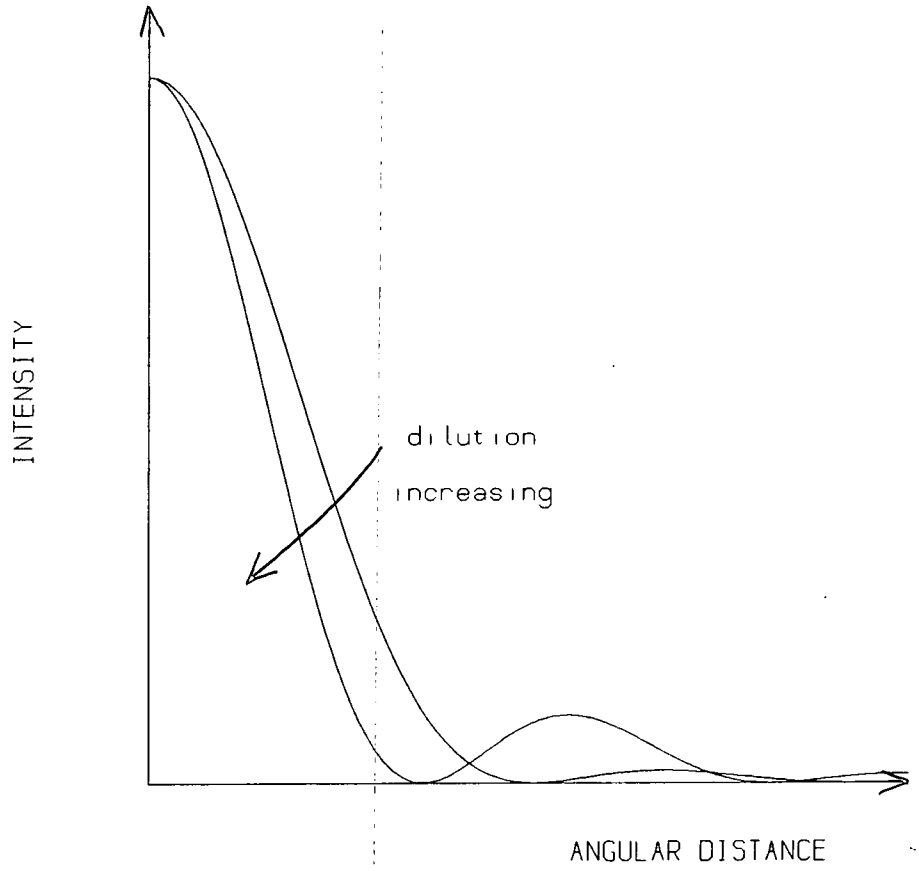


a)

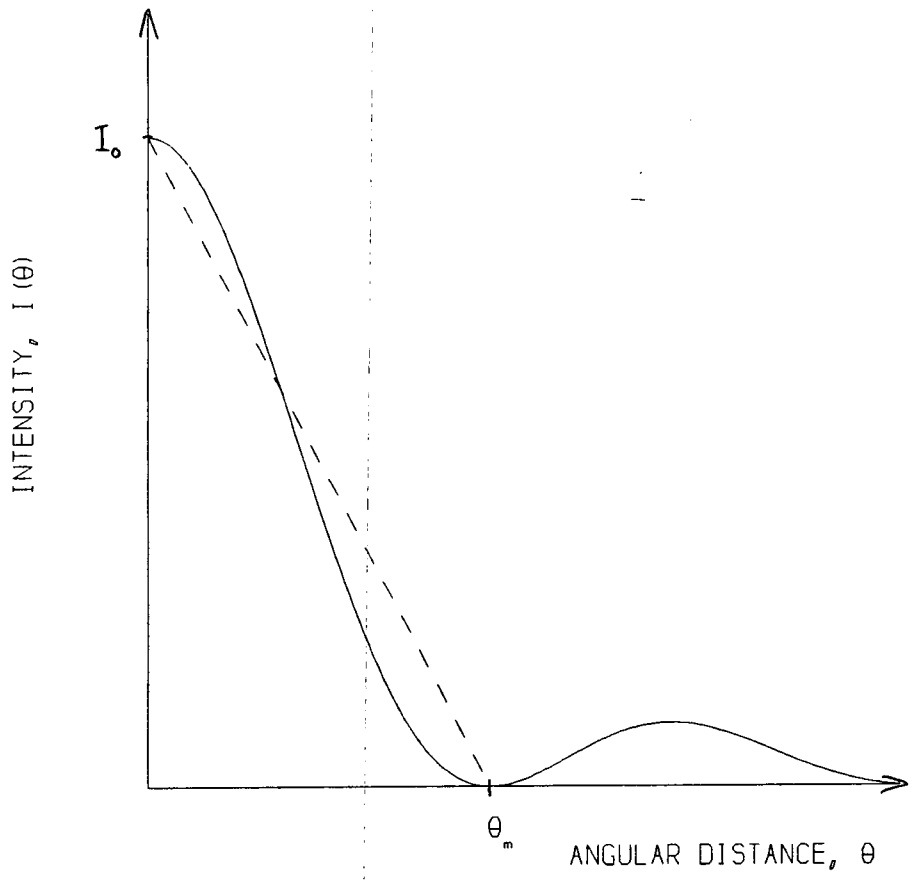


b)

FIG 6.1 Intensity pattern of diluted aperture

Hence, to a first approximation, the brightness of the Airy disc will remain unchanged since less energy is passed into the smaller Airy disc as the dilution increases. As will be seen later, as a result of more accurate numerical integration, the average brightness of the Airy disc does change and increase but by less than 20-30% even under severe dilution. Moreover, more energy will pass into the secondary maxima. So although a higher resolution is achieved by dilution it is at the expense of tolerating enhanced secondary maxima.

The diffraction patterns and encircled energies have been calculated for an annular mirror of constant collecting area for a series of ratios of $\eta = r_2 / r_1$, ranging from 0 (no dilution) to 0.95 (extreme dilution). These results are shown in figures 6.2 and 6.3 with a starting outer radius, $r_1 = 1.0$m. The normalising values of $\Theta_o$ and $E_o$ correspond to those for a circular mirror of the same area without dilution ($\eta = 0$). From the encircled energy graph the same feature is seen again but now more quantitatively. The proportion of encircled energy in the Airy disc changes from 84% (no dilution) to 8% under extreme dilution as the size of the Airy disc decreases. In fig 6.4 the variation of enclosed energy with size of Airy disc is shown and is seen to be almost linear as suggested by the approximation of equations 6.1 and 6.3. The brightness of the disc is shown in fig 6.5 and this increases by about 20% from the brightness for the undiluted aperture. In fig 6.6 the fractions of energy passing into the secondary maxima are shown as the dilution is increased. As expected these generally increase with dilution.

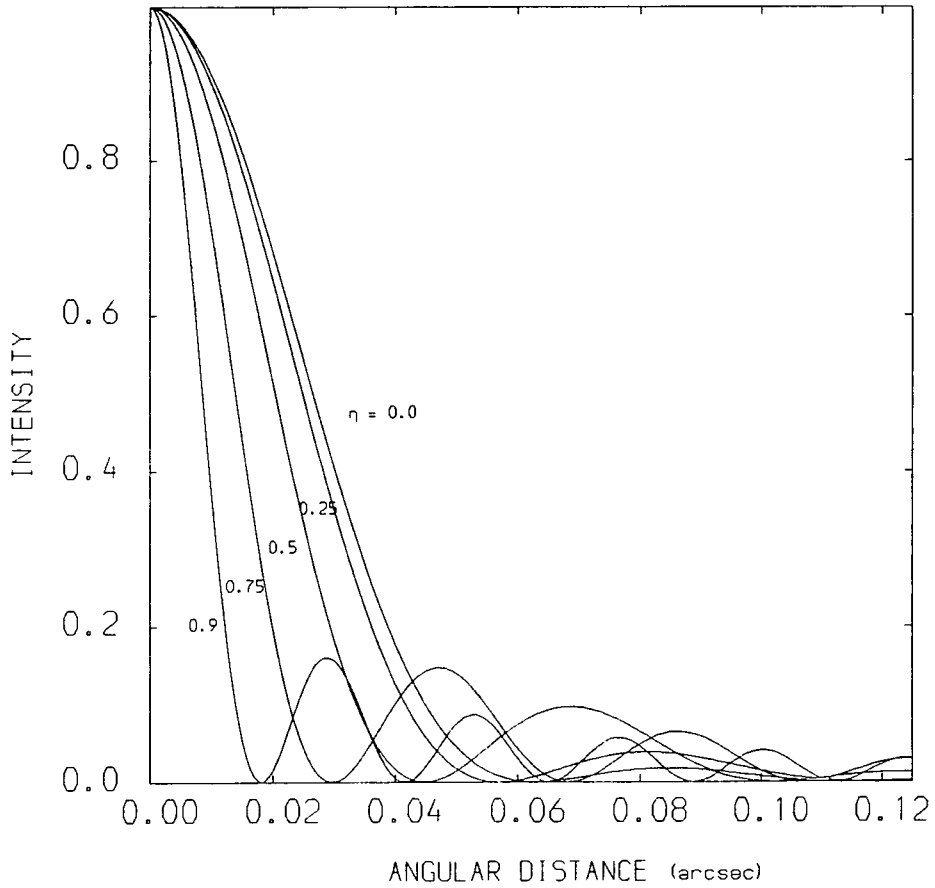


FIG 6.2 Intensity pattern of various diluted apertures

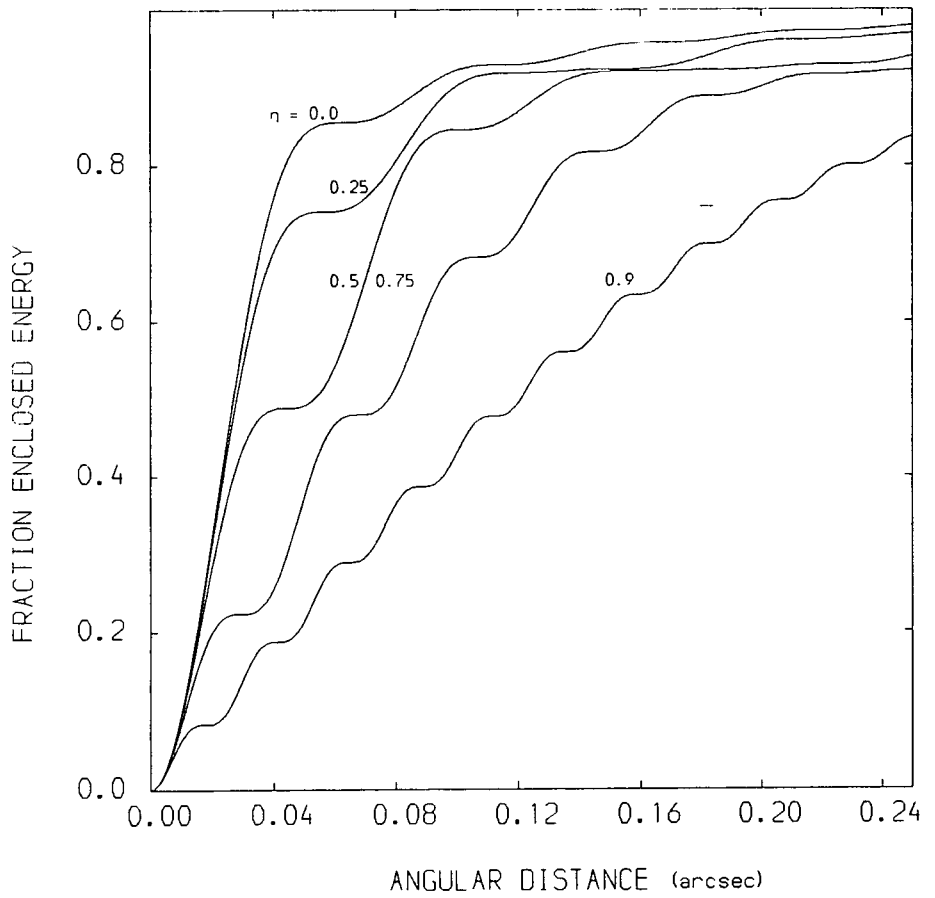


FIG 6.3 Enclosed energy of various diluted apertures

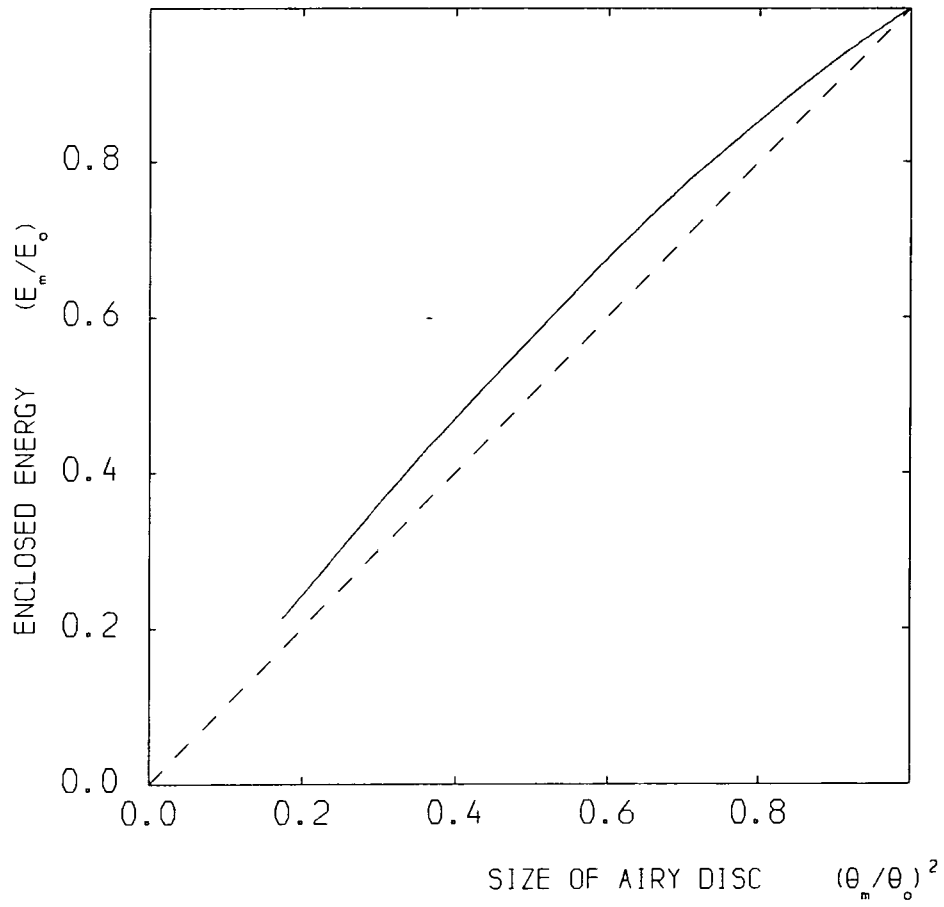


FIG 6.4 Variation of enclosed energy of the Airy disc

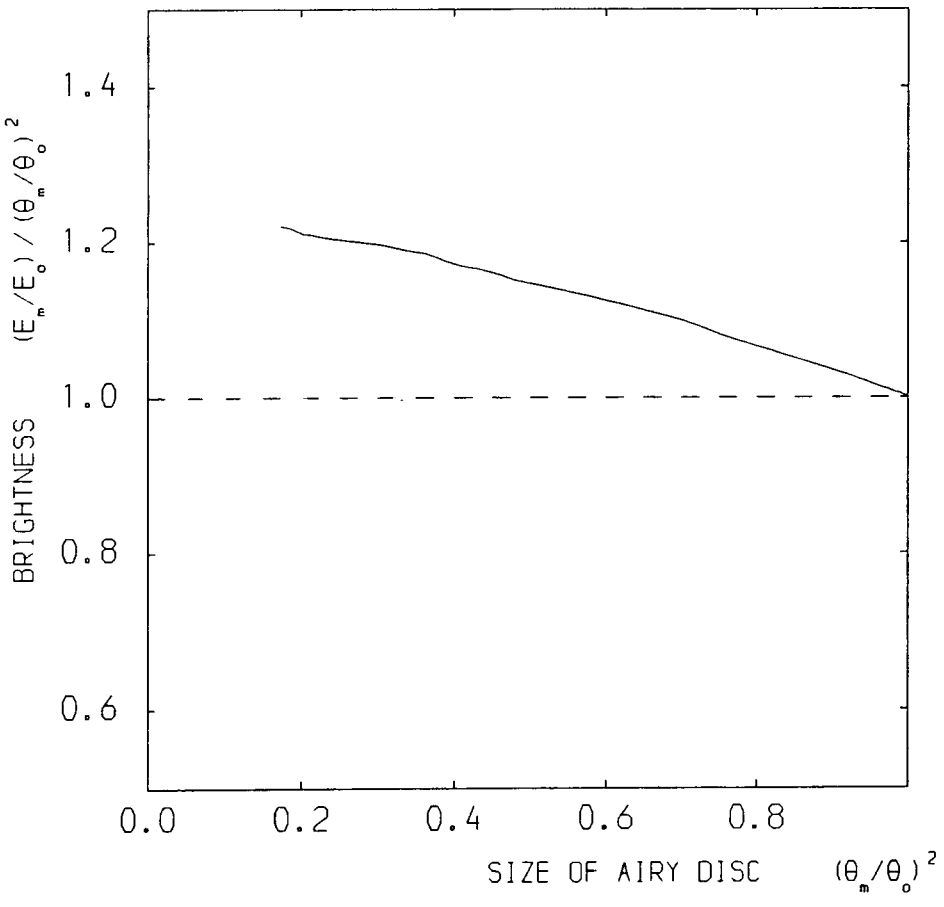


FIG 6.5 Variation of brightness of the Airy disc

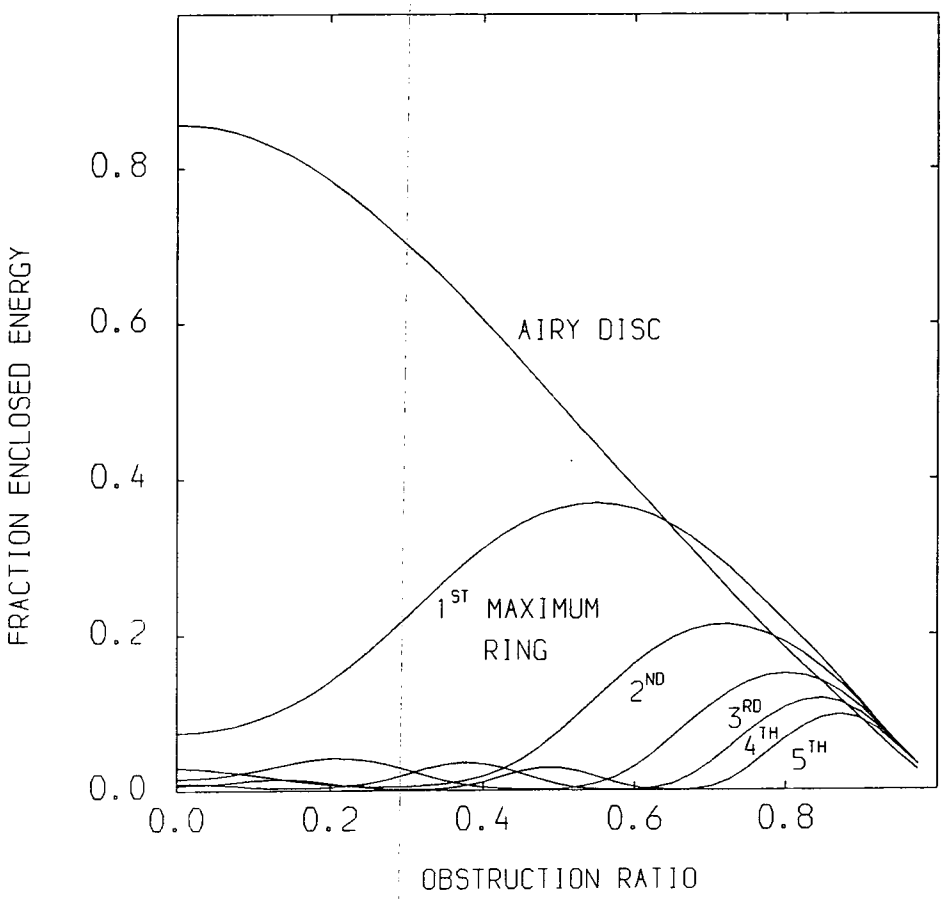


FIG 6.6 Variation of energy of several maxima

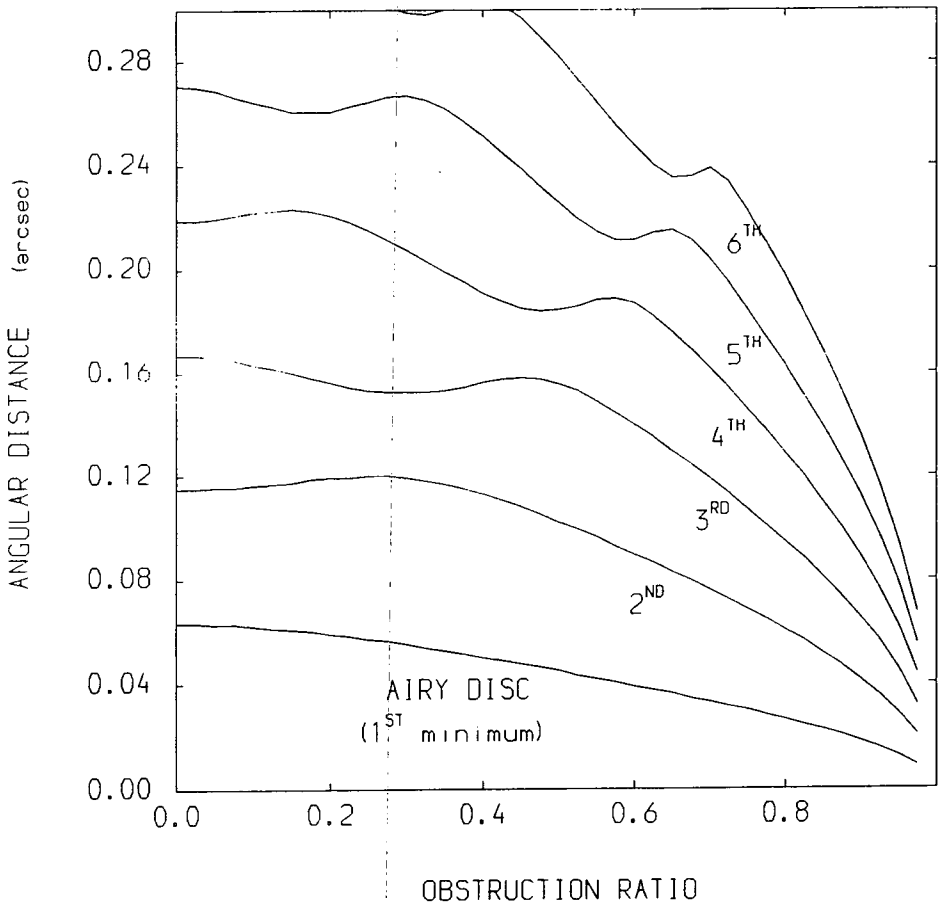


FIG 6.7 Variation of resolution of several minima

Curiously, for an obstruction ratio between 0.2 and 0.3 of the diameter, the second bright ring is very much suppressed compared to the first and third rings with the second apparently missing. This can be seen in fig 6.6.

Fig 6.7 shows the variation in the resolution of several minima. As the dilution is increased, the Airy disc is reduced from 0.067 arcsec at zero dilution ($\eta$ = 0.0) to 0.005 arcsec at extreme dilution ($\eta$ = 0.95). Also it shows that the second minimum increases from $\eta$ = 0.0 and reaches a peak at $\eta$ = 0.3 and then reduces while the third minimum reduces from $\eta$ = 0.0 until at $\eta$ = 0.3, then it increases to a peak. This explains why the fraction of the enclosed energy of the second bright ring is reduced at $\eta$ = 0.3 (see fig 6.6).

Most telescopes do have an obstruction ratio of about 0.3, so their Airy discs are reduced to 68% of total energy. But the average brightness is about the same and the resolution is higher.

These features are expected to be dominant in all diluted apertures systems, for example, in multi-mirror systems.

## 6.2 MULTI-MIRROR

The combination of the multi-mirror system leads to a diluted aperture whose diameter can be controlled from a minimum value ie when all the mirrors are touching, to higher values which are controlled by the cost of mounting well separated mirrors. As the overall diameter largely controls the resolving power, the Airy disc size is reduced as the individual mirrors

are separated (or the aperture is diluted). The diffraction pattern for a multi-mirror system consists of a convolution of two basic patterns - one due to a single mirror and another due to the centres of the mirrors, which produce a pattern of maxima and minima. These patterns can be changed by increasing the separations between the centres. It has a considerable effect on the relative intensities of the maxima surrounding the central peak. When the separations are increased, it will cause the first ring of bright secondary maxima to move away from the first dark ring (Airy disc) in the single mirror aperture, thus effectively increasing the intensity of these maxima. This means, in fact that, some of the energy is transferred into secondary maxima from the central peak. These effects can be seen by comparing fig 6.8a for when all the mirrors are touching and fig 6.8b for when the separation is increased to 0.4m separation, with six circular apertures.

The diffraction patterns and enclosed energies have been calculated for six circular apertures (1m diameter each) on a hexagonal array and for four circular apertures on a square array for a set of dilution values ranging from a situation when all the mirrors are touching to 2.45m gap between the edges of the mirrors. These results are shown in figures 6.9a for six apertures and 6.10a for four apertures. The normalising value of $\Theta_o$ and $E_o$ correspond to the angular size of the Airy disc and its enclosed energy for a single circular solid mirror of the same surface area. The corresponding variations of brightness of the Airy disc of the central peak are shown in figs 6.9b and

FIG 6.8 PSF of 6 circular aperture with two different gap

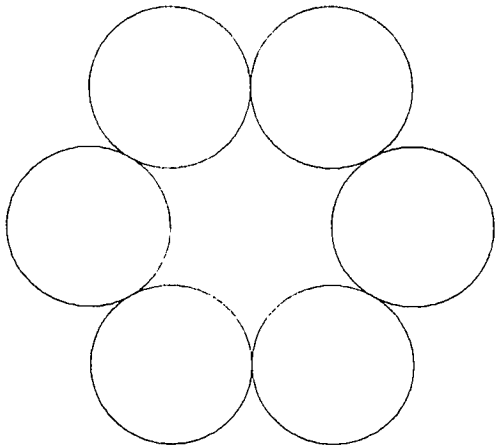

radius = 0.5m

separation between centres = 1.0m

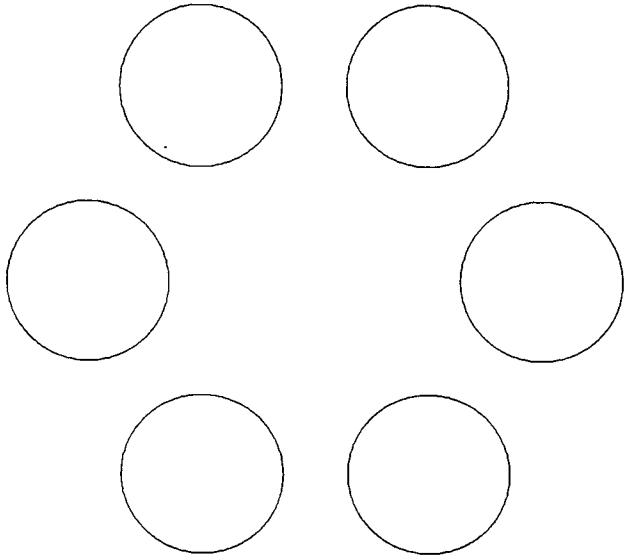

radius = 0.5m

separation between centres = 1.4m

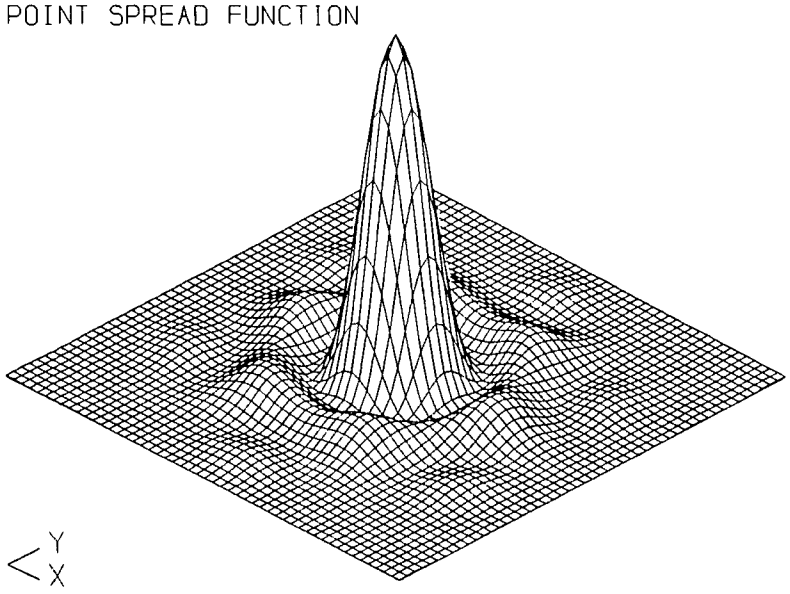


a) all the apertures are touching

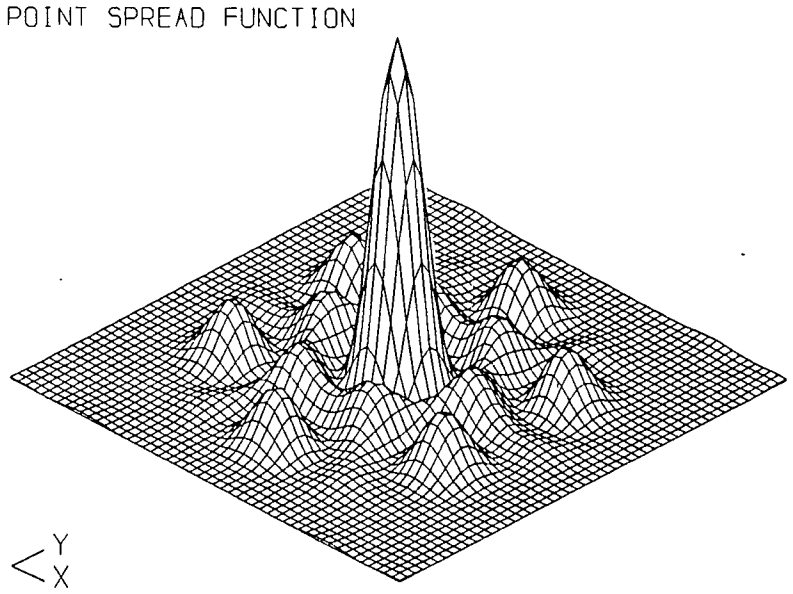


b) the gap is increased to 0.4m

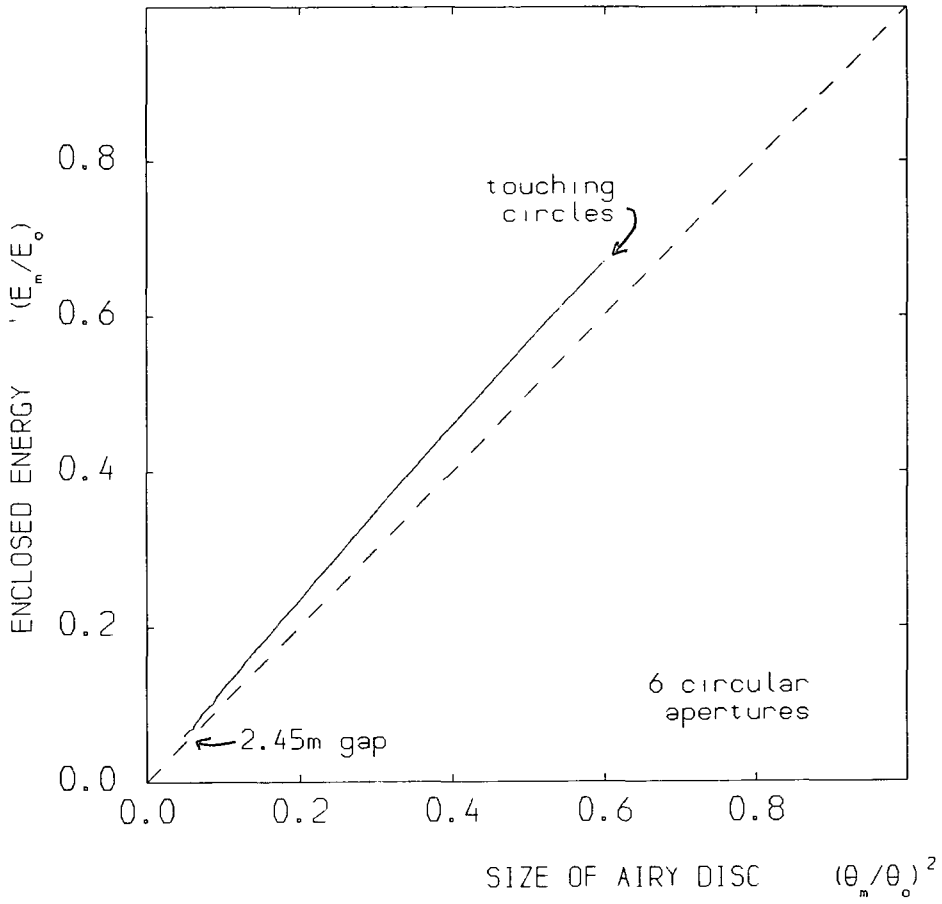


FIG 6.9a Variation of enclosed energy of the Airy disc

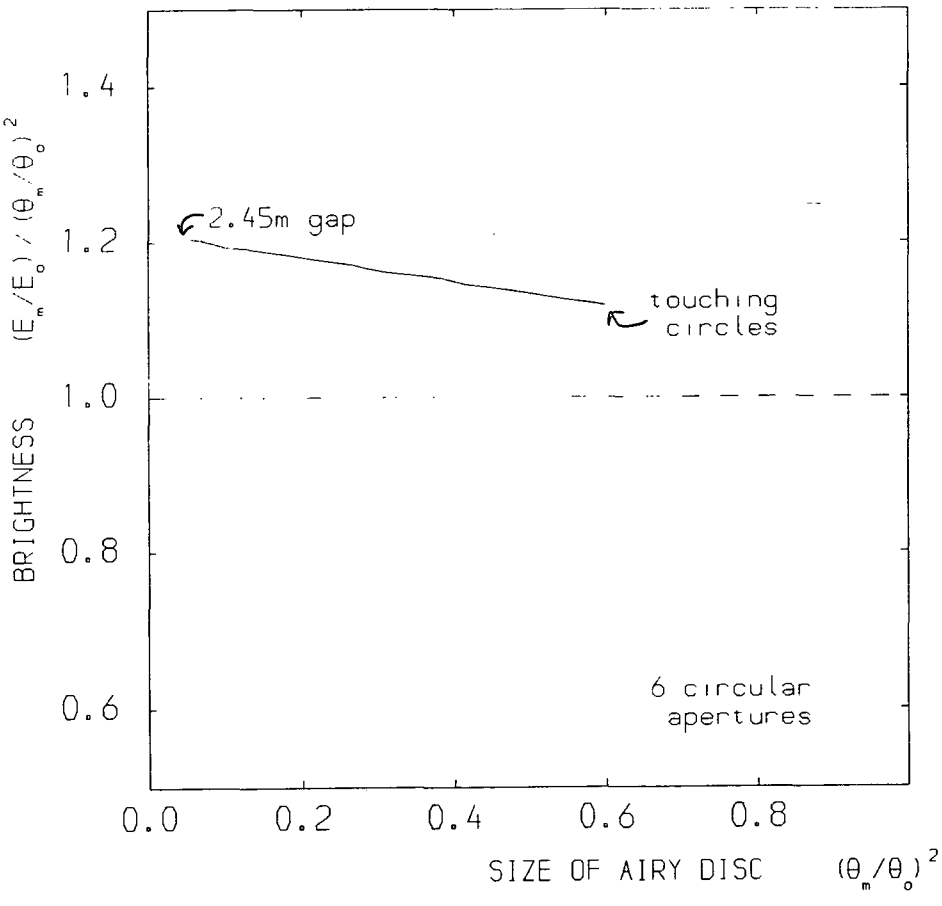


FIG 6.9b Variation of brightness of the Airy disc

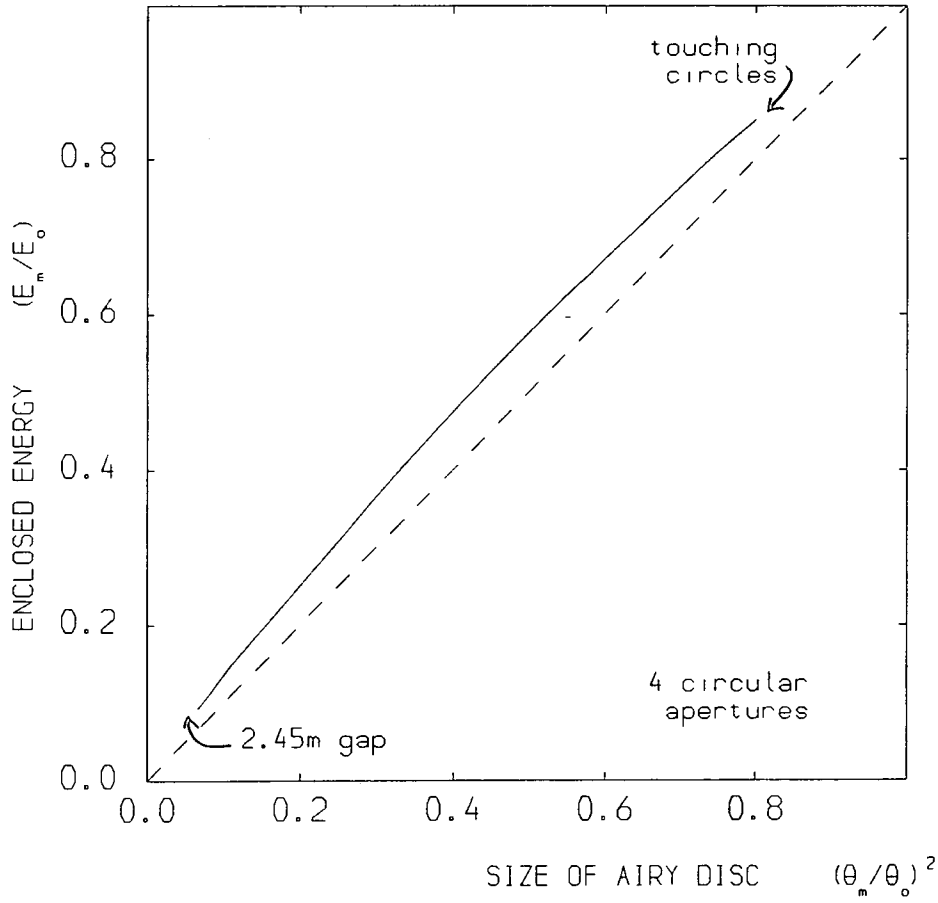


FIG 6.10a Variation of enclosed energy of the Airy disc

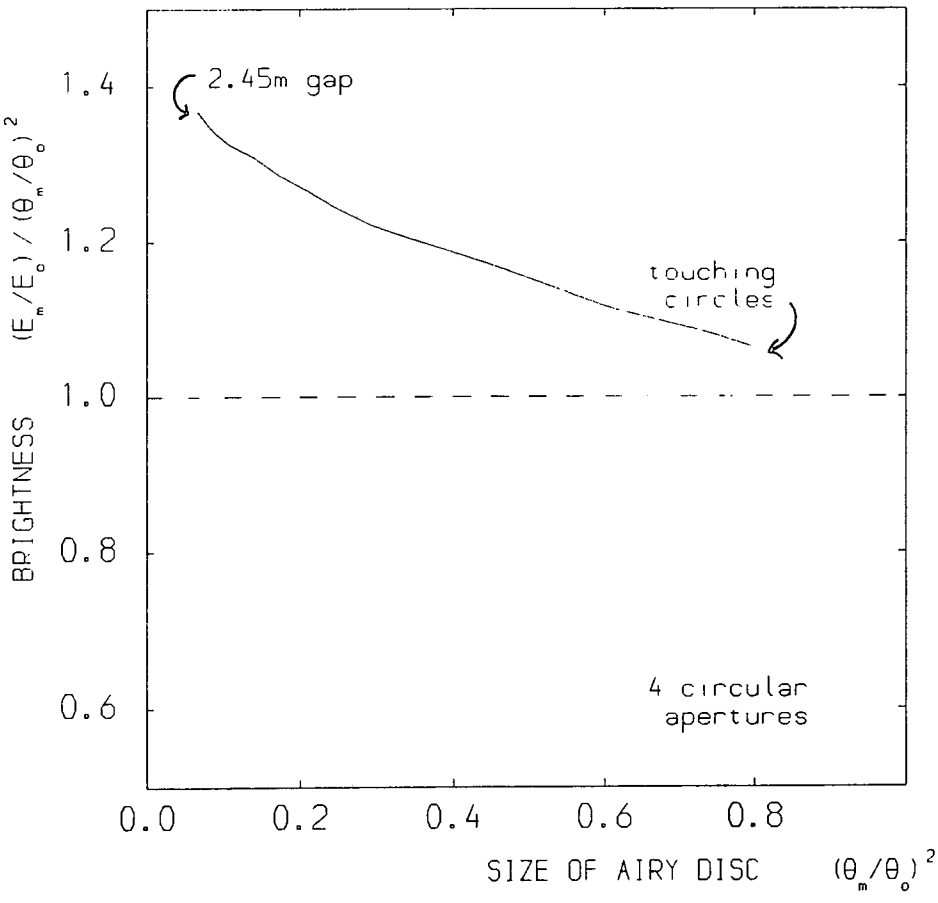


FIG 6.10b Variation of brightness of the Airy disc

6.10b.

In figs 6.9a and 6.10a, the variation of enclosed energy with Airy disc size, is seen to be almost linear as suggested by the approximation of equations 6.1 and 6.3. The brightness of the Airy disc is seen to increase by about 10% from the brightness for the zero gap between the edges.

When two apertures are considered, the dilution is difficult to define. Further the average radial intensity and energy are not useful quantities because of the high degree of asymmetry of the pattern.

# CHAPTER 7 DURHAM POLARIS SEEING MONITOR

## 7.1 INTRODUCTION

There are various ways to characterise seeing. A straightforward way is to measure the FWHM of the blurred stellar image usually called the seeing disc. When this is measured for a large telescope then the image is largely a convolution of atmospheric seeing and dome seeing. Similarly, in stand-alone devices such as the Polaris Trail Monitor with a typical aperture of 15cm the image is then largely a convolution of the atmospheric seeing with the diffraction at the aperture. To estimate the contribution of seeing alone to the size of the image, detailed measurements and deconvolution of these images are required. However, the size of the image, though not a precise quantification of atmospheric seeing, is a useful means for comparative measurements of observatory sites.

A more precise characterisation of seeing can be made by determining the value of the coherence length, $r_o$, which is the distance over which the phase of the wavefront changes by one radian. Using Fried's model, $r_o$ can be found from the MTF for seeing, (see eq. 3.25):

$$MTF(w) = \exp[-3.44(w\lambda/r)^{5/3}] , \qquad (7.1)$$

where

$$r = r_o (\lambda/\lambda_o)^{6/5} .$$

The MTF is conveniently measured interferometrically. Then with a stand-alone device with an aperture of sufficient minimum size (~30cm so that diffraction is relatively unimportant), the MTF

of the atmosphere alone can be found and there are no important deconvolutions to be made. The MTF is the proper measure of the optical properties of the atmosphere pertinent to imaging.

Interferometric measurements of the MTF for seeing have been made using horizontal laser beam propagation (1970-71, ref 7.1). These provided the first experimental check of the expression given by eq 7.1 and especially of the 5/3 law. Similar measurements were later performed on stellar sources (ref 7.2).

The Polaris monitor which is described in this chapter is based on the shear interferometer as described by Brown and Scaddan (ref 7.3). Their paper describes a simple interferometer suitable for direct photographic use and capable of giving data for shear distances of 0-10cm. It can be modified for use with a telescope of 20-30cm aperture. The monitor has been built in the workshops of the University of Durham with some financial support from the Royal Greenwich Observatory. It is designed to monitor the seeing at La Palma in the Canary Islands. So far, the monitor has been tested at Durham (60m above sea level) and it has been to used to measure the local seeing, which is typically in the range of $r_o \sim 1$-2cm.

In a recent review (ref 7.4) Woolf summarised the value of $r_o$ as ranging from 3 to 25cm from site to site and varying with time. The Durham shear interferometer can record values of $r_o$ throughout this range. Consequently, typical average seeing at a mountain site ($r_o$ = 10cm) can be deterimined and, more importantly, the number of times and the duration of those times

that seeing is good (say $r_o$ >20cm) can also be found.

Monitoring seeing is needed for several reasons, which include:-

a) testing the suitability of new sites for telescopes.

b) monitoring external and internal (dome) seeing to highlight worsening dome conditions.

c) with real time monitoring of $r_o$, the use of telescope time with respect to good seeing can be optimised.

d) providing basic statistics from which optimised designs of devices for wavefronts tilt (or full) corrections can be made.

## 7.2 SUMMARY OF THE SEEING CONDITIONS AT LA PALMA

The shear interferometer has to be matched to local seeing conditions at La Palma. There have been several measurements of seeing at the Canary Islands since 1971 when the Royal Observatory, Edinburgh, started measurements. McInnes and Walker (ref 7.5) have given results of studies of astronomical observing conditions using polar star trail observations and meteorological data at two sites in the Canary Islands. These are Izana on Tenerife and on La Palma. They found that the seeing conditions at La Palma were very good or better than those known at any other site outside the Canary Islands at that time, including Tenerife. The seeing disc was smaller than 1 arcsec for 40 percent of the time on La Palma. Their observations strengthen the earlier conclusion by Walker (ref 7.6) that the best astronomical seeing occurs at sites on peaks

near a coast with a cold ocean current offshore or on isolated peaks on small islands where, in both cases, the peak projects above the inversion layer and where laminar airflow over the ocean still persists.

Further measurements of the seeing conditions at the Canary Islands were made by the testing groups for the Joint Organization for Solar Observations (JOSO) who investigated daytime observing conditions. After many years of extensive comparative observations on La Palma and Tenerife, these investigators came to the conclusion that La Palma may have excellent nighttime conditions but Tenerife (Izana) was a better site for daytime observing. The results of JOSO's testing groups are described below.

During 1973 and 1974, Barletti and others (ref 7.7) measured the values of $r_o$ by indirect means in the atmosphere above La Palma and Tenerife. The results were obtained from measurements of the atmospheric temperature variation up to 20km using balloon-borne radiosondes. From these the temperature structure coefficient, $\bar{C}_T^2$, was found, and hence the refractive index structure coefficient, $C_n^2$, was calculated using the associated pressure and temperature. Finally $r_o$ was deduced using eq 3.19. It was found that the values of $r_o$ above the altitude of the balloon varied from 20cm to well over 40cm during both day- and night-time. It is important to realise that this corresponds to the atmosphere above 5km. When this is reduced to the mountain site altitude then smaller values of $r_o$ result.

In 1979, Brandt and Wohl (ref 7.8) used two telescopes on the Canary Islands, ie a 40cm telescope on Tenerife and 45cm telescope on La Palma, taking photographs of the solar granulation during daytime. After measuring the resolution of the solar granulation from the apparent width of the granulation edges, they obtained daytime seeing measurements showing that Tenerife was superior to La Palma since in 23% of the observing time at Tenerife images in the range $0.6 \leq FWHM \leq 1.2$ arcsec were found compared to 17% of the time at La Palma. The highest resolution obtained with both telescopes was $0.5 \leq FWHM \leq 0.6$ arcsec at an observing wavelength, 0.55 micron.

From above it can be seen that an average value of $r_o$ deduced from indirect measurements at La Palma is about 10cm. There are no direct measurements of $r_o$.

It should be noted that the value of $r_o$ varies with zenith angle, $\Theta$, and decreases as:

$$r_o(\Theta) = r_o(0^\circ)(\cos\Theta)^{3/5}. \qquad (7.2)$$

Since La Palma is situated at $28^\circ$N, then the zenith angle of Polaris is $62^\circ$ and from the cosine term above, $r_o$ of 10cm would be reduced to $r_o$ of 6.4cm and the average seeing disc increased to 1.6 arcsec.

## 7.3 SHEAR INTERFEROMETERS

The most important part of the Durham Polaris monitor, (to be described later), is its shear interferometer which is used to measure the MTF of the atmosphere. This MTF results from the varying optical path lengths in the atmosphere which lead to the

wavefront at the aperture of a telescope becoming corrugated. Beside the phase variations, the amplitude may also vary, although this is unlikely to contribute more than 20% to the structure of the final image. The instantaneous optical transfer function is given by the autocorrelation of the wavefront sheared upon itself by a shear interferometer, ie

$$T(w) = \frac{\int_{-\infty}^{\infty} \alpha(x)\alpha(x-\lambda w)\, \exp(-i(\phi(x)-\phi(x-\lambda w))\, dx}{\int_{-\infty}^{\infty} |\alpha(x)|^2\, dx} . \qquad (7.3)$$

In the overlap region of the shifted wavefront, a complicated interference pattern results. Moreover this pattern fluctuates with a high frequency (~100Hz) so that any integrated pattern will give uniform illumination.

As the stellar light level of Polaris is low only time-integrated patterns are available and so the interference pattern needs to be converted into an integrable form. This is done by putting a small wedge angle between the sheared and unsheared wavefronts to produce wedge fringes. Then the effect of the instantaneous phase differences due to seeing is that of de-modulating the shape of the fringes. For time-integrated seeing, the moving fringes will result in broadened recorded fringes and their intensity modulation will be reduced. The time averaged MTF(w) can be determined from the ratio between the modulation function without seeing, $M_o$, and the function with seeing, $M_i$, ie

$$MTF(w) = M_i/M_o . \qquad (7.4)$$

There are various kinds of shear interferometers in use. The simplest form divides the wavefront into two circular images which are sheared relative to each other by a fixed amount. The

modulation of associated wedge fringes is measured. This method requires the fringe pattern without seeing for normalisation and it needs resetting for each shear; this is a time consuming procedure. So a method is needed which contains a normalisation reference and also includes a range of shears (range of spatial frequencies, w) so that the atmospheric MTF as a function of w can be determined in a single recording of fringes. There are three instruments in which the range of shear and the normalisation point can be included.

i) One instrument is a reversing (or folding) interferometer, such as that described by Dainty and Scaddan (ref 7.9), in which the wavefront is reversed upon itself. This gives a range of shears from zero to the size of the wavefront. The aperture needs to be relatively large (~30cm) to avoid diffraction limitations. However, beyond shears equal to about $r_o$, the visibility of the fringes will be zero so only the central area of the aperture is used and the rest of the light is wasted (ie 2/3 of the area if a 30cm aperture is used). This means that the interferometer has to be used with a very bright star or with a long exposure time for the photographic recording when using 10cm aperture.

ii) The second instrument is a shear rotation interferometer, such as that described by Roddier (ref 7.10). The shear rotation interferometer consists of a beamsplitter and two prisms. One of the prisms is rotated to give a rotational shear on one of the two interfering beams. The fringe can cover the whole field of view and the shear values can be varied by

rotating one of prisms, so it is possible to use a 30cm mirror. There is a small problem in that zero shear occurs only at one point (at the centre of the field of view) and only the fringe passing through the centre of the field is useful.

iii) The third instrument is a Jamin-based shearing interferometer with a pair of prisms, such as that described by Brown and Scaddan (ref 7.3). With this, maximum shear can be adjusted to be equal to about $r_o$ and hence it will use most of the light. The Durham shear interferometer unit is the same in principle as this and details of this instrument are given in section 7.3.3.

### 7.3.1 Brown and Scaddan Shear Interferometer

The Brown and Scaddan shear interferometer consists of a Jamin interferometer, a pair of opposed prisms and a compensating glass plate within the two light paths as shown in fig 7.1. A pair of opposed prisms will cause an anamorphic magnification of one wavefront passing through it. When the wavefronts are superimposed and a wedge angle is introduced, then fringes are seen in the overlap region. On the diameter of the two images, the two wavefronts are unsheared and are exactly in phase. The fringe modulation there is unaffected by seeing and this gives the normalisation modulation, $M_o$. In this way it is possible to ensure that the useful area of interference almost completely fills the telescope aperture, regardless of its diameter, so that all parts of the aperture contribute useful information. It can produce a desired range of shears by

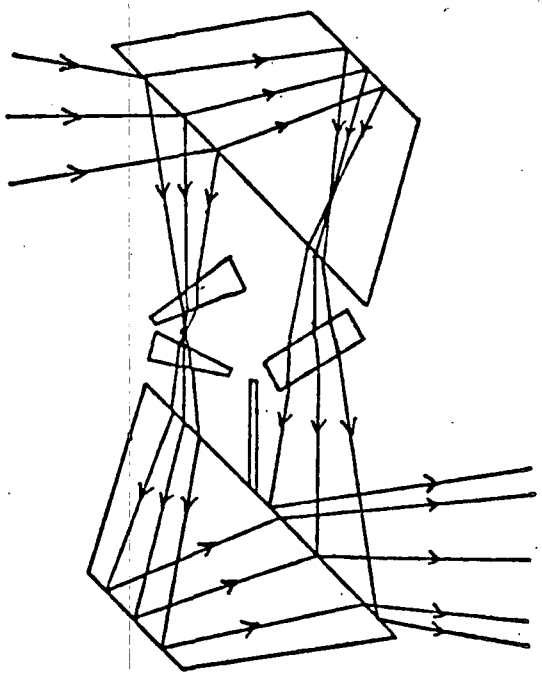

FIG 7.1 Brown and Scaddan shear interferometer

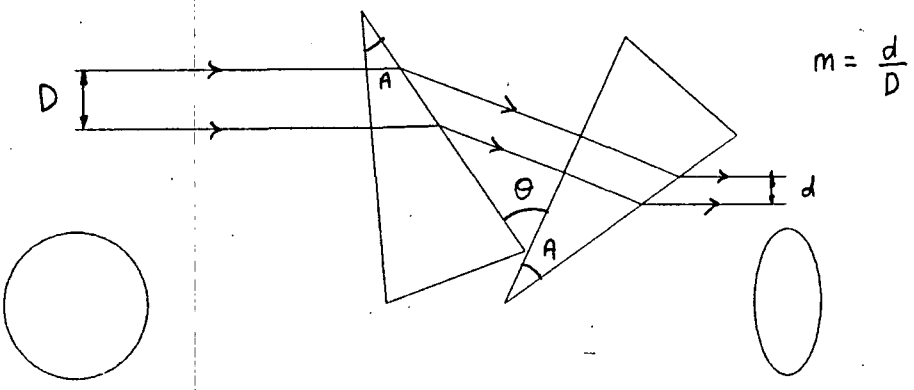


a) demagnification

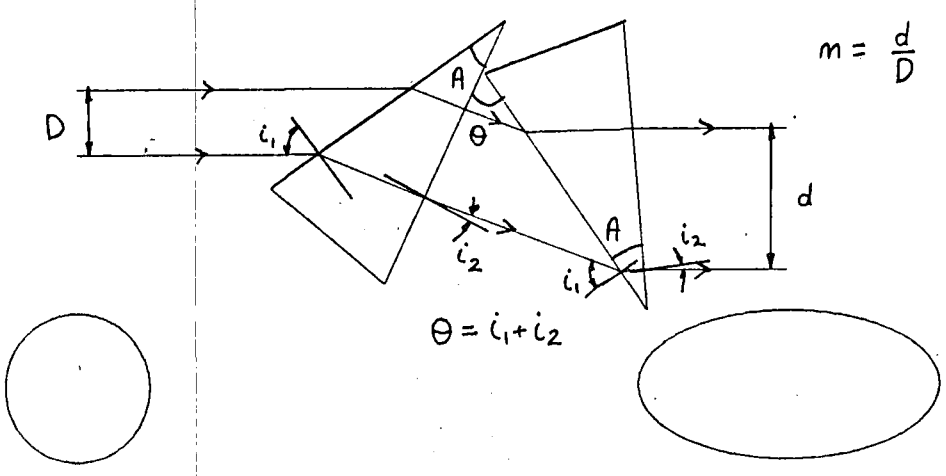


b) magnification

FIG 7.2 Anamphoric prism pair showing two different magnifications

adjusting the magnification of the prisms by using suitable prism angles and orientations.

Brown and Scaddan used the 74-inch telescope of the Helwan Observatory at Kottamia to test the shear interferometer unit. The interferogram was recorded with an exposure time of two minutes using Vega as the star source. They found a value of $r_o$ of about 5cm for Kottamia from microdensitometer measurements across the interferogram. They also deduced that it should be possible to use the shear interferometer with a magnification of 0.75 in a static telescope of 20-30cm aperture with Polaris as the star source and with an exposure time of about 2 minutes to give the MTF for the atmosphere.

In the Durham Polaris Monitor, there is a 30cm mirror, so the magnification should be about 0.75 giving a full view of the fringes. The magnification can be adjusted by varying the prism angles and orientations. This is described in next section.

### 7.3.2 Anamorphic Prism Pair

An anamorphic prism pair consists of a pair of opposed prisms such as shown in fig 7.2. There, it can be seen that when the light rays pass from left to right, there is a demagnification and when the prism pair is placed in a reverse position, there is a magnification. This causes the image, after passing through a prism pair, to increase or decrease in one direction whilst remaining unchanged in the other direction. The results of this effect are shown in fig 7.2 for a circular image. This arrangement is used in wide-screen cinema

projection. By the use of suitable prism angles and orientations, magnifications in the range 0.4 to 2.5 can be obtained.

There are two ways to change the magnification by a prism pair. Either the prism apex angle, A, is varied, or the angle between the two prisms, Θ, is varied. The relationship between the apex angle, A, and the incident and emergent angles, $i_1$ and $i_2$, is given by:

$$A = \sin^{-1}(\sin i_1/n) + \sin^{-1}(\sin i_2/n) , \qquad (7.5)$$

where n is the refractive index of the glass of the prisms. The angle between two prisms, Θ, as shown in fig 7.2b, can be found as a sum of the two angles $i_1$ and $i_2$, ie:

$$\Theta = i_1 + i_2 .$$

This is the case for zero overall angular deviation, where the angular deviation by the second prism is equal and opposite to the first. So equation 7.5 can be written as

$$A = \sin^{-1}(\sin i_1/n) + \sin^{-1}(\sin(\Theta - i_1)/n) . \qquad (7.6)$$

This can only be solved numerically to determine the value of $i_1$ when the values of A and Θ are given. The relationship between the incident angle, $i_1$ and the magnification of two prisms, m, is given by:

$$m = \frac{\cos^2 i_1 \, n^2 - \sin^2 i_2}{\cos^2 i_2 \, n^2 - \sin^2 i_1} , \qquad (7.7)$$

where $i_2 = \Theta - i_1$.

Using equations 7.6 and 7.7, the three curves for each of three different prism apex angles, ($A = 45^\circ$, $30^\circ$ and $12.5^\circ$) as shown in fig 7.3, represent the relationship between the angle of the prism pair, Θ, and the magnification, m. From this

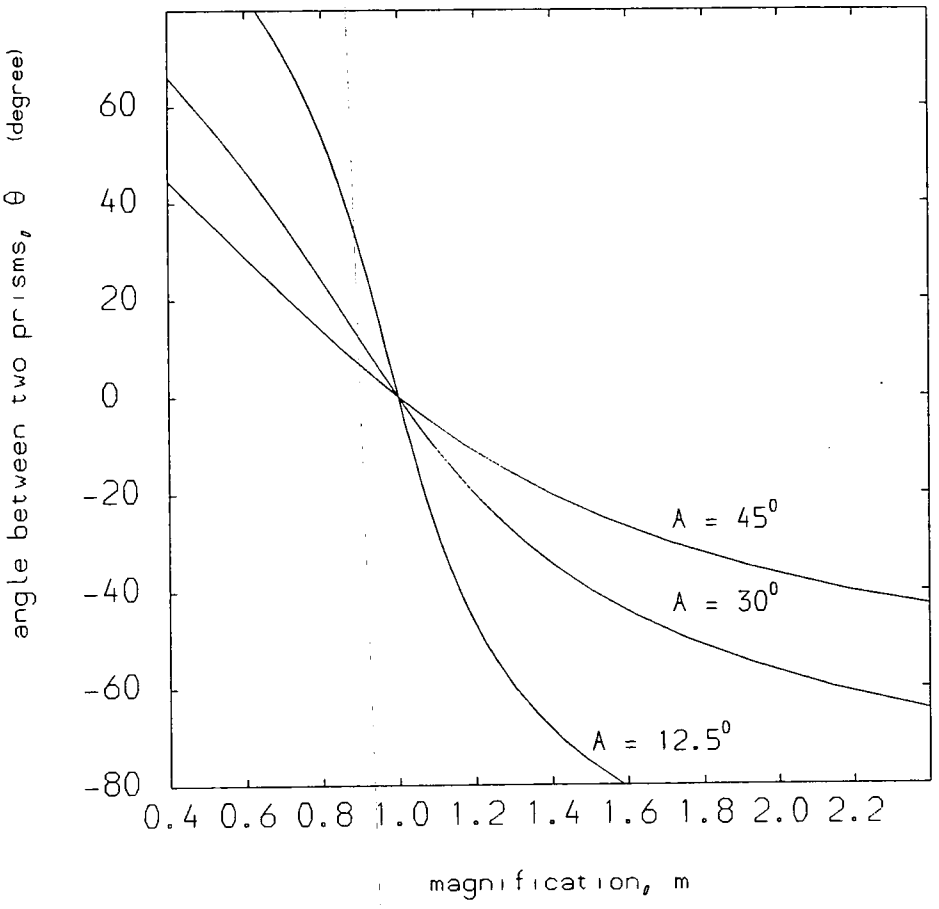


FIG 7.3 Variation of magnification with angle between two prisms

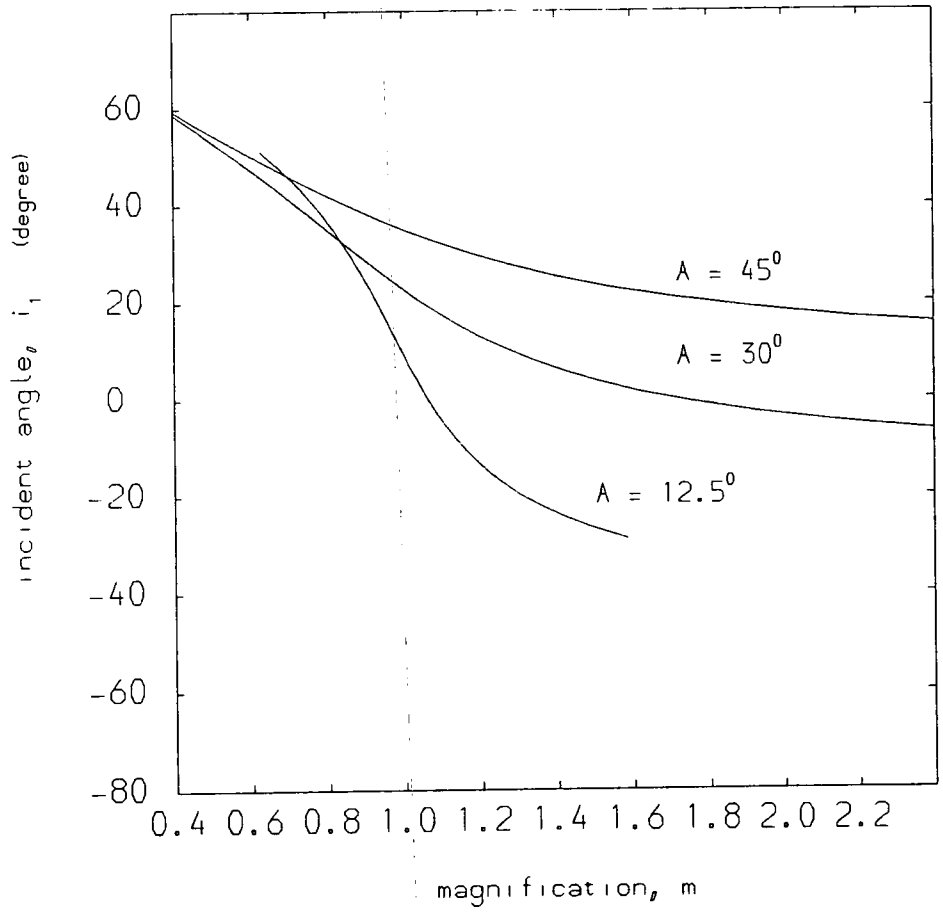


FIG 7.4 Variation of magnification with incident angle

figure, for an angle, A = 12.5°, the rate of change in magnification with Θ is small whilst for A = 45°, the change is large.

Once the angles, A and Θ, are arranged to give a required magnification, it is necessary to make the overall angular deviation of the central ray by the prism pair equal to zero. The beams emerging from the interferometer should be parallel. This is done by rotating the whole prism about the central axis which varies the incident angle, $i_1$. The relationship of equation 7.6 is shown in fig 7.4 by curves corresponding to three different prism apex angles, (A = 45°, 30° and 12.5°). For an angle, A = 45°, there is a large rate of change in magnification when the incident angle is varying, while for A = 12.5°, there is small rate of change. It is easier to rotate the prism pair with angle, A = 12.5°, since the movement of the image is correspondingly small.

### 7.3.3. Durham shear interferometer

The Durham shear interferometer consists of a Jamin interferometer, a pair of opposed prisms and a compensating glass plate. It is shown in photographic plate, no. 7.1 and in fig 7.5. The two Jamin glasses are enclosed in metal cases and each is fixed kinematically to a rectangular support at three points. This arrangement can be moved about two axes controlled by screws A and B for block B and screws F and G for block A. The screw A (or F) controls the alignment about the horizontal axis along the plane of the Jamin block while screw B (or G)

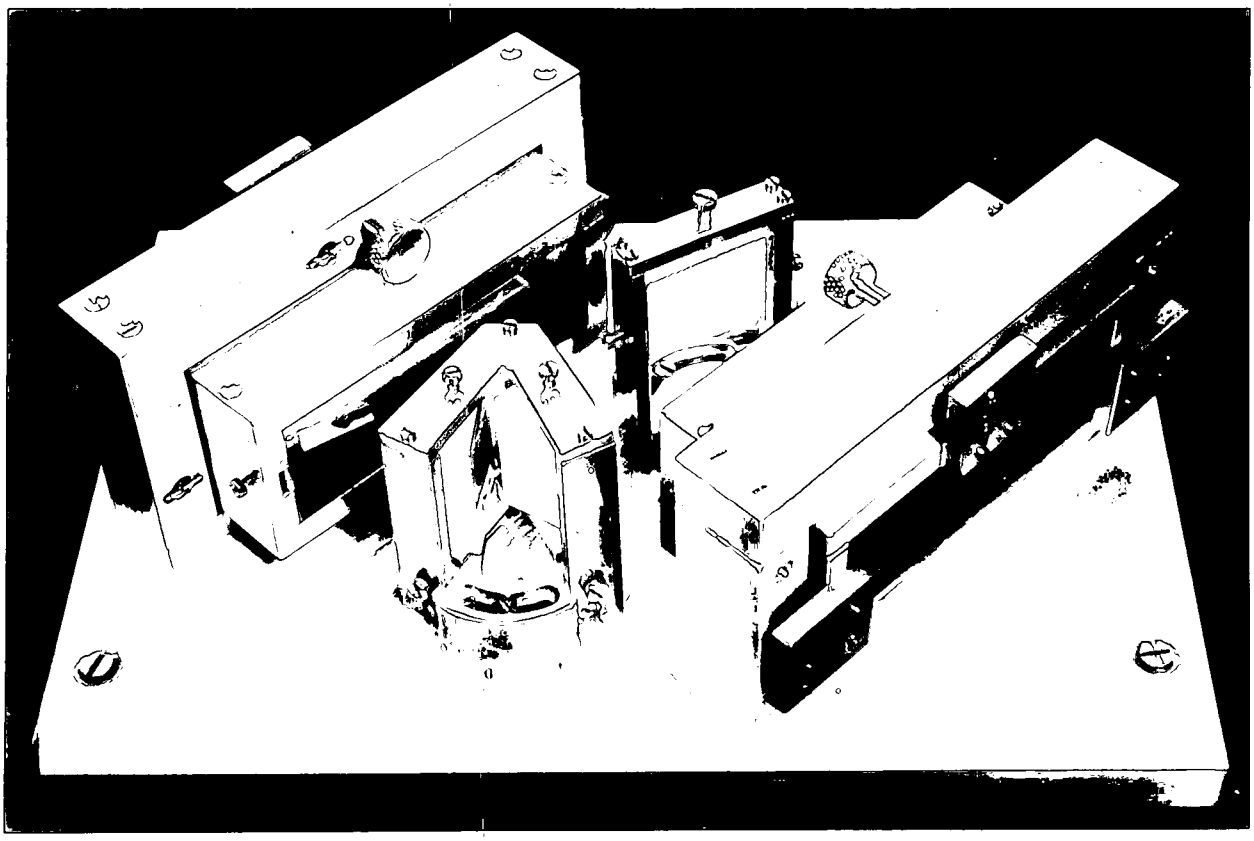

PLATE No. 7.1 Durham shear interferometer

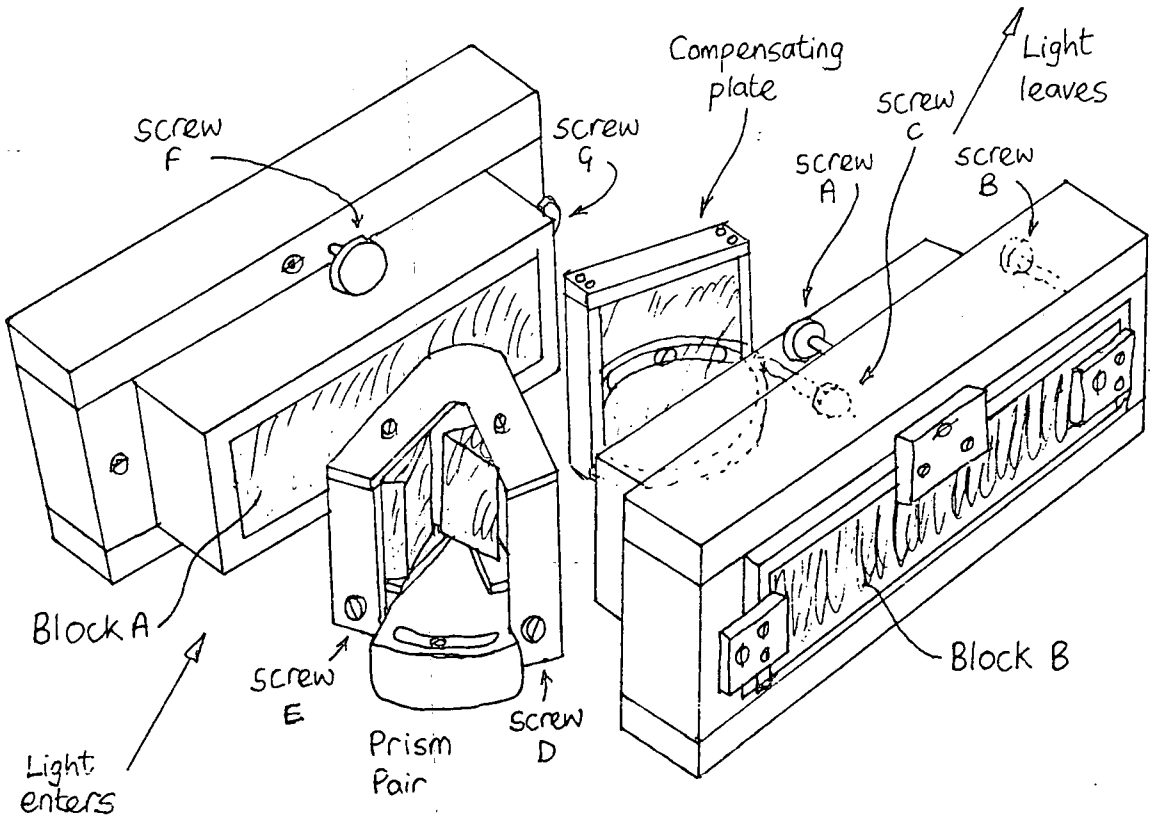


FIG 7.5 Durham shear interferometer

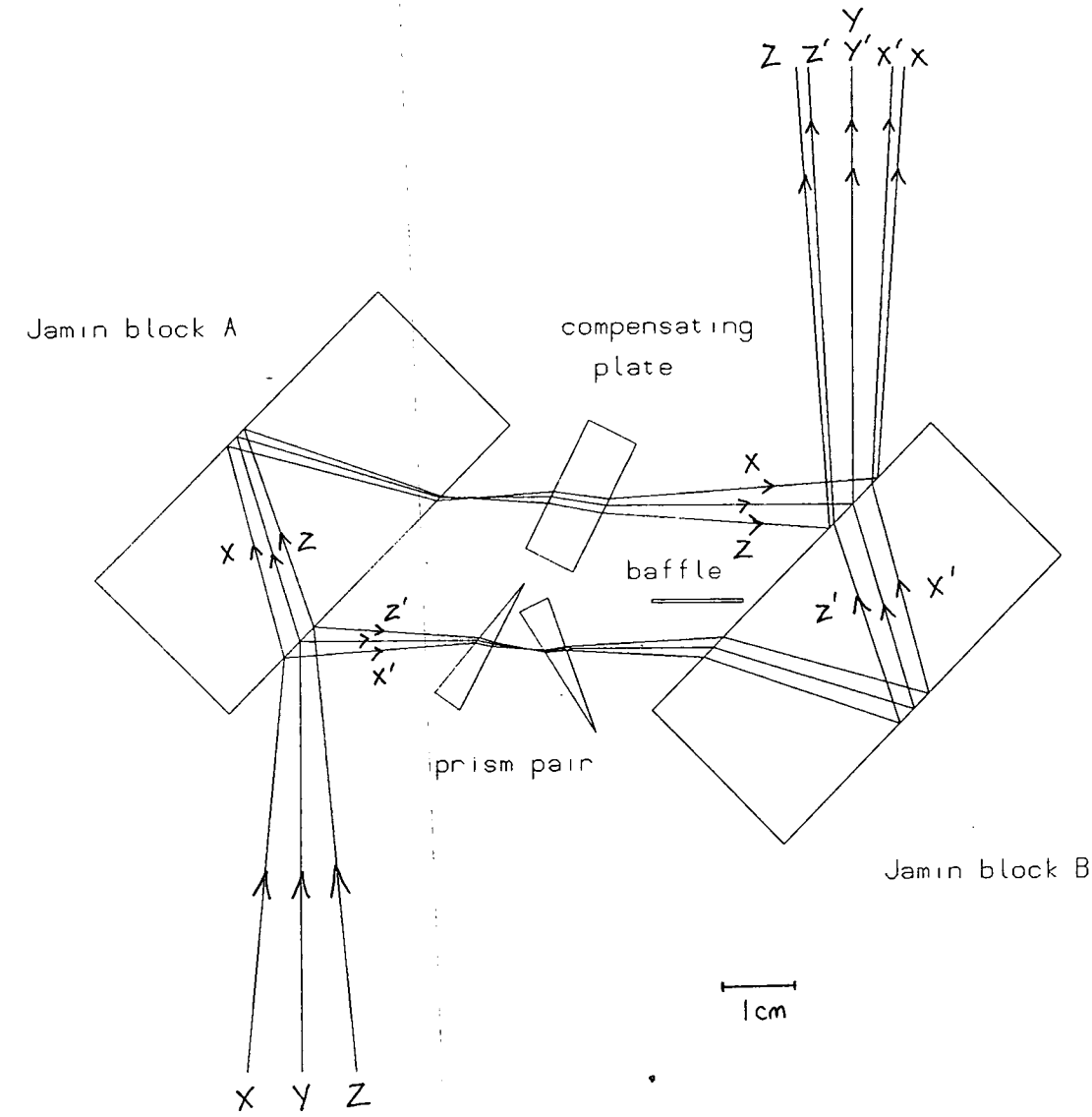


FIG 7.6 Durham shear interferometer

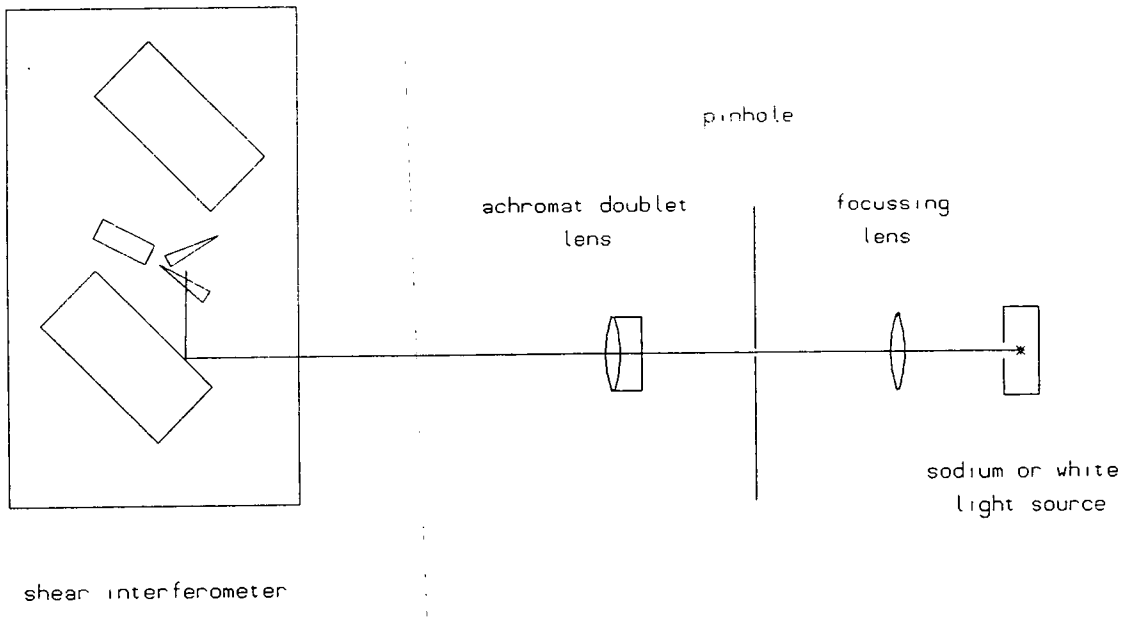


FIG 7.7 Set-up of experiment for testing Durham shear interferometer

controls the alignment about the vertical axis.

Each of the two prisms is fixed to a movable metal base with adhesive. The metal base can move forward or backwards using screws D and E to change the overall path length of the prism pair before being locked into a permanent position. They are encased with a rotating support so that the incident angle to the first prism can be varied by rotating the whole prism pair about the central vertical axis. The compensating glass plate is supported in a metal frame which is fixed to the rotating plate controlled by screw C, so that the displacement of the image and optical path length can be varied. The light paths through the device are shown in fig 7.6. None of the optical surfaces is coated so only about 10% of the initial light emerges in the interfering beams. A baffle removes the effect of other reflections. Optical coating could lead to a light efficiency of 25%.

Tests with various prism apex angles and orientations and with compensating plates of different thicknesses are needed to get an understanding of the principle of the shear interferometer since there is no published literature on the subject. The results of the tests will be given below and the principle of the shear interferometer will be explained in the next section.

### 7.3.4 Tests with the Durham shear interferometer

The shear interferometer, initially without the prism pair and compensating plate, is placed on the optical bench, which

also contains an achromatic doublet lens, a pinhole holder with various sizes of pinholes, a white light source (or a sodium source) with a focussing lens. This is shown in fig 7.7. With a sodium source and a pinhole of, say, 12.5 microns, fringes are seen immediately and made to be horizontal by adjusting the screws A and B (fig 7.5). They cover the whole of the field of view. The white light source with a bandpass filter (about 1000Å) then replaces the sodium source and the screws A and B are further adjusted to obtain fringes in the field of view. Because of the bandpass the visibility of the fringe extends only over 2 or 3 fields of view. The fringes are positioned so that those of maximum visibility are in the field of view. Then, when the filter is removed, white light fringes will be close by as seen in plate no. 7.2. The fringes are at infinity so that the size and position of the pinhole has no effect in visibility.

The prism pair and compensating plate are inserted. With the sodium source, the prism pair is adjusted until an oval field of view from the prism pair and a circular field from the compensating plate overlap in the centre. If the fringes are not found, then the screw D is needed to move the second prism forward or backwards to adjust the optical path length within the prism pair, or screw C can be used again to rotate the compensating plate to change the path length, until the fringes are found. The fringes are made to be horizontal by adjusting screws A and B. The white light source is then used and similar adjustments as before are made to obtain white light fringes;

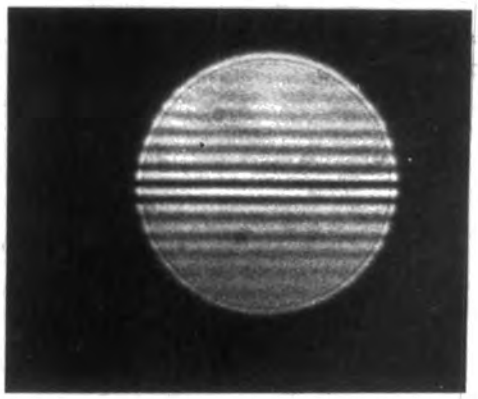

PLATE No. 7.2 Jamin interferogram

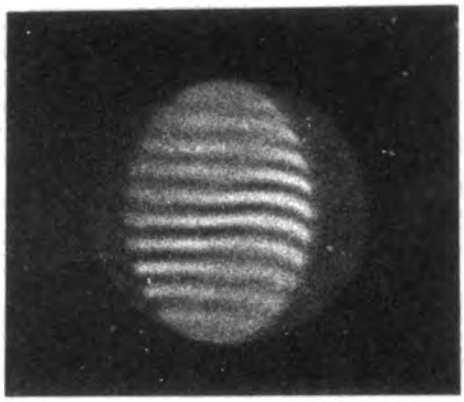

PLATE No. 7.3 5μm hole at normal position

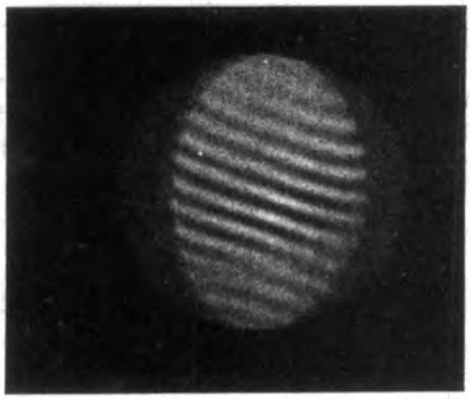

PLATE No. 7.4 5μm hole at 40 um lateral movement

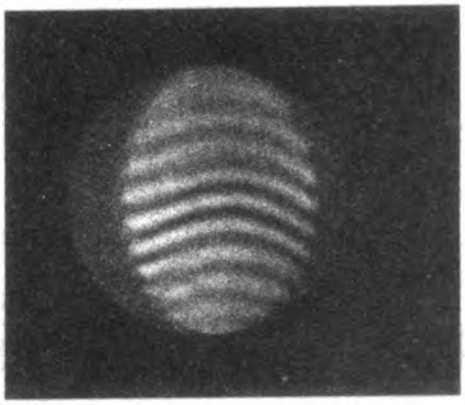

PLATE No. 7.5 5μm hole at 1mm longitudinal movement

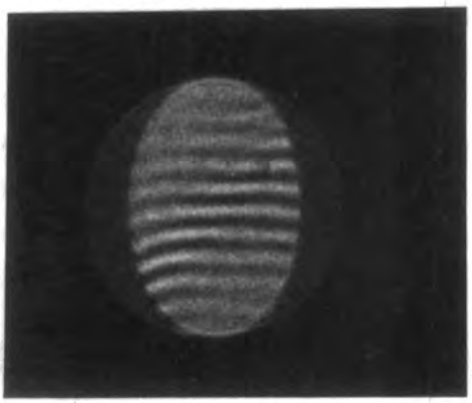

PLATE No. 7.6 12.5μm hole at normal position

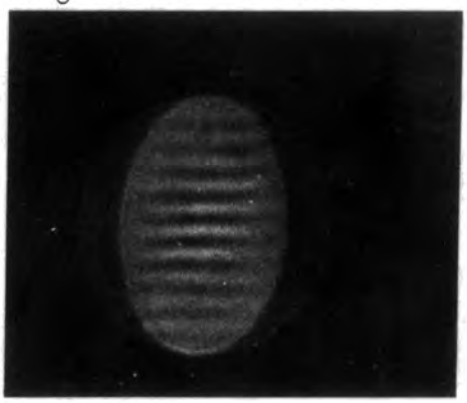

PLATE No. 7.7 25μm hole at normal position

PLATE No. 7.8 50μm hole at normal position

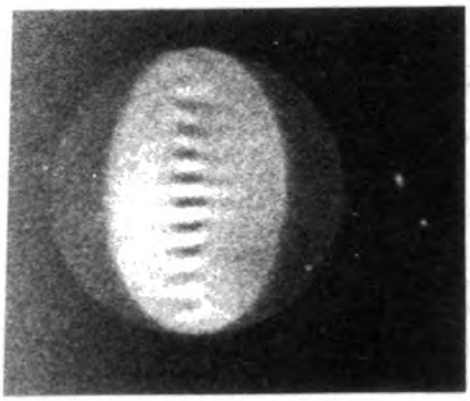

PLATE No. 7.9 100μm hole at normal position

that is when the optical path length of the prism pair is equal to that of the compensating plate. The white light fringe patterns are shown in plates nos. 7.3 to 7.9 for prism angles $A = 30^{\circ}$, $\Theta = 40^{\circ}$.

With two different prism apex angles, $30^{\circ}$ and $12.5^{\circ}$ and three different thickness of compensating plate, ie 12.5mm, 7mm, 1mm, the results of the movements of the pinhole in three dimensions are found to be follows:

i) Lateral shift of the pinhole source - this has a major effect on the fringe pattern as it causes the fringes to incline as shown in plate no. 7.4. Here the pinhole, with a size of 5 microns, has been displaced by 40 microns compared to the normal position (plate no. 7.3). When the pinhole is displaced in the other direction, then the fringes incline in the other direction.

ii) Longitudinal movement of the pinhole source - this has a minor effect on the fringe pattern and causes the fringes to curve, as shown in plate no. 7.5. Here the pinhole is displaced longitudinally by 1mm from a normal position. When the pinhole is displaced in the other direction, the fringes curve in the reverse direction.

iii) Vertical shift of the pinhole source - this has no effect on the fringe pattern as there is no sheared effect along the vertical lines of the image.

iv) Different sizes of pinhole - these have a major effect on the fringe pattern as source size causes the fringes to lose their visibility at the edges, as shown in plates nos. 7.6 to

7.9 when the pinhole is increasing in size from 12.5 to 100 microns. This can be understood in terms of the lateral shift as mentioned above. For example a pinhole 50 microns in size can be thought of as a succession of pinholes, 5 microns in size, all side by side. The outermost 5 micron holes are then displaced $\pm$ 25 microns from the central hole. Consequently, there will be horizontal fringes from the central part of the 50 microns hole and inclined fringes from the outermost parts of the pinhole. Intermediate parts will give fringes of reduced inclination. When all the fringe patterns are added together the inclined fringes demodulate the outer parts of the resulting pattern giving rise to fringes which are reduced in extent (plate no. 7.8). The fringe patterns in plate nos. 7.3 and 7.6 to 7.9 have been measured with a microdensitometer and their MTFs have been found and are given in section 7.3.7.

The results of the all the above tests are summarised in Table 7.1. It can be seen that it is better to use a prism pair with an apex angle of $12.5^{\circ}$ to reduce the sensitivity of the fringe pattern to source motions. However with $12.5^{\circ}$ angles the magnification is nearer to unity.

Because of dispersion, the zero order of the fringe patterns corresponding to different wavelengths may not coincide at the centre. Then the overall fringe pattern (white light) has reduced visibility. The screws B and C are needed to bring all the zero order fringe patterns of each wavelength to coincide at the centre (with some checks using filters). This gives better modulated fringes with two well defined black

| | magnif-ication m | incident angle $i_1$ | angle of inclined fringes per 10μm movement | longitudual maximum tolerance (1) (mm) | maximum size of pinhole (2) (μm) |
|---|---|---|---|---|---|
| A = 30°<br>Θ = 60° | 0.5 | 54° | 15° | 0.25 | 25 |
| A = 30°<br>Θ = 40° | 0.667 | 43° | 3.5° | 1.0 | 50 |
| A = 12.5°<br>Θ = 60° | 0.75 | 39° | 1° | 3.0 | 100 |

TABLE 7.1 The results of the effects on the fringe patterns

Notes:

(1) - The longitudual tolerance is a subjective estimate of how far the source can be moved longitudually before the curved fringes become unusable.

(2) - Maximum size of pinhole giving usable fringes ie fringes extending to 2/3 the maximum width of pattern.

fringes at either side of the single bright zero order fringe.

The image from the prism pair is astigmatic. If crossed hairlines are put behind the re-imaging lens then in the circular field, both lines are in focus. For the oval beam, the horizontal hairline is also in focus but the vertical line has a virtual image about 2m distance upstream. This is due to the demagnification of the wavefront curvature of the image which causes the focal point to change with shear distance. So the overlap image will show a sharp border at the top and bottom of the oval field, but a blurred border on either side of the oval field, as seen in plate no. 7.9.

The problem of chromatic aberration is considered later.

### 7.3.5 Diagrammatic understanding of fringe patterns

In the Jamin interferometer (fig 7.8), the amplitude of a wavefront in a converging beam from a light soure is divided into two beams at a point, P, on the surface of the first Jamin block. These beams converge to separate image points at A and B. From these points, the diverging beams are refracted (reflected) and recombined at Q situated on the surface of the second Jamin block. The apparent images will appear to be coincident at $A'B'$ if there is no wedge angle between the blocks.

When a slight wedge angle between the two blocks is introduced by tilting the second block out of the plane then there is no difference between the beams until the surface of the second block is reached. With reference to fig 7.8, the normal to the surface at Q is tilted out of the surface and so

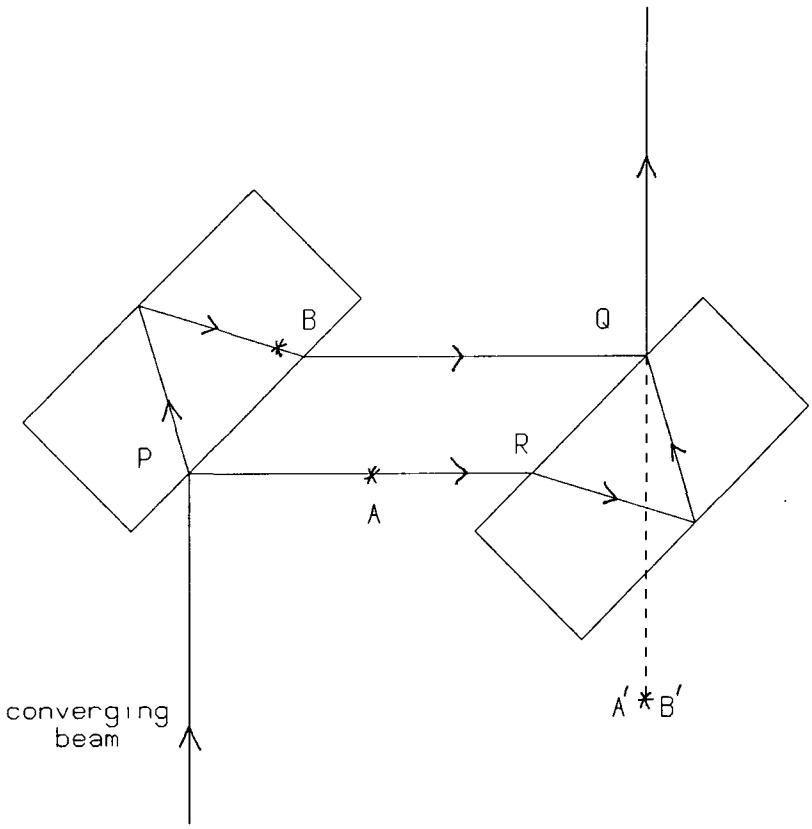


FIG 7.8 Jamin interferometer

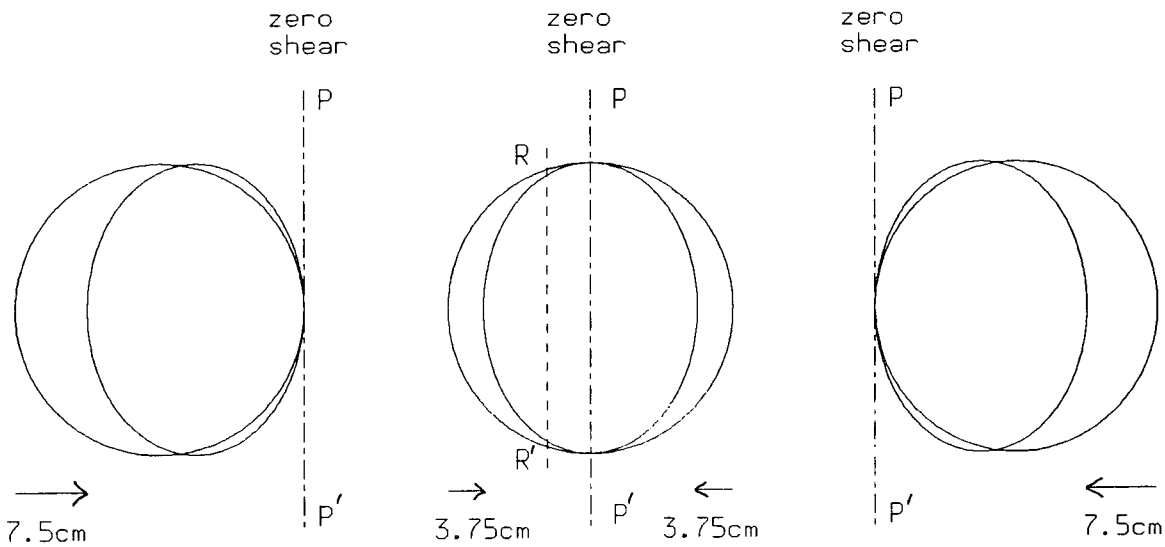


a) b) c)

FIG 7.9 Interferograms with different positions of zero shear line

the reflected beam at Q moves out of the paper and its apparent source, $B'$, is below the paper. At the point, R, the refracted beam will move down below the plane of the paper and its reflection at the back surface will continue to move downwards and arrive just below Q. On projection its apparent source, $A'$, will appear to be above $B'$. The in-phase apparent sources $A'$ and $B'$ will give rise to Young's fringes and several horizontal fringes are then obtained with white light.

If the converging beam from a point source is moved to the left (or right), so that the point of incidence P moves along the surface of the Jamin glass, then A and B move which will cause the apparent images $A'$ and $B'$ to move also to the left (or right) by the same amount and so the fringes are not affected. Hence the finite size of the source has no effect on the fringes when it is focussed at infinity.

When the prism pair and compensating plate are introduced and adjusted, the apparent images $A'$ and $B'$ are unaffected and fringes are produced as before. When the converging beam from a point source is moved to the left or right, it will cause the $B'$ image to move to the left or right as before since the compensating plate has no differential effect. However, as the image moves between the prism pair, the length of the air path between the prisms changes. Hence the displacement of light on exit from the prisms is less than in the compensating plate and this will cause the $A'$ image to move to the left or right by a smaller amount than the $B'$ image and so inclined fringes are seen.

This gives the clue to the operation of the system. To reduce the limitations from the inclination of fringes just mentioned then the seeing disc is imaged between the prisms. However when the system is adjusted so that the centre of the seeing disc gives horizontal fringes, then points taken progressively further away from the centre will lead to more inclined fringes as described earlier. As the time-averaged seeing disc is formed by speckles over about one arcsec, then fringes due to each speckle in turn can be considered.

Seeing typically alters phase rather than amplitude and so a wavefront of constant phase has fixed amplitude but is corrugated. Without the prism pair and compensating plate, the recombined wavefronts interfere due to path differences introduced by the wedge angle and the white light fringes would be the same as without seeing.

However, when the wavefront is sheared by the prism pair, the differences in phase due to its variation by seeing across the wavefront will introduce further path differences. On the short time scale involved, this will distort the fringe pattern except along the zero shear line, PP′, (fig 7.9b) where the phases match. With a longer time scale the fringes move up and down leading to increasing broadening further from the zero shear line, PP′. Measuring along RR′ gives the modulation transfer function with shear, s, or with spatial frequency, w, where $w = s/\lambda$. The zero shear line can be moved across the aperture image by rotating the whole prism pair unit about an axis normal to the plane of the optical diagram. When an outer

get an average central of the amplitude, d. Then the atmospheric MTF can be found as (fig 7.12),

$$MTF(s) = 10^{(c(s) - c(0))/\gamma d}, \qquad (7.11)$$

where c(0) is the height from the average at the zero shear and c(s) is the height at the shear, s. This method needs only two scans and is quicker than the first method described.

The MTF for the atmosphere can be determined in terms of spatial frequency by dividing the shear values by the averaged wavelength (say 0.5μm) and the value of 206300 (eq 2.17), ie

$$\text{spatial frequency, } w = s/206300\lambda , \qquad (7.12)$$

since the zero orders of all wavelengths coincide at the central bright fringe.

### 7.3.7 Results of optical bench tests

In the experiment, the seeing disc is simulated by illuminating pinholes of various sizes (from 5 to 100 microns) and imaging these between the prisms of the shear interferometer. The fringe patterns are shown in plates nos. 7.3 and 7.6 to 7.9 for prism angle, $A = 30^{\circ}$. These interferograms are inspected visually and scanned using a Joyce-Loebl microdensitometer with a $40x100\mu m^2$ beam. The interferogram has a scale of approximately 1/100 (ie 1mm on the interferogram = 10cm in the telescope aperture). Density MTF curves are shown in fig 7.13 for pinhole sizes ranging from 5 to 100μm. These correspond approximately to seeing conditions ranging from $r_o \sim$ 20cm to $r_o \sim$ 2cm. Clearly the interferometer is matched to the range of seeing on La Palma. Changing to the

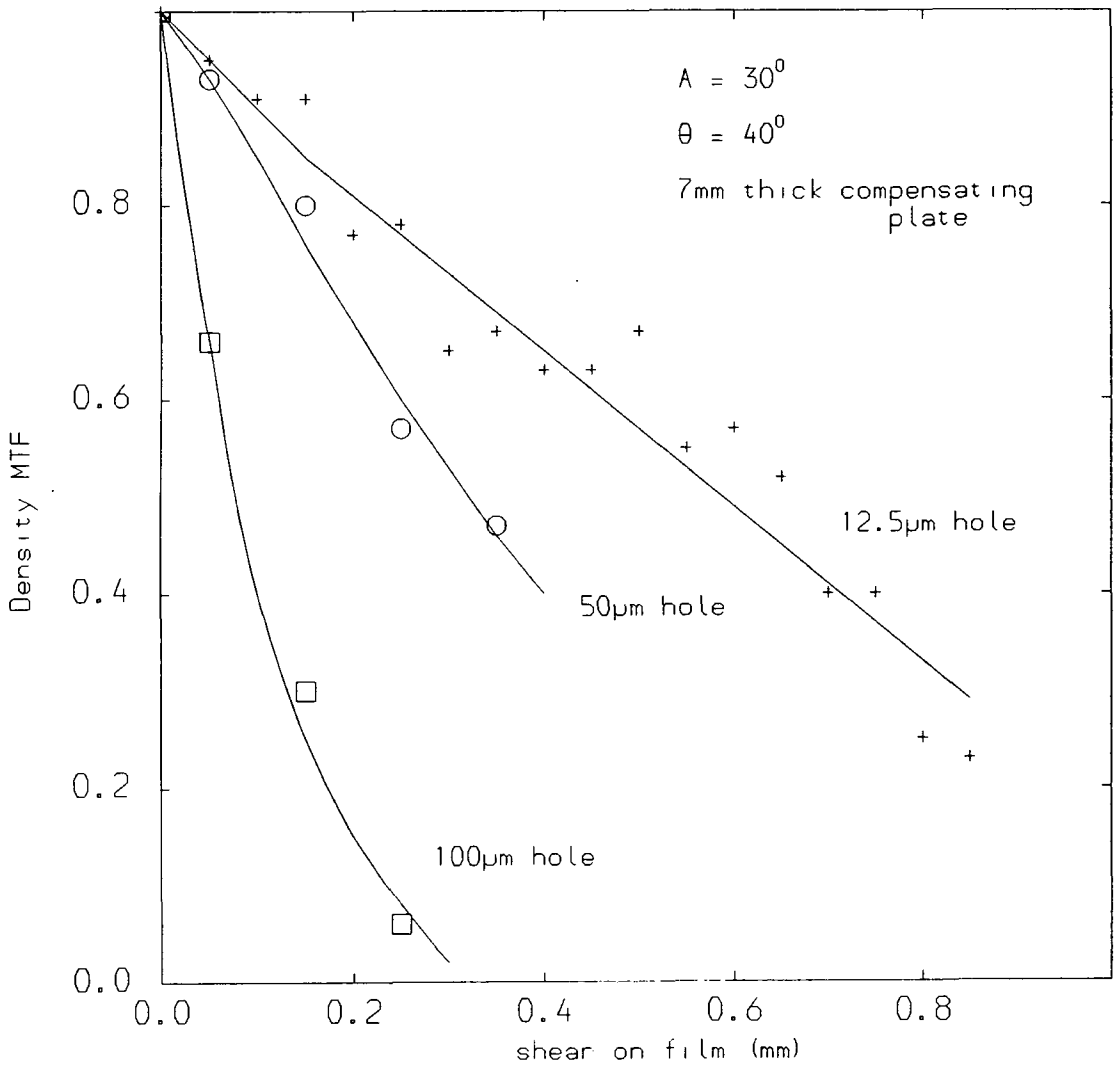


FIG 7.13 Density MTF curves for several sizes of pinhole

prism angle of 12.5° in the final version of the interferometer will not change this conclusion.

## 7.4 OVERALL DESIGN OF THE DURHAM POLARIS MONITOR

### 7.4.1 General optical design

The light from Polaris is collected by an F/6 30cm mirror and directed onto the 45° ellipical plane mirror (see fig 7.14) which reflects the light beam to an external primary focal point just below another 45° elliptical plane mirror, where it is then reflected towards a re-imaging lens. This lens focusses a second image of Polaris between the prism pair. The lens is controlled in the x- and y-directions with two screws so that the fringe pattern can be adjusted properly and made to appear horizontal and straight. The movable plane mirror is placed outside the re-imaging lens (see fig 7.14 and plate no. 7.13). When this plane mirror is in an up position, the light will pass through to the shear interferometer. When it is down, it causes the image of Polaris to reflect and form at the ocular eyepiece which has a cross hairline and a movable hairline controlled by a micrometer screw. The purpose of this plane mirror is to help with the alignment of the telescope with Polaris.

The camera with an automatic winder is fixed at the back of the shear interferometer (as shown in plate no. 7.13) to photograph the interferogram. The shutter is opened by a miniature solenoid which is controlled by an automatic switch box at the right of the camera. This is powered by a 12 volts

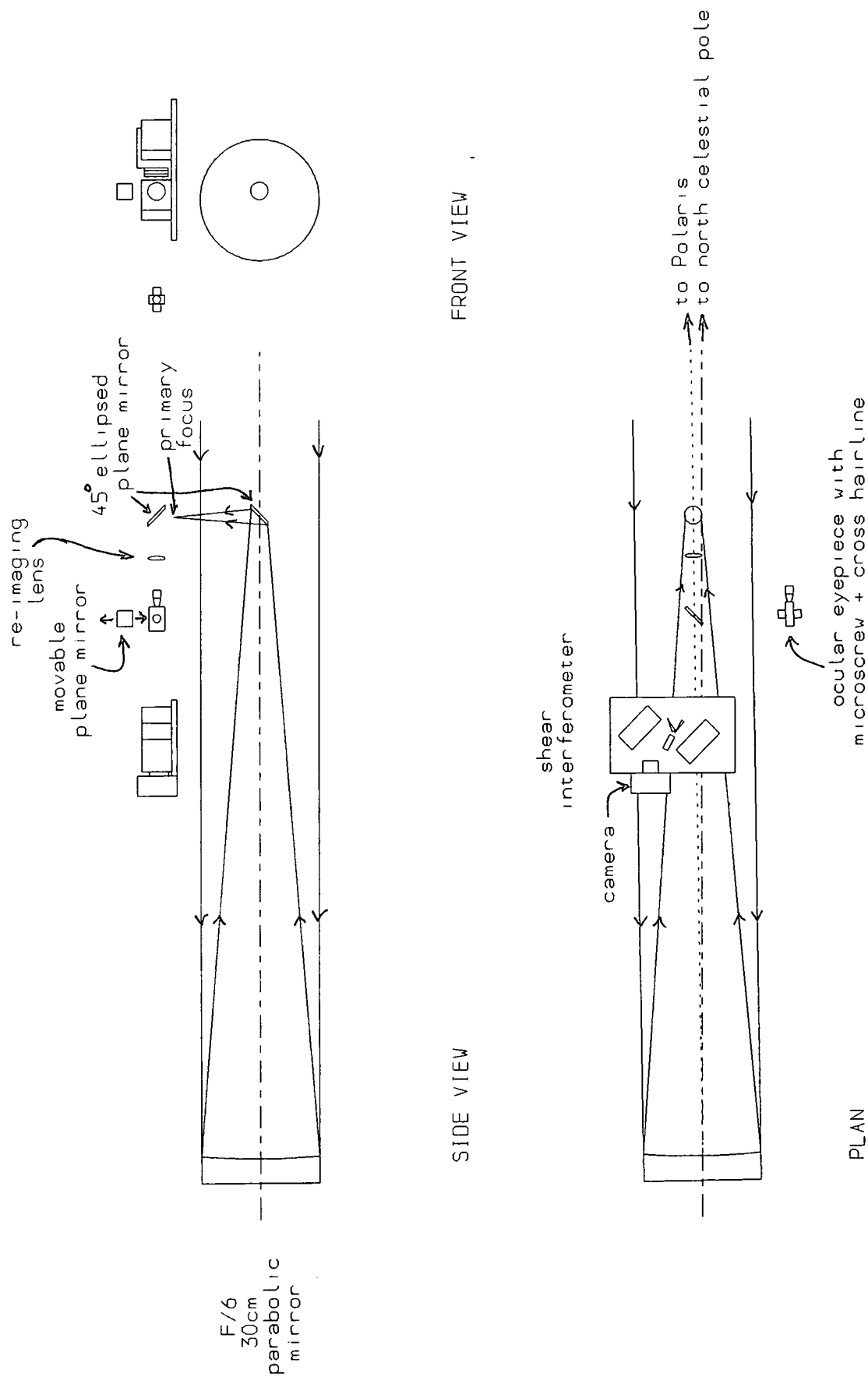


FIG 7.14 Durham Polaris monitor

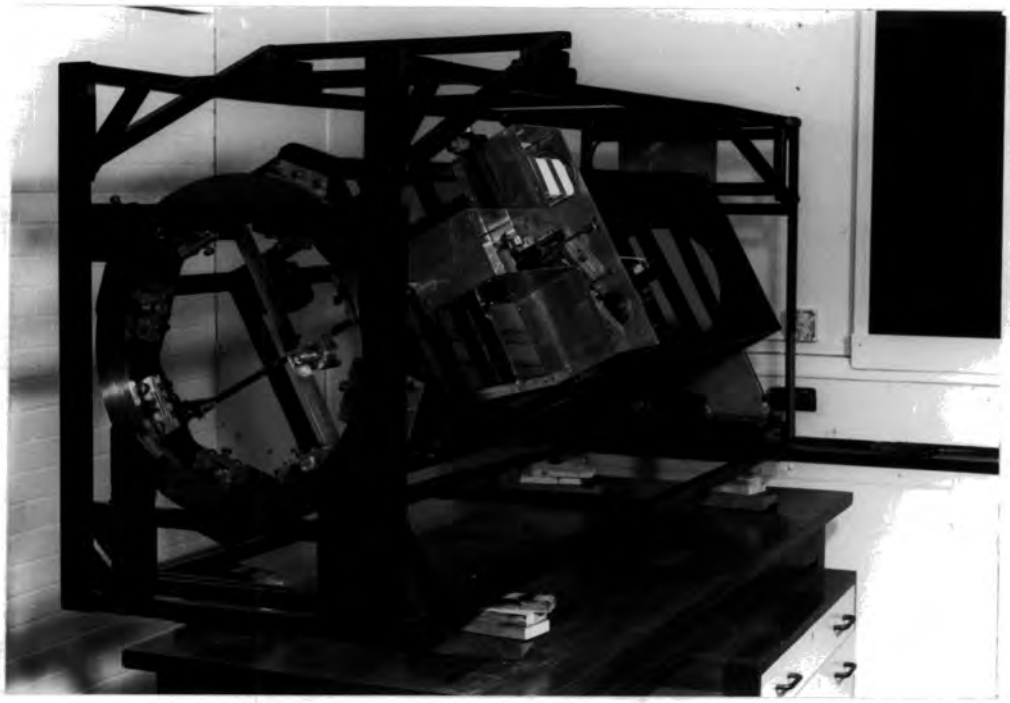

PLATE No. 7.12 Durham Polaris monitor

PLATE No. 7.13 Close up of Durham Polaris monitor showing shear interferometer

rechargeable battery inside the box. The sequential switch can be adjusted so that a two or four minutes exposure every 30 minutes can be taken.

7.4.2 Mechanical design

In order to get adequate illumination for an exposure it is necessary that the telescope should track Polaris for 2 to 4 minutes. Instead of a conventional telescope mounting, the telescope framework is rotated about its mechanical axis, which is pointed at the north celestial pole. The 30cm parabolic mirror is placed so that its optical axis is offset by an angle of 48 arcminutes to the celestial axis checked using a laser. Provided that the hour angle of the telescope is correct, then Polaris will lie on the optical axis. This means that the monitor will track Polaris around the north celestial pole and the image will form at the same position in the shear interferometer. Further, on the optical axis, coma and astigmatism in the image are zero. If the angle between the optical axis and Polaris reaches 1′ then the coma becomes the order of the size of the seeing disc. The telescope framework is rotated on eight stud rollers attached on the inside of a stainless steel ring which is fixed at the front. At the back there is a roller bearing to hold a shaft which is fixed to the telescope framework and is driven by a motor via a worm and wheel gear. The motor is powered by a 12 volts rechargeable battery (plate no 7.14).

Seeing for La Palma is usually quoted at about 1 arcsec.

PLATE NO.7.14 Back view of Durham Polaris monitor

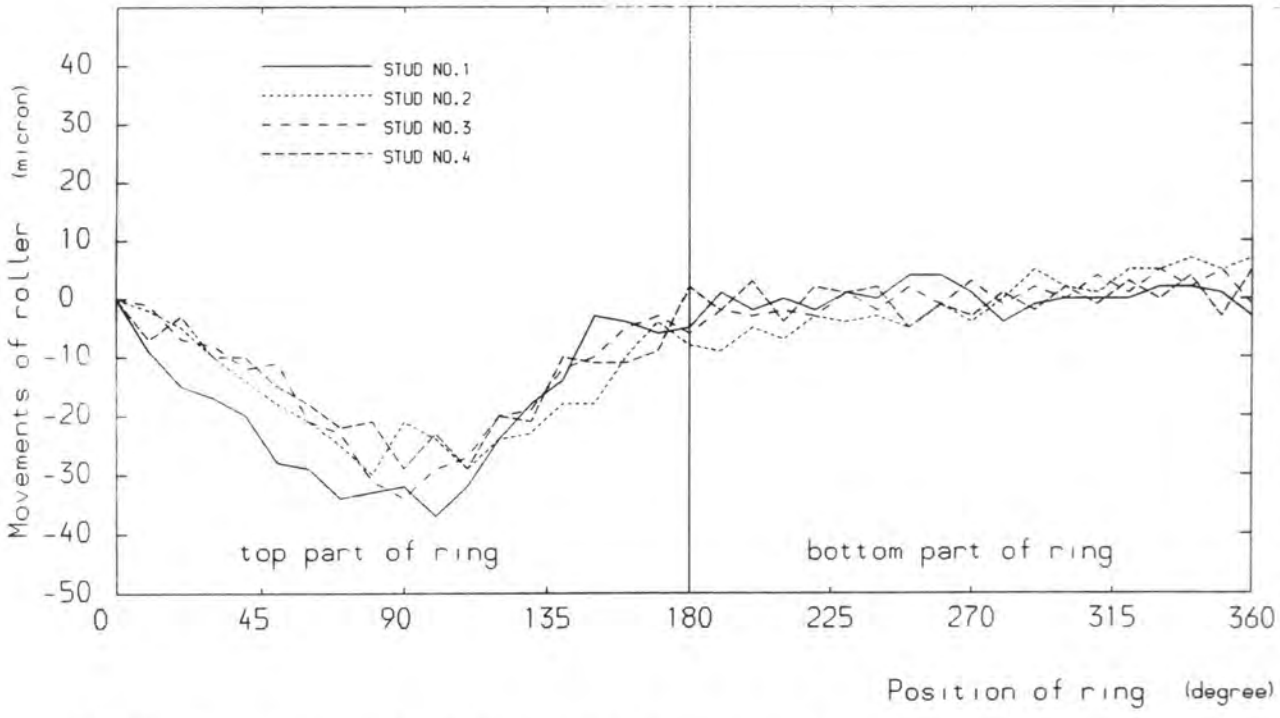


FIG 7.15 Movements of four different stud rollers

However there will be a sec $\Theta$ effect due to the zenith angle so the image will be about 1.6 arcsec as measured from Polaris. Hence it is required that the RMS of the movement of the telescope perpendicular to the mechanical axis as it rotates should be much less than 20 microns (which corresponds to 2 arcsec).

a) Telescope rotational motion

The RMS motion of the telescope rotation has been tested both mechanically and optically.

i) Mechanical test

A dial gauge, which can be read to 2 microns, was fastened to the telescope framework, so that its plunger rested on one of the stud rollers. The relative movement of four different studs at $0^{\circ}$, $90^{\circ}$, $180^{\circ}$ and $270^{\circ}$ along the frame were measured in turn for every $10^{\circ}$ of rotation. The results are shown in fig 7.15. Between $0^{\circ}$ and $180^{\circ}$, ie the top part of the ring, there was a large movement of between 0 and 40 microns. This is not important because the top part of the ring carries no weight of the telescope framework and the stud rollers are probably relaxing. There was a small movement of between $\pm$10 microns at the bottom part of the ring, ie between $180^{\circ}$ and $360^{\circ}$. This is where the most of the telescope framework weight is supported. The RMS (long term) of the movement of the stud relative to the rim of the ring for the bottom part was 7.2$\pm$2.0 microns based on measurements made for every $10^{\circ}$ of rotation. For the RMS (short term), the measurements were taken at intervals of half minute for 10 minutes with the telescope framework rotating under

power. The RMS (10 minutes) variation of the stud was 1.5 microns. Referring to Table 7.1, within a two minutes exposure the inclination of fringes will be negligible; over long term viewing the change in inclination is less than 1°.

ii) Optical test

The previous measurements were concerned with individual stud rollers. However the motion of the mechanical axis is a result of the concerted movements of all the rollers and it may show up as a 'wobble' on the optical axis. Consequently an optical test was devised. A plane mirror replaced the paraboloid and was aligned at the back of telescope so that on rotation there was no visible movement of an image, produced by a narrow beam laser, on the lens (see fig 7.16) which was temporarily covered with paper. This lens is clamped on the front of the telescope framework. Then a pinhole, 5 microns diameter, was placed in front of the laser. As the telescope was rotated about its mechanical axis, carrying a plane mirror and focussing lens, then a focussed track of the 5 microns source was mapped out on the photographic plate. The telescope was driven by its motor. The trail on the photographic plate was about 45 microns in width. The edge of the trail was used as the path of the image and a scatter measurement of this trail was made using a microscope. This gave an RMS (long term) value of 4.3 microns after correcting for grain noise. This measurement is likely to be an overestimate because of uncertainties in defining the trail edge.

If the short term and long term RMS motion of individual

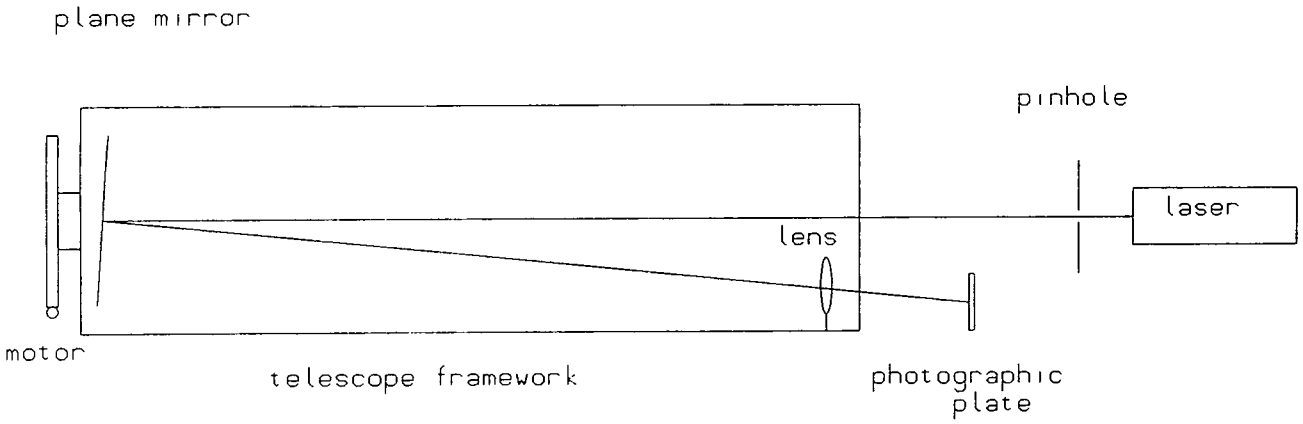


FIG 7.16 Set-up of experiment for testing the alignment of the rotating telescope

stud rollers scale to the RMS motion of the mechanical axis in the same way, then the short term RMS motion of the optical axis will be less than 1 micron. This noise will contribute an RMS noise of about 0.05 arcsec to the seeing disc and is completely negligible.

## 7.5 LOCAL GROUND LEVEL TESTING

Testing of the monitor is essential. There are two questions to be answered:-

a) are the light levels sufficiently high to be able to obtain exposures in a reasonable time?

b) is the tracking of Polaris by the monitor sufficiently accurate that there is a negligible rotation of the fringes during an exposure?

Both of these questions can be answered by examining the seeing which is local to Durham. The quality of seeing is not important in these tests. However, since it will be poor then fringes limited in extent can be expected in the interferograms.

### 7.5.1 Exposure times

The estimate of exposure time necessary for the Durham Polaris monitor can be found by scaling from Brown and Scaddan's experiment. Although the 74-inch telescope of the Helwan Observatory at Kottamia was used, the shear interferometer only sampled a $(5x75)cm^2$ rectangular aperture. The interferogram was recorded at a reduction of 180:1 at an exposure time of 2 minutes on Pan F emulsion (ASA 50) using Vega ($0.04^m$) as the

source star.

The Durham monitor is based on a 30cm mirror which collapses the interferogram of Polaris ($2.1^m$) to a 3mm image on 400 ASA film. The reduction is 100:1. Scaling from the Kottamia telescope to the monitor, then similar levels of light intensity in the image will be obtained in under 3 minutes of exposure.

7.5.2. Experimental results

The Durham Polaris monitor rests on a standing frame so that it faces the north celestial pole from one of the laboratory rooms. The internal siting of the instrument is very convenient at this early stage of adjustment as power and other facilities are readily available. The telescope alignment is adjusted so that the mechanical axis is parallel to the north celestial pole. When they are not parallel, there are four values to adjust, ie the two angles, f and g (at right angles to each other) between the mechanical axis and north celestial pole, the hour angle of the telescope, h, and the angular offset of the parabolic mirror, d. When these values are properly adjusted then Polaris will stay in position when looking through the eyepiece. If the hour angle or offset of the mirror is changed, Polaris does not appear to move as the telescope rotates but is simply displaced from its normal position to another fixed position in the eyepiece. This is not very important unless the displacement is large when coma of the image will appear. But if the mechanical axis does not coincide

with the celestial pole, then it will cause the image of Polaris to move along a circular path in the eyepiece as the telescope rotates; the radius of the circle being $(f^2+g^2)^{1/2}$. It can be reduced by the following procedure:- the displacement of the image of Polaris in the eyepiece is measured using crossed hairlines of an ocular eyepiece with a micrometer screw every 10 minutes for half or one hour. Then the telescope is moved up or down to adjust g and the measurements of the movement are repeated. If the total displacement is less than before, the telescope continues to be moved down until a minimum displacement is obtained. Then the procedure is repeated for the sideways movement, f, and this cycle continued until a position of no apparent movement of Polaris is reached. Then the telescope is ready to use. (For more expla nation of these movements and theory see Appendix F).

Initially there is some general adjustment of the optical parts so that when an image of Polaris is sharp in the ocular eyepiece, then straight fringes are seen through the interferometer. All the controls in the shear interferometer are then locked in position. The telescope alignment is adjusted so that Polaris is at the centre of the field of view in the eyepiece. The movable plane mirror is placed at the up position. Then images of the overlapping circular and oval field of view can be seen through a small telescope which replaces the camera. The fringes are difficult to see as there is only a very low light level from Polaris and the edges of the fringes move rapidly because of seeing. However with the light

adapted eye there is sufficient light to be able to judge (and to adjust) how horizontal the fringes are. If the fringes are not horizontal, then the re-imaging lens is adjusted sideways (as described in section 7.3.4). The small telescope is replaced by an automatic camera and interferograms of Polaris are taken. By experimenting it is found that HP5 (ASA400) film requires 2 minutes exposure.

The image of Polaris, when seen through the eyepiece, appears to be dancing about and changing in size. Sometimes these effects are much smaller when the seeing conditions are better such as when there is a smaller temperature difference between the inside and the outside of the laboratory in which the monitor is placed.

Several interferograms of various seeing conditions have been taken. A typical interferogram is shown in plate no. 7.15. This plate contains short fringes due to the local ground level seeing. The measurements of the MTF from the fringes in the interferogram are given in the next section.

### 7.5.3 Densitometer measurements

The interferogram, as shown in plate no. 7.15, of the local ground level seeing has been scanned along the fringes using a Joyce-Loebl microdensitometer. The results of the scanning are shown in fig 7.17 and the MTF curve of the interferogram is shown in fig 7.18. The value of $r_o$ can be found by fitting a curve of equation 7.1 to this curve, or from the shear value where MTF is effectively zero. The value of $r_o$ for

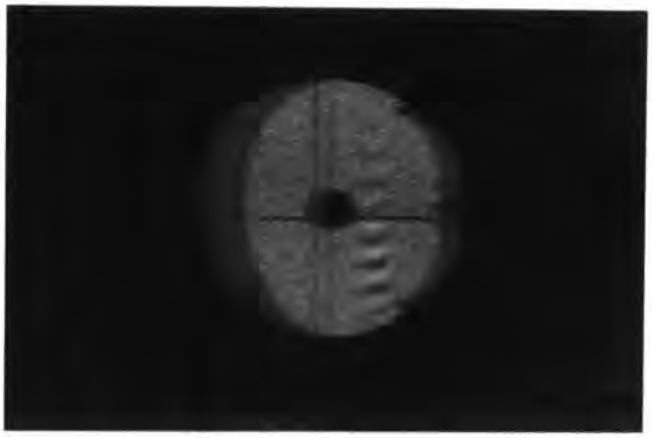

PLATE No 7.15 Interferogram of local ground level seeing

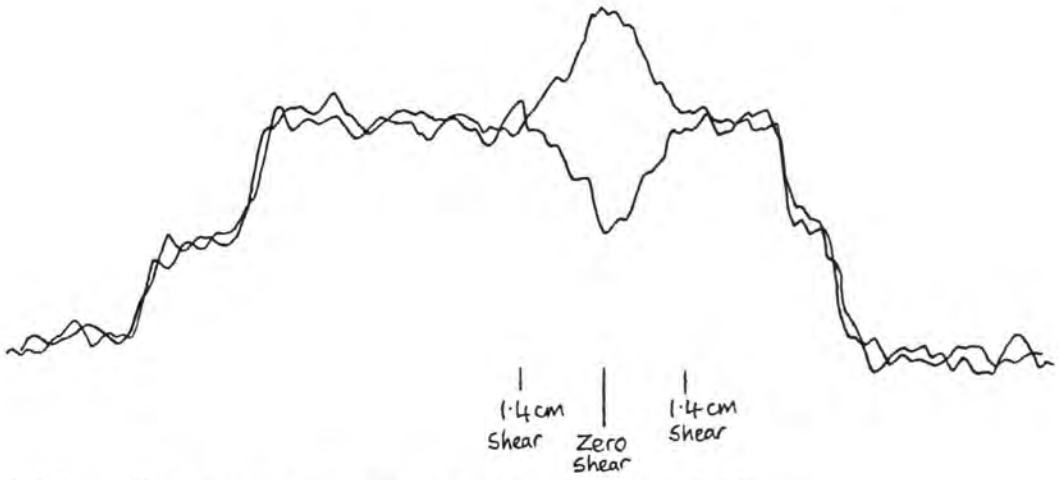


FIG 7.17 Densitometer scan traces of plate 7.15

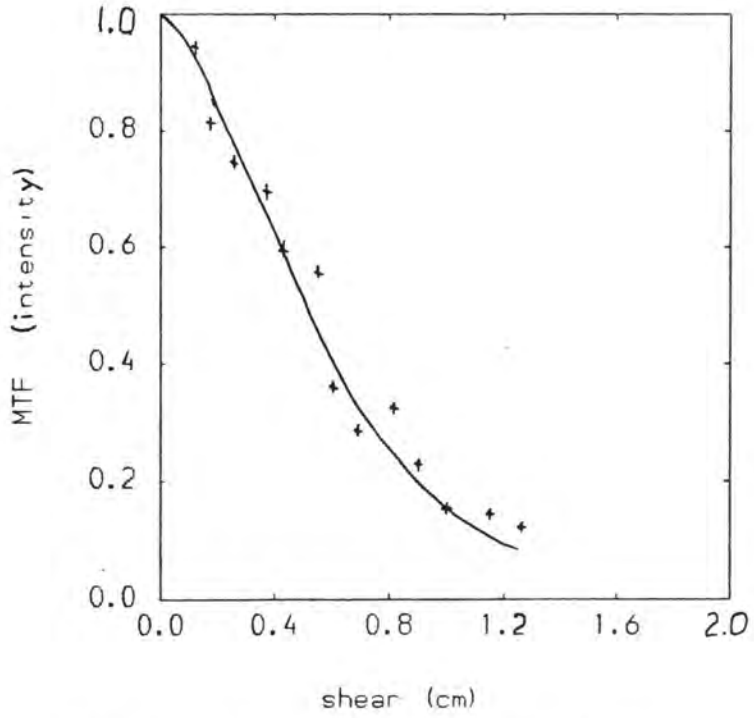


FIG 7.18 MTF curve of local seeing (plate 7.15)

plate no. 7.15 is found to be equal to 1.4cm. Several other interferograms have been measured. Values of $r_o$ were found in the range 0.5 to 2.0cm.

These measurements conclude the testing of the monitor. Soon it will be transported to La Palma where it will be used to gather statistical information on seeing.

## 7.6 FUTURE IMPROVEMENTS

It is envisaged that in the future the photographic film in the seeing monitor would be replaced by a CCD device or an image intensifer and a TV scanning device running automatically. The fringes would then be scanned with automatic read-out recorded onto magnetic disc, using a microprocessor. This would lead to automatic recording and data-reduction, and real time determinations of the quality of seeing. Exposure times would be reduced since photographic film is inefficient (about 1% efficient) whereas CCD devices are about 70-80% efficient. There is a possibility that the required time for a short exposure could be reached.

The Jamin glass blocks could be optically coated to give an increase in the light efficiency from 10% to about 25%.

The size of the shear interferometer can be reduced since only the prism ends and a thin compensator plate are really needed, so it could be placed in the primary focus of Polaris to avoid the chromatic aberration of the re-imaging lens of the present design.

## APPENDIX A Basic Model of Photographic Density

In the unprocessed emulsion, there are $N_A$ grains in projected area A. There is a distribution of grain sizes (areas), a, and quantum sensitivities, Q (where Q is the minimum number of photons to be absorbed by a grain to make it developable). The proportion of grains of size, a, is $\beta$ and the proportion of grains wth quantum sensitivities, Q is $\alpha$.

The probability that a grain of size, a, will absorb Q or more photons and be made developable is assumed to follow a Poisson distribution. The number absorbed will depend upon size, a and also to an exposure to q absorbed photons per unit area. The average number absorbed per grain is (aq) and the distribution of absorption of 0,1,2,...Q,.. photons is given by the Poisson series,

$$1 = \exp(-aq)+aq\exp(aq)+\frac{(aq)^2}{2!}\exp(-aq)+\ldots+\frac{(aq)^Q}{Q!}\exp(-aq)+\ldots$$

The fraction of grains of size, a, absorbing Q or more photons and hence becoming developable, is

$$P_{Q,a} = \sum_{r=Q}^{\infty} \exp(-aq)\,\frac{(aq)^r}{r!} = 1 - \sum_{0}^{Q-1} \exp(-aq)\,\frac{(aq)^r}{r!} .$$

Now the number of grains unexposed (Q,a) in area A is

$$N_{Q,a} = \alpha\beta N_A ,$$

and so the number made developable is

$$\begin{aligned} n_{Q,a} &= \alpha\beta N_A P_{Q,a} , \\ &= \alpha\beta N_A \{1 - \sum_{0}^{Q-1} \exp(-aq)\,\frac{(aq)^r}{r!}\} . \end{aligned} \qquad (A.1)$$

After development, grains of size a have scaled to size d. Each grain will represent area d to a microdensitometer scanning beam

and so the transmission T is given by

$$T = \frac{A - \sum_Q \sum_a dn_{Q,a}}{A} = 1 - \frac{1}{A} \sum_Q \sum_a dn_{Q,a} ,$$

assuming no overlap of grains. With overlap, the transmission becomes an exponential function of which $1 - 1/A \sum_Q \sum_a dn_{Q,a}$ is an expansion. So

$$T = \exp\left[ - \frac{1}{A} \sum_Q \sum_a dn_{Q,a} \right] .$$

The photographic density, is then

$$D = \log \exp\left[ \frac{1}{A} \sum_Q \sum_a dn_{Q,a} \right] ,$$

using eq A.1

$$D = 0.434 \frac{N_A}{A} \sum_Q \sum_a \alpha_Q \beta_a d \left\{ 1 - \sum_0^{Q-1} \exp(-aq) \frac{(aq)^r}{r!} \right\} ,$$

$$D = 0.434 \frac{N_A \bar{d}}{A} \sum_Q \sum_a \alpha_Q \beta_a \frac{d}{\bar{d}} \left\{ 1 - \sum_0^{Q-1} \exp(-aq) \frac{(aq)^r}{r!} \right\} .$$

Now $d/\bar{d}$ is assumed equal to $a/\bar{a}$ where a is the average size of undeveloped grains. So

$$D = 0.434 \frac{N_A \bar{d}}{A} \sum_Q \sum_a \alpha_Q \beta_a \frac{a}{\bar{a}} \left\{ 1 - \sum_0^{Q-1} \exp(-aq) \frac{(aq)^r}{r!} \right\} .$$

Now $\sum_Q \sum_a \alpha_a \beta_a \, a/\bar{a} = 1$

$$D = \frac{0.434 \, N_A \bar{d}}{A} \left[ 1 \sum_Q \sum_a \alpha_Q \beta_a \frac{a}{\bar{a}} \exp(-aq) \sum_0^{Q-1} \frac{(aq)^r}{r!} \right] . \quad (A.2)$$

There will be a maximum density when all the grains are developable ie the value of the bracket is equal to 1.

$$D_{max} = \frac{0.434 \, N_A \bar{d}}{A} . \quad (A.3)$$

Experimentally there is a $D_{min}$ due to fog. Hence

$$D = D_{max} \left[ 1 - \sum_Q \sum_a \alpha_Q \beta_a \frac{a}{\bar{a}} \exp(aq) \sum_0^{Q-1} \frac{(aq)^r}{r!} \right] + D_{min} . \quad (A.4)$$

## APPENDIX B MTF and PSF for a hexagonal aperture

The modulation transfer function for a hexagonal aperture is calculated as the ratio of the overlap area between two sheared hexagonal apertures and the total area, (fig B.1) ie,

$$MTF(x,y) = \frac{\text{overlap area}}{\text{total area}} = A(x,y) \Big/ \frac{3\sqrt{3}b}{2} , \qquad (B.1)$$

where b is the base length of the hexagon and A(x,y) is given below. But there are four conditions because there are four different rates of change in the overlap area. These conditions are shown diagrammatically in fig B.2 and are given below. It can be calculated only in the top right quarter since MTF(x,y) = MTF(-x,-y), and because of symmetry, for which MTF(x,y) = MTF(x,-y).

1) $A(x,y) = (3b-2x)(\sqrt{3}b/2-y) + y(2b-x-y/\sqrt{3})$

condition: $y = 0,\ 0 \leq x \leq b$ $\qquad y \leq \sqrt{3}x,\ 0 \leq x \leq b/2$

$y = h,\ b/2 \leq x \leq 3b/2$ $\qquad y \geq \sqrt{3}(x-b),\ 0 \leq x \leq \sqrt{3}b/2$

2) $A(x,y) = (3b-x-y/\sqrt{3})(\sqrt{3}b/2-\sqrt{3}x/2-y/2)+\sqrt{3}x(2b-x-y/\sqrt{3})$

condition: $x = 0,\ 0 \leq y \leq 2h$

$y \geq \sqrt{3}x,\ 0 \leq x \leq b/2$ $\qquad y \leq 2h - \sqrt{3}x,\ 0 \leq x \leq b/2$

3) $A(x,y) = (\sqrt{3}b-y)(2b-x-y/\sqrt{3})$

condition: $y = 2h,\ 0 \leq x \leq b$ $\qquad y \leq (2h-\sqrt{3}x),\ 0 \leq x \leq b/2$

$y = h,\ b/2 \leq x \leq 3b/2$ $\qquad y \geq (2h-\sqrt{3}(x-b)),\ b \leq x \leq 3b/2$

4) $A(x,y) = (2b-x-y/\sqrt{3})(\sqrt{3}b-\sqrt{3}x/2+y/2)$

condition: $y = 0,\ b \leq x \leq 2b$

$y < \sqrt{3}(x-b),\ b \leq x \leq 3b/2$ $\qquad y \leq h-\sqrt{3}(x-b),\ 3b/2 \leq x \leq 2b$

where $h = \sqrt{3}b/2$

Fig B.5 shows the MTF for the hexagonal aperture; it has six

corners, which will cause its Fourier transform, the PSF to contain six fans (or spikes) in the diffraction pattern. The shape of the MTF is more similar to the MTF for a circular aperture (see fig 3.22) except at the base which is hexagonal in shape.

After a Fourier transform, the PSF obtained is shown in fig B.6 and is similar to the circular aperture (see fig 3.23) except that the first diffraction ring is not completely circular, but is a hexagonal shape with six shallow peaks at the corners of the hexagon.

Instead of using the Fourier transform of the MTF and to save computing time, the PSF of the hexagonal aperture can be calculated from the square of the amplitude, (fig B.3)

$$PSF(\Theta,\phi) = |a(\Theta,\phi)|^2 ,$$

where

$$a(\Theta,\phi) = \iint \exp[\frac{2\pi i}{\lambda} \sin\Theta\ (x\cos\phi + y\sin\phi)]\ dxdy \ . \qquad (B.2)$$

For each x,y there is a corresponding -x,-y and so the terms of expi(..) and exp-i(..) can be collected to give real terms. Further from symmetry, the amplitude needs to be calculated using only the top half of the hexagon, so

$$a(x,y) = \iint 2\ \cos[k(x\cos\phi + y\sin\phi)]\ dxdy ,$$

where $k = 2\pi \sin\Theta/\lambda$. The top half of the hexagon can be split into three regions for the integration (fig B.4), ie

$$a(\Theta,\phi) = 2(A + B + C) .$$

After calculation, the three amplitudes, A, B and C are obtained and then are added to give an overall amplitude, ie,

$$a(\Theta,\phi)=\frac{4}{k^2\sin\phi}\left[\left(-\cos(kb\cos\phi)\sqrt{3}\sin\phi-\cos\phi\left(\sin\left(\frac{kb}{2}\cos\phi\right)\sin\left(\frac{\sqrt{3}kb}{2}\sin\phi\right)\right.\right.\right.$$

$$\left.\left.\left.+\sqrt{3}\sin\phi\left\{\cos\left(\frac{kb}{2}\cos\phi\right)\cos\left(\frac{\sqrt{3}kb}{2}\sin\phi\right)\right\}\right)\Big/(\cos^2\phi-3\sin^2\phi)\right.\right.$$

$$\left.\left.+\sin\left(\frac{kb}{2}\cos\phi\right)\sin\left(\frac{\sqrt{3}kb}{2}\sin\phi\right)\Big/\cos\phi\right]\right. . \qquad (B.3)$$

The PSF is found by squaring the amplitude and is shown in fig B.6.

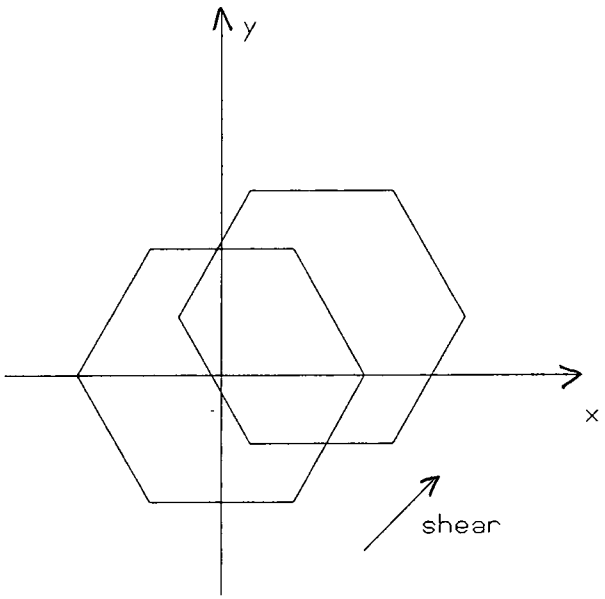


FIG B.1 Two sheared hexagonal apertures

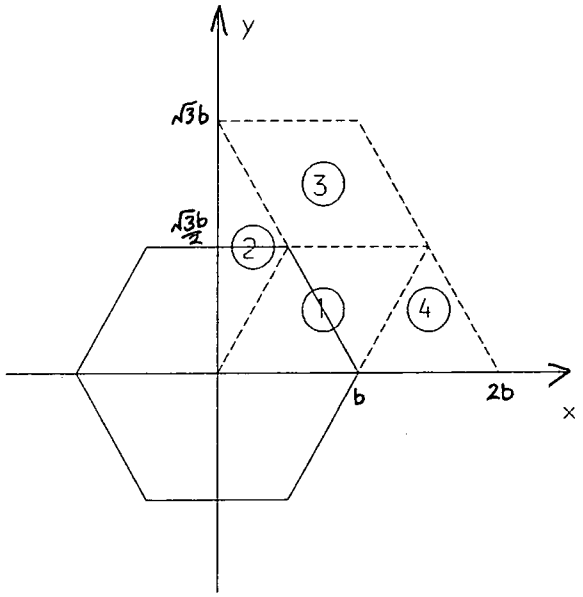


FIG B.2 Conditions of overlap area

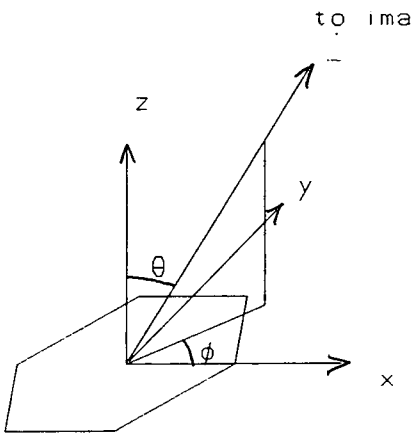


FIG B.3 Hexagon on polar coordinates

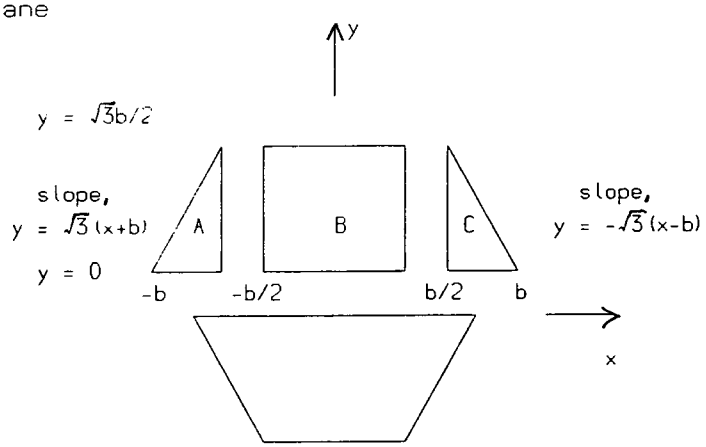


FIG B.4 Top part of hexagon split into 3 parts for integration

MODULATION TRANSFER FUNCTION

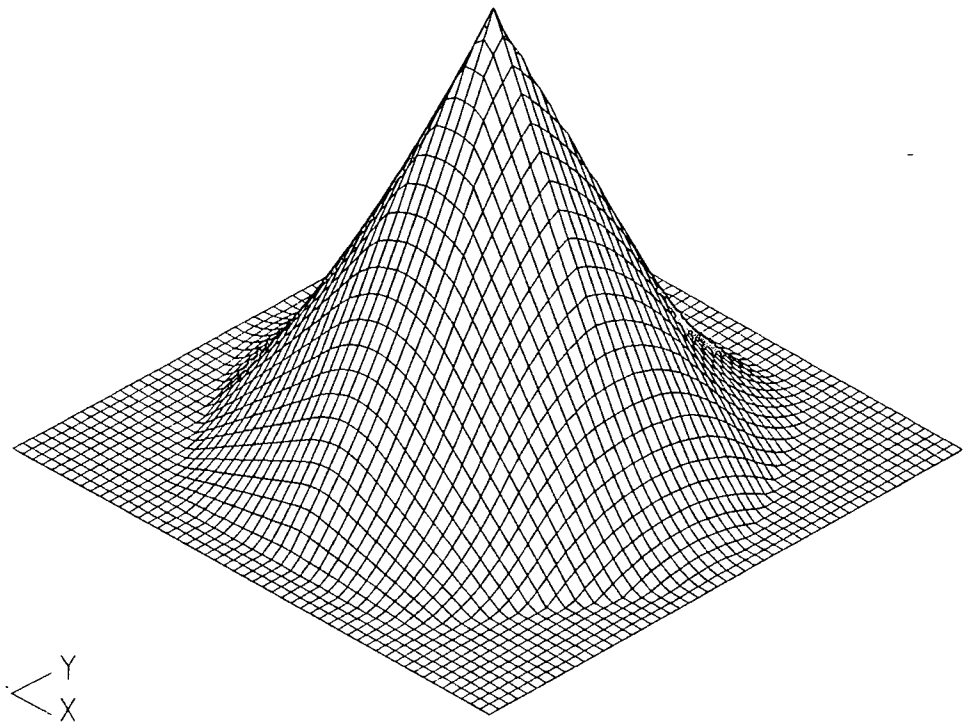


FIG B.5 MTF of the hexagonal aperture

POINT SPREAD FUNCTION

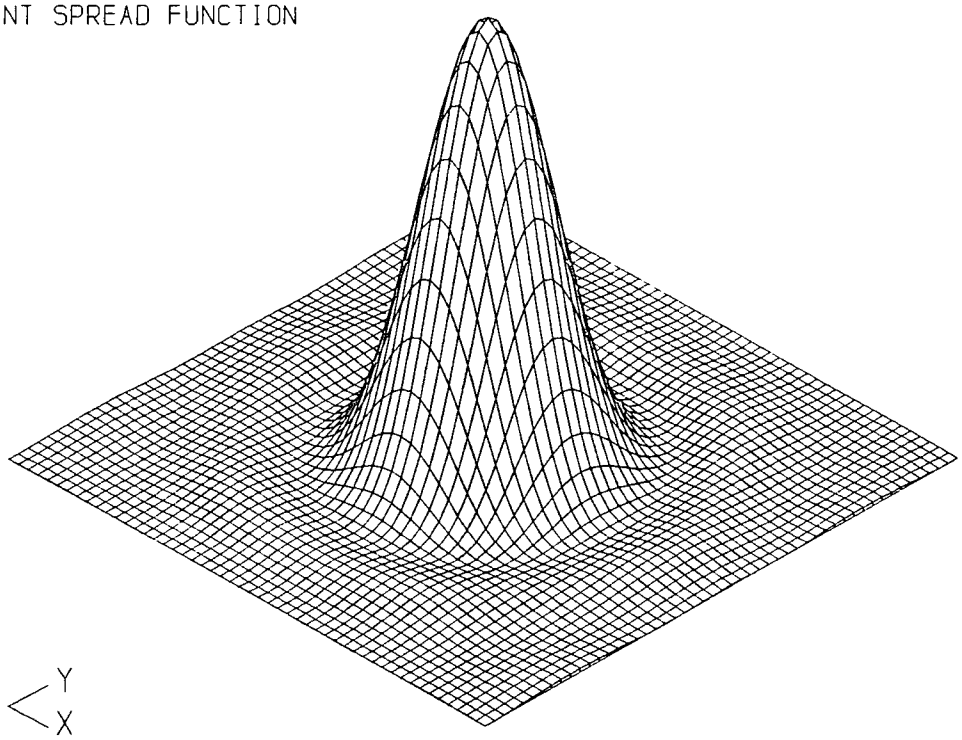


FIG B.6 PSF of the hexagonal aperture

## APPENDIX C MTF for annular aperture

Modulation transfer function for annular aperture is (O'Neill, ref 3.1)

$$MTF(w) = \frac{(A + B + C)}{(1 - \eta^2)},$$

where $\eta = r_2 / r_1$, the ratio of the internal and external radii and

$$A = \begin{cases} \frac{2}{\pi}\left[\cos^{-1}\frac{\lambda w}{2r_1} - \frac{\lambda w}{2r_1}\left[1 - \left(\frac{\lambda w}{2r_1}\right)^2\right]^{1/2}\right] & 0 \leq \lambda w \leq 2r_1 \\ 0 & \lambda w > 2r_1 \end{cases}$$

$$B = \begin{cases} \frac{2\eta}{\pi}\left[\cos^{-1}\frac{\lambda w}{2r_2} - \frac{\lambda w}{2r_2}\left[1 - \left(\frac{\lambda w}{2r_2}\right)^2\right]^{1/2}\right] & 0 \leq \lambda w \leq 2r_2 \\ 0 & \lambda w > 2r_2 \end{cases}$$

$$C = \begin{cases} -2\eta^2 & 0 \leq \lambda w \leq r_2(1-\eta) \\ -2\eta^2 + \frac{2\eta}{\pi}\sin\phi + \left(\frac{1+\eta^2}{\pi}\right)\phi - 2\left(\frac{1-\eta^2}{\pi}\right)\tan\left[\left(\frac{1+\eta}{1-\eta}\right)\tan\frac{\phi}{2}\right] & r_2(1-\eta) \leq \lambda w \leq r_1(1-\eta) \\ 0 & \lambda w > r_1(1-\eta) \end{cases}$$

where $\phi = \cos^{-1}\left(\frac{1+\eta^2 - (\lambda w/\eta)^2}{2\eta}\right)$

## APPENDIX D RGO Large Multi-mirror telescope

The design of the RGO large multi-mirror telescope consists of six parabolic primary mirrors, each of 7.5m diameter and each with a central hole of 2m diameter, as shown in fig D.1. This shows a different configuration from the Arizona MMT, as each circular mirror has a slice cut off two of its sides to form scallop shapes. These correspond to the hexagons with circumscribed circles which form a compact system.

The diffraction pattern for the scallopped mirrors can only be handled approximately since they do not meet the symmetry requirements detailed in section 3.3. The approximation comes about from considering them as circular mirrors with a degree of overlap and allowing for this. This is difficult analytically except by approximating the overlap by a rectangle (too large) or by a rhomboid of half the area of the rectangle (too small). Since it is found that the amplitude is essentially the same for the two overlap geometries at small image sizes, the amplitude correction for the rectangular area is taken scaled to the correct overlapping area of two circles. The PSF for the scallopped mirrors is shown in fig D.2

The radius of the Airy disc is 0.006 arcsec and the enclosed energy is 58% of the total energy. The scallopped mirrors produce less pronounced secondary maxima than the six touching circular mirrors (see fig 6.8b), hence the Airy disc has more enclosed energy. However, there is a reduction in the resolution since the overall diameter of the six circular mirrors with the same area is bigger.

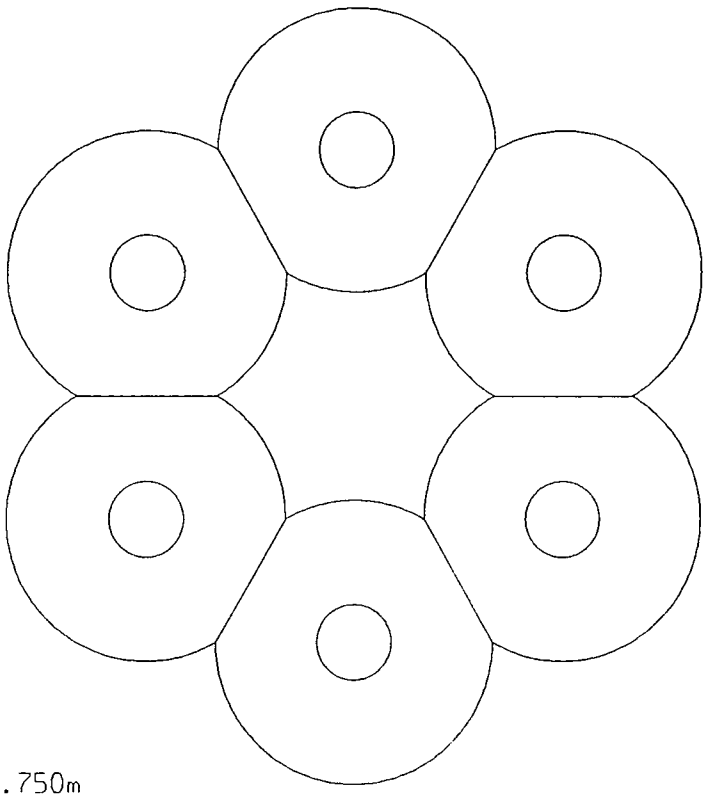

radius, r= 3.750m

separation between centres, e= 6.495m

FIG D.1 Configuration of RGO Large multi-mirror telescope

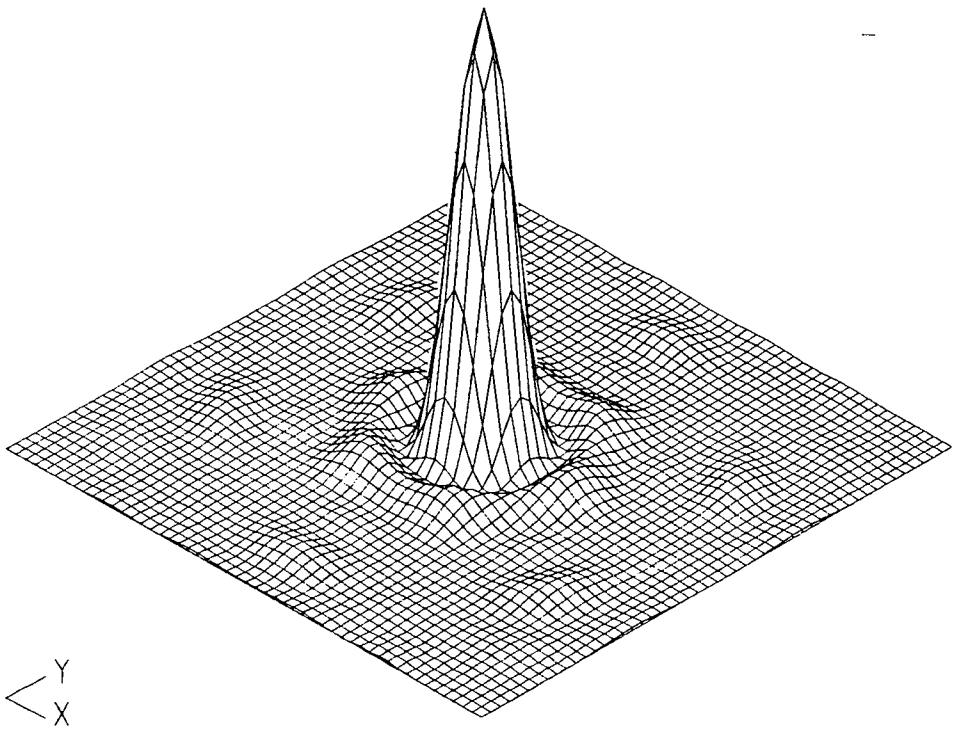


FIG D.2 PSF of RGO Large multi-mirror telescope

## APPENDIX E Theory of fringe formation in the Durham Polaris monitor

In the shear interferometer (as described in section 7.3.3), there are two interfering beams, of which one is a direct beam with a complex amplitude, $A(x,y,t)$ and the other is a sheared beam with a complex amplitude, $A'(x+s,y,t)$. The angular magnification, m, of the prism pair is independent of shear to a good approximation, ie $A'(x+s,y,t) = fA(x+s,y,t)$ where $f \approx 1/m$. The second Jamin block is tilted to introduce a wedge angle, $\alpha$, which changes the phase of $A'$ by $\exp(4\pi i \alpha y/\lambda)$. The amplitude is seen to be wavelength dependent. Hence the contribution to the intensity of the fringe pattern is:

$$dI_\lambda = \left| A_\lambda(x,y,t) + fA_\lambda(x+s,y,t)\exp(4\pi i \alpha y/\lambda) \right|^2 d\lambda \quad . \qquad (E.1)$$

An assumption is made that seeing is manifestly a change in phase rather than a change in amplitude, therefore

$$A'_\lambda(x+s,y,t) = A_\lambda(x,y,t)\exp(i\phi_o) \text{ and } |A_\lambda(x,y,t)|^2 = |A'_\lambda(x+s,y,t)|^2 ,$$

where $\phi_o$ is the phase difference between two amplitudes at a shear. Hence equation E.1 becomes:

$$dI_\lambda = |A_\lambda(x,y,t)|^2 [\ 1 + f^2 + 2f\cos(4\pi\alpha y/\lambda + \phi_o)\ ]\ d\lambda ,$$

and can be rewritten as:

$$dI_\lambda = R [\ 1 + f^2 + 2f\cos(4\pi\alpha y/\lambda + \phi_o)\ ]\ i_\lambda(x,y,t)\ d\lambda ,$$

where $i_\lambda$ is the intensity of the incident wavefront and R is the light efficiency of the shear interferometer. The phase difference, $\phi_o$, is wavelength dependent, ie $\phi_o$ becomes $\lambda_o \phi_o/\lambda$. Then

$$I_\lambda = (1+f^2)R \int i_\lambda\, d\lambda + 2fR \int \cos(4\pi\alpha y/\lambda + \lambda_o \phi_o/\lambda)\ i_\lambda\, d\lambda .$$

This intensity, $I_\lambda$, needs to be averaged over the representative

set of phases associated with that particular shear, s. Therefore

$$I(s) = (1+f^2)R \int_\lambda i_\lambda d\lambda + 2fR \sum_{\phi_o} \overline{\int_\lambda \cos(4\pi\alpha y/\lambda + \lambda_o \phi_o/\lambda)\, i_\lambda d\lambda} .$$

Since $\lambda$ and $\phi_o$ are independent of each other, the order of integrating and summing can be reversed and the cosine term is expanded into the sine and cosine terms. At a fixed wavelength, the average of the sum of the sine terms will be reduced to zero for the full range of $\phi_o$ values (positive and negative ones), whereas the average of the sum of the cosine terms will only be reduced to zero if $\phi_o$ values stretch uniformly through $\pm\pi$. Therefore

$$I(s) = (1+f^2)R \int_\lambda i_\lambda d\lambda + 2fR \int_\lambda \cos(4\pi\alpha y/\lambda)\, \overline{\cos(\lambda_o \phi_o/\lambda)}\, i_\lambda d\lambda . \quad (E.2)$$

Without seeing or at the zero shear where the phase differences, $\phi_o$, are zero, equation E.2 becomes:

$$I(s) = (1+f^2)R \int_\lambda i_\lambda d\lambda + 2fR \int_\lambda \cos(4\pi\alpha y/\lambda)\, i_\lambda d\lambda . \quad (E.3)$$

By comparing the two equations, E.2 and E.3, at a given wavelength the effect of seeing is to reduce the effective f from f to $\overline{f\cos(\lambda_o \phi_o/\lambda)}$ (see fig E.1). Consequently for a single wavelength, $\lambda_o$, the fringes will have a cosine intensity whose modulation reduces with increased shear (ie broader phase difference distribution): ie,

$$\text{modulation at shear, } M_i = \frac{I_{max} - I_{min}}{I_{max} + I_{min}} = \frac{2f\overline{\cos\phi_o}}{1 + f^2}$$

$$\text{modulation at zero shear or without seeing, } M_o = \frac{2f}{1 + f^2}$$

Hence MTF(s) = $\overline{\cos\phi_o}$. For each value of $\phi_o$, the cosine fringes are shifted, but the individually shifted fringes add up in total to give the cosine term with reduced modulation.

For a spectrum of wavelengths, the white light fringe pattern will be demodulated when phase shifts are introduced. However the phase shifts are wavelength dependent, so not only is the pattern demodulated but its detailed shape changes (see fig E.2). This is quite severe for a square spectrum of wavelengths. Then the information given by the pattern shows the central maximum at $1+f^2+2f\overline{\cos(\lambda_o \phi_o/\lambda)}$ and the average intensity still at $1+f^2$. Therefore modulation at shear is $2f\overline{\cos(\lambda_o \phi_o/\lambda)} \;/\; (1+f^2)$ and MTF = $\overline{\cos(\lambda_o \phi_o/\lambda)}$.

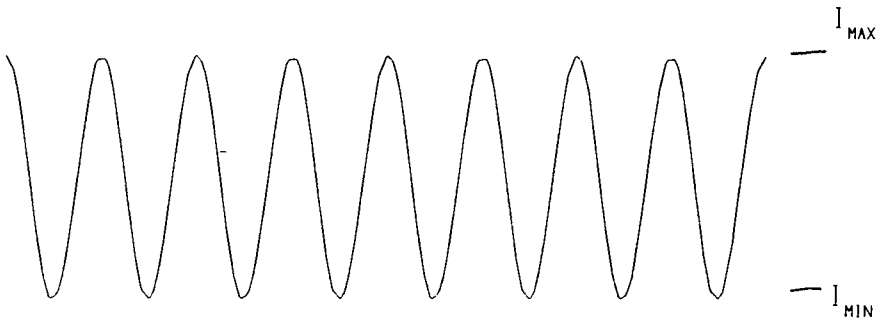


a) at zero shear


b) at shear, s

FIG E.1 Single wavelength fringe pattern

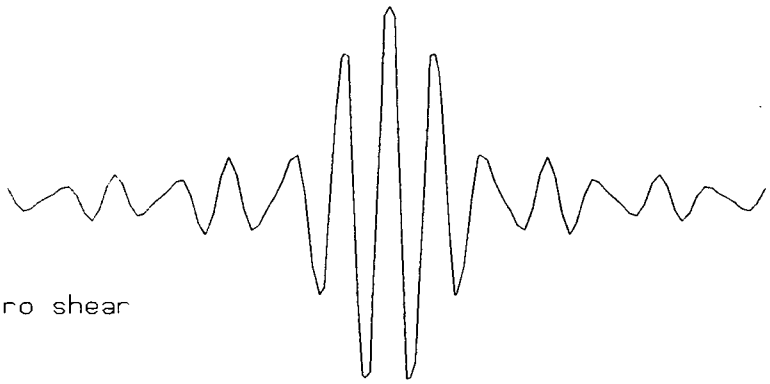

a) at zero shear

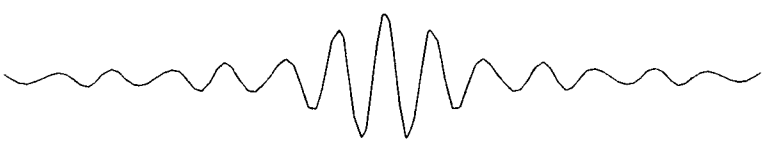

b) at shear, s

FIG E.2 White light fringe pattern

## APPENDIX F Apparent motion of Polaris in the field of view in the Durham Polaris monitor

The ocular eyepiece of the Durham Polaris monitor (as shown in fig 7.14 and plate no. 7.13) rotates with the telescope frame about the mechanical axis of the telescope. The optical axis, OA, is approximately at the centre of the field of view with the appropriate values of the hour angle, H, and the angular offset, d, of the parabolic mirror, ie the angle between the mechanical axis, MA, and the optical axis. These are shown in fig F.1.

Suppose that the mechanical axis, MA, does not coincide with the north celestial pole, CP, but is displaced by two angles, f and g, (at right angles to each other) from the celestial pole. $H_o$ is the true hour angle of Polaris. The difference between this hour angle and the telescope's hour angle is h. The angular offset of Polaris from the north celestial pole is $d_o$.

The position of Polaris, P, relative to MA is

$$x = -d_o \sin H_o + f \ ,$$
$$y = d_o \cos H_o + g \ , \qquad (F.1)$$

and the position of OA relative to MA is

$$x_o = -d\sin H \ ,$$
$$y_o = d\cos H \ . \qquad (F.2)$$

Then the difference between P and OA is

$$r^2 = (x - x_o)^2 + (y - y_o)^2 \ , \qquad (F.3)$$

and using equations (F.1) and (F.2), this gives

$$r^2 = d_o^2 + d^2 + f^2 + g^2 - 2d_o d\cos(H - H_o) + 2f(d\sin H - d_o \sin H_o) - 2g(d\cos H - d_o \cos H_o). \qquad (F.4)$$

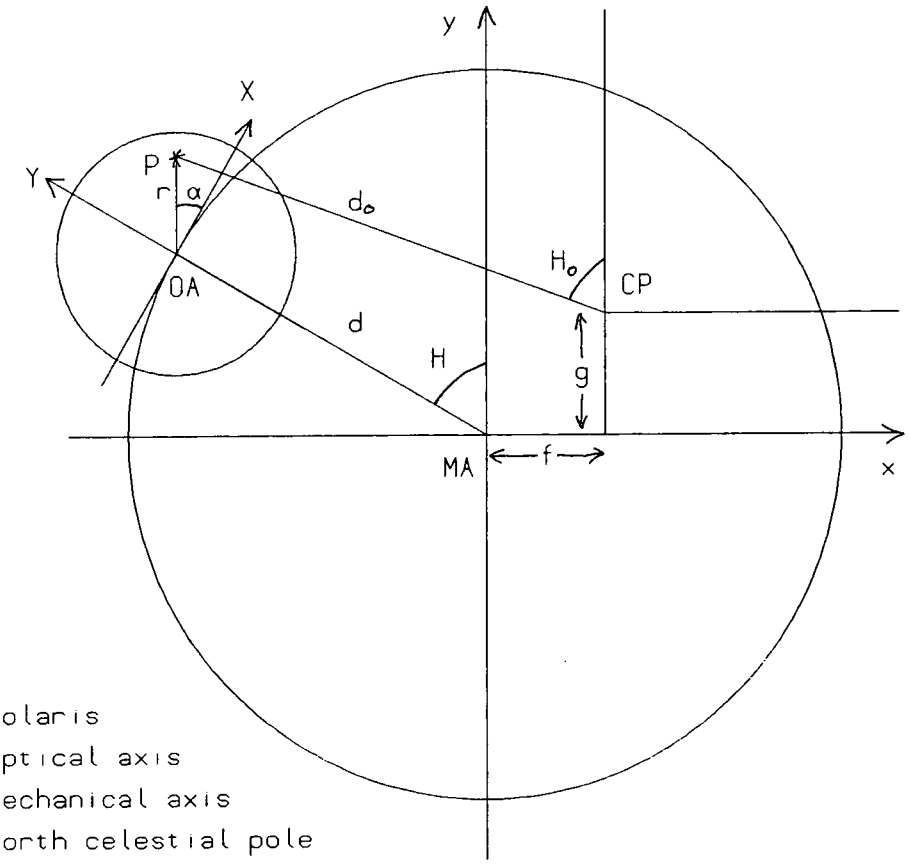


P - Polaris
OA - Optical axis
MA - Mechanical axis
CP - North celestial pole

FIG F.1 Field of view in the Durham Polaris monitor

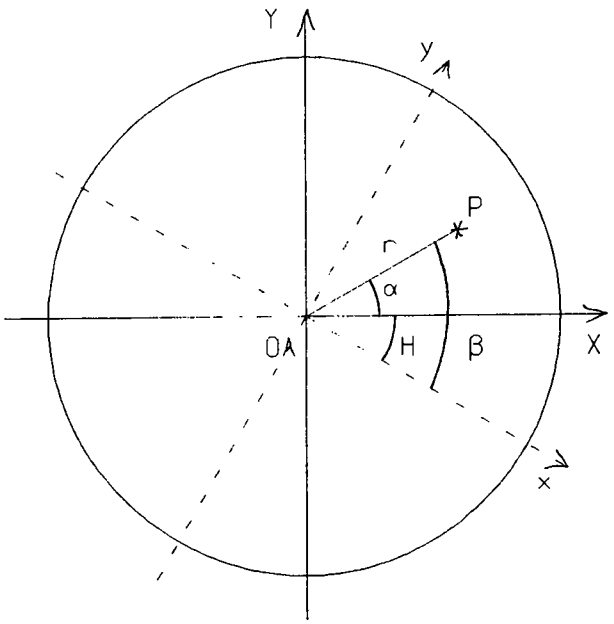


FIG F.2 Field of view

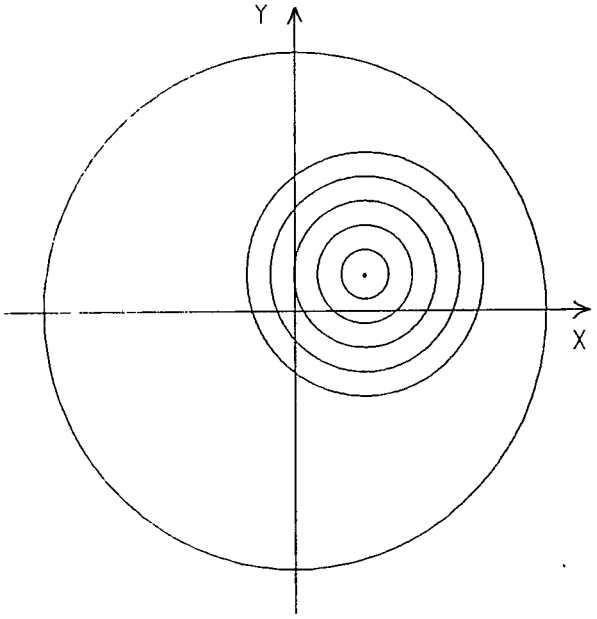


FIG F.3 Image tracks of Polaris in the field of view

The angle between the X-axis and a line between P and OA, $\alpha$, (as shown in fig F.2) is given as

$$\alpha = \beta - H \ , \qquad (F.5)$$

where $\beta = \tan^{-1}(y - y_o)/(x - x_o)$ and using equations (F.1) and (F.2),

$$\beta = \tan^{-1}\left\{\frac{d_o\cos H_o - d\cos H + f}{-d_o\sin H_o + d\sin H + g}\right\} \ , \qquad (F.6)$$

hence

$$\alpha = \tan^{-1}\left\{\frac{d_o\cos H_o - d\cos H + f}{-d_o\sin H_o + d\sin H + g}\right\} - H \ . \qquad (F.7)$$

The values of r and $\alpha$ will describe the apparent motion of Polaris in the field of view. Some examples of the motion are given below:-

i) The angle between the mechanical axis, MA, and the north celestial pole, CP, is assumed to be equal to zero, ie f = 0 and g = 0. Then

$$r^2 = d_o^2 + d^2 - 2d_od\cos h \ ,$$

ie constant and independent of hour angle, $H_o$.

$$\alpha = \tan^{-1}\left\{\frac{d_o\cos H_o - d\cos H}{-d_o\sin H_o + d\sin H}\right\} - H \ .$$

Further,

a) if $H = H_o$ and $d \neq d_o$, then $r^2 = d_o^2 + d^2 - 2d_od$ and

$$\alpha = \tan^{-1}\left\{\frac{d_o\cos H_o - d\cos H_o}{-d_o\sin H_o + d\sin H_o}\right\} - H_o \ ,$$

$$\alpha = \tan^{-1}\left(\cot H_o\left\{\frac{d_o - d}{-d_o + d}\right\}\right) - H_o \ ,$$

$$\alpha = \tan^{-1}(\cot(-H_o)) - H_o = -\pi/2 \ ,$$

ie constant and does not depend on the hour angle, $H_o$. There will be fixed position whose distance from OA is $d_o^2 + d^2 - 2d_od$ along y-direction. Alternatively

b) if $d = d_o$ and $H \neq H_o$ and $H = H_o + h$, then $r^2 = 2d_o^2(1 - \cos h)$ and

$$\alpha = \beta - H \ ,$$

taking tan of both sides, ie

$$\tan\alpha = \tan(\beta - H) \ ,$$

$$\tan\alpha = \frac{\tan\beta - \tan H}{1 + \tan\beta\tan H} \ ,$$

using equation (F.6)

$$\tan\alpha = \frac{\frac{\cos H_o - \cos H}{-\sin H_o + \sin H} - \frac{\sin H}{\cos H}}{1 + \left[\frac{\cos H_o - \cos H}{-\sin H_o + \sin H}\right]\left[\frac{\sin H}{\cos H}\right]} \ ,$$

$$\tan\alpha = \frac{\cos H_o\cos H - \cos^2 H + \sin H_o\sin H - \sin^2 H}{-\sin H_o\cos H + \sin H\cos H + \cos H_o\sin H - \cos H\sin H} \ ,$$

$$\tan\alpha = \frac{\cos(H_o - H) - 1}{\sin(H_o - H)} \ ,$$

hence

$$\tan\alpha = \frac{\cos h - 1}{\sin h} \ .$$

Expanding

$$\tan\alpha = \frac{\cos^2(h/2) - \sin^2(h/2) - \sin^2(h/2) - \cos^2(h/2)}{2\cos(h/2)\sin(h/2)} \ .$$

Hence $\alpha = h/2$ ie constant and does not depend on the hour angle, $H_o$. There will be a fixed position whose distance from OA is $2d_o^2(1 - \cos h)$.

ii) If there is a displacement between the mechanical axis and the north celestial pole ie $f \neq 0$ and $g \neq 0$.

a) when d is equal to $d_o$ and H is equal to $H_o$ (ie $h = 0$), then $r^2 = f^2 + g^2$ does not depend on the hour angle and is constant. However $\alpha = \tan^{-1}(f/g) - H_o$ depends on the hour angle, so the image of Polaris will move round about the centre, OA, with a radius of $(f^2 + g^2)^{1/2}$.

b) For the general case of all parameters out of adjustment, then the image of Polaris will move along a circular path about a point displaced from OA. This is shown in fig F.3 as a series

of circles for decreasing values of $(f^2 + g^2)^{1/2}$. This means that f and g are the most important parameters on the adjustment of the alignment of the telescope.

## REFERENCES


| ref.no | | | |
|---|---|---|---|
| 3.1 | O'Neill | J.Opt.Soc.Am. 46 p285 | (1956) |
| 3.2 | Kolmogorov | Dokl. Akad. Nauk SSSR 30 p301 | (1941) |
| 3.3 | Tatarski | 'Wave Propagation in a Turbulent Medium' (McGraw-Hill) | (1961) |
| 3.4 | Gur'yanov | Sov. Astron 28 p343 | (1984) |
| 3.5 | Wyngaard et al | J.Opt.Soc.Am. 61 p1646 | (1971) |
| 3.6 | Fried | J.Opt.Soc.Am. 56 p1372 | (1966) |
| 3.7 | Hufnagel and Stanley | J.Opt.Soc.Am. 54 p52 | (1964) |
| 3.8 | ref 3.7 p58 | | |
| 3.9 | Boyd | J.Opt.Soc.Am. 68 p877 | (1978) |
| 3.10 | Selby, Wade and Sanchez Magro | Mon.Not.R.Astr.Soc 187 p553 | (1979) |
| 3.11 | D.S.Brown | Optical and IR telescopes for the 1990's ed A.Hewitt (KPNO) p999 | (1980) |
| 3.12 | Fried | IAU Colloquium No.50 p4.1-4.43 | (1978) |
| 4.1 | Bowen | 'Telescopes' ed Kuiper and Middlehurst (Chicago Press) | (1960) |
| | D.S.Brown | Private paper | |
| 4.2 | Kodak Publication P-315 | | (1973) |
| 4.3 | Dainty and Shaw | 'Image Science' (Academic Press) | (1974) |
| 4.4 | 'MINUIT' CERN Computer program library D506/D516 | | (1977) |
| 4.5 | Furenlid | Modern Techinques in Astronomical Photography ed Hendier+West p153 | (1978) |
| 4.6 | Farnell | Jour. of Photo. Sci. 17 p116 | (1969) |
| 4.7 | Brown et al | IAU Colloquium 78 p185 | (1983) |
| 5.1 | Beckers et al | Telescopes for the 1980's ed Burbidge and Hewitt p63 | (1981) |
| 5.2 | Bingham | IAU Colloquium 79 p347 | (1984) |
| 5.3 | Barr et al | SPIE Proceedings 444 p37 | (1983) |
| 5.4 | Mack | SPIE Proceedings 444 p23 | (1983) |

| | | | |
|---|---|---|---|
| 5.5 | Nelson | SPIE Proceedings 332 p109 | (1982) |
| 5.6 | Nelson et al | SPIE Proceedings 444 p274 | (1983) |
| 7.1 | Wessely et al | J.Opt.Soc.Am. 60 p678 | (1970) |
| | Bertolotti et al | J.Opt.Soc.Am. 60 p1603 | (1970) |
| 7.2 | Roddier and Roddier | J.Opt.Soc.Am. 63 p661 | (1973) |
| | ref 7.3, ref 7.9 and ref 7.10 | | |
| 7.3 | Brown and Scaddan | Observatory 99 p125 | (1979) |
| 7.4 | Woolf | Opt. and IR Telescopes for the 1990's ed Hewitt (Kitt Peak Nat.Ob.) p1112 | (1980) |
| 7.5 | McInnes and Walker | Pub.Astro.Soc.Pacific 86 p529 | (1974) |
| 7.6 | Walker | Pub.Astro.Soc.Pacific 83 p401 | (1971) |
| 7.7 | Barletti et al | Astron. Astrophys. 54 p649 | (1977) |
| 7.8 | Brandt and Wohl | Astron. Astrophys. 109 p77 | (1982) |
| 7.9 | Dainty and Scaddan | Mon.Not.R.Astr.Soc. 170 p519 | (1975) |
| 7.10 | Roddier | J.Opt.Soc.Am. 66 p478 | (1976) |

ACKNOWLEDGEMENTS

I would like to thank Professors A.W. Wolfendale FRS and B.H. Bransden who as sequential heads of the Physics department in Durham, made available the facilities of the department throughout this work.

I wish particularly to thank Dr J.V. Major who, as my supervisor, has been of considerable help throughout and a constant source of advice.

Thanks also go to Dr D.S. Brown of Grubb Parsons, (now at the Physics department in Durham) for advice on shear interferometers and corrector plates of Schmidt telescopes.

I acknowledge the financial support given to me by a Durham University research studentship for the first three years and two awards from the Snowdon and Greatham Trusts.

Thanks are due to Mr E.C. Davies who, as a tutor for hearing-impaired students has provided much support and also to Dr Margaret Collins who has put in many hours of checking my thesis.